KINETIC STUDIES AND COMPUTATIONAL MODELING OF ATOMIC CHLORINE REACTIONS IN THE GAS PHASE

Ionut M. Alecu, B.A.

Dissertation Prepared for the Degree of

DOCTOR OF PHILOSOPHY

UNIVERSITY OF NORTH TEXAS

August 2009

APPROVED:

Paul Marshall, Major Professor
Weston T. Borden, Committee Member
Martin Schwartz, Committee Member
Mohammad A. Omary, Committee Member
Michael G. Richmond, Chair of the Department of Chemistry
Michael Monticino, Dean of the Robert B. Toulouse School of Graduate Studies

Alecu, Ionut M. Kinetic studies and computational modeling of atomic chlorine reactions in the gas phase. Doctor of Philosophy (Chemistry), August 2009, 315 pp., 48 tables, 69 illustrations, references, 254 titles.

The gas phase reactions of atomic chlorine with hydrogen sulfide, ammonia, benzene, and ethylene are investigated using the laser flash photolysis / resonance fluorescence experimental technique. In addition, the kinetics of the reverse processes for the latter two elementary reactions are also studied experimentally. The absolute rate constants for these processes are measured over a wide range of conditions, and the results offer new accurate information about the reactivity and thermochemistry of these systems. The temperature dependences of these reactions are interpreted via the Arrhenius equation, which yields significantly negative activation energies for the reaction of the chlorine atom and hydrogen sulfide as well as for that between the phenyl radical and hydrogen chloride. Positive activation energies which are smaller than the overall endothermicity are measured for the reactions between atomic chlorine with ammonia and ethylene, which suggests that the reverse processes for these reactions also possess negative activation energies. The enthalpies of formation of the phenyl and β-chlorovinyl radicals are assessed via the third-law method.

The stability and reactivity of each reaction system is further rationalized based on potential energy surfaces, computed with high-level *ab initio* quantum mechanical methods and refined through the inclusion of effects which arise from the special theory of relativity. Large amounts of spin-contamination are found to result in inaccurate computed thermochemistry for the phenyl and ethyl radicals. A reformulation of the computational approach to incorporate spin-restricted reference wavefunctions yields computed thermochemistry in good accord with experiment. The computed potential energy surfaces rationalize the observed negative

temperature dependences in terms of a chemical activation mechanism, and the possibility that an energized adduct may contribute to product formation is investigated via RRKM theory.

ACKNOWLEDGEMENTS

I am eternally grateful to my major professor, Dr. Paul Marshall, who has patiently guided me throughout my academic endeavors at the University of North Texas. I have had the pleasure of learning from him in the classroom and in the research laboratory, and have found him to be equally extraordinary in both roles. His high regard for the scientific method, profound knowledge of chemistry, and infectious passion for chemical kinetics have inspired me and shaped my thinking. I feel truly privileged to have had the benefit of being mentored by a scientist and educator of his caliber.

I am also indebted to the other members comprising my Ph. D. committee: Dr. Martin Schwartz, Dr. Weston T. Borden, and Dr. Mohammad Omary. Drawing upon their endless wisdom during thought-provoking discussions has undoubtedly furthered my academic development.

I wish to thank the members of the research group for their help in carrying out this research. In particular, I would like to express my gratitude to Dr. Yide Gao, who aside from assisting with the data acquisition for all four projects in this dissertation, has also been instrumental in aiding me with the understanding, use, maintenance, and troubleshooting of the experimental apparatus. I would also like to thank Pao-Ching Hsieh for assistance with the data acquisition for the NH_3Cl and C_6H_6Cl projects, Andrew McLeod, Jordan Sand, and Ahmet Ors for assistance with the data acquisition for the C_6H_6Cl project, Katherine Kerr, Kristopher Thompson, and Nicole Wallace for their assistance with the data acquisition for the C_2H_4Cl project.

I have been very fortunate and am extremely thankful to have had continual support and encouragement from my wife, Allison, my parents, Marius and Rodica, and the rest of my wonderful family.

Finally, I wish to thank the Department of Chemistry at the University of North Texas and the Robert A. Welch Foundation (Grant B-1174) for financial support. I would also like to thank the National Center for Supercomputing Applications (Grant CHE000015N) and the Center for Advanced Scientific Computing and Modeling at the University of North Texas (funded in part by the National Science Foundation with Grant CHE-0342824) for computational resources.

TABLE OF CONTENTS

LIST OF TABLES

LIST OF ILLUSTRATIONS

CHAPTER 1

INTRODUCTION

The chlorine atom belongs to the highly reactive class of free radicals, which are species that possess an unpaired electron, and are often also denoted as open-shell systems.[1,2] Chlorine atoms have been implicated in important processes such as surface etching, chemical laser operation, and, most notably, ozone layer depletion.[3,4] In light of their notorious effect on the ozone layer, an accurate assessment of the reactivity of chlorine atoms towards other atmospherically relevant species becomes important. Effective experimental and computational techniques for accurately treating such systems of reactions are discussed in chapters 2 and 3, respectively.

The reaction of hydrogen sulfide with chlorine atoms, which is the subject of chapter 4, is not only relevant in the Earth's stratosphere but also in the lower atmosphere of Venus. On Earth, hydrogen sulfide can be generated in local high concentrations in the stratosphere as a result of volcanic eruptions. For example, recent measurements of H_2S concentrations by UV spectroscopy at volcanic sites in Italy have shown that this quantity can be on the order of hundreds of parts per million (much larger than its average atmospheric concentration of just fractions of a part per billion), and is between two to three times more abundant than SO_2.[5] On Venus, where hydrogen sulfide is more abundant, studies have suggested a coupling between chlorine and sulfur chemistries.[6-8]

The reactions between chlorine atoms and another atmospherically significant species - ammonia, are explored in chapter 5. Ammonia constantly escapes into the atmosphere as a result of the volatilization of nitrogen-containing organic compounds such as urea, which are formed through bacterial decomposition of soil fertilizers.[9] As early as the late 1960s, it was recognized that in terms of natural abundance among nitrogen-containing species being released into the atmosphere, ammonia is second only to nitrous oxide.[9] Due to its abundance and short residence time in the atmosphere, ammonia is important in the generation of nitrogen atoms via sun-powered photolysis, and participates in their circulation through the atmosphere.[9] Aside from atmospheric applications, the reaction between ammonia and chlorine atoms has also generated interest from the field of propulsion kinetics, as ammonium perchlorate is a widely used modern propellant.[10] Finally, ammonia has been implicated in interstellar chemistry and has also been found in the atmospheres of other planets such as Jupiter, Saturn, and Uranus.[11,12]

The interaction between chlorine atoms and non-methane hydrocarbons such as ethylene and benzene in the atmosphere will change its composition, which can lead to reduced stratospheric ozone layer destruction and alterations in the stability of the environment.[13] Combustion processes such as the incineration of chlorinated wastes and fuel contaminants release chlorine atoms, providing another context for reactions between these free radicals and hydrocarbons, though under much different external conditions.[14,15] The chlorination of hydrocarbons leftover from the incomplete combustion of organic waste is particularly significant when the ratio of H to Cl atoms is low, resulting in the release of undesirable side products into the atmosphere.[15] The reactions between chlorine atoms with benzene and ethylene are examined in chapters 6 and 7, respectively.

The goal of these projects is to simulate environments similar to those in the regions of interest of the atmosphere and in various combustion processes. This is achieved by varying conditions such as temperature, pressure, and the concentrations of the species of interest in the reactor. The chlorine atoms are generated photolytically via ultra violet pulsed laser radiation, and their relative concentration is monitored as a function of time. This technique (which is described in more detail in chapter 2) is known as flash photolysis, and due to its considerable value and practicality in the field of radical kinetics, Norrish and Porter were awarded the Nobel prize in 1967 for its development.[16] The ensuing results from these experiments not only provide more accurate rate constants than previously available to the scientific community, but also encompass larger ranges of conditions, resulting in more extensive studies than in the past. In many cases, these comprehensive studies have revealed new information about the system in question, such as Arrhenius parameters, which provide fundamental insight into important chemical details such as the nature of the transition state. In fact, the benzene reaction has only been previously investigated at room temperature, and only a single study has been reported in the case of the ammonia reaction, also focusing just on room temperature. It is important to examine the behavior of reactions over a wide range of temperature as this leads to useful information such as activation energies and thermochemistry, which are the fundamental concepts used to interpret a system's reactivity and stability. One of the most noteworthy discoveries has been that the reverse of the benzene and chlorine atom abstraction reaction, which involves the phenyl radical and hydrogen chloride and has never been studied before, yielded a significantly negative activation energy. This is an unusual result, as activation energies are generally expected to be positive for classical abstraction reactions.[16]

Furthermore, the experiments are supplemented with high-level theoretical quantum mechanical computations using the chemistry department's state-of-the-art computational resources. As with the experiments, these theoretical studies have provided more accurate and extensive information regarding the systems of interest than can be found in the existing literature, and in some cases, completely pioneering results as none were previously available. A description of the computational methodologies employed in these studies constitutes the content of chapter 3. Theoretical computations can be used to calculate barriers to reactions and their thermochemistry, making it even more desirable that these quantities also be determined experimentally to have a basis for comparison between theory and experiment. Computational methods found to be accurate can then be used as a predictive tool in future projects, and have in many cases already helped immensely in elucidating the mechanism of the reactions in question. For example, high-level computations have rationalized the negative activation energy for the phenyl radical and hydrogen chloride observed experimentally, and have also shown that the reverse reactions of all of the abstraction reactions comprising this dissertation should also possess negative activation energies, with the exception of the H_2SCl system, in which computations have validated the observed negative activation energy for the forward reaction.

In certain instances, however, it has been found that some usually accurate and frequently used computational methods fail to describe a system correctly. For example, during the computational study of the benzene / chlorine atom system presented in chapter 6, it has been found that many mainstream computational methods significantly miscalculate the carbon-hydrogen bond strength in benzene, a quantity that is of importance due to the many uses of benzene in the industry. This has been attributed to the fact that when a carbon-hydrogen bond is cleaved in benzene, the ensuing phenyl radical that is formed is not described correctly by the

typical spin unrestricted reference wavefunctions employed by most electronic structure methods, as these wavefunctions are affected by spin-contamination.[17] Therefore, several less frequently employed methods relying on restricted reference wavefunctions have been investigated in the study, and have been found to perform better. Consequently, the study has emphasized the value of using methods that rely on restricted reference wavefunctions in order to eliminate spin-contamination and give accurate results even for difficult to treat species such as the phenyl radical and similar systems.

CHAPTER 2

EXPERIMENTAL TECHNIQUE

2.1. Background

Since its development in the late 1940s by Norrish and Porter, flash photolysis has proven to be a very valuable kinetic technique. Unlike techniques relying on flow systems, flash photolysis is not affected by mixing times nor limited to the low pressure regime. Furthermore, because flash photolysis typically occurs in the center of a reactor, other complications that generally arise in flow methods, such as heterogeneous catalysis from interactions between the reactants and the reactor wall are not an issue. These advantages of flash photolysis coupled with its relative ease of implementation have established it as a powerful method not only for investigating reactions in the gas phase, but also as an aid in the study of liquid kinetics.[16]

Flash photolysis is based upon the notion that energetic photons directed toward a pair of species that are initially inert toward one another can alter one of the species in a way that makes it labile toward the other, thus initiating a chemical reaction. The transient species usually produced by flash photolysis are atoms, molecular radicals, or reactive excited states, the concentration of which can then be monitored as a function of time. The limitation regarding time scales of the reactions that can be investigated is that the reactions must occur slower than the duration of the light pulse produced by the photolysis source; however, with modern lasers capable of producing intense light pulses that last nanoseconds or less, the range of potential reactions for study is continually increasing.

Detection techniques for flash photolysis experiments must have the capacity to respond to rapidly changing concentrations as the reactions studied can occur very fast. Upon initiation, the course of the reaction can be followed by either the absorption or fluorescence of the transient species. In the present case, the experimental design is set up for monitoring fluorescence, and more specifically: resonance fluorescence (RF). Resonance fluorescence is the process of irradiating a species with photons of the exact energy that it in turn emits, and it was first combined with flash photolysis to measure absolute rate constants by Braun and Lenzi in 1967.[18] Resonance fluorescence is primarily used for detecting and monitoring atomic species because they possess sharp transitions that are generally very atom-specific; the likelihood of two atomic species having the same transition is very small. Resonance fluorescence can also be implemented in the case of molecules which are known to exhibit sharp transitions as well, however, RF has been largely replaced by laser induced fluorescence (LIF) in the case of such molecular radicals due to the higher intensities that can be achieved with the latter method.[16]

Resonance fluorescence is achieved by passing a bath gas containing trace amounts of precursors to the same species formed in the reactor through a microwave discharge flow lamp, also known as a resonance lamp. The microwave discharge causes some of the precursor molecules to dissociate, and subsequent collisions and/or neutralization reactions with ions or electrons in the plasma excite a fraction of these radicals to a higher electronic state. Because the lifetime for emission of the upper electronic state in the species used for RF is short ($\sim 10^{-9}$ s) when compared to that of quenching ($\sim 10^{-6}$ s), these excited species primarily return to the ground state via fluorescence, and some of the emitted photons are directed into the reactor through a channel that is at a right angle to the pulsed radiation coming in from the photolysis laser. These photons are of the exact energy needed for the radicals inside the reactor to undergo

the same specific electronic transition (resonant transition) that the same radicals in the microwave flow lamp underwent, and so they are absorbed and eventually emitted once more – hence the term resonance fluorescence. This fluorescence is emitted isotropically throughout the reactor, and the relative photon intensity can be detected and converted into a real-time viewable signal by a very sensitive transducer known as a photomultiplier tube (PMT).

2.2. Gas Preparation and Handling

Partial pressures rather than concentrations may be used to quantify substances in the gas phase. One of the reactants and the photolytic precursor to the second reactant are each separately introduced into a Pyrex vacuum line that was kept under high vacuum (pressure $\leq 1.0 \times 10^{-3}$ torr). Some reactants are naturally in the gas phase at room temperature, while others are liquids and have to be introduced via cold traps onto the vacuum line and must first be purified by at least two freeze-pump-thaw cycles before use. This procedure entails submerging the trap in a liquid nitrogen bath, allowing the reagent to freeze, and then vacuuming off the remaining more volatile impurities. The vapor given off by these liquids (or the gaseous reactant) can then be manipulated along the vacuum line to a glass bulb where these gases are mixed with a large excess of Ar to a pressure of roughly 1000 torr. The amount of vapor introduced in each glass bulb depends on the desired reactant concentration, and in most cases, the partial pressure of the reactant is within the range of 2 – 20 torr. Pressures are measured with a capacitance manometer system (MKS Instruments Type 226A). These mixtures are stored for several hours in order to allow for thorough mixing before use.

The ensuing homogeneous reactant/Ar mixture and the precursor/Ar mixture are then pre-mixed in the rear-tube of the vacuum line by releasing a set predetermined flow of each from

their respective bulbs through mass flow controllers (MKS Instruments Types 1159A and 1159B). The mass flow controllers are typically calibrated at the outset of each new project following the procedure described in Appendix A. Typical flow rates used are within the range of 0-50 sccm (standard cubic cm) of either the reactant or precursor in Ar, and 100-1000 sccm of Ar (bath gas). A brief discussion on the sccm unit of measurement can also be found in Appendix A. After combining in the rear-tube, the subsequent gas mixture flows into the reactor described in the next section. The pressure of the reactor is also measured with the capacitance manometer system, and it can be adjusted to the desired pressure by controlling the reactor exit valve.

2.3. Reactor and Detection System

The reactor is composed of three identical stainless steel cylindrical tubes bisecting one another in a manner that makes them mutually perpendicular, as shown in Figure 2.1. The intersection region of the tubes establishes a roughly cubic reaction zone of 8 cm^3. The resultant six side arms are each 11 cm long, as measured from the reaction zone boundaries, with an inner diameter of 2.2 cm. Nichrome resistance heating wire, electrically insulated with ceramic beads, was wrapped along the inner 7 cm portion of each side arm. A cubic thermally insulating box, 20 cm on a side, made of 2.5 cm thick alumina boards (Zircar Products ZAL-50) houses the reactor almost in its entirety, with only the outermost 1.5 cm portion of each side arm extending past the insulation. These terminal sections of each side arm are continuously water-cooled, and connections to the end of each side arm are made through standard ISO NW25 KF fittings.

Pulsed radiation from the laser enters the reactor at right angles to the continuous probe resonance radiation, and fluorescence is detected through a mutually perpendicular side arm.

Two of the side arms are used for conducting the gas mixtures in and out of the reactor while another serves as a port for a thermocouple. The sheathed Type K thermocouple (chromel/alumel) is used to monitor the gas temperature inside the reaction zone, which is displayed on an Omega DP 285 readout. This thermocouple is not shielded against radiative heat exchange with the walls of the reactor, which can introduce radiation errors.[19] Separate experiments to derive empirical corrections have been outlined previously,[20] and an uncertainty of ± 2 % for the corrected temperature was recommended. The thermocouple is removed from the reaction zone during kinetic measurements. A second sheathed thermocouple is placed outside the reactor for temperature control (Omega CN 3910 KC/S). A range from room temperature to over 1100 K can be achieved in this apparatus if working with thermally stable reagents.

The resonance radiation is produced from a flow of approximately 0.2 torr of a dilution of 0.1% of Cl_2 in Ar through a microwave discharge flow lamp operated at 30-50 Watts. The discharge is initiated with a Tesla coil, and the flowing gas is constantly removed from the lamp by a rotary pump (Welch Model 1399). Calcium fluoride optics are used to block any H-atom radiation at 121.6 nm that might be excited by trace impurities in the resonance lamp while also transmitting photons from the electronic transitions of Cl atoms (which occur in the range of 134 – 140 nm). The intensity of the fluorescence is monitored by a solar-blind UV PMT (Hamamatsu R212) powered by a Bertran Model 215 power supply whose output was set at 2490 V in the present case. The PMT is mounted onto the reactor perpendicularly to both the port through which the light from the microwave flow lamp enters and the port through which the radiation from the laser enters in order to minimize the interference from these sources. As can be seen from Figure 1, the PMT is connected to a computer-controlled multichannel scaler

(EG&G Ortec ACE) via a preamplifier/discriminator (MIT Model F-100T) to count emitted photons as a function of time. The preamplifier/discriminator's detection threshold for current signal pulses arriving from the PMT has been calibrated to filter out weak current signal pulses generated as a result of thermally displaced electrons from the PMT and to achieve the optimal signal-to-noise ratio. Current signal pulses above the threshold are converted into voltage signal pulses, amplified, and then sent to the multichannel scaler. Signals following 50-5,000 laser pulses are accumulated and analyzed on a computer. The timing of the experiments is controlled by a digital delay/pulse generator (Stanford Research Systems, DG 535), which triggers the excimer laser (MPB PSX-100 or Lambda Physik Compex 102, beam cross section 7 x 8 mm^2) ahead of the multichannel scaler to allow measurement of the steady background signal that arises from scattered light from the resonance lamp.

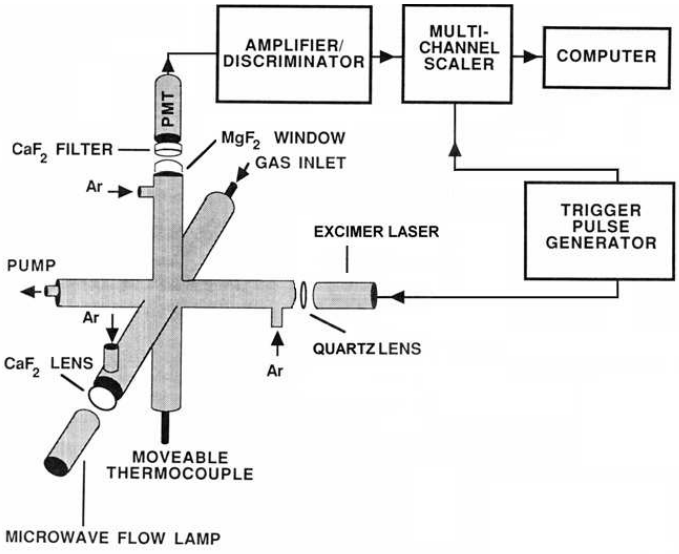

Figure 2.1. Schematic diagram of the apparatus used for laser flash photolysis / resonance fluorescence.

In the reaction zone, the precursors are photolyzed and the ensuing transient species initiate the chemical reaction of interest, the course of which can then be followed by resonance fluorescence. The gas mixtures described in the previous section are flowed slowly through the reactor so that a fresh sample reaches the reaction zone before each photolysis pulse, thus avoiding the accumulation and interference of reaction products in the reaction zone. As previously mentioned, the reagents are diluted in a large excess of argon, which thermalizes the radicals generated, increases the heat capacity of the gas mixture to maintain isothermal conditions during the reactions, and slows diffusion of the transient radicals to the reactor surfaces. The average time spent by the gases in the reaction zone is long compared to the time scale of the reaction (~1 ms), so that the reactor is kinetically equivalent to a static system.

2.4. Data Analysis

Formally, all of the elementary reactions considered in this work are second order bimolecular processes, so the rate of reaction in each case depends on the concentrations of both the reactant and the photolytically-generated transient species. For example, when benzene reacts with the chorine atom with a rate constant k_1, such that

$$C_6H_6 + Cl \xrightarrow{k_1} \text{products} \tag{2.1}$$

the overall rate of reaction (or the rate of chlorine loss with respect to time) is expected to depend on the concentrations of both species in the manner shown in equation 2.2.

$$\text{Rate} = d[Cl]/dt = -k_1[Cl][C_6H_6] \tag{2.2}$$

This equation can be integrated and solved to yield

$$\frac{1}{[C_6H_6]_0 - [Cl]_0} \ln \frac{([Cl]_0 \times [C_6H_6]_t)}{([C_6H_6]_0 \times [Cl]_t)} = k_1 t \tag{2.3}$$

where the subscripts 0 and t indicate concentrations at time 0 and time t, respectively. In addition to being consumed via a second order reaction, the transient species can also be lost through diffusion and any reaction with photolysis fragments, so equation 2.4 must also be added to the mechanism

$$Cl \xrightarrow{k'} \text{loss} \qquad (2.4)$$

The rate of chlorine loss for the two step mechanism composed of equations 2.1 and 2.4 is given by

$$d[Cl]/dt = -k_1[Cl][C_6H_6] - k'[Cl] \qquad (2.5)$$

where, k_1 is the second order rate constant and the constant k' accounts for the rate of Cl loss via diffusion and any secondary processes such as reaction with photolysis fragments. Equation 2.5 can only be solved analytically in cases in which the concentration of the two species can be related, such as when both the initial concentrations are known.[21]

In second order kinetic processes involving photolytically generated radicals, the initial concentration of these transient species at time 0 (immediately following the photolysis of the precursor) must be approximated based on photochemical considerations. Certainly, in cases where the photochemistry of the precursor is well established in the literature, it is possible to approximate the concentration of the transient species, and such calculations along with other photochemically-related considerations are outlined in section 2.5. However, one is unlikely to find detailed photochemical information that spans the entire range of experimental conditions, regardless of the molecule in question. Furthermore, even when some information is available, error margins of typically at least 20% end up accompanying the calculated transient concentration due to the propagation of large uncertainties associated with photochemical

measurements. Therefore, it seems sensible to try to revise the experimental design to yield first order kinetics in order to eliminate the need to know $[Cl]_t$ and simplify the data analysis.

The desired simplification can be achieved by flooding the system with a much higher concentration of the other reactant relative to that of the transient species. In the scenario above, if the concentration of Cl is much smaller than that of benzene, the second order rate constant k_1 can be combined with the essentially unchanging $[C_6H_6]$ and k' into an effective rate coefficient k_{ps1}, yielding first order kinetics as shown in equation 2.6 below. This is known as the pseudo-first order approximation, and k_{ps1} is often referred to as the pseudo-first order decay coefficient.

$$d[Cl]/dt = -k_1[Cl][C_6H_6] - k'[Cl] = -k_{ps1}[Cl] \tag{2.6}$$

where

$$k_{ps1} = k_1[C_6H_6] - k' \tag{2.7}$$

The fluorescence intensity signal from the transient species being monitored, Cl, is proportional to its concentration, thus k_{ps1} can be directly obtained from fitting to the intensity signal as a function of time. Some of the light from the resonance lamp is scattered throughout the reactor, and because this light source is continuous, this creates a steady background signal B, so that for the general mechanism described above, the total signal intensity I_f can be expressed as

$$I_f = Ae^{-k_{ps1}t} + B \tag{2.8}$$

where A and B are both constants. A non-linear least squares fitting algorithm[22,23] is used to fit the fluorescence signal temporal profiles to equation 2.8, yielding k_{ps1} and its uncertainty. More sophisticated methods for analyzing the fluorescence signal are implemented (and are discussed in later chapters) for more complex mechanisms, such as those proposed for HCl + C_6H_5 in chapter 6 and Cl + C_2H_4 in chapter 7.

The accuracy limits for the concentration of the reactant in excess, benzene, are assessed from the propagation of the uncertainties in relevant quantities as shown in equation 2.9

$$\sigma_{[C_6H_6]} = [C_6H_6] \times \left\{ \left(\frac{\sigma_{P_{tot}}}{P_{tot}} \right)^2 + \left(\frac{\sigma_{F_{C_6H_6}}}{F_{C_6H_6}} \right)^2 + \left(\frac{\sigma_{F_{tot}}}{F_{tot}} \right)^2 + \left(\frac{\sigma_{a_{bulb}}}{a_{bulb}} \right)^2 + \left(\frac{\sigma_T}{T} \right)^2 \right\}^{1/2} \qquad (2.9)$$

where the squared terms in parentheses represent the error to quantity ratios of the total pressure, the flow of benzene, the total flow, the dilution ratio, and the temperature, respectively. A justification of this result and other considerations regarding the treatment of uncertainties are presented in Appendix B.

Typically, k_{ps1} is obtained at five different concentrations of the reactant in excess at each set of conditions, with the lowest concentration being zero. According to equation 2.7, a plot of k_{ps1} against $[C_6H_6]$ should be linear, with a slope of k_1 and an intercept of k'. Such a plot is shown in Figure 2.2, in which the line through the data represents a weighted linear least squares fit, which yields the statistical uncertainty in the slope and therefore also in k_1.

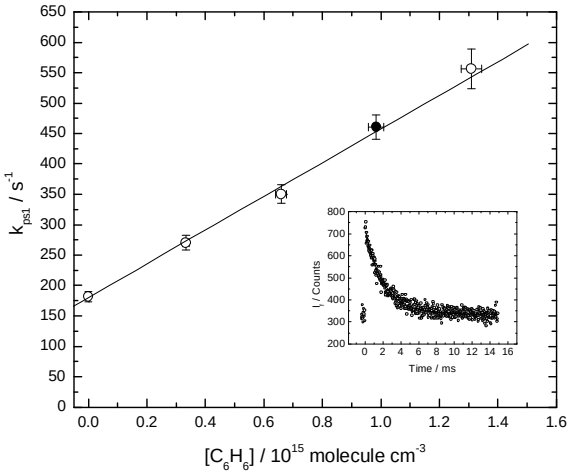

Figure 2.2. Pseudo-first-order decay coefficient for Cl in the presence of excess C_6H_6 at 676 K and 69 mbar total pressure with Ar. Error bars represent ± 1σ. The inset shows the signal corresponding to the filled point.

2.5. Photochemistry of the Cl Atom

2.5.1. Electronic States and Transitions

Chlorine atoms are monitored by time-resolved resonance fluorescence at 130-140 nm which encompasses the two electronic transitions, $(4s)^2P_{3/2,1/2} \rightarrow (3p)^2P_{3/2,1/2}$.[24] Because the $(4s)^2P_{3/2} \rightarrow (3p)^2P_{3/2}$ and $(4s)^2P_{1/2} \rightarrow (3p)^2P_{1/2}$ Cl atom electronic transitions have large Einstein coefficients for spontaneous emission of 4.19×10^8 s^{-1} and 3.23×10^8 s^{-1}, respectively, it can be shown that the overall emission lifetime for these two processes, defined as the reciprocal of the sum of the two transition probabilities, is 1.35 ns.[24,25] The lifetime for Cl atom fluorescence is significantly shorter than the typical lifetimes of competing non-radiative processes such as quenching, which tend to happen on the μs scale with the concentrations of quenchers normally used here.

Carbon tetrachloride has been the precursor predominantly used in the photolytic generation of Cl atoms throughout this work. Hanf et al. have investigated the photochemistry of this process at room temperature, and found the absorption cross-section and total Cl quantum yield of CCl_4, $8.6 \pm 0.5 \times 10^{-19}$ cm^2 and 1.5 ± 0.1, respectively, with 27% in the $(3p)^2P_{1/2}$ excited state.[26] The energy difference between the $^2P_{1/2}$ excited state and the $^2P_{3/2}$ electronic ground state of Cl has been measured to be ~882 cm^{-1} by Davies and Russell[27], and with the knowledge of this quantity, the equilibrium constant K_{eq} for the inter-conversion between the two electronic states shown in equation 2.10 can be estimated via statistical mechanical relations.

$$Cl(^2P_{3/2}) \xleftrightarrow{K_{eq}} Cl(^2P_{1/2}) \tag{2.10}$$

The equilibrium constant between two species is given by equation 2.11 below,

$$K_{eq} = \frac{q_A}{q_B} e^{-\Delta E/k_B T} \tag{2.11}$$

where q_A and q_B represent the total partition functions for species A and B, respectively, ΔE is the energy difference between the two species (882 cm^{-1} = 1.75 × 10^{-20} J in this case), k_B is Boltzmann's constant (1.38 × 10^{-23} J K^{-1}), and T is the temperature. In the present case, when A and B are an excited and the ground electronic state of the same atom, respectively, the translational partition functions cancel leaving only the electronic partition functions. Over the temperature range that can be achieved in our reactor, ~290 – 1100 K, the electronic partition functions can be accurately approximated by the electronic degeneracies of the $^2P_{3/2}$ and $^2P_{1/2}$ states, which are 4 and 2, respectively. Therefore, the ratio of the partition functions is 0.5, and at 298 K, K_{eq} has a value of 7.06 × 10^{-2}. The equilibrium constant can also be defined in terms of the concentrations of the two species as shown in equation 2.12.

$$K_{eq} = \frac{[Cl(^2P_{1/2})]}{[Cl(^2P_{3/2})]} \tag{2.12}$$

Addition of 1 to each side of equation 2.12 before taking the inverse yields equation 2.13, from which the ratio of the concentrations of ground state to total Cl atoms can be calculated, and it can be shown that at 298 K this ratio is 99.3 %, and that even at the highest temperature at which CCl_4 was used, 915 K, the ratio is 88.9 %.

$$\frac{1}{1+K_{eq}} = \frac{[Cl(^2P_{3/2})]}{[Cl(^2P_{3/2})]+[Cl(^2P_{1/2})]} = \frac{[Cl(^2P_{3/2})]}{[Cl]_{total}} \tag{2.13}$$

If equilibration occurs faster than the time scale of the reaction, the reactions studied involve a thermal equilibrium distribution of the two Cl electronic state populations, and therefore the measurements represent the average kinetics for the two spin states of Cl. This assessment can be made by comparing the collisional lifetime of excess of $Cl(^2P_{1/2})$ with the time scale for kinetic measurements. Quenching of $Cl(^2P_{1/2})$ occurs via collisions with the bath gas Ar and the precursor CCl_4 as shown in equation 2.14 and 2.15, respectively.

$$Cl(^2P_{1/2}) + Ar \xrightarrow{k_{Q1}} Cl(^2P_{3/2}) + Ar \quad (2.14)$$

$$Cl(^2P_{1/2}) + CCl_4 \xrightarrow{k_{Q2}} Cl(^2P_{3/2}) + CCl_4 \quad (2.15)$$

Based on reactions 2.14 and 2.15 above, the overall rate of loss of $Cl(^2P_{1/2})$ is given by

$$d[Cl(^2P_{1/2})]/dt = -k_{Q_1}[Cl(^2P_{1/2})][Ar] - k_{Q_2}[Cl(^2P_{1/2})][CCl_4] \quad (2.16)$$

where k_{Q1} and k_{Q2} are the rate constants for the quenching of $Cl(^2P_{1/2})$ by Ar (3.0×10^{-16} cm^3 $molecule^{-1}$ s^{-1})[28] and by CCl_4 (2.1×10^{-10} cm^3 $molecule^{-1}$ s^{-1})[29], respectively. Because the typical [Ar] (~10^{18} atoms cm^3) and [CCl_4] (~10^{15} molecules cm^3) are much larger than the typical [Cl] (~10^{11} atoms cm^3, see sample calculation below), [Ar] and [CCl_4] are essentially constant, and equation 2.16 can be reduced to

$$d[Cl(^2P_{1/2})]/dt = -k_Q[Cl(^2P_{1/2})] \quad (2.17)$$

where k_Q is the total quenching rate constant and is given by

$$k_Q = k_{Q_1}[Ar] + k_{Q_2}[CCl_4] \quad (2.18)$$

Based on the given information above, the calculation of k_Q yields 210300 s^{-1}, out of which 210000 s^{-1} is due to CCl_4 and only 300 s^{-1} is due to Ar, clearly indicating that CCl_4 is the dominant quencher. Equation 2.17 can be integrated to yield

$$\frac{[Cl(^2P_{1/2})]_t}{[Cl(^2P_{1/2})]_0} = e^{-k_Q t} \quad (2.19)$$

and since the lifetime τ is defined as the time necessary for the concentration to drop to 1/e of its initial value at time 0, it can be shown that τ is equal to the reciprocal of k_Q and has a value of ~5 μs in the present case. Because τ is two orders of magnitude shorter than the typical ms time scale used for kinetic measurements here, it can be concluded that, in general, the reactions studied involve a Boltzmann distribution of the $Cl(^2P_{1/2})$ and $Cl(^2P_{3/2})$ populations.

2.5.2. Calculation of $[Cl]_0$

To calculate $[Cl]_0$, a 1 cm^3 reaction zone is considered. As explained in section 2.4, knowledge of $[Cl]_0$ is not necessary for first-order kinetics, but its estimation can be useful in checking that $[Cl]_0$ is much smaller than the concentration of the reactant in excess, as required for the pseudo first-order approximation. The value of $[Cl]_0$ can be calculated by taking the product of the quantum yield for the formation of Cl atoms from the precursor (CCl_4 for this example) Φ_{Cl} and the intensity of laser photon absorption I_{abs}.

$$[Cl]_0 = \Phi_{Cl} \times I_{abs} \tag{2.20}$$

Hanf et al. have found the Cl quantum yield of CCl_4 to be 1.5 ± 0.1.[26] The intensity of absorption can be found by subtracting the intensity of laser photon transmission I_{trans} from the initial laser photon intensity before passage through the CCl_4 sample I_0.

$$I_{abs} = I_0 - I_{trans} \tag{2.21}$$

The initial laser photon intensity I_0 is simply a measure of the number of laser photons per cm^2, which can be calculated from the laser beam cross section σ_L (0.56 cm^2) and the number of photons produced by the 193.3 nm laser radiation. The number of photons produced by the laser can be obtained by dividing the measured pulse energy F by 1.028×10^{-18} J, the energy of a 193.3 nm photon (E_{photon}). So, for a typical pulse energy of 0.1 mJ, it can be shown through equation 2.22 that I_0 should have a value of 1.74×10^{14} photons cm^{-2}.

$$I_0 = \frac{F / E_{photon}}{\sigma_L} \tag{2.22}$$

In actuality, because F is measured in front of the quartz entrance window (shown in Figure 2.1), and the laser radiation is not completely transmitted through the window, equation 2.22 only approximates I_0 in the reaction zone. For a more accurate determination of I_0 in the

reaction zone, the average laser pulse energy is also measured as the radiation exits through the second quartz window, and then the pulse energy in the reaction zone can be evaluated by calculating how much radiation passes through just the entrance window. The ratio of the energy that exits the reactor F' to the energy that enters the reactor F has been experimentally found to be ~0.70 by Dr. Yide Gao.[30] Because I_0 is proportional to the photolysis energy, it can be seen from equation 2.23 that the F'/F ratio of 0.70 is equivalent to the respective I_0'/I_0 ratio.

$$\frac{I_0'}{I_0} = \frac{F'}{F} \tag{2.23}$$

Because I_0' is technically the intensity of transmission of laser photons through the reactor I_{trans}', taking the negative logarithm of I_0'/I_0 gives the overall absorbance of photons by the two quartz windows A', as shown in equation 2.24.[24]

$$A' = -\log\left(\frac{I_{trans}'}{I_0}\right) \tag{2.24}$$

The absorbance can also be defined in terms of the absorption coefficient ε, the concentration c, and the path length of the quartz window l, as shown in equation 2.25.[24]

$$A = \varepsilon \times c \times l \tag{2.25}$$

Since the entrance and exit windows are both quartz, have equal path lengths, and the volume separating them is essentially a vacuum, the absorbance of passing through just one window A* is simply half of A' (the absorbance of two quartz windows). Once A* is known, the ratio of the energy at the reaction zone to the energy as measured in front of the entrance window F*/F can be obtained. In the present case, this ratio can be shown to have a value of 0.84 via equation 2.26. F* can then be used calculate the actual I_0 in the reaction zone according to equation 2.27, yielding $I_0 = 1.46 \times 10^{14}$ photons cm^{-2} in the present example.

$$10^{-A^*} = \left(\frac{I_{trans}^*}{I_0} \right) = \left(\frac{F^*}{F} \right) \tag{2.26}$$

$$I_0 = \frac{F^* / E_{photon}}{\sigma_L} \tag{2.27}$$

Resuming the quest for the calculation of $[Cl]_0$, I_{trans} must also be evaluated in order to obtain I_{abs} via equation 2.21, which can then in turn be used to solve for $[Cl]_0$ in equation 2.20. I_{trans} can be obtained from the Beer-Lambert law via equation 2.28[16,24]

$$I_{trans} = I_0 \times e^{-\sigma c l} \tag{2.28}$$

where σ is the absorption cross-section of CCl_4 ($8.6 \pm 0.5 \times 10^{-19}$ cm^2)[26], c is $[CCl_4]$ (~10^{15} molecules cm^{-3}), and l is the path length of the reaction zone which is 1 cm in this case because a 1 cm^3 reaction zone volume is considered in this example. Therefore, I_{trans} can be shown to have a value of 99.91% of I_0 in the present example, leading to a value of 1.26×10^{11} photons cm^{-2} for I_{abs}, ultimately yielding 1.88×10^{11} atoms cm^{-3} for $[Cl]_0$.

2.6. Assessment of Experimental Conditions and Parameters

Judicious consideration must be used in selecting a suitable reaction and reaction conditions for analysis, such as to ensure that the reaction of interest occurs much faster than any possible secondary chemistry resulting from potential interactions between other photolysis fragments. Experimental parameters such as pressure P, photolysis energy F, $[Cl]_0$, and the average gas residence time inside the reactor τ_{res}, must be varied in order to assess any possible systematic dependence of the second-order rate constants on such parameters. The systematic variation of P, F, τ_{res}, and $[Cl]_0$ can indicate if the reactions studied are effectively bimolecular, and unaffected significantly by secondary chemistry, thermal decomposition, and mixing time.

By varying the photolysis energy F, the energy range over which secondary chemistry is negligible for the reaction in question can be found. This series of low energies defines the usable energy range over which the second order rate constant is unvarying and therefore independent of energy. If the rate constant is found to depend on energy, it is likely that secondary chemical processes such as reactions with photolysis fragments are contributing to the overall rate of Cl loss. In certain cases, energies low enough to eliminate secondary chemistry yield too little fluorescence for analysis. In such cases, an interpolation of the rate constant to zero energy is utilized to remove the effects of secondary processes (chapter 6). Similarly, testing for the variation of the kinetics with $[Cl]_0$ can also be a good indicator of whether the reaction is influenced by secondary chemistry processes.

Varying the average gas residence time inside the reactor τ_{res}, can determine if thermal decomposition and mixing effects are occurring. For example, it has been found that CCl_4 is not thermally stable above ~900 K, so different Cl atom precursors had to be used to carry out investigations at higher temperatures (chapters 6 and 7). Also, in certain cases it has been found that the radical precursor is not inert toward the reactant, resulting in undesired reactions between the two in the mixing tube prior to being introduced into the reactor. It is for this reason that certain precursors such as Cl_2 are not suitable. Furthermore, variation of τ_{res} can also ensure that the mixing times for the reactant and radical precursor are adequate.

In particular, the presence of a systematic dependence on pressure or temperature, or indeed the lack thereof, can lead to a wealth of information about the system being investigated. For instance, if a reaction is found to be dependent on pressure, this can be attributed to the formation of an adduct in most cases. According to Lindemann theory[21,31], an energetic complex AB* formed from the collision between A and B can either dissociate back to the reactants, or it

can have its excess energy removed through collisions with a bath gas M leading to the formation of an adduct:

$$A + B \xrightarrow{k_a} AB^* \tag{2.29}$$

$$AB^* \xrightarrow{k_b} A + B \tag{2.30}$$

$$AB^* + M \xrightarrow{k_c} AB + M \tag{2.31}$$

Increasing the concentration of the bath gas (i.e., its pressure), will favor the formation of the adduct, and so if by increasing the pressure the rate constant k_c increases systematically, one would predict that the reaction goes through an associative mechanism as described above.

The Arrhenius equation, given below, is empirical in nature and is named after its proponent Svante Arrhenius, who published a paper in 1889 in which he noted that a multitude of reactions have rate constants whose dependence on temperature conform to this equation:[32]

$$k = A \times e^{-E_a RT} \tag{2.32}$$

This equation can be made linear by taking the natural logarithm of both sides, yielding

$$\ln(k) = -E_a / R \times (1/T) + \ln(A) \tag{2.33}$$

implying that a plot of ln(k) against the reciprocal temperature should give a straight line with a slope equal to $-E_a/R$ and with an intercept of ln(A). Equation 2.33 defines the activation energy E_a. In most cases, such a plot will have a negative slope revealing that there is a positive energy of activation. The simplest interpretation is that E_a represents an energy barrier that must be overcome by the reactant species in order to be converted into the products. However, there are some reactions which have activation energies that are less than or equal to zero, such as reactions in which an adduct is formed, in which case it is said that the reactions are barrierless.[21] Examples of such reactions are encountered in chapters 4 – 7.

CHAPTER 3

THEORETICAL MODELING

3.1. Introduction

The theoretical modeling of gas-phase reactions is central to the understanding of the reaction mechanism involved in a particular reaction system. If experimental results are available, theoretical kinetic analyses can be carried out to test the plausibility of the suggested mechanism, as well as derive molecular properties of interest from macromolecular measurements. If no information is known regarding a certain reaction system, modeling it theoretically beforehand can aid the experimentalist in predicting a reasonable reaction mechanism and selecting suitable experimental conditions to carry out the investigation. Furthermore, the interplay between theory and experiment can lead to their mutual verification and to the development of more sophisticated experimental setups and theoretical foundations, yielding increasingly accurate results.

The modeling of gas-phase reactions has been facilitated by the rapid development of high accuracy quantum mechanical electronic structure methods. These methods are essential for calculating the potential energy surface (PES) of a reaction system, which can then be used to derive information about the relative stability, molecular motion, and energy transfer among species on the PES. In particular, these quantum mechanical methods are important for the identification, geometrical optimization, and characterization of important stationary points along the PES, such as wells and saddle points, which can be used to designate the reaction

coordinate. The reaction coordinate, sometimes also called the minimum-energy path (MEP), is the path of lowest energy connecting the reactants with the products on the PES.[33] The computational methods used to calculate these quantities for the various reaction systems considered in this work are described in section 3.2 below.

Bunker was the first to show that detailed knowledge of the dynamics on the PES permits the exact evaluation of kinetic information via calculations of classical trajectories.[34] Classical trajectory calculations entail solving the classical equations of motion on the PES characterizing the system. A very large amount of classical trajectories have to be considered to achieve accurate results, and the calculation of the numerical solutions of classical trajectories is very computationally demanding. Furthermore, since the potential energy of a system is generally expressed in terms of the system's internal coordinates n, where n = 3N – 6 for a polyatomic system or 3N – 5 for a linear species containing N atoms, a hypersurface of (n + 1) dimensions is generated when the potential energy is plotted against the n coordinates, which actually results in numerous PESs, further complicating the calculation of classical trajectories. However, these calculations have led to an increased understanding of dynamical processes, resulting in the development of reasonable approximations that greatly reduce the computational cost and time associated with theoretical kinetic analyses. These approximations and the theories that resulted from their implementation are discussed in section 3.3.

3.2. Computational Methodology

3.2.1. MPWB1K Theory

The PES of several reaction systems were investigated using the hybrid meta density functional theory (HMDFT)[35] method MPWB1K developed by Zhao and Truhlar.[36] The

MPWB1K method incorporates the modified Perdew and Wang 1991 exchange functional (MPW)[37] along with Becke's 1995 meta correlation functional (B95).[38] The GTMP2Large[39] basis set was used in conjunction with this method, which is essentially 6-311++G(3d2f,2df,2p)[40] for H-Si, but has been improved[41] for P-Ar. This was the largest basis set tested by Zhao and Truhlar, who refer to it as the modified[39,42] G3Large[41] basis set (MG3),[42] and their recommended value of 0.9567 was used to scale the frequencies obtained with MPWB1K/MG3.[36]

This method is appealing for several reasons: Firstly, the pure density functional theory (DFT) portion of the functional is based on the generalized gradient approximation (GGA), meaning that it depends on the local electron density as well as its gradient, and because this is a meta functional, it also takes into account the kinetic energy density, all of which have been shown to lead to increased overall accuracy.[36] Secondly, it was calibrated against thermodynamic and kinetic databases in order to yield accurate reaction barriers, and has been shown to treat weak hydrogen bonded and van der Waal complexes reasonably well.[36,43] Thirdly, while the frequencies obtained with popular DFT methods such B3LYP typically need only be scaled by a factor of 0.99, it has been shown that the optimal scaling factor for MPWB1K/MG3 is 0.9567, which is consistent with the general rule of thumb that harmonic frequencies are approximately 5% larger than observed v = 0 to v = 1 transitions. Lastly, MPWB1K is a DFT method so it is also relatively computationally inexpensive.

3.2.2. *Ab Initio* Methods

The QCISD[44] and CCSD(T)[45-50] *ab initio* electronic structure theories have been used to explore the geometries, frequencies, and energies of many of the reactive systems considered. Both of these theories rely on multi-configurational wavefunctions, in which the effects of

electron correlation are approximated via the explicit calculations of single and double excitations from a single-reference Hartree-Fock determinant. QCISD theory, which stands for Quadratic Configuration Interaction Singles and Doubles, includes the quadratic correction developed by Langhoff and Davidson and implemented by Pople et al., which successfully removes the size inconsistency that resulted due to truncation in the original CISD method.[44,51,52] Furthermore, in addition to the inclusion of single and double excitations, QCISD theory also approximately accounts for the effects of quadruple excitations by taking the quadrature of the effects resulting from double excitations. Similarly, CCSD(T) theory, Coupled-Cluster with Singles and Doubles, includes single, double, and the approximate effects of quadruple excitations in the wavefunction via the cluster operator, but it is superior to QCISD theory in that it also estimates the effects of triple excitations via a quasiperturbative formalism (T), and accounts for the effects of excitations beyond quadruples.[52]

3.2.3. The Correlation Consistent Basis Sets

The correlation consistent basis sets (cc-pVnZ, n = D, T, Q) developed by Dunning et al. have been frequently used with CCSD(T) theory to carry out single point energy calculations for species throughout this work.[53-55] The advantage of the correlation consistent basis sets is that they have been specifically constructed to account for the correlation energy in a systematic manner. For the energy of a system, as well as many other important properties, the use of successively larger correlation consistent basis sets usually leads to a smooth convergence to the complete basis set limit (CBS). At the CBS limit, any of the error arising from the incompleteness of the basis set is effectively removed, leaving only the intrinsic error from the method used. In this work, the triple-zeta and quadruple-zeta correlation consistent basis sets, or

wherever it could be afforded, the augmented triple-zeta and quadruple-zeta correlation consistent basis sets[56,57] were extended to the complete basis set (CBS) limit using the two-point extrapolation[58]:

$$E^{\infty} = (E_X X^3 - E_Y Y^3) / (X^3 - Y^3) \quad (3.1)$$

where E_X and E_Y here represent the energies obtained with the triple-zeta (X = 3) and quadruple-zeta (Y = 4) correlation consistent basis sets, respectively.

3.2.4. Composite Methods for Open Shell Systems

In general, a composite method consisting of QCISD/6-311G(d,p) geometry optimizations and single-point CCSD(T) computations extrapolated to the CBS limit using the triple-zeta and quadruple-zeta correlation consistent basis sets has been used to explore the PESs of the various reaction systems considered. In cases where the spin-unrestricted Hartree-Fock (UHF) wavefunction yielded expectation values for doublet species that were significantly higher than the ideal value of $\langle S^2 \rangle = 0.75$, the single-point unrestricted CCSD(T) computations were performed on an spin-restricted open-shell Hartree-Fock reference wave function (ROHF) in order to effectively remove the impact of spin contamination. By constraining the spatial components of α and β electrons to be the same in the wavefunction, ROHF reference wavefunctions eliminate the spin polarization effects that give rise to the spin contamination in the UHF doublet wavefunction, which will prove to be critical in properly treating the phenyl radical in chapter 6.

In addition to the QCISD/6-311G(d,p) geometry optimizations and the CCSD(T)/CBS energy evaluations, the zero point energies (ZPEs) for all species are also calculated with the

QCISD/6-311G(d,p) theory, scaled by the appropriate scaling factor of 0.954[59], and included in the composite scheme. The energies of the atomic species considered are also corrected for the effects of spin-orbit coupling.[60] The ensuing composite methods are denoted as CCSD(T)/CBS when the two-point CBS extrapolation is performed with unaugmented basis sets, and CCSD(T)/CBS-aug when augmented basis sets are used in the extrapolation. Wherever indicated, frozen-core and all-electron correlation calculations have been carried out using CCSD(T)/cc-pwVTZ theory, and the ensuing core-valence corrections have been applied to all species. Finally, in order to better describe the kinetic energy of electrons near the large Cl nucleus, the mass-velocity and Darwin scalar relativistic effects were also evaluated using CISD/cc-pwVTZ theory on the fixed QCISD/6-311G(d,p) geometries, and the CCSD(T)/CBS-aug energies were corrected for these effects where ever indicated. The scalar relativistic corrections, the core-valence corrections, and the UCCSD(T)/ROHF calculations were performed using the Molpro 2002.6 program.[61] All other calculations have been carried out using the Gaussian 03 program suite.[62]

3.3. Kinetic Analyses

3.3.1. Transition State Theory

One of the most important and widely employed theories describing the motion of point masses and the location of the barrier for a reaction channel along the PES is canonical transition state theory (CTST).[63-65] CTST is based on a statistical treatment of the equilibrium properties of a macromolecular reactive system, and therefore it implicitly assumes a Boltzmann population of the energy levels of the reactants. This theory also assumes that all of the molecules that react to form products must pass through a special intermediate configuration known as the transition

state, which is located at the energetic maximum on the PES.[33] The expression for the canonical rate constant, given in equation 3.2, can be obtained by assuming that the transition state is in equilibrium with the reactant molecules,[33] though it has been argued that placing an equilibrium condition on the reactive system is unnecessary, and that the same transition state formula can be obtained by instead assuming that no re-crossings of the transition state occur.[66]

$$k(T) = \frac{k_B T}{h} \frac{Q^{TS}}{\prod_i Q_i^{reac}} \times \exp(-E_0 / k_B T) \qquad (3.2)$$

In equation 3.2, $\prod Q^{reac}$ is the product of the total molecular partition functions of the reactants and Q^{TS} is the partition function of the transition state without the special mode corresponding to the motion along the reaction coordinate. This special motion is treated as a separate vibration or translation, and in either case its partition function can be shown to have a value of the product of the temperature and the ratio of the Boltzmann to Planck constants ($k_B T/h$), corresponding to the first term of equation 3.2. The exponential term in equation 3.2 contains the quantity E_0, which is defined as the energy difference between the transition state and the reactants at 0 K, and is usually referred to as the critical energy.

All of the partition functions obtained in chapters 4 – 7 were calculated with Gaussian 03 via standard statistical mechanics formulas.[67] The rotational and electronic partition functions for all species were directly taken from the Gaussian 03 output files, with the exception of the Cl atom, in which the electronic partition function was manually calculated to include the correct degeneracies which arise from the spin-orbit coupling in Cl, of four for the $^2P_{3/2}$ electronic ground state and of two for the $^2P_{1/2}$ first excited state. The vibrational partition function was calculated from the v = 0 state as opposed to from the bottom of the potential, both of which are given in the Gaussian 03 output file. The translational partition function obtained by Gaussian

includes the volume term, and must therefore be divided by k_BT/P and to get the conventional translational partition function in m^{-3}, which can then be converted to units of cm^{-3} to directly yield second-order rate constants with typical units.[62,67]

Transition state theory is a convenient approach for obtaining theoretical canonical rate constants directly from the PES. Furthermore, it has been shown that the application of transition state theory variationally results in rate constants which represent the exact upper bounds to the rate constants that would be obtained through extensive classical trajectory calculations.[66] In this variational formulation of transition state theory, commonly referred to as variational transition state theory (VTST),[68-71] the no re-crossing of the transition state rule is removed, and the passage of reactants through a plane perpendicular to the MEP with multiple crossings of this dividing plane by the transition states is considered. The variational method requires that the calculation be repeated with multiple planes until the minimum rate constant is found, which can then be used as an upper estimate of the actual rate constant. In its microcanonical formulation, VTST involves the calculation of rate constants as a function of the internal energy of the reactant, which are referred to as energy-specific or microcanonical rate constants. Averaging these microcanonical rate constants over all the energy levels of the reactant in a Boltzmann distribution, yields the canonical rate constant.[66]

3.3.2. The Lindemann-Hinshelwood Mechanism

Because transition state theory assumes that the energy levels of the reactant are in their equilibrium population, its application to situations in which non-Boltzmann population distributions are encountered does not produce sensible results. One example in which non-equilibrium reactant populations are generated is adduct formation. As discussed in section 2.6,

the process of adduct formation is usually indicated when the rate constant shows a pressure dependence. The Lindemann-Hinshelwood mechanism[16,31], adapted for a recombination process, is comprised of equations 3.3 – 3. 5.

$$A + B \xrightarrow{k_a} AB^* \tag{3.3}$$

$$AB^* \xrightarrow{k_b} A + B \tag{3.4}$$

$$AB^* + M \xrightarrow{k_c} AB + M \tag{3.5}$$

This mechanism describes how two reactants, A and B, can react to form an adduct with vibrational excitation energy, denoted by the * superscript, which can then return back to the reactants via a unimolecular dissociation, or be collisionally stabilized by the bath gas M to yield the ground state adduct. Many texts have elected to discuss the effects of pressure on the rate constant for the unimolecular dissociation of the adduct k_{uni}, in which the reaction mechanism is composed of reaction 3.5, its reverse, and reaction 3.3, and have noted that since the recombination of A and B occurs on the same PES, the ensuing rate constant for recombination k_{rec} can be obtained by dividing k_{uni} by K_{eq}.[16,21,33] However, the present work largely deals with bimolecular reactions, some of which result in adduct formation, and therefore the equations describing the effects of pressure on the recombination rate constant are directly derived in the formalism that follows. For the overall process of A and B producing the adduct AB, the net rate of reaction is given by

$$\frac{d[AB]}{dt} = k_{rec}[A][B] \tag{3.6}$$

and because AB* is an unstable short-lived species, the steady state approximation ($d[AB^*]_{ss}/dt \approx 0$) can be used to calculate its concentration, yielding equation 3.7.

$$[AB^*]_{ss} = \frac{k_a[A][B]}{k_b + k_c[M]} \tag{3.7}$$

The subscript ss denotes that the steady state approximation has been employed to calculate the relevant quantities. The rate of adduct formation can also be evaluated by simply considering reaction 3.5, which yields

$$\frac{d[AB]}{dt} = k_c[AB^*]_{ss}[M] = \frac{k_c k_a[A][B][M]}{k_b + k_c[M]} \tag{3.8}$$

and by comparing equations 3.6 and 3.8, it can be seen that the recombination rate constant k_{rec} can be obtained through equation 3.9.

$$k_{rec} = \frac{k_c k_a[M]}{k_b + k_c[M]} \tag{3.9}$$

At high pressures (as [M] goes to infinity), it can be seen that expression 3.9 for k_{rec} reduces to

$$k_{rec} = k_a \equiv k_\infty \tag{3.10}$$

where k_∞ is defined as the high-pressure limiting rate constant, is independent of pressure, and is second order in nature (units of cm^3 $molecule^{-1}$ s^{-1}). Because at very high pressures the adduct achieves its Boltzmann population distribution via collisions with the bath gas, the reactive system is at equilibrium at the infinite pressure limit and the TST equation (3.2) can be used to evaluate k_∞. At low pressures, k_{rec} is proportional to the bath gas concentration, as shown in equation 3.11

$$k_{rec} = \frac{k_a k_c[M]}{k_b} \equiv k_0[M] \tag{3.11}$$

where k_0 is defined as the low-pressure limiting rate constant and has third order units of cm^6 $molecule^{-2}$ s^{-1}. Substituting in k_0 and k_∞ into equation 3.9 yields equation 3.12, which describes k_{rec} purely in terms of the low- and high-pressure limiting rate constants and [M].

$$k_{rec} = \left(\frac{k_0[M]}{1 + k_0[M]/k_\infty} \right) \tag{3.12}$$

At the center of the pressure range, the bath gas has the concentration $[M]_c$, and it can be shown that $k_0[M]$ is equal to k_∞ at this value. A typical plot of the Lindemann-Hinshelwood fall-off curve involving the reduced quantities for k_{rec}/k_∞ against $[M]/[M]_c$ is shown in Figure 3.1. As can be seen from this figure, the rate constant starts out being proportional to [M] at low pressures and then gradually falls-off to its high-pressure limit. The pressure dependence of the k_{rec} can also be interpreted linearly via a plot of $1/k_{rec}$ vs. $1/[M]$, as shown in equation 3.13, which results from taking the reciprocal of equation 3.9 and substituting in k_0 and k_∞.

$$\frac{1}{k_{rec}} = \frac{1}{k_0} \times \frac{1}{[M]} + \frac{1}{k_\infty} \tag{3.13}$$

In equation 3.13, $1/k_0$ represents the slope and the intercept is given by $1/k_\infty$.

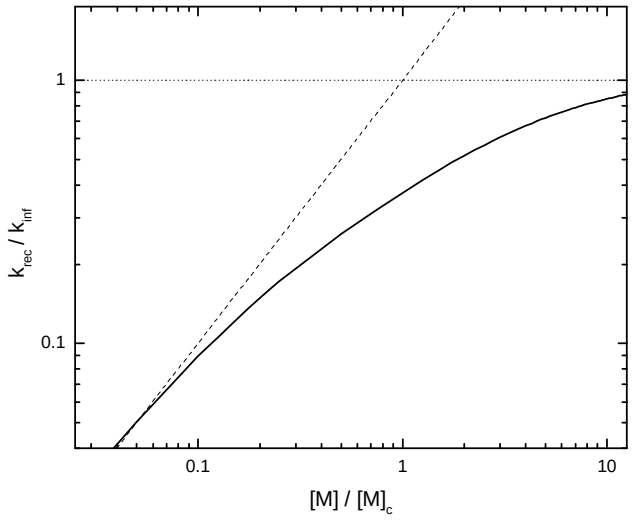

Figure 3.1. Typical Lindemann-Hinshelwood fall-off curve for recombination reactions. The dotted line represents the high-pressure limit for the recombination rate constant and the dashed line corresponds to the low-pressure limit for the rate constant.

3.3.3. Troe's Empirical Formalism

Though the Lindemann-Hinshelwood description of how k_{rec} depends on the pressure is in qualitative accord with experimental findings, it has long been known that curves generated by this interpretation exhibit fall-off regions that are too broad to be in quantitative agreement with experiment. To improve the agreement in the fall-off region between theory and experiment, Troe showed that the multiplication of the Lindemann-Hinshelwood expression for k_{rec} by an empirical scaling factor F led to more realistic fall-off curves.[72-74] The scaling factor has been shown to take on the form of

$$F = F_{cent}^{\left\{1+\left[\log_{10}(k_0[M]/k_\infty)/(0.75\text{-}1.27\log_{10}F_{cent})\right]^2\right\}^{-1}} \tag{3.14}$$

which leads to

$$k_{rec} = \left(\frac{k_0[M]}{1+k_0[M]/k_\infty}\right) F_{cent}^{\left\{1+\left[\log_{10}(k_0[M]/k_\infty)/(0.75\text{-}1.27\log_{10}F_{cent})\right]^2\right\}^{-1}} \tag{3.15}$$

where F_{cent} represents the depression of the fall-off curve from the Lindemann-Hinshelwood curve and is usually referred to as the broadening factor. The expression for F_{cent} was formulated by fitting to empirical formulas, and can be estimated from knowledge of properties of the transition state, as discussed by Cobos and Troe.[75]

3.3.4. Modified Transition State Theory

As previously discussed, conventional TST is inappropriate in non-equilibrium scenarios, such as the fall-off region, though it can be used to provide the high-pressure limiting rate constant because the system reaches its equilibrium population distribution at infinite pressure. Obviously, an "infinite" pressure cannot be achieved in experiments, so in most cases, when the

observed rate constant is found to be independent of pressure over a given pressure range, the rate constant is believed to be in the high-pressure limiting regime, and TST calculations may be used to compare to and rationalize the measured rate constants. However, it has recently been shown that in cases where the products are produced via a "chemical activation" mechanism, the use of conventional TST results in rate constants that are considerably overestimated.[76,77] In many of the systems studied in this dissertation, chemical activation was found to be the principal reaction mechanism, therefore this mechanism and a suitable way to treat it via an appropriately modified version of TST, known as modified TST (MTST),[76] are discussed here.

In several of the reactions in this study, it was found that while the adduct formed via bimolecular collisions can be stabilized or dissociate, as shown in reactions 3.3 – 3.5, it can also often undergo a subsequent reaction leading to a new product set denoted C in the reaction below.

$$AB^* \xrightarrow{k_d} C \qquad (3.16)$$

A schematic representation of this four-step mechanism characteristic of the reaction systems studied here is shown in Figure 3.2. The formation of a product set from an energized adduct, which, as a consequence of being produced via a bimolecular collision, has enough vibrational energy to overcome the low-lying TS, is referred to as chemical activation. In terms of the general mechanism comprised of reactions 3.3 – 3.5 and 3.16, chemical activation alludes to the notion that the adduct AB is formed with an amount of excess energy which corresponds to the energy difference between A + B and AB in their respective vibrational ground states, and since this excess energy exceeds the energetic barrier to the formation of product set C, AB has been "activated" and can undergo reaction 3.16 (Figure 3.2).

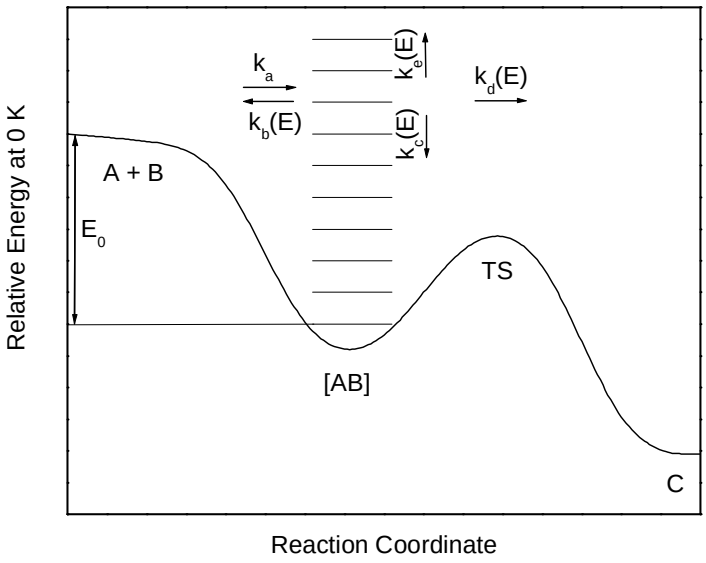

Figure 3.2. Representation of typical PES for the reaction systems studied in this dissertation thought to proceed via a chemical activation mechanism. The terms defined on the PES pertain to RRKM theory and the unlabeled horizontal lines designate vibrational energy levels of the adduct [AB].

Conceptually, the main difference between MTST and general TST approaches is in the way the partition function of a TS with a lower energy than that of the reactants is calculated. While in standard TST all of the vibrational states of the TS, assumed to be in Boltzmann distribution, are used in the calculation of its partition function, MTST does not include the states of the TS that are energetically below the reactants. This is done because at normal pressures, the frequency of gas-phase collisions is not large enough to thermalize the energy levels of the TS, so the TS energy levels that lie below the energy of the reactants are inaccessible. The exclusion of these vibrational states in MTST has been shown to have the effect of reducing the overall thermal rate constant obtained with standard TST. The mathematical derivation and

theoretical formulation of MTST has been described in detail elsewhere,[76,77] and it suffices at this point to just give the MTST result for the thermal rate constant,

$$k(T) = \frac{k_B T}{h} \frac{Q^{TS}}{\prod_i Q_i^{reac}} \exp\left(\frac{-E_0/k_B T}{k_B T}\right) \int_{-E_0}^{\infty} G^*(E - E_0) \exp\left[-\frac{(E - E_0)/k_B T}{k_B T}\right] \frac{d(E - E_0)}{k_B T} \quad (3.17)$$

where $G^*(E - E_0)$ is the sum of states of the TS and all other terms have been previously defined.

3.3.5. RRKM Theory

3.3.5.1. The Master Equation

An alternative treatment of recombination reactions can be achieved through the application of TST to a microcanonical ensemble of the energized adducts formed via collisions. This sophisticated yet still approximate theory is known as RRKM theory, was developed by Rice, Ramsperger, Kasssel, and Marcus, and relies on two central assumptions: that all reactive encounters pass through a critical geometry (the TS assumption) and that intramolecular vibrational redistribution is rapid when compared to the timescale for reaction (the assumption of ergodicity).[78-81] RRKM theory is concerned with the fate of the energized adduct, which in the case of adduct formation via recombination reactions achieves its initial energy via chemical activation, and can then dissociate back to the reactants, undergo collisional stabilization by the bath gas, or even go on to form other products in some cases.

In RRKM theory, the nature of the competition between collisional stabilization of the adduct, dissociation to reactants, and reaction to form products is assessed based on the evaluation of the energy-specific rate constants for these processes as a function of the internal energy of the newly formed excited adduct. Further mechanistic considerations lead to a set of coupled inegro-differential equations in which the time evolution of an energy-dependent

population of adduct molecules is mathematically described.[21,66,82] Collectively, this set of integro-differential equations is called the master equation, which can take on continuum or discrete forms, and can be solved through direct numerical integration, stochastic methods,[21,83] or, if the master equation is set in a matrix, through the use of eigenvalue methods.[84] The master equation, conventionally expressed in its continuum form, is given below, and good discussions on its discrete formulation for use in stochastic and matrix methods are provided elsewhere.[66,82]

$$\frac{dy(E',t)}{dt} = \int_0^\infty [R(E',E)y(E,t) - R(E,E')y(E',t)] - \sum_{i=1}^{channels} k_i(E')y(E',t) \qquad (3.18)$$

In equation 3.18, the time evolution of the adduct y is described in terms of the quantities R(E',E), R(E, E'), and $k_i(E')$, which represent the rate coefficient for collisional deactivation (energy transfer from energy E' to energy E where E' > E), the rate coefficient for collisional activation, and the microcanonical rate constant for unimolecular dissociation via the i^{th} channel, respectively. In some regards, these energy-specific rate constants in the master equation of RRKM theory are analogous to k_b – k_d from Lindemann-Hinshelwood theory in section 3.4.2, and for consistency, R(E',E) and R(E,E') are denoted $k_c(E)$ and $k_e(E)$, respectively, in Figure 3.2 and will be termed thusly from this point forward.

The rate coefficients for dissociation can be expressed by the general equation

$$k_i(E) = \left[\frac{m^*}{m}\frac{\sigma_{ext}}{\sigma^*_{ext}}\right]\frac{g_e^*}{g_e}\frac{1}{h}\frac{G^*(E-E_0)}{p(E)} \qquad (3.19)$$

where h is Planck's constant, E_0 is the reaction threshold energy (defined as $E_{TS} - E_{Adduct}$), $G^*(E-E_0)$ is the sum of states of the TS, p(E) is the density of states of the adduct, m is the number of optical isomers, σ_{ext} is the external rotation symmetry number, and g_e is the degeneracy of the electronic ground state of the adduct, whereas the TS counterparts of these quantities are denoted

by an asterisk. In the absence of information regarding the nature of the TS, the Inverse Laplace Transform method can be used to obtain microcanonical rate constants via equation 3.20.[82,85-87]

$$k(E) = \left[\frac{m^*}{m} \frac{\sigma_{ext}}{\sigma^*_{ext}} \right] A_\infty \frac{p(E - E_\infty)}{p(E)} \tag{3.20}$$

In equation 3.20, A_∞ and E_∞ are the preexponential factor and the activation energy for the high-pressure limiting rate constant. It should be noted, however, that the replacement of the E_∞ parameter with the reaction critical energy E_0 has been shown to "improve accuracy just above the reaction threshold,"[87] and as such, the ILT procedure is sometimes amended thusly (this is done in the MultiWell program, which is described below).

The reaction threshold energy can also be corrected for angular momentum effects, generally approximated via the use of a pseudodiatomic model,[85,86] in which the temperature-corrected reaction threshold energy E_0^T can be expressed in terms of the original E_0 and the external two-dimensional moments of inertia of the adduct and of the TS, denoted by I_{2D} and I_{2D}^* respectively in equation 3.21 below.

$$E_0^T = E_0 - k_B T \left\{ 1 - \frac{I_{2D}}{I_{2D}^*} \right\} \tag{3.21}$$

The extent of collisional stabilization of the excited adduct is most commonly calculated from Lennard-Jones parameters, such as the collision diameter σ and the well depth ε for the adduct and the bath gas, as well as from the selection of a suitable model for the description of the probability of collisions leading to the transfer of energy from and to the adduct. In general, the simple exponential-down model given in equation 3.22 was selected to describe the probability of a deactivating collision $P_d(E,E')$.

$$P_d(E, E') = \frac{1}{N(E')} \times \exp^{-\frac{E'-E}{\alpha(E')}} \tag{3.22}$$

In equation 3.22, E' is the initial energy and is always larger than the final energy E, N(E') is the normalization factor that sets the probability of a deactivating collision equal to unity, and $\alpha(E')$ is a parameter that is related to the collision efficiency of the specific bath gas.[88] The estimation of $\alpha(E')$ will be discussed later. The probability of a collision leading to an increase in the energy of the adduct, or an activating collision, can be obtained from detailed balance:[89]

$$P_a(E,E') = \frac{p(E')}{p(E)} \times P_d(E',E) \times \exp^{-\frac{E'-E}{k_B T}} \tag{3.23}$$

To obtain the rate constants for collisional stabilization and collisional activation ($k_c(E)$ and $k_e(E)$), the appropriate probabilities for these processes are multiplied by the bath gas concentration and inelastic collision frequency, k_{coll}, which is usually assumed to be equivalent to the collision frequency between two molecules subject to a Lennard-Jones intermolecular potential,[90] and has the form

$$k_{coll} = \pi\sigma^2 \langle v \rangle \Omega^{(2,2)*} \tag{3.24}$$

in which σ is the Lennard-Jones diameter, $\Omega^{(2,2)*}$ is the collision integral,[91] and <v> is the average molecular velocity at a given translational temperature.[21]

$$\langle v \rangle = \left(\frac{8 k_B T}{\pi \mu} \right)^{1/2} \tag{3.25}$$

In equation 3.25, it is assumed that the two interacting molecules constitute a pseudo-diatomic system, and μ is simply the reduced mass calculated using the masses of the two molecules.

3.3.5.2. RRKM implementation in MultiWell

Throughout this work, the RRKM calculations were performed using the MultiWell suite of computer programs, and the formalism used therein is briefly outlined here.[85,86] The

MultiWell program solves the linear system of ordinary differential equations comprising the master equation through Gillespie's stochastic approach.[83,85] In the MultiWell implementation of RRKM theory, a hybrid master equation approach is adopted, in which the master equation in its continuum form is used at high vibrational energies and a discrete energy-grained master equation is used at low energies. This use of a continuum master equation is advantageous in terms of computational cost reduction, and is justified by the fact that unlike the distinctly discontinuous state density that exists at low energies, a quasicontinuum of vibrational states arises at high vibrational energies as a result of the significant amount of overlap between these states.[85]

MultiWell relies on collision parameters, sums and densities of states, and the relative energies of the TSs in relation to the adduct to calculate energy-specific rate constants as well as the fractional yield of each well and set of products as a function of time or number of collisions. Due to the scarcity of experimental information, energy transfer and collision parameters have been assessed via the simple exponential-down model and Lennard-Jones intermolecular potential, respectively, throughout this dissertation. According to Barker et al.[88], when not much is known regarding the energy transfer parameters, it is reasonable to adopt a simple exponential-down model. In this model, and $\alpha(E')$ parameter, which is related to the collision efficiency of the specific bath gas, may be expressed as a linear function of the internal energy by $c_1 + c_2 \times E$. The first coefficient, c_1, was approximated by Barker to be ~ 40.0 cm^{-1}, which is the average of the existing c_1 values for benzene, toluene, and pyrazine. The second coefficient can be approximated by the expression

$$c_2 = (\langle \Delta E \rangle_{down} - 40.0\ cm^{-1}) / E_0 \qquad (3.26)$$

where $\langle \Delta E \rangle_{down}$ is the average energy transferred per deactivating collision and E_0 is the reaction threshold energy, or the critical energy. To approximate $\langle \Delta E \rangle_{down}$, another relation is provided by Barker et al.[88]

$$\langle \Delta E \rangle_{all} = k_B \times T - \langle \Delta E \rangle_{down} \quad (3.27)$$

where $\langle \Delta E \rangle_{all}$ is the average energy transferred per collision. In the case of the bath gas used predominantly throughout this dissertation, Ar, this quantity has been approximated as was done by Dean et al.,[92] by averaging the three experimental values given by Troe and Gardiner, resulting in the transfer of 2.63 kJ mol^{-1} on average, per collision.[93]

For Ar bath gas, the Lennard-Jones parameters used for this collider are σ = 3.47 Å and ε/k_B = 114 K, which were taken from Hippler et al.[94] For the adducts characterized in the various studies comprising this dissertation, σ was approximated according to the modified empirical rules of Reid and Sherwood[95], which equate this quantity with $1.45 \times (\Sigma V_i)^{1/3}$, where the V_i terms are the additive volume increments of the i^{th} atom. The ε/k_B value for all adducts was arbitrarily assigned as 400 K.

The calculations of the sums and densities of vibrational states, necessary for the evaluation of microcanonical rate constants for dissociation via equation 3.19, are performed via the Stein-Rabinovitch[96] adaptation of the Beyer-Swinehart[97] exact count algorithm. The energy-specific rate constants k(E), or the relative product population, can then be used to evaluate the canonical rate constant under any conditions, including the low-pressure limiting rate constant k_0 and rate constants in the fall-off region, both of which pertain to non-equilibrium conditions.[85,86] Furthermore, averaging the k(E) rate constants over a Boltzmann distribution yields the high-pressure limiting thermal rate constant k_∞. The low- and high-limiting rate constants are calculated in MultiWell using equations 3.28 and 3.29 below,

$$k_{\infty}(T) = \frac{1}{Q}\int_{E_0}^{\infty} k(E) \times p(E) \times \exp^{(-E/k_B T)} dE \tag{3.28}$$

$$k_0^{SC}(T) = \frac{k_{coll}}{Q}\int_{E_0}^{\infty} p(E) \times \exp^{(-E/k_B T)} dE \tag{3.29}$$

where again, p(E) is the density of states of the adduct, Q the vibrational partition function for the adduct, k_B is Boltzmann's constant (1.38×10^{-23} J/K), and k_{coll} is the Lennard-Jones collision frequency.[90,91] The "SC" superscript following k_0 denotes that this is the strong-collider rate constant that would be obtained if the bath gas had the maximum collision efficiency (β) of 1. The collision efficiency provides some measure of the energy transferred during a collision, $\langle \Delta E \rangle_{all}$, and is related to this quantity via equation 3.30 below,

$$\frac{\beta}{(1-\sqrt{\beta})} = -\frac{\langle \Delta E \rangle_{all}}{F_E k_B T} \tag{3.30}$$

where F_E is a correction factor accounting for the energy dependence of the density of states, with typical values of $F_E \approx 1.1$.[93,98] The collision efficiency depends on the nature of the collider and can have a value between 0 and 1. For example, in the case of Ar, $\beta_{Ar} \approx 0.4$ at room temperature.[99] To obtain the low-pressure limiting rate constant k_0, k_0^{SC} must be multiplied by the appropriate collision efficiency, as shown in equation 3.31.[98]

$$k_0(T) = \beta \times k_0^{SC} \tag{3.31}$$

Though these rate constants correspond to unimolecular dissociation processes, the canonical rate constants for the corresponding recombination reactions can be obtained from

$$k_{rec}(T) = f_i \times k_{uni,\infty} \times \frac{1}{K_{eq}(T)} \tag{3.32}$$

in which f_i fractional population of the i^{th} product of interest, and $K_{eq}(T)$ is the equilibrium constant at the temperature of interest and is interpreted in terms of the recombination reaction

being the forward reaction.[85,86] Much more extensive reviews of RRKM theory can be found in the books by Gilbert and Smith (1990)[66], Holbrook et al. (1996)[33], and Forst (2003)[82], a full description of MultiWell and its theoretical formulation has been given by Barker,[85,86] and a guide to the operation of MultiWell comprised of examples pertaining to the reaction systems studied in this work is presented in Appendix D.

3.3.5.3. Assessment of Loose TS and k_a for Entrance Channel

Finally, the estimation of a suitable collision rate coefficient for reaction 3.3, denoted k_a, is somewhat more involved, and will be briefly discussed here. As can be seen in Figure 3.2, most of the time the process of A + B = AB proceeds without any energetic barrier, making it difficult to locate a formal transition state. In fact, the entire "shoulder" on PES corresponding to this process can be thought of as the TS area, and the TS structures characteristic of this area are often termed "loose," as they generally possess long bonds, loose vibrations, and large moments of inertia. In these kinds of situations, the loose TS must be located variationally, or in other words, the point along the PES which minimizes the rate constant determines to the location of the TS. One suitable method for locating a loose TS is VTST, which was previously discussed above. This method is particularly appealing if the vibrationally adiabatic ground-state potential is mapped out, and the properties of points along this potential can be accessed. A canonical VTST approach based on these considerations is implemented for the H_2SCl reaction system studied in chapter 4.

An alternative method for the assessment of k_a is also adopted in chapters 4 – 7, which is based on interpreting the loose transition state at the entrance channel via a hindered Gorin model.[66,100,101] According to the general Gorin model,[102] as the two species come together along

the effective bonding potential, a centrifugal maximum is reached at distance r_{max}, and in the Gorin-type TS corresponding to this energetic maximum the two molecular fragments rotate independently of one another. In MultiWell, the value of r_{max} is obtained at the energetic maxiumum along a Morse potential, and from it, the two-dimensional adiabatic moment of inertia (J-Rotor) for the loose Gorin-type TS is calculated from equation 3.33.

$$I_{2D}^{*} = \mu r^{2}_{max} \tag{3.33}$$

In this equation, the two interacting species are interpreted via a pseudo-diatomic model, such that μ is simply the reduced mass and can be calculated from the masses of the two species via equation 3.34, in which H_2S + Cl is used as an illustrative example. For the Morse potential analysis, MultiWell requires the equilibrium center-of-mass distance between the two molecular fragments bound in the adduct, the equilibrium frequency of the dissociating bond in the adduct, and the classical dissociation energy of the adduct into the two fragments.

$$\mu = \frac{m_{H_2S} \times m_{Cl}}{m_{H_2S} + m_{Cl}} \tag{3.34}$$

In the Gorin model, the transitional modes of the Gorin-type TS are actually better described as hindered rotations than vibrations, therefore their contributions to the overall thermochemistry are calculated as for usual rotational degrees of freedom, so, for example, the rotational energy in the J-Rotor is assumed to have a value of RT. In addition to the J-Rotor, the Gorin-type TS includes the vibrations of the two separate molecular species, their two-dimensional moments of inertia, and a one-dimensional external moment of inertia (K-rotor) for the Gorin-type TS as supplementary degrees of freedom. The value for the K-rotor of the Gorin-type TS was assumed to be the same as the one for the dissociating adduct.

In contrast, the hindered Gorin model[66,100,101] assumes that the two species cannot rotate freely, because their rotations are effectively hindered due to mutual steric interference. This steric hindrance has the effect of reducing the sum of states in the Gorin-type transition state, and is accomplished by scaling the two-dimensional moments of inertia from the two molecular fragments by a hindrance parameter, γ. The γ parameter actually depends on another hindrance parameter, η, which can vary between 0 at free rotation to 1 at completely hindered rotation, and is defined in equation 3.35.

$$\gamma = (1 - \eta)^{1/2} \tag{3.35}$$

When it was possible, the hindrance parameters were selected such as to match the experimental rate constants for recombination at each temperature of interest. If no experimental rate constants were available, they were approximated based on an assumed "hard-sphere" collision model. In this model, k_a is evaluated at each temperature based on the expression

$$k_{a(HS)} = \left(\frac{8k_B T}{\pi \mu} \right)^{1/2} \times \pi d^2 \tag{3.36}$$

where d is the hard-sphere collision diameter, but throughout this dissertation, this parameter has been approximated by the Lennard-Jones collision diameter σ.

CHAPTER 4

THE REACTION BETWEEN HYDROGEN SULFIDE AND ATOMIC CHLORINE

4.1. Introduction

The reaction

$$Cl + H_2S \rightarrow SH + HCl \qquad (4.1)$$

is of dynamic interest as a prototypical heavy-light-heavy system of atoms.[103] Several studies have focused on the production of vibrationally excited products whose distribution may readily be monitored by infra-red techniques, and a population inversion between newly formed HCl(v=0) and HCl(v=1) allows laser action.[104] Reaction 4.1 may also be of significance in the atmosphere of Venus, where it could couple sulfur and chlorine chemistry, and possibly in the terrestrial atmosphere as well.

Dill and Heydtmann generated Cl atoms in a discharge through Cl_2 at low pressures and detected infrared chemiluminescence (IRCL) from HCl in v>0.[105] Leone and co-workers used laser flash photolysis (LFP) of precursor molecules to generate atomic chlorine, and monitored the IRCL of the HCl product, attributed mainly to HCl in the v=1 and v=2 states.[106,107] Agrawalla and Setser were able to detect the weak emission from vibrationally excited SD produced via

$$Cl + D_2S \rightarrow SD + DCl \qquad (4.2)$$

and deduced that approximately 3% of the reaction exoergicity led to SD vibrational excitation, with 7±4% of the SD produced in v=1.[108] Hossenlopp et al. monitored the DCl distribution via time-resolved IR diode laser spectroscopy, and found the ratio for v=0:v=1:v=2 to be

0.33:0.56:0.11.[109] The most recent dynamics study by Chen et al. was based on time-resolved FTIR monitoring of reaction 4.1, and these workers obtained the ratio for v=0:v=1:v=2 to be 0.41:0.52:0.07.[110] These distributions are consistent with the general interpretation of heavy-light-heavy systems, where most of the energy release is expected to result in excitation of the new H-Cl bond.[103]

There is uncertainty about the detailed mechanism of reaction 4.1. One possibility is direct abstraction, but an addition/elimination pathway has been discussed by several groups.[107,111,112] The *ab initio* work of Wilson and Hirst indicated the existence of a bound H_2S-Cl adduct, but not whether it could decompose to SH + HCl.[113] They also characterized a transition state (TS) for direct abstraction. Their transition state theory calculations for direct abstraction gave a room temperature rate constant an order of magnitude below that observed, which left open the possibility that addition/elimination dominates the kinetics. In contrast, Resende et al. found that the adduct previously characterized by Wilson and Hirst can lead to the elimination of HCl based on high level *ab initio* computations.[114] However, the room temperature rate constant they obtained via canonical variational transition state theory was an order of magnitude larger than the experimental quantity. They conducted classical trajectory calculations which indicated that the lifetime of the adduct is very short, and this led Resende et al. to conjecture that "only a small fraction of the collisions are adequate to promote stabilization of the adduct and its reaction," and that "in the other cases, recrossing of the transition state and breakdown of the canonical variational transition state theory would take place."[114] Nicovich et al. commented that the available dynamics data "do not appear to allow clear differentiation between the two possible mechanisms".[112] Subsequently, Chen et al. were unable to explain their

measured rotational energy distributions in terms of a direct abstraction model, and speculated that an addition/elimination model might rationalize their observations.[110]

Prior measurements of the rate constant k_1 for reaction 4.1 are listed in Table 4.1. It may be seen that at room temperature these span a factor of 3. In addition to some of the IR studies mentioned already, kinetic data have been obtained via the discharge-flow (DF) method combined with resonance fluorescence (RF) and molecular-beam mass spectrometry (MBMS) detection,[115,116] via flashlamp photolysis (FP) or LFP combined with RF detection,[111,112] and via relative rate measurements where radioactive ^{38}Cl was produced by irradiation of CF_3Cl.[117] As well as disagreements concerning the magnitude of k_1, there are disagreements concerning its temperature dependence, where zero or slightly negative activation energies (E_a) have been reported.[111,112,117] The NASA-JPL critical evaluation[118] is based on the kinetics studies of Nicovich et al.,[112] who applied the LFP-RF technique over 200-430 K to both reactions 4.1 and 4.2.

One aim of the present work is to extend the temperature range for k_1, to more closely determine its temperature dependence. Incidentally, our extension to beyond 900 K encompasses all regions of the Venusian atmosphere. A second aim is to gain insight into the mechanism by computational methods. Stationary points along the direct abstraction and addition/elimination pathways are characterized by high-accuracy *ab initio* methods, which allows quantitative tests to see if either can reproduce the measured rate constants. Here, it is argued that the reaction proceeds via a bound $Cl\text{-}SH_2$ intermediate which then dissociates over a barrier lower in energy than the reactants to the final HS + HCl products.

4.2. Methodology

4.2.1. Measurements of Cl + H_2S Kinetics

The laser flash photolysis – resonance fluorescence technique was employed to study the kinetics of reaction 4.1. Excimer laser radiation of 193 nm was used to generate Cl atoms from the photolysis of CCl_4. Cl atoms were excited by a microwave-powered discharge lamp and their time-resolved fluorescence intensity was monitored with a solar-blind photomultiplier tube. More details regarding the experimental procedure and apparatus may be found in chapter 2.

The fluorescence intensity decays resulting from pseudo-first order kinetics were analyzed as described in chapter 2, and an example of a typical decay of the fluorescence intensity signal I_f can be seen in the inset of Figure 4.1. The statistical uncertainty in the slope of the line through the data in Figure 4.1 leads to the overall 1σ uncertainty in the second order rate constant k_1 via the procedure in section B2 of appendix B. The photolysis energy F, pressure, and the average gas residence time inside the reactor before photolysis, τ_{res}, were varied in order to assess any dependence of the second-order rate constants upon these parameters.

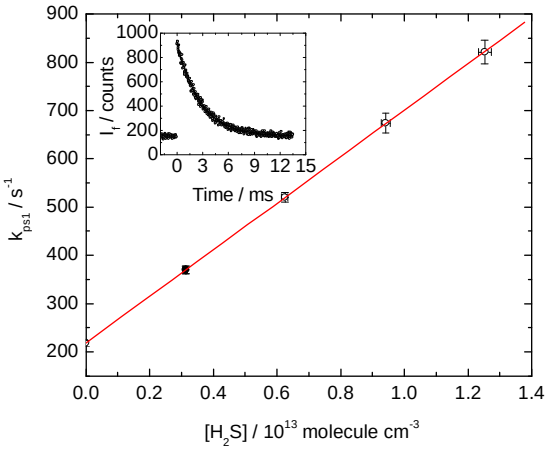

Figure 4.1. Plot of k_{ps1} vs [H_2S] obtained at 536 K and 21 mbar. The error bars are 2 σ. The inset shows the decay of fluorescence signal plus background corresponding to the filled point.

4.2.2. Computational Method

The CCSD(T)/CBS-aug theory, previously discussed in chapter 3, has been implemented to characterize stationary points along the potential energy surface of the H_2SCl system. At this level of theory, spin-unrestricted QCISD/6-311G(d,p) theory is used for geometry optimizations and harmonic frequency calculations, and a scaling factor of 0.954[59] is applied to correct the harmonic frequencies for anharmonicity. Because spin-contamination was found to be negligible in the H_2SCl doublet species ($<S^2>$ of less than 0.8), the usual single-point UCCSD(T)/ROHF calculations are replaced with single-point UCCSD(T)/UHF calculations in this work. These single-point UCCSD(T)/UHF calculations, with the augmented triple and quadruple zeta correlation-consistent basis sets (aug-cc-pVnZ, n = T, Q), are performed on the QCISD/6-311G(d,p) geometries, and a two-point extrapolation scheme is utilized to approximate the CCSD(T) result at the complete basis set limit. The energy of the Cl atom has been corrected for the effect of spin-orbit coupling, and scalar relativistic corrections, comprised of the Darwin and mass-velocity corrections calculated with CISD/cc-pwVTZ theory, have been made for all species. Furthermore, frozen-core and all-electron correlation calculations have been carried out using CCSD(T)/cc-pwVTZ theory, and the ensuing core-valence corrections have been applied to all species. All of the geometry optimization and frequency calculations have been carried out using the Gaussian 03 program suite,[62] while the scalar relativistic corrections, and core-valence corrections have been calculated with Molpro 2002.6.[61]

4.2.3. Theoretical Kinetic Model

Canonical Variational Transition State Theory has been applied to locate the loose transition state of the entrance channel. The vibrationally adiabatic ground-state potential for

H_2S + Cl forming the adduct A1 was generated via a relaxed scan at the QCISD/6-311G(d,p) level of theory, with the vibrational frequency corresponding to the motion along the potential being projected[119] out for each of the ensuing points using the Gaussian 03 keyword Freq=Projected. In all, nineteen points have been calculated along the potential at 0.1 Å intervals. To further refine the energy of these points, the CCSD(T)/CBS-aug treatment including all of the relativistic and core-valence corrections previously described was employed.

At each of the seven temperatures considered, the TST rate constants obtained have been plotted against the S-Cl bond distance ($r_{S\text{-}Cl}$), and in each case, it was found that third-order polynomial functions reasonably fit the data (Tables 4.2 – 4.3 and Figure 4.2). Differentiation of these polynomials yielded the $r_{S\text{-}Cl}$ values at which the TST rate constant is at a minimum at each temperature. Similar fitting procedures have been used to plot the behavior of the rotational constants (Figure 4.3), vibrational modes (Figure 4.4), and energy (Figure 4.5) of the nineteen points as a function of $r_{S\text{-}Cl}$ at each temperature. Table 4.4 gives the rotational constants B and C, the two lowest frequencies (1 and 2, respectively), and the relative energy data as a function of $r_{S\text{-}Cl}$ in the loose TS structures, and Table 4.5 gives the fitting expressions and parameters for these properties.

The two lowest frequencies in the loose TS can be described by wobbling motions of the H_2S plane about the x and y axes, respectively, where Cl – S is defined as the z-axis, the C_{2V} axis in H_2S as the approximate y-axis ($A_{Cl\text{-}S\text{-}C2V} = 89.0°$), and the remaining third nearly perpendicular axis as the x-axis. These two modes have also been called the H-S-H twisting and wagging modes by Wilson and Hirst,[113] where twisting is the lower in energy of the two, and will be denoted as such in this work from this point onward. The remaining three frequencies are the usual bending, symmetric stretching, and asymmetric stretching modes of H_2S, and since they

remained roughly constant as $r_{S\text{-}Cl}$ was increased, the average value of each mode was used throughout the VTST analysis. Furthermore, rotational constant A showed only minor non-systematic fluctuations with respect to $r_{S\text{-}Cl}$, so its value was interpolated at the $r_{S\text{-}Cl}$ values of interest. A comprehensive summary of the resulting optimal properties of the loose transition state at each temperature, along with the equilibrium constants derived from the partition functions, is presented in Table 4.6.

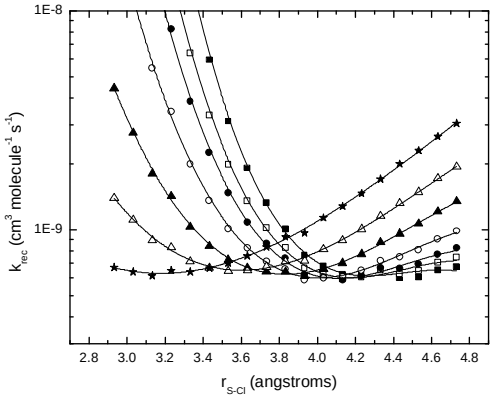

Figure 4.2. Plot of the temperature-specific high-pressure limiting rate constants as a function of the S – Cl distance in the loose TS: filled squares 298 K; open squares 350 K; filled circles 400 K; open circles 500 K; filled triangles 700 K; open triangles 1000 K; stars 1500 K; lines represent fits to temperature-specific data.

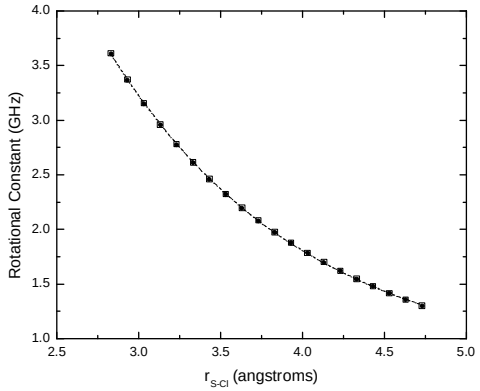

Figure 4.3. Plot of rotational constants B and C as a function of the S – Cl distance in the loose TS: open squares rotational constant B; filled circles rotational constant C; dashed line fit to rotational constant B data; dotted line fit to rotational constant C data.

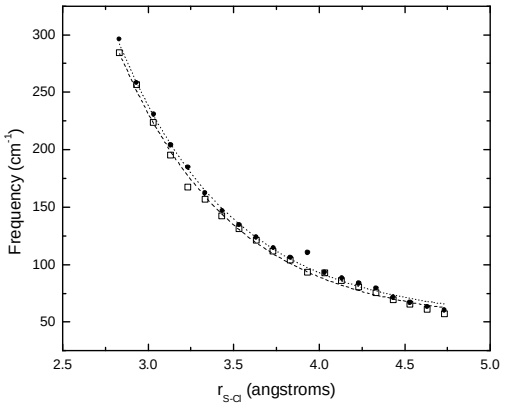

Figure 4.4. Plot of the two lowest frequencies as a function of the S – Cl distance in the loose TS: open squares twisting mode; filled circles wagging mode; dashed line fit to twisting mode data; dotted line fit to wagging mode data.

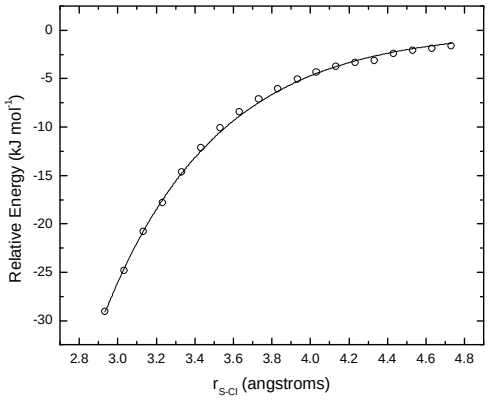

Figure 4.5. Plot of relative UCCSD(T)/CBS-aug energy as a function of the S – Cl distance in the loose TS.

The high-pressure-limiting recombination rate constants obtained from VTST were then converted into the corresponding unimolecular rate constants via the equilibrium constants, which were then plotted Arrhenius-style and are shown in Figure 4.6. The resulting fit to the data indicates that the unimolecular high-pressure-limiting thermal rate constant can be expressed in Arrhenius form by

$$k_{(uni)\infty} = 4.72 \times 10^{13}\ s^{-1} \times \exp(-26.1\ kJ\ mol^{-1} / RT) \quad (4.3)$$

Similarly, the temperature dependence of the TST rate constant for A1 going to SH + HCl was fitted to the Arrhenius equation, shown in Figure 4.7, and the result can be expressed as

$$k_{(uni)\infty} = 5.26 \times 10^{12}\ s^{-1} \times \exp(-27.4\ kJ\ mol^{-1} / RT) \quad (4.4)$$

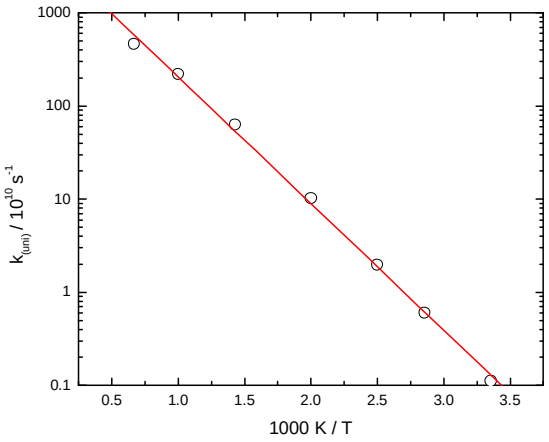

Figure 4.6. Arrhenius plot of the high-pressure-limiting rate constants for A1 = H_2S + Cl.

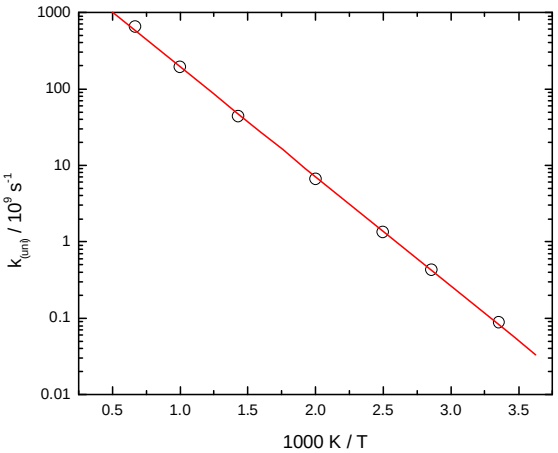

Figure 4.7. Arrhenius plot of the high-pressure-limiting rate constants for A1 = SH + HCl.

MultiWell-based RRKM calculations were carried out for reaction 4.1. The selection of Lennard-Jones parameters for the collider and adduct were discussed in detail in the preceding chapter. A simple exponential-down model was selected to describe the probability of a deactivating collision. According to Barker et al.[88], when not much is known regarding the energy transfer parameters, it is reasonable to adopt a model that is in essence equivalent to Klaus Luther's empirical function, denoted as ITYPE = 10 in the MultiWell manual, and given below.

$$P_d(E,E') = \frac{1}{N(E')} \times \exp^{-\left[\frac{E'-E}{\alpha(E')}\right]^{\beta}} \tag{4.5}$$

In this model, the exponent "β" is set equal to 1 to reduce this function to the general exponential-down model expression given in chapter 3, E' is the initial energy and is always larger than the final energy E, N(E') is the normalization factor determined by MultiWell, and the α(E') parameter is related to the collision efficiency of the specific bath gas and was also previously discussed in chapter 3.

4.3. Results and Discussion

4.3.1. Kinetics

One hundred and three measurements over the range 289-915 K are summarized in Table 4.7. Systematic variation of p, F, τ_{res}, and $[Cl]_0$ yielded k_1 values that were not significantly different within ± σ_{k1}, suggesting that the reaction is effectively bimolecular and unaffected significantly by secondary chemistry, thermal decomposition, and mixing time. Above 915 K the constant background signal became high, which could be indicative of heterogeneous CCl_4 dissociation. Table 4.8 shows the weighted mean k_1 values at each average temperature. The

temperature dependence of the second-order rate constant is depicted in Arrhenius form in Figure 4.8. A linear least squares algorithm[120] was used to perform a weighted linear fit based on the 1σ uncertainties in the k_1 values listed in Table 4.8, combined with the uncertainty in T. It yielded

$$k_1 = (2.88 \pm 0.06) \times 10^{-11} \exp(2.41 \pm 0.10 \text{ kJ mol}^{-1}/RT) \text{ cm}^3 \text{ molecule}^{-1} \text{ s}^{-1} \quad (4.6)$$

where the uncertainties in the Arrhenius parameters are ± 2σ. Combining these uncertainties with the covariance from a plot of $\ln(k_1)$ vs. T^{-1}, -0.0699 K^{-1}, yields statistical 95% confidence limits of 1 to 3 % for k_1 over the temperature range explored, with a minimum at the central temperature. Combination in quadrature with a 5 % allowance for potential systematic errors yields final 95 % confidence limits of ± 5 % for k_1. Based on these considerations, a value of $(7.6 \pm 0.4) \times 10^{-11}$ cm^3 molecule^{-1} s^{-1} is obtained for k_1 at 298 K. Table 4.1 and Figure 4.9 summarize literature data for reaction 4.1 which have been reviewed recently.[118] There is good accord between the present results and those of Nesbitt and Leone[107] and Nicovich et al.,[112] and we confirm the negative activation energy observed by the latter group.

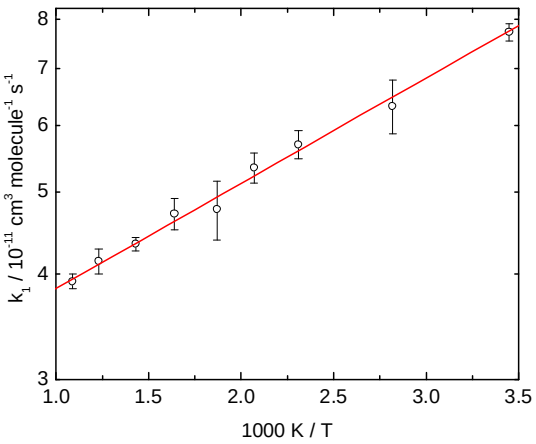

Figure 4.8. Arrhenius plot for Cl + H_2S. Each point represents the weighted average of the measurements at that temperature. Errors bars represent ± 2σ.

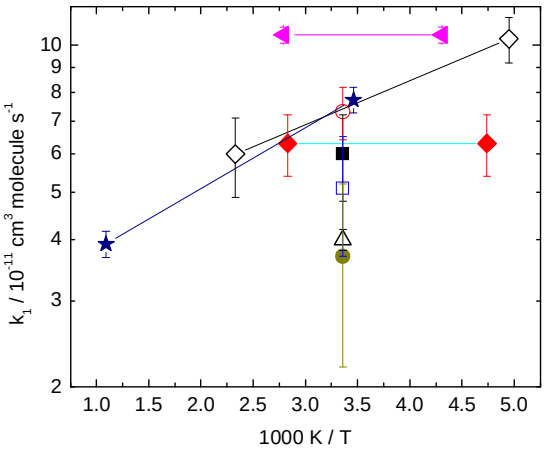

Figure 4.9. Arrhenius plot of kinetic data for Cl + H_2S with 2σ error bars: filled square ref. [106]; open circle ref. [107]; open triangle ref. [115]; open square ref. [116]; filled diamond ref. [111]; filled triangle ref. [117]; open diamond ref.[112]; filled circle ref. [110]; star current work.

4.3.2. Computational Analysis

All stationary points obtained with UQCISD/6-311G(d,p) theory are depicted in Figure 4.10 and Appendix C contains all of the relevant Cartesian coordinates, unscaled vibrational frequencies, and rotational constants obtained from Marshall and Goumri.[121] The electronic energy of each species, calculated with UCCSD(T)/CBS-aug theory,[121] as well as the atomic spin-orbit coupling correction for Cl, the scalar relativistic corrections, and core-valence corrections discussed in section 4.2.4, are given in Table 4.9. The ensuing relative energies for all species are shown in the potential energy diagram of Figure 4.11, and as can be seen, the Cl atom can react with H_2S via two different channels, both initially going through an intermediate H_2S-Cl adduct, denoted A1. The first channel corresponds to an addition-elimination reaction, as A1 isomerizes via transition state TS1 to form the H-bonded adduct A2, which in turn eliminates HCl. The other channel corresponds to a H-atom displacement, in which A1 goes through the

transition state TS2 to yield HSCl and H. Both of these reaction channels have been verified by following each reaction path using the intrinsic reaction coordinate (IRC) feature of Gaussian 03.

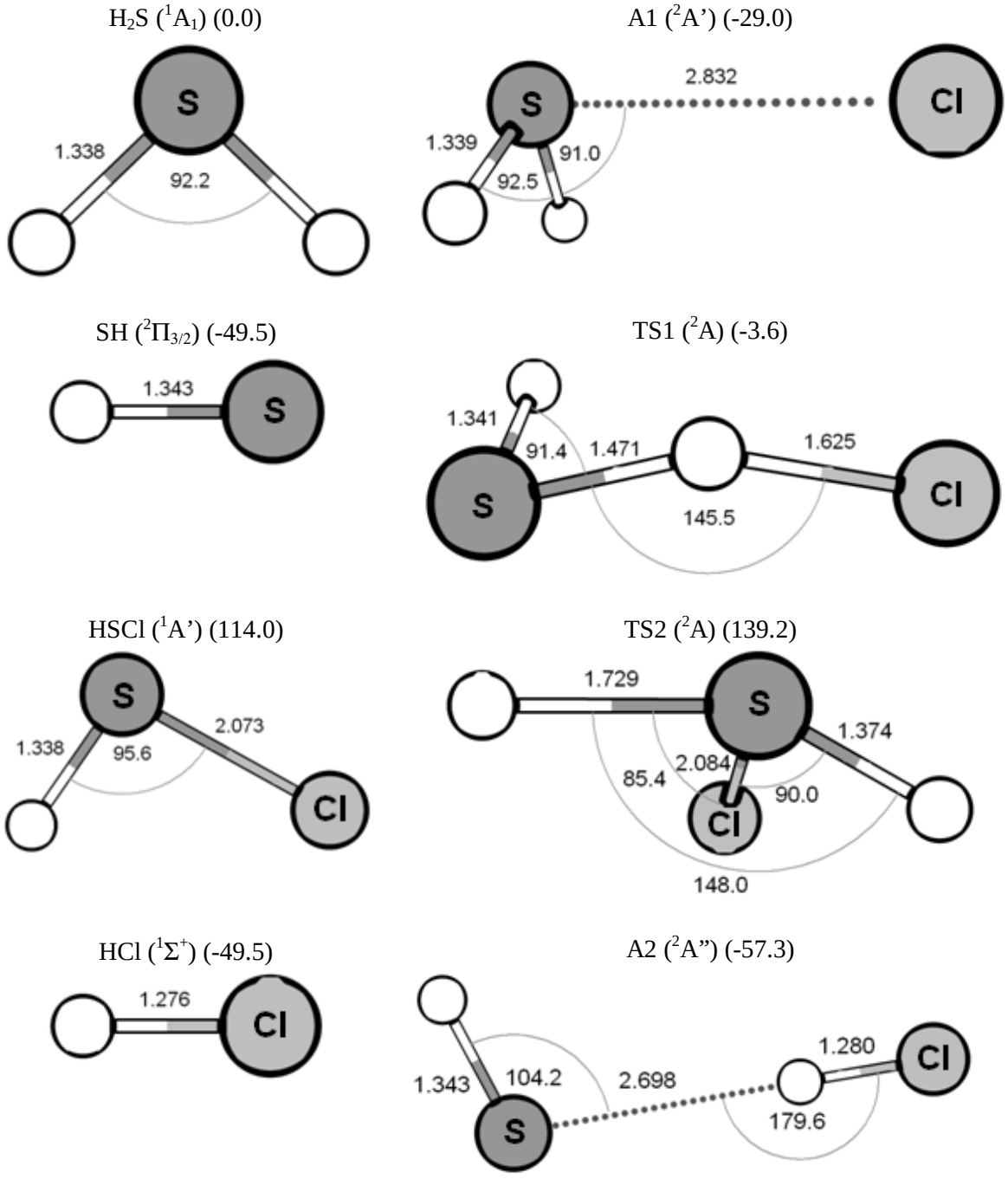

Figure 4.10. Species involved in the H_2SCl reaction system. Geometrical parameters were obtained with QCISD/6-311G(d,p) theory. The values in parentheses represent the relative CCSD(T)/CBS-aug enthalpies in kJ mol^{-1} at 0 K, and also include relativistic and core-valence effects. The values listed for individual fragments of a product set represent the total enthalpy difference between the product set and the reactants.

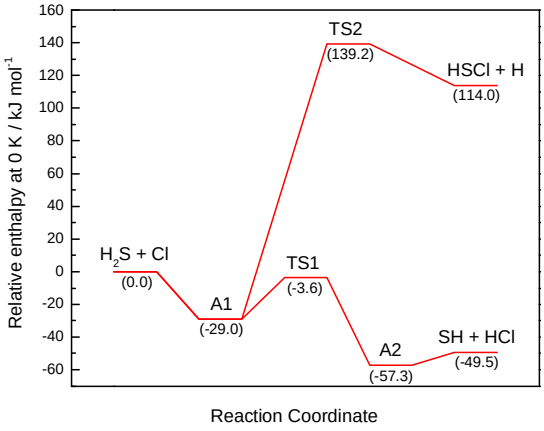

Figure 4.11. Potential energy diagram of the H_2SCl system obtained with CCSD(T)/CBS-aug theory.

The addition process of the addition-elimination channel was found to occur without an electronic energy barrier, which is in accord with both of the only two other computational results of Wilson and Hirst, and Resende et al.[113,114] Because the displacement channel has a high barrier, it is inaccessible throughout the temperature range considered in this work, and is therefore not considered further. The weakly-bound A2 is also neglected, yielding the simplified potential energy diagram used in the ensuing kinetic analysis of section 4.3.3, depicted in Figure 4.12. This simplified potential energy diagram contains the same species located by Resende et al., who used a composite approach denoted as $E_{UCCSD(T,full)/CBS}$.[114] This method relies on geometry optimizations using QCISD/cc-pV(T+d)Z theory, followed by PMP2 single-point energy calculations extrapolated to the CBS limit using the tight d-augmented correlation consistent basis sets[122], the inclusion of more electronic correlation via a single point UCCSD(T,full)/cc-pV(T+d)Z calculation, and the estimation of the CCSD(T,full)/CBS result via the additivity approximation.[123] Previously, Wilson and Hirst also characterized the A1 and TS1

stationary points using a composite scheme that effectively approximates the MP4(Full)/6-311G+(2df,p) single point energies of structures geometrically optimized with MP2(Full)/6-311G** theory, but they treated the addition and abstraction pathways as separate processes as opposed to combining them in an addition/elimination mechanism.[113]

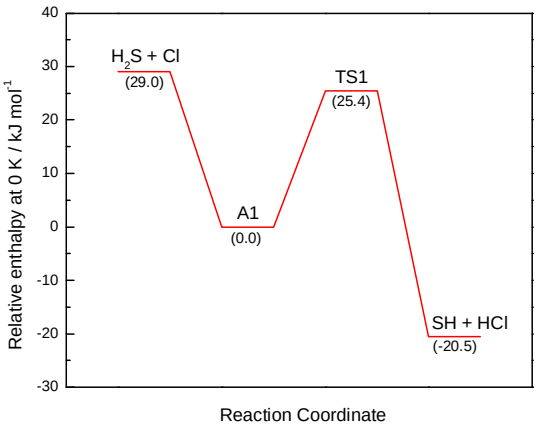

Figure 4.12. Simplified potential energy diagram of the H_2SCl system used for RRKM calculations, obtained with CCSD(T)/CBS-aug theory.

The relative electronic energies of these species are also in good agreement between the three studies, including the overall enthalpy of reaction at 0 K Δ_rH_0 calculated with MP4(Full)/6-311G+(2df,p), $E_{UCCSD(T,full)/CBS,}$ and with CCSD(T)/CBS-aug, with values of -45.0, -54.0, and -49.5 kJ mol^{-1}, respectively. These Δ_rH_0 values are also in reasonable accord with the best experimental determination for this quantity of -51.41 ± 0.05 kJ mol^{-1}, obtained from the difference between the bond dissociation enthalpies of H-Cl (D_0(H-Cl) = 427.648 ± 0.0066 kJ mol^{-1})[124] and HS-H (D_0(H-SH) = 376.24 ± 0.05 kJ mol^{-1}).[125] However, we note that while the barrier heights for reaction 4.1 at 0 K obtained by Wilson and Hirst and by Resende et al. of 4.8 and -14.6 kJ mol^{-1}, respectively, do not compare well to the activation energy of -2.41 ± 0.10 kJ

mol^{-1} measured using the LFP-RF method in this work, the value of -3.6 kJ mol^{-1} obtained with CCSD(T)/CBS-aug is in reasonable agreement. Table 4.10 further compares the $\Delta_r H_0$ values obtained by the three studies for the stationary points in common.

4.3.3. Theoretical Kinetic Analysis

A simple TST analysis was initially performed starting with H_2S + Cl and going through TS1 directly, and the resulting rate constants were assumed to be the upper limits of any RRKM analysis to follow. The densities and sums of states for A1, TS1, and the loose TS at each temperature, were all calculated using scaled QCISD/6-311G(d,p) frequencies by the Densum program available with MultiWell.[86] An RRKM analysis was then carried out at the average experimental pressure of 30 mBar at the seven different temperatures of Table 4.6, using the sums of states of the transition states.

A second analysis was carried out with the k(E) values being evaluated via the Inverse Laplace Transform (ILT)[82] procedure for the A1 = H_2S + Cl channel. In this analysis, the suggestion of Barker et al. of replacing the high-pressure-limiting activation energy E_∞ (26.1 kJ mol^{-1}) with the reaction threshold energy E_0 (29.0 kJ mol^{-1}) for improved description of the fall-off behavior,[85,87] was implemented. Finally, a third RRKM analysis was performed, which was based on a hindered Gorin model[66,100,101] for the loose transition state at the entrance channel, as described in chapter 3. The Morse parameters used for A1, required as input in the Gorin treatment, were r_e = 2.832 Å, υ_e = 136.2 cm^{-1}, and D_e = 33.0 kJ mol^{-1}. The ensuing hindrance parameters, listed in Table 4.11, were selected such as to match the high-pressure limiting rate constants for recombination obtained from the aforementioned VTST procedure at each temperature of interest (Table 4.6). To be consistent with the TST procedure, the calculation of

rotational effects (equation 3.21) has been omitted from the MultiWell-based RRKM analyses. Sample input files for the conventional TS Sum of States, ILT, and Gorin-type TS treatments may be found in Appendix D.

Figure 4.13 depicts the results of the four kinetic analyses graphically. Also contained in figure 4.13, are the experimental data obtained at the same temperatures. Surprisingly, the TST result seems to be lower than any of the RRKM results at nearly all temperatures. All of the kinetic analyses yielded non-linear Arrhenius behavior which is in qualitative and quantitative disagreement with the experimental measurements. Interestingly, recent theoretical calculations for the similar H_2S + OH reaction have found that this system also exhibits non-Arrhenius behavior of comparable curvature.[126] It was also found that the ILT-based RRKM procedure has not met the criteria set forth by John Barker, where the Multiwell-calculated high-pressure-limiting Arrhenius parameters agree with the input parameters within 0.1 %.[85] The hindered Gorin-type TS RRKM analysis overestimates the rate constant by the largest margin, with a calculated rate constant of 1.5 times that observed at room temperature, and ~4 times that observed at 914 K. The ensuing high-pressure limiting recombination rate constants agreed well with the ones used to fit to in the hindered Gorin analysis, indicating that the equilibrium constants K_c listed in Table 4.6 are probably reasonable and that the problem may be that the k_∞ values calculated via VTST are too large. Finally, when using the sums of states of the transition states, the high-pressure-limiting unimolecular rate constant for A1 = H_2S + Cl calculated by MultiWell is usually a factor of 3 smaller than that which was expected from the VTST analysis. This can be reconciled if instead of using the constant E_0 of 29.0 kJ mol^{-1} for this channel, one takes E_0 to be the energy of the loose TS at that particular temperature relative to the energy of A1 (given in Table 4.6), which is how the reaction threshold energy is usually defined for

systems with a positive activation energy. This raises the question of how should the reaction threshold energy be defined in cases with a negative activation energy.

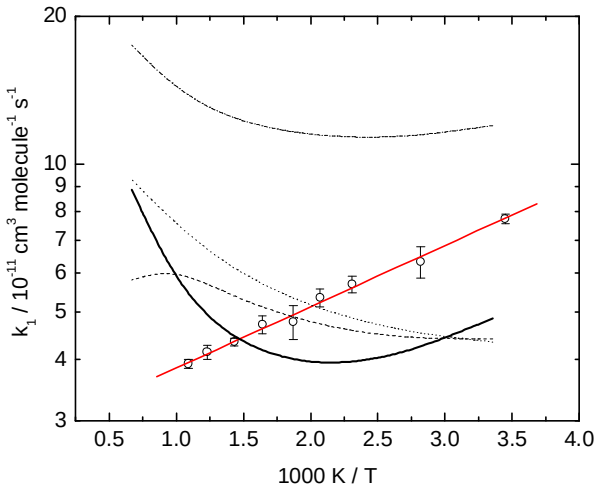

Figure 4.13. Arrhenius plots of the rate constant obtained for $H_2S + Cl = SH + HCl$. Open circles: experimental data points (2σ uncertainties). Bold line: TST result. Dashed line: RRKM result using sums of states for both channels. Dotted line: RRKM with ILT for the loose transition state channel. Dash-dot line: RRKM result with Gorin-type TS (see text).

Regardless of how the MultiWell rate constants were calculated, it was clearly found in each case that the rate of adduct formation does not become significant until unrealistic pressures of thousands of atmospheres are reached, which is in accord with the pressure-independence observed experimentally. Furthermore, while all of the MultiWell-based recombination rate constants exhibited dubious temperature dependences, it can be seen from Figure 4.13 below that at room temperature, these rate constants ranged from ~4 – 12 × 10^{-11} cm^3 $molecule^{-1}$ s^{-1}, all of which are in reasonable agreement with the experimental value of (7.6 ± 0.4) × 10^{-11} cm^3 $molecule^{-1}$ s^{-1} obtained for k_1 at 298 K, unlike the 2.8 × 10^{-12} cm^3 $molecule^{-1}$ s^{-1} and 1.2 × 10^{-9} cm^3 $molecule^{-1}$ s^{-1} values obtained by Wilson and Hirst and Resende et al., respectively.[113,114] The order of magnitude underestimation of the rate constant in the work of Wilson and Hirst may

be attributed to the use of a larger calculated energy barrier in the TST calculation. On the other hand, the assumption by Resende et al. that the loose entrance TS is rate-controlling leads to the neglect of the tighter TS in the adduct-to-products channel. The fact that the adduct more readily dissociates back to reactants rather than to products is the likely cause of the order of magnitude overestimation of the rate constant by Resende et al.

4.4. Conclusions

The kinetics of the reaction between hydrogen sulfide and atomic chlorine have been investigated over 290 – 915 K via the LFP – RF experimental technique. The measured rate constant agrees well with prior determinations under similar conditions in the literature and the observed negative activation energy is also in accord with previous studies. The reaction was found to be independent of pressure over the range of 15.8 – 42 mbar. CCSD(T)/CBS-aug *ab initio* calculations revealed the possibility of an addition - elimination mechanism and an RRKM analysis confirmed the observed pressure independence of the system due to the result that the weakly bound entrance adduct is not significantly stabilized until extreme pressures. MultiWell-based RRKM analyses yielded non-Arrhenius temperature behavior for reaction 4.1, which is qualitative disagreement with the observed temperature dependence of k_1, an issue that is currently being investigated further in collaboration with Dr. David Golden of Stanford University. Overall, the RRKM results were found to be in reasonable accord with experiment at room temperature.

Table 4.1. Comparison of kinetic data for Cl + H_2S.

Experimental Technique	$k_{(298 \pm 2\ K)}$, 10^{-11} cm^3 $molecule^{-1}$ s^{-1}	$E_a \pm 2\sigma$, kJ mol^{-1}	T range, K
LFP-ICL[a]	6.0 ± 1.2		
LFP-ICL[b]	7.3 ± 0.9		
DF-RF[c]	4.0 ± 0.2		
DF-MBMS[d]	5.1 ± 1.4		
FP-RF[e]	6.3 ± 0.9	0[f]	211-353
CR[g]	10.5 ± 0.4	0[f]	232-359
LFP-RF[h]	7.4 ± 1.1	-1.73 ± 0.20	202-430
LFP-FTIR[i]	3.7 ± 1.5		
LFP-RF[j]	7.6 ± 0.4	-2.41 ± 0.10	289-915

[a] ref. 4; [b] ref. 5; [c] ref. 12; [d] ref. 13; [e] ref. 9; [f] no uncertainty reported; [g] ref. 14; [h] ref. 10; [i] ref. 8; [j] current work.

Table 4.2. High-pressure limiting rate constants for H_2S + Cl = A1 obtained via TST.

r_{S-Cl} (Å)	$k_{\infty,rec}(298)$ (cm^3 $molec^{-1}$ s^{-1})	$k_{\infty,rec}(350)$ (cm^3 $molec^{-1}$ s^{-1})	$k_{\infty,rec}(400)$ (cm^3 $molec^{-1}$ s^{-1})	$k_{\infty,rec}(500)$ (cm^3 $molec^{-1}$ s^{-1})	$k_{\infty,rec}(700)$ (cm^3 $molec^{-1}$ s^{-1})	$k_{\infty,rec}(1000)$ (cm^3 $molec^{-1}$ s^{-1})	$k_{\infty,rec}(1500)$ (cm^3 $molec^{-1}$ s^{-1})
2.93	1.99E-06	3.81E-07	1.19E-07	2.44E-08	4.41E-09	1.39E-09	6.72E-10
3.03	4.41E-07	1.10E-07	4.18E-08	1.12E-08	2.77E-09	1.10E-09	6.40E-10
3.13	1.07E-07	3.45E-08	1.57E-08	5.46E-09	1.80E-09	8.95E-10	6.15E-10
3.23	4.02E-08	1.57E-08	8.20E-09	3.45E-09	1.42E-09	8.32E-10	6.50E-10
3.33	1.34E-08	6.39E-09	3.85E-09	1.98E-09	1.03E-09	7.16E-10	6.41E-10
3.43	5.95E-09	3.33E-09	2.24E-09	1.35E-09	8.40E-10	6.70E-10	6.66E-10
3.53	3.12E-09	1.98E-09	1.47E-09	1.01E-09	7.26E-10	6.48E-10	7.03E-10
3.63	1.91E-09	1.35E-09	1.08E-09	8.20E-10	6.67E-10	6.51E-10	7.58E-10
3.73	1.32E-09	1.02E-09	8.63E-10	7.17E-10	6.43E-10	6.76E-10	8.33E-10
3.83	1.00E-09	8.28E-10	7.38E-10	6.59E-10	6.40E-10	7.16E-10	9.26E-10
3.93	7.62E-10	6.67E-10	6.20E-10	5.87E-10	6.11E-10	7.19E-10	9.67E-10
4.03	6.80E-10	6.25E-10	6.03E-10	6.00E-10	6.61E-10	8.12E-10	1.13E-09
4.13	6.23E-10	5.95E-10	5.90E-10	6.10E-10	7.03E-10	8.93E-10	1.28E-09
4.23	6.18E-10	6.06E-10	6.12E-10	6.51E-10	7.73E-10	1.01E-09	1.46E-09
4.33	6.56E-10	6.54E-10	6.68E-10	7.21E-10	8.73E-10	1.15E-09	1.70E-09
4.43	6.00E-10	6.27E-10	6.63E-10	7.50E-10	9.58E-10	1.32E-09	2.00E-09
4.53	6.06E-10	6.48E-10	6.97E-10	8.08E-10	1.06E-09	1.48E-09	2.29E-09
4.63	6.53E-10	7.09E-10	7.70E-10	9.05E-10	1.21E-09	1.71E-09	2.66E-09
4.73	6.75E-10	7.46E-10	8.21E-10	9.85E-10	1.34E-09	1.94E-09	3.05E-09

Table 4.3. Fits of $k_{\infty,rec}(T)$ vs. $r_{S\text{-}Cl}$ data to the third-order polynomial expression $\log(k_{\infty,rec}(T)) = A + B(r_{S\text{-}Cl}) + C(r_{S\text{-}Cl})^2 + D(r_{S\text{-}Cl})^3$.

Parameter	298 K	350 K	400 K	500 K	700 K	1000 K	1500 K
A	82.5974	66.8979	55.6338	39.8519	21.8350	8.3891	-1.9653
B	-62.0783	-51.6191	-44.1071	-33.5685	-21.5096	-12.4757	-5.4745
C	13.9675	11.6255	9.9432	7.5831	4.8829	2.8612	1.2956
D	-1.0456	-0.8691	-0.7424	-0.5645	-0.3611	-0.2089	-0.0911

Table 4.4. Unscaled frequencies, rotational constants, and relative energy of loose transition state structure used in VTST calculations.

$r_{S\text{-}Cl}$ (Å)	[a]Twisting (cm^{-1})	[a]Wagging (cm^{-1})	Rot. Const. B (GHz)	Rot. Const. C (GHz)	[b]($E_{TS} - E_{Reac}$) (kJ mol^{-1})	[b]($E_{TS} - E_{A1}$) (kJ mol^{-1})
2.93	256.1	258.4	3.37	3.36	-29.1	-0.1
3.03	223.8	230.9	3.15	3.15	-24.8	4.2
3.13	195.1	204.1	2.96	2.95	-20.8	8.2
3.23	167.4	184.8	2.78	2.77	-17.8	11.2
3.33	156.6	162.1	2.61	2.61	-14.6	14.4
3.43	142.3	146.9	2.46	2.46	-12.1	16.9
3.53	130.9	134.5	2.32	2.32	-10.1	18.9
3.63	120.7	123.8	2.19	2.19	-8.5	20.5
3.73	111.6	114.5	2.08	2.08	-7.1	21.9
3.83	103.7	106.1	1.97	1.97	-6.0	23.0
3.93	92.8	110.3	1.87	1.87	-5.1	23.9
4.03	92.4	93.1	1.78	1.78	-4.3	24.7
4.13	86.1	88.2	1.70	1.70	-3.8	25.2
4.23	80.4	83.7	1.62	1.62	-3.4	25.6
4.33	75.2	79.5	1.55	1.54	-3.2	25.8
4.43	69.1	71.5	1.48	1.48	-2.4	26.6
4.53	65.1	67.0	1.41	1.41	-2.1	26.9
4.63	60.7	63.3	1.35	1.35	-1.9	27.1
4.73	56.7	60.2	1.30	1.30	-1.6	27.4

[a] The two lowest frequencies in Loose TS calculated with UQCISD/6-311G(d,p) theory (see text).

[b] Calculated with UCCSD(T)/CBS-aug theory and includes core-valence and relativistic corrections (see text).

Table 4.5. Fits of rotational constants B and C, the twisting and wagging modes, and relative energy vs. $r_{S\text{-}Cl}$ data to the function $y = A + B \times \exp(-r_{S\text{-}Cl} / C)$.

Parameter	Rot. B	Rot. C	Twisting	Wagging	$(E_{TS} - E_{Reac})$
A	0.7165	0.7153	49.3897	52.2357	3.01×10^{-76}
B	30.6081	30.4743	17460.83	17696.52	-4414.314
C	1.1988	1.2001	0.6572	0.6585	0.5841

Table 4.6. Energy transfer parameters, loose transition state properties, and equilibrium constants for H_2S + Cl = A1.

T (K)	298	350	400	500	700	1000	1500
Unscaled Frequencies (cm^{-1})	76.1	80.0	83.1	89.0	100.9	122.7	188.2
	79.7	83.6	86.8	92.9	105.1	127.3	194.3
	1224.3	1224.3	1224.3	1224.3	1224.3	1224.3	1224.3
	2757.4	2757.4	2757.4	2757.4	2757.4	2757.4	2757.4
	2779.0	2779.0	2779.0	2779.0	2779.0	2779.0	2779.0
Rotational Constants (GHz)	148.2	148.2	148.2	148.0	147.5	146.9	144.1
	1.6	1.7	1.7	1.8	2.0	2.2	2.9
	1.6	1.7	1.7	1.8	2.0	2.2	2.9
$r_{S\text{-}Cl}$ (Å)	4.26	4.17	4.11	4.00	3.83	3.60	3.18
$(E_{TS} - E_{A1})$ (kJ mol^{-1})	26.0	25.5	25.1	24.3	22.7	19.7	9.8
$k_{\infty,uni}$ (s^{-1})	1.11E9	5.99E9	1.97E10	1.02E11	6.26E11	2.19E12	4.59E12
$k_{\infty,rec}$ (cm^3 $molec^{-1}$ s^{-1})	6.12E-10	5.99E-10	5.95E-10	5.98E-10	6.21E-10	6.49E-10	6.29E-10
K_c (cm^3 $molec^{-1}$)	5.50E-19	1.00E-19	3.02E-20	5.87E-21	9.92E-22	2.97E-22	1.37E-22
$<\Delta E>_{down}$ (cm^{-1})	427.4	463.4	498.1	567.6	706.6	915.1	1262.7
c_2 (cm^{-1})	0.16	0.17	0.19	0.22	0.27	0.36	0.50

Table 4.7. Summary of measurements of the rate constant k_1 for Cl + H_2S.

T, K	τ_{res}, s	F, mJ	p, mbar	$[CCl_4]$, 10^{15} molecule cm^{-3}	$[H_2S]_{max}$, 10^{13} molecule cm^{-3}	$[Cl]_0$, 10^{11} molecule cm^{-3}	$k_1 \pm \sigma_{k1}$, 10^{-11} cm^3 $molecule^{-1}$ s^{-1}
289	0.5	0.55	21	0.98	3.62	10.1	7.79 ± 0.31
289	0.5	0.43	21	0.98	3.62	7.9	7.90 ± 0.29
289	0.5	0.25	21	0.98	3.62	4.6	7.92 ± 0.32
289	0.5	0.17	21	0.98	3.62	3.1	7.91 ± 0.29
291	1.0	1.05	41	1.21	5.25	23.8	7.57 ± 0.22
291	1.0	0.80	41	1.21	5.25	18.2	7.56 ± 0.20
291	1.0	0.44	41	1.21	5.25	10.0	7.77 ± 0.23
291	1.0	0.29	41	1.21	5.25	6.6	7.77 ± 0.24
355	0.8	1.34	42	0.99	2.77	24.9	6.33 ± 0.48
355	0.8	0.89	42	0.99	2.77	16.5	6.17 ± 0.50
355	0.8	0.58	42	0.99	2.77	10.8	6.37 ± 0.53
355	0.8	0.41	42	0.99	2.77	7.6	6.33 ± 0.50
355	0.8	0.27	42	0.99	2.77	5.0	6.40 ± 0.51
433	0.3	0.89	21	0.69	1.46	11.5	5.72 ± 0.50
433	0.3	0.70	21	0.69	1.46	9.1	5.99 ± 0.52
433	0.3	0.46	21	0.69	1.46	6.0	5.63 ± 0.50
433	0.3	0.35	21	0.69	1.46	4.5	5.76 ± 0.49
433	0.6	0.79	41	1.03	1.94	15.3	5.58 ± 0.48
433	0.6	0.64	41	1.03	1.94	12.4	5.74 ± 0.51
433	0.6	0.42	41	1.03	1.94	8.1	5.71 ± 0.49
433	0.6	0.27	41	1.03	1.94	5.2	5.61 ± 0.48
434	1.1	0.87	41	1.32	3.76	21.5	5.52 ± 0.48
434	1.1	0.59	41	1.32	3.76	14.6	5.61 ± 0.49
434	1.1	0.40	41	1.32	3.76	9.8	5.70 ± 0.48
434	1.1	0.26	41	1.32	3.76	6.4	5.64 ± 0.48
482	0.3	0.61	21	0.58	2.30	6.6	5.49 ± 0.37
482	0.3	0.49	21	0.58	2.30	5.3	5.52 ± 0.40
482	0.3	0.34	21	0.58	2.30	3.7	5.50 ± 0.39
482	0.3	0.22	21	0.58	2.30	2.4	5.45 ± 0.36
483	1.1	0.80	42	0.76	4.53	11.4	4.98 ± 0.32
483	1.1	0.57	42	0.76	4.53	8.1	5.16 ± 0.34
483	1.1	0.41	42	0.76	4.53	5.8	5.16 ± 0.34

(Table continues on next page)

(Table 4.7. Continued)

T, K	τ_{res}, s	F, mJ	p, mbar	$[CCl_4]$, 10^{15} molecule cm^{-3}	$[H_2S]_{max}$, 10^{13} molecule cm^{-3}	$[Cl]_0$, 10^{11} molecule cm^{-3}	$k_1 \pm \sigma_{k1}$, 10^{-11} cm^3 $molecule^{-1}$ s^{-1}
483	1.1	0.28	42	0.76	4.53	4.0	5.15 ± 0.34
484	0.6	0.89	32	0.67	1.86	11.2	5.48 ± 0.52
484	0.6	0.63	32	0.67	1.86	7.9	5.58 ± 0.49
484	0.6	0.43	32	0.67	1.86	5.4	5.60 ± 0.50
484	0.6	0.25	32	0.67	1.86	3.1	5.63 ± 0.49
536	0.5	0.71	33.2	0.60	2.04	8.0	4.90 ± 0.67
536	0.5	0.44	33.2	0.60	2.04	5.0	4.85 ± 0.67
536	0.5	0.27	33.2	0.60	2.04	3.0	4.80 ± 0.67
536	0.5	0.21	33.2	0.60	2.04	2.4	4.88 ± 0.69
536	0.9	0.86	32.4	0.65	1.82	10.5	4.68 ± 0.64
536	0.9	0.53	32.4	0.65	1.82	6.5	4.76 ± 0.66
536	0.9	0.37	32.4	0.65	1.82	4.5	4.53 ± 0.62
536	0.9	0.24	32.4	0.65	1.82	2.9	4.57 ± 0.63
536	0.3	0.79	15.8	0.59	1.25	8.7	4.83 ± 0.66
536	0.3	0.56	15.8	0.59	1.25	6.2	4.90 ± 0.67
536	0.3	0.33	15.8	0.59	1.25	3.7	4.91 ± 0.67
536	0.3	0.21	15.8	0.59	1.25	2.3	4.70 ± 0.63
610	0.2	0.45	15.8	0.49	1.71	4.1	4.68 ± 0.24
610	0.2	0.30	15.8	0.49	1.71	2.8	4.74 ± 0.21
610	0.2	0.21	15.8	0.49	1.71	1.9	4.89 ± 0.18
610	0.3	0.70	31.2	0.46	1.91	6.0	4.54 ± 0.39
610	0.3	0.49	31.2	0.46	1.91	4.2	4.51 ± 0.38
610	0.3	0.38	31.2	0.46	1.91	3.3	4.51 ± 0.38
610	0.3	0.25	31.2	0.46	1.91	2.2	4.41 ± 0.45
696	0.2	0.79	25.3	0.37	2.61	5.5	4.41 ± 0.12
696	0.2	0.47	25.3	0.37	2.61	3.3	4.32 ± 0.15
696	0.2	0.33	25.3	0.37	2.61	2.3	4.45 ± 0.16
696	0.2	0.24	25.3	0.37	2.61	1.7	4.56 ± 0.16
698	0.2	0.74	34.3	0.41	3.57	5.7	4.36 ± 0.21
698	0.2	0.47	34.3	0.41	3.57	3.6	4.50 ± 0.12
698	0.2	0.29	34.3	0.41	3.57	2.2	4.49 ± 0.14
698	0.2	0.21	34.3	0.41	3.57	1.6	4.55 ± 0.19

(Table continues on next page)

(Table 4.7. Continued)

T, K	τ_{res}, s	F, mJ	p, mbar	$[CCl_4]$, 10^{15} molecule cm^{-3}	$[H_2S]_{max}$, 10^{13} molecule cm^{-3}	$[Cl]_0$, 10^{11} molecule cm^{-3}	$k_1 \pm \sigma_{k1}$, 10^{-11} cm^3 $molecule^{-1}$ s^{-1}
701	0.3	0.99	24.1	0.38	3.62	7.1	4.04 ± 0.13
701	0.3	0.67	24.1	0.38	3.62	4.8	3.99 ± 0.13
701	0.3	0.44	24.1	0.38	3.62	3.1	4.14 ± 0.14
701	0.3	0.28	24.1	0.38	3.62	2.0	4.28 ± 0.18
814	0.2	0.82	40	0.36	2.16	5.5	3.96 ± 0.33
814	0.2	0.55	40	0.36	2.16	3.7	3.91 ± 0.33
814	0.2	0.38	40	0.36	2.16	2.6	3.93 ± 0.24
814	0.2	0.28	40	0.36	2.16	1.9	4.10 ± 0.28
815	0.3	0.84	34	0.38	1.79	6.0	4.17 ± 0.65
815	0.3	0.59	34	0.38	1.79	4.2	4.01 ± 0.45
815	0.3	0.40	34	0.38	1.79	2.9	3.76 ± 0.44
815	0.3	0.24	34	0.38	1.79	1.7	3.93 ± 0.68
815	0.2	0.75	21	0.31	2.04	4.4	3.79 ± 0.36
815	0.2	0.54	21	0.31	2.04	3.1	3.83 ± 0.23
815	0.2	0.35	21	0.31	2.04	2.0	4.01 ± 0.15
815	0.2	0.22	21	0.31	2.04	1.3	4.03 ± 0.33
816	0.1	0.51	40	0.37	4.25	3.5	4.30 ± 0.15
816	0.1	0.36	40	0.37	4.25	2.5	4.32 ± 0.15
816	0.1	0.24	40	0.37	4.25	1.7	4.44 ± 0.16
912	0.1	0.74	22	0.29	4.85	4.0	3.97 ± 0.15
912	0.1	0.53	22	0.29	4.85	2.9	4.07 ± 0.19
912	0.1	0.42	22	0.29	4.85	2.3	4.22 ± 0.18
912	0.1	0.21	22	0.29	4.85	1.1	4.29 ± 0.19
914	0.1	0.74	35	0.30	2.94	4.2	3.86 ± 0.19
914	0.1	0.50	35	0.30	2.94	2.8	3.90 ± 0.25
914	0.1	0.31	35	0.30	2.94	1.7	3.87 ± 0.18
914	0.1	0.21	35	0.30	2.94	1.2	4.13 ± 0.12
914	0.1	0.80	28	0.37	2.27	5.6	3.82 ± 0.15
914	0.1	0.51	28	0.37	2.27	3.5	3.86 ± 0.36
914	0.1	0.36	28	0.37	2.27	2.5	3.66 ± 0.32
914	0.1	0.23	28	0.37	2.27	1.6	4.07 ± 0.27
915	0.2	0.84	22	0.29	3.38	4.6	3.77 ± 0.31

(Table continues on next page)

(Table 4.7. Continued)

T, K	τ_{res}, s	F, mJ	p, mbar	$[CCl_4]$, 10^{15} molecule cm^{-3}	$[H_2S]_{max}$, 10^{13} molecule cm^{-3}	$[Cl]_0$, 10^{11} molecule cm^{-3}	$k_1 \pm \sigma_{k1}$, 10^{-11} cm^3 $molecule^{-1}$ s^{-1}
915	0.2	0.54	22	0.29	3.38	2.9	3.84 ± 0.34
915	0.2	0.35	22	0.29	3.38	1.9	3.74 ± 0.32
915	0.2	0.24	22	0.29	3.38	1.3	3.79 ± 0.21
915	0.2	0.83	28	0.29	3.35	4.5	3.72 ± 0.37
915	0.2	0.61	28	0.29	3.35	3.3	3.54 ± 0.35
915	0.2	0.42	28	0.29	3.35	2.3	3.61 ± 0.32
915	0.2	0.24	28	0.29	3.35	1.3	3.65 ± 0.32

Table 4.8. Weighted mean k_1 values for Cl + H_2S with statistical uncertainties.

T, K	$k_1 \pm \sigma_{k1}$, 10^{-11} cm^3 $molecule^{-1}$ s^{-1}
290	7.73 ± 0.09
355	6.32 ± 0.23
433	5.69 ± 0.11
483	5.34 ± 0.11
536	4.77 ± 0.19
610	4.71 ± 0.10
698	4.34 ± 0.04
815	4.14 ± 0.07
914	3.92 ± 0.04

Table 4.9. Energies and zero point energies in E_H for species on the PES of reaction 4.1.

Species	Electronic Energy QCISD/ 6-311G(d,p)	Unscaled ZPE QCISD/ 6-311G(d,p)	[a]Scalar Relativistic correction	[b]Core-Valence correction	Electronic Energy CCSD(T)/ aug-cc-pVTZ	Electronic Energy CCSD(T)/ aug-cc-pVQZ	Electronic Energy aug-CBS	[c]Total Energy
H	-0.49981	0	-0.00001	0	-0.49982	-0.49995	-0.50004	-0.50005
Cl	-459.60167	0	-1.40334	-0.30271	-459.67622	-459.69474	-460.70826	-461.41566
H_2S	-398.86817	0.01545	-1.07682	-0.29621	-398.94081	-398.95731	-398.96934	-400.32764
HCl	-460.26032	0.00694	-1.40294	-0.30305	-460.34324	-460.36417	-460.37944	-462.07882
SH	-398.22521	0.00623	-1.07716	-0.29591	-398.29133	-398.30572	-398.31622	-399.68334
HSCl	-857.90231	0.00959	-2.48005	-0.59898	-858.06482	-858.10247	-858.12994	-861.19982
A1	-858.47547	0.01705	-2.48020	-0.59897	-858.62924	-858.66520	-858.69143	-861.75434
A2	-858.48887	0.01468	-2.48005	-0.59901	-858.63922	-858.67439	-858.70005	-861.76511
TS1	-858.45907	0.01246	-2.48028	-0.59909	-858.61556	-858.65119	-858.67718	-861.74466
TS2	-858.38599	0.01146	-2.48004	-0.59894	-858.55548	-858.59408	-858.62224	-861.69028

[a] Correction was calculated with CISD/cc-pwVTZ theory (see text).
[b] Correction was calculated with CCSD/cc-pwVTZ theory (see text).
[c] Energy calculated by adding scaled ZPE, scalar relativistic and core-valence corrections, and a correction of -0.00134 for Cl-atom spin-orbit coupling to aug-CBS electronic energy (see text).

Table 4.10. Comparison of computed thermochemistry for H_2SCl stationary points relative to $Cl + H_2S$.

Δ_rH_0(A1) (kJ mol^{-1})	Δ_rH_0(Abs TS) (kJ mol^{-1})	Δ_rH_0(SH + HCl) (kJ mol^{-1})	Investigators
-34.2	4.8 / 9.7[a]	-45.0	[b]Wilson and Hirst
-41.4	-14.6	-54.0	[c]Resende et al.
-29.0	-3.6	-49.5	[d]Current Work
		-51.41 ± 0.05	[e]Experimental

[a] The authors claim that this value is 4.8 kJ mol^{-1} but 9.7 kJ mol^{-1} is obtained from their tabulated energies.

[b] Computed with MP4(Full)/6-311G+(2df,p)//MP2(Full)/6-311G** theory, ref. [113] (see text).

[c] Computed with UCCSD(T,full)/CBS theory, ref. [114] (see text).

[d] Computed with CCSD(T)/CBS-aug theory (see text).

[e] From (D_0(H-Cl) = 427.648 ± 0.0066 kJ mol^{-1}), ref. [124], and (D_0(H-SH) = 376.24 ± 0.05 kJ mol^{-1}), ref. [125].

Table 4.11. Energy transfer parameters, loose Gorin-type transition state properties, and rate constants for reaction 4.1.

T (K)	298	350	400	500	700	1000	1500
r_{max} (Å)	6.43	6.28	6.17	5.97	5.67	5.34	4.95
Hindrance Parameter (γ)	0.780	0.741	0.720	0.704	0.715	0.743	0.728
Hindrance Parameter (η)	0.391	0.451	0.481	0.504	0.489	0.448	0.470
K-Rotor (amu Å^2)	3.436	3.436	3.436	3.436	3.436	3.436	3.436
[a]2D Moment of Inertia-H_2S (amu Å^2)	1.365	1.296	1.260	1.232	1.250	1.300	1.273
J-Rotor (amu Å^2)	717.99	681.09	655.83	614.40	533.72	491.52	422.97
$<\Delta E>_{down}$ (cm^{-1})	427.2	463.4	498.1	567.6	706.6	915.1	1262.6
c_2 (cm^{-1})	0.16	0.17	0.19	0.22	0.27	0.36	0.50
$k_{\infty,uni}$ (s^{-1})	1.18E9	6.20E9	2.04E10	1.05E11	6.36E11	2.20E12	4.61E+12
$k_{\infty,rec}$ (cm^3 $molec^{-1}$ s^{-1})	6.49E-10	6.20E-10	6.16E-10	6.16E-10	6.31E-10	6.54E-10	6.32E-10
k_d (cm^3 $molec^{-1}$ s^{-1})	1.20E-10	1.15E-10	1.13E-10	1.14E-10	1.22E-10	1.41E-10	1.75E-10

[a] Two-dimensional Moment of Inertia of H_2S scaled by the γ hindrance parameter.

CHAPTER 5

THE REACTION BETWEEN AMMONIA AND ATOMIC CHLORINE*

5.1. Introduction

Ammonia is a compound that is abundant throughout the universe. It has been found in the atmospheres of other planets such as Jupiter, Saturn, and Uranus, and has also been implicated in interstellar chemistry.[11,12] On Earth, the constant production of gaseous ammonia via the volatilization of soil fertilizers has made it the third most abundant nitrogen-containing species in the atmosphere. As early as the late 1960s, it was realized that although ammonia is less abundant than N_2 and N_2O, due to its shorter residence time, it is actually the most important species involved in the sun-powered photolytic generation and circulation of nitrogen atoms through the atmosphere.[9] Nitrogen atoms can also be generated via repetitive homolytic N-H bond cleavage in ammonia during chain reactions involving radicals, such as the Cl atom. The simple H-abstraction in reaction 5.1 corresponds to the first step in such a sequence.

$$NH_3 + Cl \rightarrow NH_2 + HCl \qquad (5.1)$$

Due to the wide usage of ammonium perchlorate and related species in modern propellants, the reaction between ammonia and chlorine atoms has also generated interest from the field of propulsion kinetics.[10] Yet despite the importance of reaction 5.1, its kinetics have previously been studied only once, at room temperature.[127] In this work, this reaction has been

* This chapter was partially adapted from the publication of *J. Phys. Chem. A*, Vol. 110, Gao, Y., Alecu, I. M., Hsieh, P.-C., Morgan, B. P., Marshall, P., and Krasnoperov, L. N., "Thermochemistry is not a Lower Bound to the Activation Energy of Endothermic Reactions: A Kinetic Study of the Gas-Phase Reaction of Atomic Chlorine with Ammonia," Pages 6844-6850, Copyright (2006), with permission from the American Chemical Society.

investigated over the temperature range of 290 – 570 K via the LFP-RF experimental technique. Furthermore, Density Functional Theory and high level *ab initio* computations have been carried out to explore the PES of this reaction, which was subsequently used to theoretically assess the thermal rate constant via TST and modified TST (MTST)[76] calculations.

5.2. Methodology

5.2.1. Experimental Technique

The laser flash photolysis – resonance fluorescence (LFP – RF) technique was used to generate ground state chlorine atoms and monitor their fluorescence in the vacuum ultra-violet. The apparatus for LFP – RF and its operation have been described in detail in chapter 2. The photolytic precursor used to generate Cl atoms in this work was CCl_4, and its photochemistry as well as considerations of the laser beam cross-section and laser photon intensity have been used to estimate $[Cl]_0$, as described in section 2.5.2. As usual, the experimental parameters $[Cl]_0$, P, F, and τ_{res} have been varied in order to ensure that the measured second-order rate constant was not significantly influenced by potential secondary chemistry, thermal decomposition, or mixing effects.

Pseudo-first order conditions were achieved by flooding the reactor with excess NH_3, and the measurement of the corresponding pseudo-first order rate coefficients (k_{ps1}) at various concentrations of ammonia enabled the determination of the second order rate constant for reaction 5.1, k_1. A typical exponential decay of the fluorescence signal, used to obtain k_{ps1} via the usual non-linear least squares procedure outlined in chapter 2, is shown in the inset of Figure 5.1. Plots of k_{ps1} versus $[NH_3]$, such as the one displayed in Figure 5.1, have slopes that

correspond to k_1, and intercepts that account for the loss of Cl atoms via processes such as diffusion and reaction with photolysis fragments.

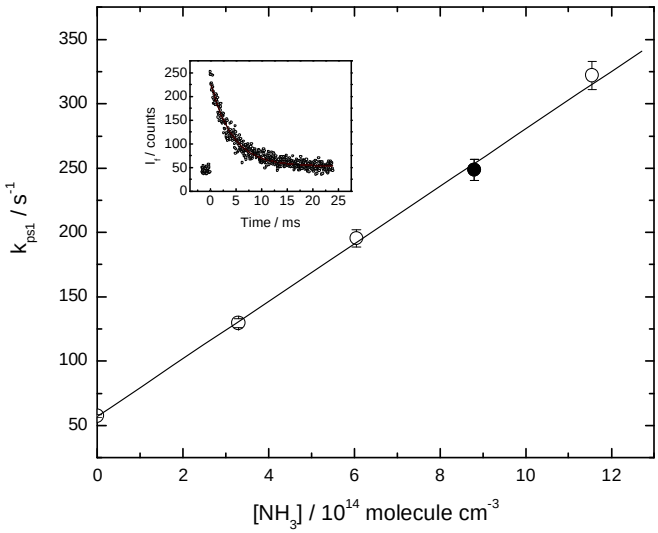

Figure 5.1. Plot of k_{ps1} vs. $[NH_3]$ obtained at 357 K. The error bars are 1σ. The inset shows the fluorescence signal plus background corresponding to the filled point.

5.2.2. Computational Method

The Gaussian 03[62] program suite has been employed to carry out Density Functional Theory and *ab initio* electronic structure theory computations. The MPWB1K functional, developed by Zhao and Truhlar to properly treat H-bonded systems and yield accurate reaction barriers and thermochemistry, has been used to locate and characterize stationary points along the PES of reaction 5.1.[36] The G3B3[128] and CBS-QB3[129] composite methods were also applied to the NH_3Cl system. Finally, spin-unrestricted CCSD(T)/aug-cc-pVTZ calculations were carried out to further refine the geometries and frequencies of the stationary points, and the

energies were used in conjunction with CCSD(T)/aug-cc-pVQZ single-point calculations in an extrapolation that estimated the CCSD(T)/CBS result. The accuracy of the CCSD(T)/CBS results was further improved by the inclusion of atomic spin-orbit coupling for Cl, as well as scalar relativistic and core-valence corrections for all species, calculated in Molpro 2006[130] with the same methods described in chapter 3.

5.3. Results and Discussion

5.3.1. Kinetics and Thermochemistry

Eighty three measurements of the second order rate constant k_1 over the range of 290 – 570 K are summarized in Table 5.1. The second order rate constant was found to be independent of P, $[Cl]_0$, F, and τ_{res}, indicating that reaction 5.1 was effectively bimolecular, and was not appreciably affected by secondary chemistry, thermal decomposition, or mixing times. Above 570 K, it was found that H atoms were produced in large enough amounts to significantly interfere with the observed kinetics, despite the use of calcium fluoride optics.

The data obtained over the 290 – 570 K range are plotted in Arrhenius form in Figure 5.2 below. These data were then taken along with their 1σ uncertainties and fit with a linear least squares algorithm[120] to yield

$$k_1 = (1.08 \pm 0.05) \times 10^{-11} \exp(-11.47 \pm 0.16 \text{ kJ mol}^{-1}/RT) \text{ cm}^3 \text{ molecule}^{-1} \text{ s}^{-1} \qquad (5.2)$$

where the uncertainties in the Arrhenius parameters represent one standard deviation. Following the error analysis procedure described in detail in section B3 of Appendix B, these uncertainties were combined with the covariance and a 10% allowance for potential systematic errors to yield the final 2σ uncertainty in k_1 of 11%. As noted earlier, the only other measurement of k_1 comes from Westenberg and DeHaas, who used a flash lamp to photolyze CCl_4 to generate Cl atoms

and study reaction 5.1 at room temperature.[131] Their measurement has also been included in Figure 5.2, and as can be seen, it agrees well with our measurements. As can also be seen from Figure 5.2, the majority of the room temperature k_1 measurements lie above the linear Arrhenius fit. This could be indicative of curvature in the Arrhenius plot or a possible contribution to the overall rate of Cl loss from a different reaction channel favored at low temperatures, such as an addition channel. However, the clear pressure-independence exhibited by the room temperature second order rate constants coupled with the *ab initio* computational results discussed in the next section, indicate that a Cl-NH_3 adduct would be thermodynamically unstable and therefore addition is unlikely to be an important reaction channel even at room temperature.

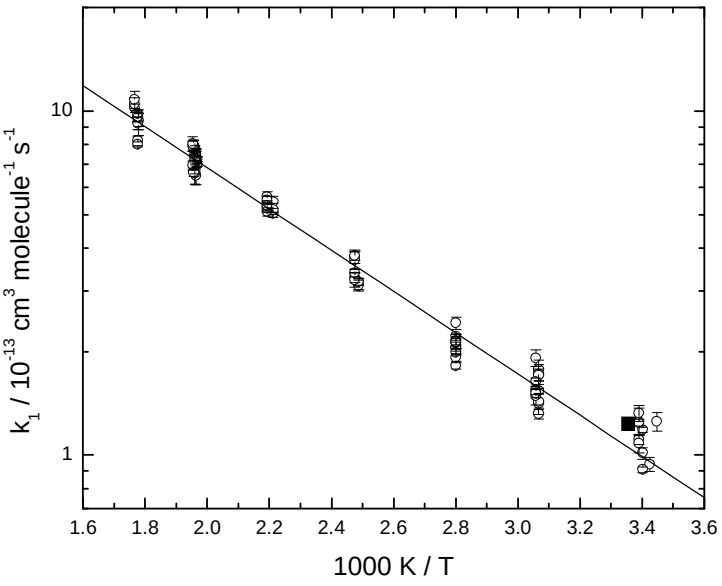

Figure 5.2. Arrhenius plot for Cl + NH_3. Open circles, present measurements with 1σ error bars; solid square, measurement by Westenberg and deHaas.[131]

The $\Delta_r H$ at 0 K for reaction 5.1 can be obtained from the spectroscopic measurement of the bond dissociation enthalpy of the N-H bond in ammonia $BDE_0(H_2N\text{-}H)$[132] = 444.0 ± 0.2 kJ mol^{-1} and the well-established H-Cl bond strength $BDE_0(H\text{-}Cl)$[124] = 427.648 ± 0.007 kJ mol^{-1}. As shown in equation 5.3, the difference between these two quantities yields the reaction enthalpy for reaction 5.1,

$$\Delta_r H_0 = BDE_0(H_2N\text{-}H) - BDE_0(H\text{-}Cl) \quad (5.3)$$

which has a value of $\Delta_r H_0$ = 16.4 ± 0.2 kJ mol^{-1}. Using the temperature dependences of the enthalpies tabulated by Gurvich et al.,[133] a value for the reaction enthalpy can be obtained near the center of the temperature range used in this study, $\Delta_r H_{400}$ = 19.1 kJ mol^{-1}, which is ~ 7.6 kJ mol^{-1} larger than the measured activation energy. Because $\Delta_r H$ can also be directly evaluated from the difference between the activation energies of the forward and reverse reactions,[134] it can be deduced that the activation energy for the reverse reaction 5.4 must be negative.

$$NH_2 + HCl \rightarrow NH_3 + Cl \quad (5.4)$$

In reaction 5.4, a hydrogen-bonded intermediate could potentially be formed from the interaction of the highly electronegative N atom with HCl. If hydrogen bonding does occur in this system, it would also stabilze the transition state for this reaction. These notions as well as the possibility of a negative energy of activation for reaction 5.4 are explored computationally in the next section.

5.3.2. Computations and Kinetic Modeling

Table 5.2 lists the enthalpies at 0 K of stationary points on the potential energy surface relative to Cl + NH_3, derived by various methods. The MPWB1K calculations were carried out with a variety of basis sets within the range used by Zhao and Truhlar in its development, with

the smallest being 6-31+G(d,p) and the largest being the MG3 basis set discussed in chapter 3 (6-311++G(3d2f,2df,2p)).[36] Zhao and Truhlar have determined that the optimal scaling factors for MPWB1K/6-31+G(d,p) and MPWB1K/MG3 frequencies are 0.9537 and 0.9567, respectively,[36] and the average of these two, 0.9552, was used to scale the vibrational frequencies obtained with all the intermediate basis sets used with this functional in this work. The G3B3 and CBS-QB3 composite methods include a spin-orbit coupling correction of -3.5 kJ mol^{-1} to the Cl atom energy within their schemes, and this correction was also made for all the DFT methods listed in Table 5.2. The extent of spin contamination in all the doublet species was found to be negligible, with $<S^2>$ spin expectation values of no more than 0.757.

As can be seen from Table 5.2, the reaction enthalpies calculated with the two composite methods are in good accord with the experimental value for this quantity, and the MPWB1K results exhibit systematic variation with the size of the basis set. While the use of MPWB1K in conjunction with the smallest basis set yielded the least accurate result, interestingly, the most accurate result for this functional was not obtained with the largest basis set. Instead, the accompaniment of MPWB1K by the intermediate 6-31++G(2df,2p) basis set gave the best agreement with the measured $\Delta_r H_0$, and the structural parameters, scaled vibrational frequencies, and energy barrier calculated with this method were therefore selected for the MTST treatment that follows.

Figure 5.3 shows the structural parameters of the various structures involved in the NH_3Cl reaction system obtained with MPWB1K/6-31++G(2df,2p) theory, and Figure 5.4 places the ensuing stationary points on a PE diagram corresponding to the reaction path. As can be seen from Figure 5.4, a potential C_{3v} adduct (A3) in which the Cl atom interacts with the lone pair on the N center has been characterized. Though this adduct has not been observed experimentally,

an analogous complex formed between Cl and pyridine has been recently observed in the gas phase.[135] The A3 adduct has been previously identified by McKee et al. using various *ab initio* methods, and they found that the Cl-N interaction can be described as a two-center – three-electron bonding of the nature $(\sigma)^2(\sigma^*)^1$.[136] Furthermore, at the highest level of theory they used, G2(MP2,SVP), McKee et al. found that while this interaction is worth only 36.3 kJ mol^{-1} in Cl-NH_3, the BDE_0 in Cl-N$(CH_3)_3$ is much more appreciable, having a value of 90.2 kJ mol^{-1}. Consequently, they concluded that "the formation of 2c – 3e bonds is favored by nitrogen bases with low ionization energies and by radicals with high electron affinities."[136]

MPWB1K/6-31++G(2df,2p) calculations find that the A3 adduct has a long Cl-N bond, 2.38×10^{-10} m, which is in relatively good agreement with the 2.38, 2.35, and 2.43×10^{-10} m values obtained by McKee et al. with UMP2(full)/6-31G(d), MP2(fc)/6-311+G(2df,p), and QCISD(T)(full)/6-31G(d) theories, respectively.[136] However, the DFT value obtained here for the BDE_0 of A3, of 47.7 kJ mol^{-1}, is considerably larger than the a 36.3 kJ mol^{-1} value McKee et al. obtained with G2(MP2,SVP), which is more in line with the values obtained with the composite methods used in this work (Table 5.2). Using the MPWB1K/6-31++G(2df,2p) geometries and frequencies to calculate the partition functions of the reactants and A3, as well as the difference in energy between them, ΔE_0 = -47.7 kJ mol^{-1}, an equilibrium constant K_c of 3.6×10^{-16} cm^3 molecule^{-1} is obtained for the formation of A3 at the average room temperature used in experiments of 294 K. The equilibrium constant was calculated via equation 5.5 below.

$$K_c(T) = \frac{Q^{A3}}{\prod_i Q_i^{reac}} \times \exp(-\Delta E_0 / RT) \qquad (5.5)$$

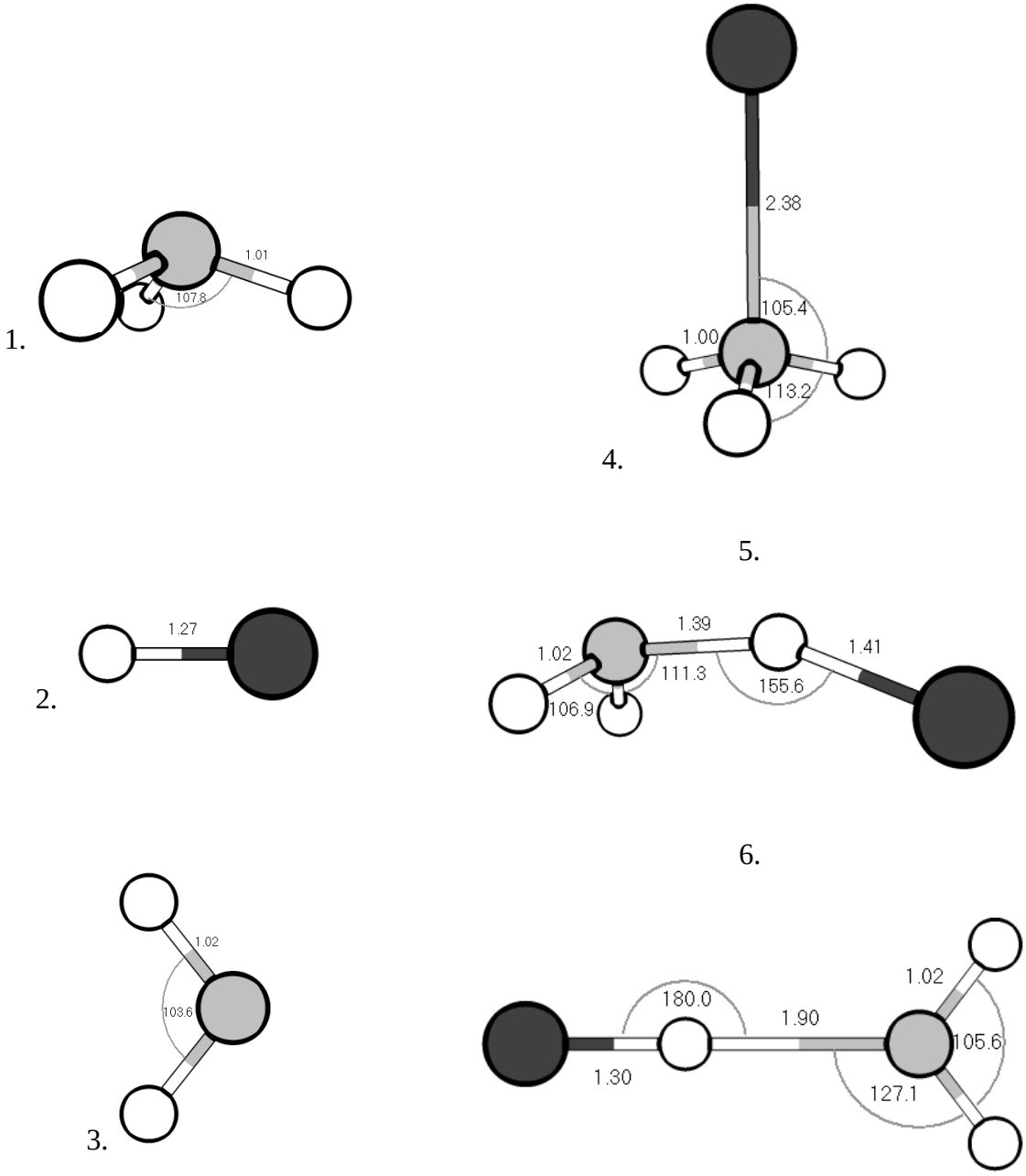

Figure 5.3. Geometries and frequencies (scaled by 0.955) of stationary points on the Cl + NH_3 potential energy surface, computed via MPWB1K/6-31++G(2df,2p) theory. 1. C_{3V} NH_3, 977, 1610 (2), 3440, 3576 (2) cm^{-1}; 2. HCl, 2932 cm^{-1}; 3. C_{2V} NH_2, 1475, 3332, 3427 cm^{-1}; 4. C_{3V} Cl-NH_3 adduct (A3), 297, 342 (2), 817, 1570 (2), 3466, 3614 (2) cm^{-1}; 5. C_S abstraction transition state (Abs TS), 622i, 391, 400, 677, 984, 1180, 1502, 3376, 3481 cm^{-1}; 6. C_{2V} H_2N-HCl complex (A2), 153, 156, 185, 556, 577, 1472, 2568, 3358, 3461 cm^{-1}.

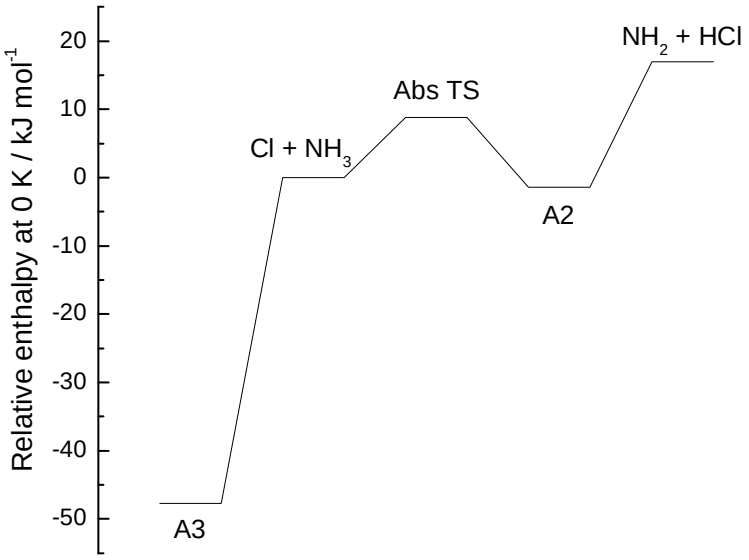

Figure 5.4. Potential energy diagram for Cl + NH_3 computed at the MPWB1K/6-31++G(2df,2p) level of theory.

The value of the equilibrium constant calculated via equation 5.5 implies that under the experimental conditions that would most favor adduct formation, the lowest average T (294 K) and average $[NH_3]_{max}$ at that T (1.99×10^{-16} molecule cm^{-3}), 71% of atomic Cl could be complexed by NH_3. The lack of observed pressure-dependence in our experiments indicates that A3 is not formed in appreciable quantity at room temperature, implying that the BDE_0 of this species has been overestimated with MPWB1K/6-31++G(2df,2p) theory. Performing the same analysis using properties for all species calculated with the CBS-QB3 composite method (ΔE_0 = -40.3 kJ mol^{-1}) yielded an equilibrium constant of 1.3×10^{-17} cm^3 $molecule^{-1}$, indicating that only ~ 3% of all Cl atoms would be involved in the formation of A3 at 294 K, a result that is in line with the pressure-independence observed.

Cl atoms can also be lost via the abstraction channel shown in Figure 5.4. Along this reaction path, the reactants pass through a TS structure (Abs TS) to form a weakly-bound complex (A2) which can then dissociate to the final products. As can be seen in Table 5.2, the TS for abstraction was calculated to be lower in energy than the final products with all theories used, supporting the negative activation energy proposed earlier for the reverse reaction. The A2 intermediate was found to dissociate to NH_2 + HCl without a barrier, and its structure and complexation energy, of only -18 kJ mol^{-1} relative to the products, are consistent with hydrogen bonding. No complexes involving a Cl-H-N arrangement were located in this work.

Dr. Lev N. Krasnoperov, who was a collaborator on this project from the New Jersey Institute of Technology, applied the MTST method described in chapter 3 to the PE diagram, structures, and vibrational frequencies obtained from MPWB1K/6-31++G(2df,2p) theory in order to explore the effects of the calculated negative reaction barrier on the kinetics of reaction 5.4. The mathematical derivation and theoretical formulation of MTST has been described in detail elsewhere.[76,77] In the present implementation of MTST, the conservation of the angular momentum (the J quantum number) and of the energy of the K rotor at the TS were taken into account. Finally, the effects of quantum mechanical tunneling/reflection through the barrier were also considered, and were found to be relatively small, increasing the rate constant for reaction 5.4 by only 9% at 300 K, 7% at 500 K, and 5% at 700 K.

The MTST results obtained for NH_2 + HCl were received from personal communications, and are shown in Arrhenius form in Figure 5.5.[137,138] The rate constant k_4 may summarized by

$$k_4(\text{MTST}) = 4.08 \times 10^{-13}\, T^{0.343} \exp(622/T)\ \text{cm}^3\ \text{molecule}^{-1}\ \text{s}^{-1} \qquad (5.6)$$

over the range of 250 – 750 K, and as can be seen, the temperature dependence is negative over this range of temperature. For comparison, standard TST was applied by Dr. Paul Marshall, and

it was found that at room temperature, TST predicts a rate constant that is a factor of 3 greater than the MTST result, and that this overestimation becomes even larger at lower temperatures, which would lead an exaggerated negative temperature dependence, as discussed by Krasnoperov et al.[76] No measurements exist for the kinetics of reaction 5.4, which precludes the direct comparison of the MTST results with experiment.

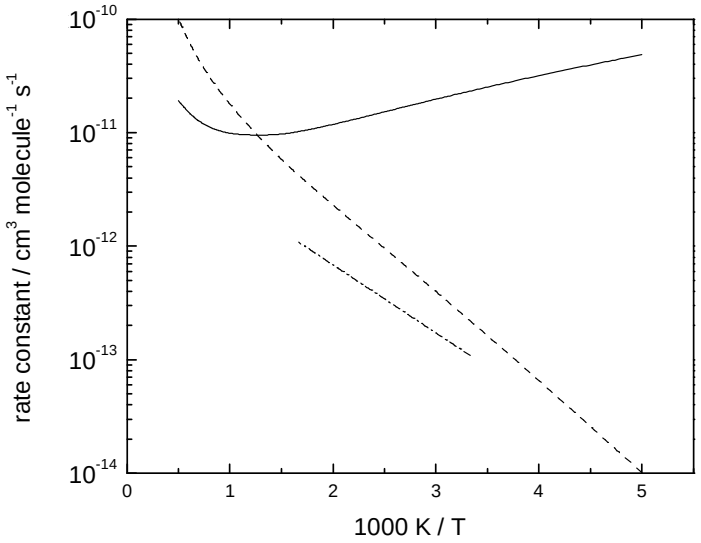

Figure 5.5. Comparison of theoretical and measured rate constants. Solid line, k_4(MTST) for NH_2 + HCl; dashed line, k_1(MTST) for Cl + NH_3; dash-dot line, experimental k_1 for Cl + NH_3.

Following the MTST analysis, k_1 was obtained from the MTST values of k_4 and the experimental values of K_{eq} via microscopic reversibility. The equilibrium constant was obtained from the combination of the experimental $\Delta_r H_0$ obtained in this work and the thermodynamic data tabulated by Gurvich et al.[133] This analysis, performed by Dr. Paul Marshall, yielded

$$K_{eq} = 27.3\ T^{-0.049} \exp(-2248/T) \qquad (5.7)$$

over the range of 200 – 2000 K, with an estimated uncertainty of 6%. From the product of K_{eq} and k_4, k_1 was obtained as a function temperature, and is shown in the Arrhenius plot of Figure 5.5. Over the range of 250 – 750 K, this rate constant may be expressed as

$$k_1(\text{MTST}) = 1.11 \times 10^{-11}\, T^{0.294} \exp(-1626/T)\ \text{cm}^3\ \text{molecule}^{-1}\ \text{s}^{-1} \qquad (5.8)$$

Considering the exponential dependence of k_1(MTST) on the computed DFT barrier height, it may be said that k_1(MTST) is actually in reasonable agreement with the experimentally measured k_1, even though it overestimates this quantity by around a factor of 3 over the overlapping temperature range. This overestimation may be caused by a potential underestimation of the barrier height computed with MPWB1K/6-31++G(2df,2dp) theory, or a computed TS structure that is too loose at the same level of theory. Nevertheless, the existence of a TS whose energy lies below that of the final products rationalizes the observed temperature dependence and approximate magnitude of k_1.

5.4. Recent Developments and Further Discussion

5.4.1. New Computational Results

Since the publication of the above results,[77] a new computational study of the NH_3Cl system has been published by Xu and Lin,[139] and their findings are discussed and compared to those in our work here. Lin and Xu applied B3LYP/6-311+G(3df,2p) theory to locate and characterize stationary points along the PES, and further refined the energies with the G2M(CC2)[140]method. The G2M(CC2) composite method relies on a PMP4/6-311G(d,p) calculation for the base energy, which is then improved by the inclusion of the effects of added diffuse and higher polarization functions calculated at the PMP2 level of theory, a higher level correction, and a coupled cluster correction. In essence, the aim of this method is to approximate

the UCCSD(T)/6-311+G(3df,2p)//B3LYP/6-311+G(3df,2p) result. As will be seen in chapter 6, this method is rather unsuccessful in terms of accurately treating highly spin-contaminated systems, such as the phenyl radical, however, since the open-shell species in the NH_3Cl system have been shown to have negligible spin-contamination, this method should be appropriate in this case.

As can be seen from Figure 1 of Xu and Lin's work,[139] the geometrical parameters they obtained for the species in the NH_3Cl system with B3LYP/6-311+G(3df,2p) are in relative agreement with those obtained with MPWB1K/6-31++G(2df,2p) theory in our work, however, they characterized three additional stationary points. As can be seen in Figure 2 of their work,[139] these three stationary points are a weakly-bound entrance complex on the abstraction PE diagram, a TS for hydrogen displacement from A3, and the displacement product set of NH_2Cl + H. The displacement channel was not studied in our previous work. Xu and Lin have calculated a large barrier for this process of 203.8 kJ mol^{-1} with G2M(CC2)//B3LYP/6-311+G(3df,2p) theory, indicating that this process would not occur over the range of temperature considered in our experiments, so it is not considered further.

The entrance complex, which they called LM1, is bound by 15 kJ mol^{-1}, and is a C_{3v} structure similar to A3, with the difference being that the Cl atom comes in toward the bottom of the pyramidal structure of ammonia along the C_{3v} axis in LM1, as opposed to the interaction with the top of ammonia in A3. In our previous work with MPWB1K/6-31++G(2df,2p) theory, the intrinsic reaction coordinate for the abstraction channel was followed using the (IRC) feature of Gaussian 03. The IRC analysis indicated that a structure equivalent to LM1 may indeed lie on the abstraction reaction path, however, the inability of MPWB1K to optimize such a structure with any of the basis sets listed in Table 5.2 led to its abandonment. The B3LYP/6-

311+G(3df,2p) results of Xu and Lin were checked, and it was verified that the LM1 structure is in fact a local minimum at this level of theory.

A closer inspection of the LM1 and A3 structures led to the idea that these two species might correspond to stationary points for the inversion of ammonia in the field of a Cl atom, and as such, they may be connected via an inversion TS. This notion was investigated by performing a series of relaxed scans with MPWB1K and various basis sets, in which the structures were constrained to C_{3v} symmetry, and optimized as the Cl-N-H angle was varied. The relaxed scans obtained with all levels of MPWB1K theory indicate that LM1 is not a bound species and that the formation of A3 along the C_{3v} axis is barrierless. This was not the case with B3LYP theory, where similar relaxed scans showed that the presence of LM1 is basis set dependent. For instance, the relaxed scan performed with B3LYP/6-311+G(3df,2p) basis set shows a shallow minimum at the angle corresponding to the LM1 structure separated by a small barrier whose structure corresponds to a possible inversion TS, while B3LYP/6-31+G(d,p) does not. These results are depicted graphically in Figure 5.6.

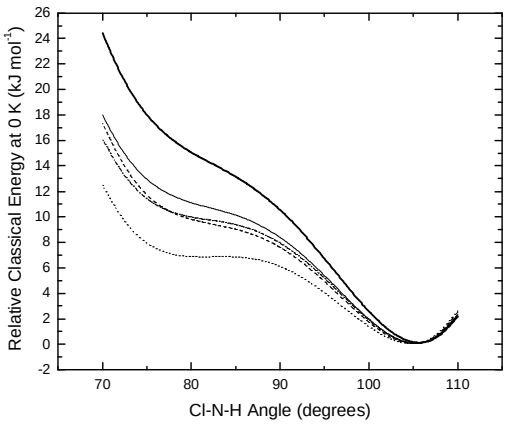

Figure 5.6. Relaxed scans of Cl-N-H angle in the C_{3v} NH_3Cl system. Dash-dot line: MPWB1K/MG3; solid line: MPWB1K/6-31+G(2df,2p); bold line: MPWB1K/6-31+G(d,p); dashed line: B3LYP/6-31+G(d,p); dotted line: B3LYP/6-311+G(3df,2p).

In an effort to locate a LM1-like structure with MPWB1K theory, the step size was reduced to 0.1 degrees in subsequent relaxed scans aiming to refine the Cl-N-H angle. Regardless of the basis set used, attempts to find the LM1-equivalent MPWB1K structure with the allowance of all geometrical parameters to be optimized during the calculation were unsuccessful, yielding the optimal structure for A3 in each case. Therefore, new MPWB1K optimizations were carried out with the Cl-N-H angle fixed at ~77 °, which is roughly at the center of the flat region of each of the DFT potentials, and was taken to correspond to the possible location of LM1. This procedure finally yielded a partially optimized LM1 structure with all levels of MPWB1K theory used, and in all cases, the RMS and Maximum Distances and Forces fully converged.

The inversion TS was successfully characterized with B3LYP/6-311+G(3df,2p), and the imaginary frequency corresponds to inversion along the C_{3v} axis. A subsequent IRC calculation confirmed inversion as the reaction path. However, it is noted that at this level of theory, the TS for inversion lies 1.3 kJ mol^{-1} lower in energy than LM1 on the vibrationally adiabatic ground-state PES. MPWB1K theory was once again problematic, failing to locate the inversion TS even after refining the Cl-N-H angle via relaxed scans with smaller step sizes. Partial optimization attempts similar to those conducted in the case of LM1 were unsuccessful in this case, as was increasing the number of radial shells and angular points per shell from the default values of 75 and 302, to 99 and 590, respectively, via the Int(Grid=99590) keyword in Gaussian 03. Therefore, we conclude that the inversion TS is not a stationary point along the PES generated with MPWB1K theory with any basis set.

In light of the new DFT findings, the NH_3Cl system was reexamined with high level *ab initio* coupled cluster theory. The PES of reaction 5.1 was reinvestigated with UCCSD(T)/aug-

cc-pVTZ theory for geometries and frequencies, and the energies were further refined by combining the TZ energy with the single-point QZ energy to extrapolate to the CBS limit in the manner previously described in section 3.2.3 (equation 3.1). The scaling factor for frequencies obtained with this method was taken to be 0.975, in accordance with the listing found at the Computational Chemistry Comparison and Benchmark Database.[141] Once again, due to the negligible spin-contamination found for the NH_3Cl open-shell species, the couple cluster calculations relied on UHF reference wavefunctions and may thus be denoted by UCCSD(T)/UHF. These results were further improved by the inclusion of atomic spin-orbit coupling for the Cl atom, core-valence effects, and scalar relativistic effects, as described in more detail in chapter 3. The Cartesian coordinates, unscaled vibrational frequencies, and rotational constants of all of the species characterized with CCSD(T)/aug-cc-pVTZ theory are given in section C2 of Appendix C. These species are also depicted in Figure 5.7, placed on a PE diagram in Figure 5.8, and their energies are given in Table 5.3. For consistency, LM1 has been renamed A1, so that the A*n* structures in our work conveniently correspond to the LM*n* structures in the study by Xu and Lin.

The A3 structure characterized with UCCSD(T)/CBS//UCCSD(T)/aug-cc-pVTZ theory was bound by 37.1 kJ mol^{-1} relative to the reactants, which corresponds to an equilibrium constant for the formation of this compound at 294 K of ~ 5.0×10^{-18} cm^3 $molecule^{-1}$. This leads to the prediction that only about 1% of all Cl atoms would be complexed by NH_3, even under the most favorable experimental conditions used, supporting the lack of pressure dependence observed for the second order rate constant. Furthermore, using partition functions calculated with UCCSD(T)/aug-cc-pVTZ, it was found that K_c may be summarized by

$$K_c(T) = 2.02 \times 10^{-28}\, T^{1.269} \exp(40.8 \text{ kJ mol}^{-1} / RT) \text{ cm}^3 \text{ molecule}^{-1} \qquad (5.9)$$

over the range of 290 – 2000 K. G2M(CC2)//B3LYP/6-311+G(3df,2p) theory also predicts negligible formation of this adduct at room temperature, as Xu and Lin have found the BDE_0 in A3 to have a value of only 29.7 kJ mol^{-1}.[139]

As with B3LYP/6-311+G(3df,2p), it was found with UCCSD(T)/CBS//UCCSD(T)/aug-cc-pVTZ theory that increasing the N-Cl distance in A3 leads to the inversion of the ammonia molecule, forming A1 via passage through an inversion TS on the classical PES. However, with the inclusion of scaled ZPEs, A1 was found to lie 4.1 kJ mol^{-1} above the energy of the TS for inversion (Inv TS), and 13.9 kJ mol^{-1} above the energy of A3, indicating that A1 may not be an isolable species (Figure 5.8). These results are in qualitative agreement with those of B3LYP/6-311+G(3df,2p), and while the inversion TS was not characterized with G2M(CC2)//B3LYP/6-311+G(3df,2p) theory by Xu and Lin, the enthalpy difference between A1 and A3 of 14.7 kJ mol^{-1} calculated with this theory is in good accord with our couple cluster results.

Along the abstraction channel, it may be seen that the relative energies of the abstraction TS (Abs TS), A2, and the final products calculated with UCCSD(T)/CBS// UCCSD(T)/aug-cc-pVTZ theory, of 13.9, -1.1, and 16.6 kJ mol^{-1}, respectively, are all lower than their G2M(CC2)//B3LYP/6-311+G(3df,2p) counterparts, which have corresponding energies of 17.6, 2.5, and 19.2 kJ mol^{-1}. We note that while the overall reaction enthalpy for abstraction calculated with UCCSD(T)/CBS//UCCSD(T)/aug-cc-pVTZ theory agrees with the experimental value of $\Delta_r H_0 = 16.4 \pm 0.2$ kJ mol^{-1}, G2M(CC2)//B3LYP/6-311+G(3df,2p) theory overestimates this quantity by 2.8 kJ mol^{-1}, which suggests that Abs TS and A2 may have also been overestimated by a similar amount with this theory. The thermochemistry of the stationary points characterized with both composite methods are further compared in Table 5.4. As previously discussed, DFT scans following the intrinsic reaction coordinate indicate that A1 may

be connected to A2 via Abs TS. However, since A1 is not a bound species, we deduce that the reactants directly form Abs TS.

The $^2B_1$ symmetry of the electronic ground-state wavefunctions of NH_2 and A2 indicate that these species do not share a PES with the reactants and the C_s $^2A'$ Abs TS. However, the low frequency of $\omega(B_1) = 211$ cm^{-1} in the $^2B_1$ A2 complex, corresponding to a Cl-N-H bending motion in the plane perpendicular to the one containing the two equivalent H atoms (taken to be reaction coordinate), results in a symmetry lowering in A2 from C_{2v} to C_s, which suggests that, in principle, the PES of the reactants and that of the products could be connected via an avoided crossing. It should also be noted that while all of the species characterized with UCCSD(T)/aug-cc-pVTZ theory have optimized geometries that have fully converged with respect to the convergence criteria for force and displacement, the frequencies in A1 and A2 do not meet the convergence criteria with respect to displacement, indicating perhaps that the classical PES may be pretty flat in the regions corresponding to these minima.[142] The maximum and RMS displacements could not be reduced to values below the convergence threshold even by imposing a tighter convergence criteria and allowing for extra iterations in the frequency calculations. The final values obtained for the maximum and RMS displacements were 0.00637 and 0.00484 Å respectively for A1, and 0.00240 and 0.00121 Å respectively for A2. Because these values are of the same order of magnitude as the upper limits assigned in Gaussian 03 (Max = 0.00180 Å, RMS = 0.00120 Å), these structures were taken to be stationary points at the UCCSD(T)/aug-cc-pVTZ level of theory.

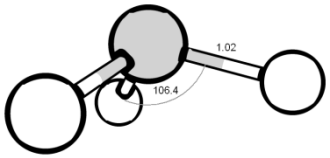

C_{3v} NH_3 ($^1A_1$) (0.0)

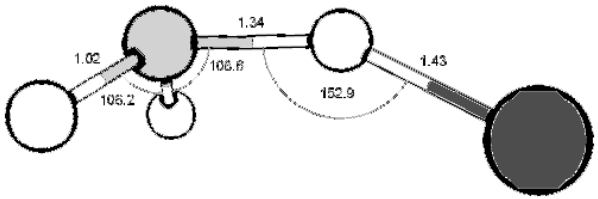

C_s Abs TS ($^2A'$) (13.9)

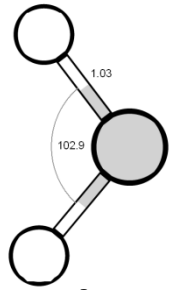

C_{2v} NH_2 ($^2B_1$) (16.6)

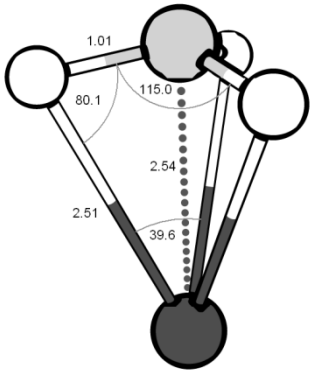

C_{3v} A1 ($^2A_1$) (-23.2)

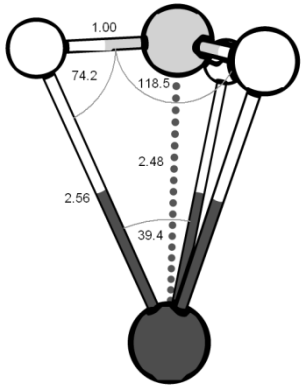

C_{3v} Inv TS ($^2A_1$) (-27.3)

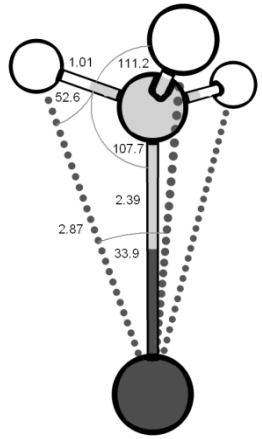

C_{3v} A3 ($^2A_1$) (-37.1)

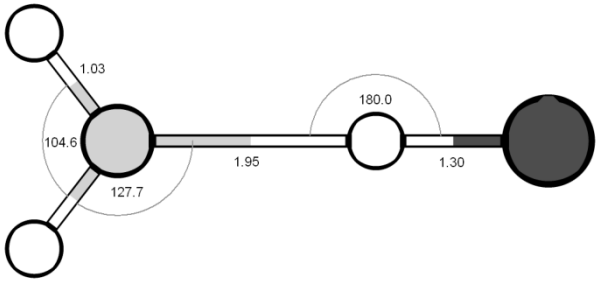

C_{2v} A2 ($^2B_1$) (-1.1)

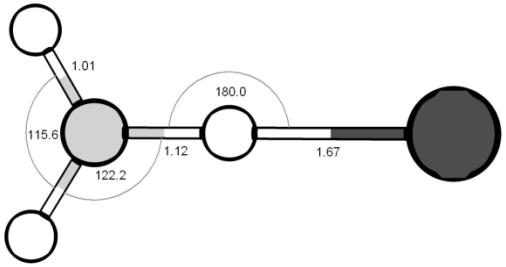

C_{2v} PCET TS ($^2B_1$) (26.0)

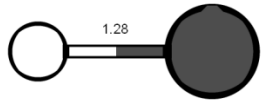

$C_{\infty v}$ HCl ($^1\Sigma^+$) (16.6)

Figure 5.7. Species in the NH_3Cl reaction system. Geometrical parameters were obtained with UCCSD(T)/aug-cc-pVTZ theory. The values in parentheses represent the relative CCSD(T)/CBS-aug enthalpies in kJ mol^{-1} at 0 K, and also include relativistic and core-valence effects. The values listed for NH_2 and HCl each represent the enthalpy difference between (NH_2 + HCl) – (NH_3 + Cl).

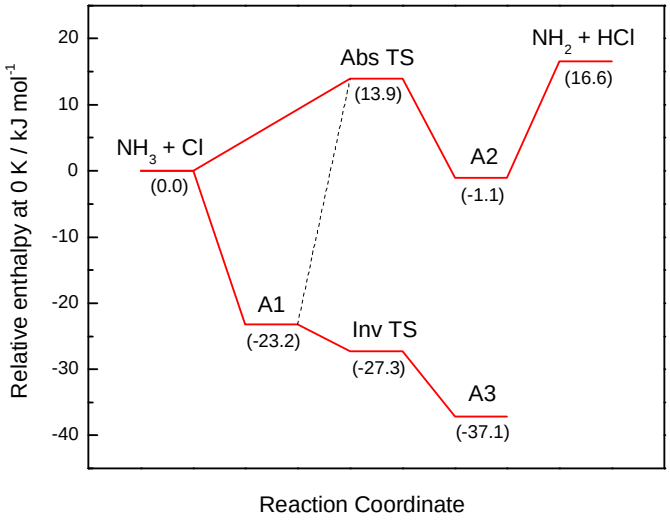

Figure 5.8. Potential energy diagram for Cl + NH_3 computed with UCCSD(T)/CBS// UCCSD(T)/aug-cc-pVTZ theory.

5.4.2. Kinetic Analyses

Canonical Transition State Theory was applied to the PES of reaction 5.1. As was previously discussed, TST overestimates the rate constant due to the erroneous inclusion of contributions from states in the TS which would not be populated at normal pressures. However, since a MTST analysis of the present coupled-cluster results is currently unavailable, the TST calculations are used for the sole purpose of estimating an upper bound to the MTST results. Unlike the previous MTST calculations, which considered the reverse reaction and indirectly yielded k_1 via microscopic reversibility, the simple conventional TST formalism described in Chapter 3 was applied to the forward rate constant to directly calculate k_1 from the PES obtained with UCCSD(T)/CBS//UCCSD(T)/aug-cc-pVTZ theory. In addition, the effect of tunneling on the TST rate constant was approximated by including the Wigner tunneling correction:[82,143]

$$\Gamma(T) = 1 + \frac{(h\nu^*/k_B T)^2}{24} \qquad (5.10)$$

where v* is the magnitude of the imaginary vibrational frequency, and the overall rate constant is obtained by simply multiplying Γ(T) by the TST rate constant at the corresponding temperature. The tunneling correction had the effect of increasing the TST rate constant by 98 % at 298 K, 33 % at 500 K, and dissipated to only 2% by 2000 K. The tunneling correction in the present case is larger than those obtained in our previous work and in the work of Xu and Lin, which is primarily attributed to the larger magnitude of the imaginary vibrational frequency calculated with UCCSD(T)/aug-cc-pVTZ, of 977 cm^{-1}, as opposed to the 622 and 319 cm^{-1} values obtained with MPWB1K/6-31+G(2df,dp) and B3LYP/6-311+G(3df,2p), respectively.[77,139] The TST results are depicted in Figure 5.9, and as can be seen, these results agree well with those obtained by Xu and Lin via VTST,[139] and are in better overall accord with our measurements of $k_1(T)$ than the latter. Furthermore, the overestimation of the rate constant by TST at high temperatures is likely to be reduced through the application of the aforementioned MTST formalism.

MultiWell-based RRKM calculations have been carried out for reaction 5.4 at a constant pressure of 0.1 bar, and the rate constants for reaction 5.1 have been obtained via the temperature-specific equilibrium constants for $NH_3 + Cl = NH_2 + HCl$. The hinderd Gorin model[66,100,101] described in chapter 3 was used to assess the properties of the loose TS at the entrance channel, and since there are no experimental determinations for the rate constant for $NH_2 + HCl$ addition from which the hindrance parameters can be assessed, these parameters were evaluated from fitting to rate constants from the hard sphere collision model (given in Table 5.5). The corresponding Morse parameters used for A2 were r_e = 3.244 Å, υ_e = 159.0 cm^{-1}, and D_e = 25.9 kJ mol^{-1}. The results of this procedure are given in Table 5.5 and also shown in Figure 5.9. For consistency, the RRKM results in Figure 5.9 also include the Wigner

tunneling correction. The σ and ε/k_B Lennard-Jones parameters used were 4.29 Å and 400 K, respectively, where σ was approximated from Reid and Sherwood's[95] empirical rules and ε/k_B was arbitrarily assigned as in the previous chapter. Energy transfer parameters were calculated based on the simple exponential-down model as outlined in chapter 3. The tunneling corrections, rate constants, equilibrium constants, energy transfer parameters, and Gorin-type TS parameters are given in Table 5.5, and sample input files may be found in Appendix D. As can be seen in Figure 5.9, the hindered Gorin-based RRKM analysis overestimates the rate constant even more than the TST analysis, which reflects the drawback of using RRKM theory when there is insufficient knowledge of the pertinent parameters, and suggests that the hard sphere collision rate coefficients represent overestimations of the actual $k_a(T)$. Nonetheless, these results can be said to be in moderate overall accord with experiment, in particular at 290 K, where the calculated rate constant is within a factor of two of the measured rate constant.

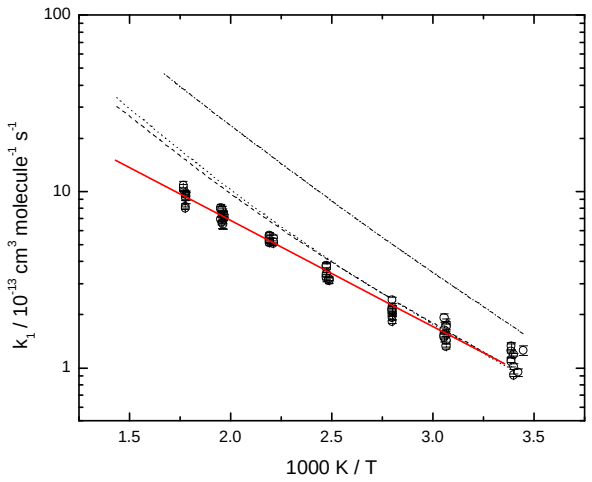

Figure 5.9. Arrhenius plot for NH_3 + Cl. Open circles (± 1σ) and solid line: Gao et al.[77]; dotted line: VTST result from Xu and Lin.[139]; dashed line: present TST result with a Wigner tunneling correction; dash-dot line: Wigner-corrected RRKM result based on hindered Gorin-type TS.

5.4.3. Proton-Coupled Electron Transfer

Finally, following a suggestion from Dr. Weston T. Borden, the possibility of a proton-coupled electron transfer (PCET) mechanism, as opposed to the typical hydrogen-atom transfer (HAT) mechanism, was investigated for reaction 5.4 using UCCSD(T)/CBS//UCCSD(T)/aug-cc-pVTZ theory. As its name implies, the PCET mechanism involves the simultaneous transfer of a proton and an electron (from different orbitals) from a species to another. This is in contrast to the usual HAT mechanism typically encountered in H-abstraction reactions, which involves the transfer of a proton and an electron from the bond being broken to the singly occupied orbital on the abstracting radical. Both theory and experiments have shown that in cases where the abstracting radical and the atom to which the H-atom to be abstracted is bonded each possess at least one unshared lone pair of electrons, PCET may be favored over HAT.[144-150] This condition is satisfied by the NH_3Cl system, therefore a PCET mechanism may indeed be viable for reaction 5.4.

Specifically, a PCET mechanism entails the transfer of a proton to the orbital containing the lone electron pair on the abstracting radical, and the simultaneous transfer of an electron from the unshared orbital on the atom from which the proton is being abstracted to the singly occupied orbital on the abstracting radical.[150] In the present case, PCET can be achieved via the simultaneous donation of the proton and of an electron from a non-bonding π-orbital in HCl, to the filled and the singly occupied 2p-π orbitals on N in NH_2, respectively. As noted by Mayer et al., the initial formation of a hydrogen-bonded intermediate is required in a PCET mechanism, such as A2 in the present case.[147] However, in going from the C_{2v} A2 to the C_s Abs TS, the optimal linear alignment of the orbitals typically involved in a PCET mechanism is compromised. Furthermore, an examination of the singly-occupied molecular orbital (SOMO)

on the Abs TS reveals that the atomic orbital (AO) on N exhibits significant density along the N-H vector, and the AO on the Cl atom also has some density along the Cl-H vector, which are characteristics that are consistent with a simple HAT mechanism.[147,150]

In fact, the NH_2 + HCl reaction is similar in many regards to the methoxyl + methanol self-exchange reaction studied by Mayer et al.[147] In the case of the MeO + MeOH reaction, which was investigated with B3LYP theory, Mayer et al. found that the reaction initially involves the formation of a weakly-bound hydrogen-bonded intermediate, with a relative energy of -19.2 kJ mol^{-1}, which is comparable to the relative energy of A2 of -17.7 kJ mol^{-1}. The next step in the MeO + MeOH reaction is the passage through a low-lying HAT TS, with relative energy of 1.7 kJ mol^{-1}, which once again compares well with the -2.7 kJ mol^{-1} found for Abs TS in the NH_3Cl system. Furthermore, the bent alignment of the three atomic centers in the MeO/MeOH TS is also analogous with the NH_3Cl Abs TS, as are the respective SOMOs, both possessing significant density in the AOs along the two R-H vectors. Like Mayer et al., we investigated the possibility of a PCET mechanism by searching for a TS structure in which the three principal atoms involved in the reaction were constrained to a linear arrangement, facilitating the interactions between the π-symmetry p-orbitals. Such a C_{2v} PCET TS structure was found with UCCSD(T)/CBS//UCCSD(T)/aug-cc-pVTZ theory, however, the structure's vibrational frequencies included two imaginary frequencies, indicating that this is actually a second-order saddle point and therefore corresponds to a hilltop rather than a TS. The geometrical parameters of this structure are shown in Figure 5.7, its energy is given in Table 5.3, and as usual, the Cartesian coordinates, vibrational frequencies, and moments of inertia are listed in Appendix C. It is worth noting that this structure's vibrational frequencies are not fully converged with respect to the maximum displacement, which was found to be 0.00233 as

opposed to the 0.00180 threshold required by the algorithm in Gaussian 03, however, this disagreement is assumed to be negligible and we thus consider PCET TS to be an optimized structure.

This result further extends the analogy between the NH_2 + HCl and the MeO + MeOH reactions, as in the latter reaction, the PCET mechanism was also found to involve a hilltop on the PES. The PCET hilltops were found to be higher in energy than the HAT TSs in each case, with comparable relative energies of 30.2 and 26.0 kJ mol^{-1} for the MeO/MeOH and NH_3Cl systems, respectively. Furthermore, the SOMOs for the two systems are also analogous, and consist of p-orbitals on the R atoms that are essentially orthogonal to the R-H-R vector. Along this hypothetical PCET reaction coordinate, the transferring hydrogen is a proton, donated from the σ-bond in HCl to the lone pair on N in NH_2, while in a different MO, an electron from a 3p-π AO on Cl is simultaneously transferred to the singly occupied 2p-π AO on N. However, because the PCET TS is actually a hilltop and is higher in energy than the HAT TS, we conclude that reaction 5.4 (and hence 5.1) occurs via a typical HAT mechanism.

5.5. Conclusions

The observed kinetics for the NH_3 + Cl = NH_2 + HCl reaction over a wide range of temperature extend the measurements for this reaction from the only previous determination at room temperature to 570 K. This H-abstraction reaction was found to possess an activation energy that is lower than its endothermicity, which provides a counterexample to the general expectation that $E_a \geq \Delta_r H$ for an endothermic process. This result can be rationalized based on similar PE diagrams obtained with both DFT and high level *ab initio* theories, which support that $E_a < \Delta_r H$ in the present case. MTST calculations based on the DFT PES clearly indicate that the

reverse process should exhibit a negative temperature dependence, though DFT calculations also predict that a weakly bound two-center/three-electron complex could be formed in significant quantities under favorable conditions at room temperature. *Ab initio* calculations revealed that this complex is in fact too weakly bound to be formed in appreciable quantity under the same conditions, which is in line with experimental observations. Conventional TST calculations based on the new *ab initio* PES produced a thermal rate constant that overestimated the measured rate constant by less than a factor of 2 over the entire temperature range studied, indicating that future MTST calculations may yield rate constants which agree nicely with experiment. The possibility of the abstraction reaction occurring via a proton-coupled electron transfer mechanism was examined with *ab initio* theory, however, this mechanism was found to require the passage through a higher energy multidimensional hilltop structure as opposed to the low-lying TS along the typical H-abstraction transfer reaction pathway.

Table 5.1. Summary of measurements of the rate constant k_1 for Cl + NH_3.

T, K	τ_{res}, s	F, mJ	p, mbar	$[CCl_4]$, 10^{15} molecule cm^{-3}	$[NH_3]_{max}$, 10^{15} molecule cm^{-3}	$[Cl]_0$, 10^{12} molecule cm^{-3}	$k_1 \pm \sigma_{k1}$, 10^{-13} cm^3 $molecule^{-1}$ s^{-1}
290	1.2	0.41	28	2.72	3.47	0.9	1.25 ± 0.08
292	0.9	0.18	43	1.80	1.51	0.3	0.94 ± 0.05
294	2.2	0.21	49	4.05	1.27	0.7	0.91 ± 0.02
294	6.9	0.20	147	5.54	2.05	0.9	1.19 ± 0.02
294	1.6	0.11	36	3.77	1.48	0.3	1.01 ± 0.04
295	4.9	0.15	155	5.45	3.09	0.7	1.25 ± 0.12
295	3.6	0.30	80	5.93	2.19	1.5	1.32 ± 0.07
295	3.6	0.19	80	5.93	2.19	0.9	1.11 ± 0.04
295	3.4	0.14	76	5.64	1.42	0.6	1.24 ± 0.03
295	3.5	0.09	79	5.94	1.24	0.4	1.08 ± 0.70
326	1.4	0.79	35	2.09	1.31	1.4	1.77 ± 0.12
326	1.4	0.59	35	2.09	1.31	1.0	1.72 ± 0.11
326	1.4	0.36	35	2.09	1.31	0.6	1.41 ± 0.10
326	1.4	0.25	35	2.09	1.31	0.4	1.32 ± 0.05
326	1.6	0.59	71	2.32	1.46	1.1	1.71 ± 0.07
326	1.6	0.35	71	2.32	1.46	0.7	1.54 ± 0.03
326	1.6	0.25	71	2.32	1.46	0.5	1.43 ± 0.07
327	3.0	0.49	73	2.90	1.56	1.2	1.92 ± 0.10
327	3.0	0.29	73	2.90	1.56	0.7	1.63 ± 0.05
327	3.0	0.19	73	2.90	1.56	0.5	1.48 ± 0.08
327	2.3	0.29	148	2.75	1.16	0.7	1.54 ± 0.04
327	2.3	0.19	148	2.75	1.16	0.4	1.51 ± 0.04
357	2.7	0.49	72	2.59	1.13	1.1	2.04 ± 0.09
357	2.7	0.29	72	2.59	1.13	0.6	1.82 ± 0.04
357	2.7	0.19	72	2.59	1.13	0.4	1.92 ± 0.04
357	1.4	0.69	72	2.91	1.16	1.7	2.42 ± 0.10
357	1.4	0.44	72	2.91	1.16	1.1	2.21 ± 0.03
357	1.4	0.29	72	2.91	1.16	0.7	2.06 ± 0.03
357	2.1	0.44	148	2.51	1.25	0.9	2.12 ± 0.04
357	2.1	0.29	148	2.51	1.25	0.6	1.99 ± 0.02
357	1.3	0.69	36	2.34	1.13	1.3	2.15 ± 0.11
357	1.3	0.44	36	2.34	1.13	0.9	2.14 ± 0.10

(Table continues on next page)

(Table 5.1. Continued)

T, K	τ_{res}, s	F, mJ	p, mbar	$[CCl_4]$, 10^{15} molecule cm^{-3}	$[NH_3]_{max}$, 10^{15} molecule cm^{-3}	$[Cl]_0$, 10^{12} molecule cm^{-3}	$k_1 \pm \sigma_{k1}$, 10^{-13} cm^3 $molecule^{-1}$ s^{-1}
357	1.3	0.29	36	2.34	1.13	0.6	2.13 ± 0.09
402	0.7	0.62	59	1.69	1.73	0.9	3.14 ± 0.11
402	0.7	0.39	59	1.69	1.73	0.6	3.11 ± 0.11
402	0.7	0.19	59	1.69	1.73	0.3	3.19 ± 0.08
404	1.3	0.65	61	2.01	1.18	1.1	3.77 ± 0.17
404	1.3	0.50	61	2.01	1.18	0.8	3.68 ± 0.21
404	1.3	0.20	61	2.01	1.18	0.3	3.80 ± 0.12
404	0.6	0.60	29	1.53	1.57	0.8	3.29 ± 0.11
404	0.6	0.42	29	1.53	1.57	0.5	3.23 ± 0.15
404	0.6	0.18	29	1.53	1.57	0.2	3.38 ± 0.09
452	0.6	0.79	59	1.46	1.22	1.0	5.05 ± 0.04
452	0.6	0.58	59	1.46	1.22	0.7	5.44 ± 0.22
452	0.6	0.24	59	1.46	1.22	0.3	5.16 ± 0.24
456	0.5	0.63	29	1.61	1.13	0.8	5.41 ± 0.24
456	0.5	0.45	29	1.61	1.13	0.6	5.63 ± 0.21
456	0.5	0.28	29	1.61	1.13	0.4	5.52 ± 0.13
456	1.1	0.73	57	1.65	1.21	1.0	5.10 ± 0.14
456	1.1	0.54	57	1.65	1.21	0.7	5.21 ± 0.13
456	1.1	0.26	57	1.65	1.21	0.4	5.31 ± 0.18
508	0.5	0.34	57	1.27	1.50	0.4	6.97 ± 0.06
508	0.5	0.23	57	1.27	1.50	0.2	7.26 ± 0.13
509	0.9	0.69	71	1.76	1.29	1.0	6.50 ± 0.40
509	0.9	0.37	71	1.76	1.29	0.5	7.24 ± 0.38
509	0.9	0.24	71	1.76	1.29	0.4	7.46 ± 0.26
509	0.9	0.18	71	1.76	1.29	0.3	7.54 ± 0.21
510	0.3	0.43	22	0.98	1.86	0.4	6.60 ± 0.47
510	0.3	0.20	22	0.98	1.86	0.2	7.09 ± 0.52
510	0.6	0.36	45	1.38	1.95	0.4	6.74 ± 0.62
510	0.6	0.17	45	1.38	1.95	0.2	7.47 ± 0.28
510	0.6	0.83	44	1.32	1.69	0.9	7.33 ± 0.35
510	0.6	0.34	44	1.32	1.69	0.4	7.13 ± 0.32
510	0.6	0.16	44	1.32	1.69	0.2	7.75 ± 0.18

(Table continues on next page)

(Table 5.1. Continued)

T, K	τ_{res}, s	F, mJ	p, mbar	$[CCl_4]$, 10^{15} molecule cm^{-3}	$[NH_3]_{max}$, 10^{15} molecule cm^{-3}	$[Cl]_0$, 10^{12} molecule cm^{-3}	$k_1 \pm \sigma_{k1}$, 10^{-13} cm^3 $molecule^{-1}$ s^{-1}
511	0.5	0.64	30	1.22	1.45	0.7	6.64 ± 0.19
511	0.5	0.51	30	1.22	1.45	0.5	6.98 ± 0.20
511	0.5	0.28	30	1.22	1.45	0.3	7.85 ± 0.39
511	0.8	0.41	63	2.02	1.31	0.7	7.94 ± 0.27
512	1.0	0.59	59	1.54	2.12	0.8	6.96 ± 0.20
512	1.0	0.25	59	1.54	2.12	0.3	7.91 ± 0.26
512	1.0	0.17	59	1.54	2.12	0.2	8.05 ± 0.37
562	0.5	0.67	45	1.42	1.73	0.8	9.28 ± 0.79
562	0.5	0.44	45	1.42	1.73	0.5	9.36 ± 0.51
562	0.5	0.22	45	1.42	1.73	0.3	9.43 ± 0.40
563	0.5	0.59	22	1.35	1.47	0.7	8.21 ± 0.27
563	0.5	0.37	22	1.35	1.47	0.4	9.24 ± 0.40
563	0.5	0.27	22	1.35	1.47	0.3	9.66 ± 0.32
563	0.9	0.76	44	1.84	1.48	1.2	8.00 ± 0.14
563	0.9	0.38	44	1.84	1.48	0.6	9.61 ± 0.31
563	0.9	0.24	44	1.84	1.48	0.4	9.83 ± 0.24
566	0.5	0.61	43	1.85	1.06	0.9	10.20 ± 0.27
566	0.5	0.39	43	1.85	1.06	0.6	10.50 ± 0.45
566	0.5	0.19	43	1.85	1.06	0.3	10.80 ± 0.61

Table 5.2. Enthalpies at 0 K of stationary points on the potential energy surface relative to Cl + NH_3, derived by various methods.

Method	NH_2 + HCl	A3	Abstraction TS	A2
CBS-QB3	15.1	-40.3	9.4	-1.7
G3B3	14.0	-36.6	11.2	-1.9
MPWB1K/6-31+G(d,p)	26.2	-52.5	12.8	1.5
MPWB1K/6-31+G(2d,p)	19.0	-50.2	9.8	-0.3
MPWB1K/6-31++G(2d,2p)	17.5	-49.1	8.1	-1.6
MPWB1K/6-31+G(2df,2p)	17.2	-47.7	9.0	-1.3
MPWB1K/6-31++G(2df,2p)	17.0	-47.7	8.8	-1.4
MPWB1K/6-311+G(d,p)	20.9	-51.3	9.0	-2.2
MPWB1K/6-311++G(2df,2p)	15.1	-48.3	7.3	-1.9
MPWB1K/6-311++G(3d2f,2df,2p)	14.6	-47.2	8.4	-2.5
Experiment	16.4 ± 0.2			

Table 5.3. Energies and zero point energies in E_H obtained with UCCSD(T)/CBS//UCCSD(T)/aug-cc-pVTZ for reaction 5.1.

Species	Electronic Energy CCSD(T)/ aug-cc-pVTZ	Unscaled ZPE CCSD(T)/ aug-cc-pVTZ	[a]Scalar Relativistic correction	[b]Core-Valence correction	Electronic Energy CCSD(T)/ aug-cc-pVQZ	Electronic Energy aug-CBS	[c]Total Energy
H	-0.49982	0	-0.00001	0	-0.49995	-0.50004	-0.50005
Cl	-459.67622	0	-1.40334	-0.30271	-459.69474	-460.70826	-461.41566
NH_3	-56.48056	0.03430	-0.02887	-0.05086	-56.49572	-56.50679	-56.50679
HCl	-460.34324	0.00681	-1.40294	-0.30305	-460.36417	-460.37944	-462.07878
NH_2	-55.79985	0.01903	-0.02902	-0.05041	-55.81308	-55.82273	-55.88361
A1	-516.16666	0.03624[d]	-1.43220	-0.35371	-516.20154	-516.22699	-517.97756
A2	-516.15295	0.02912[d]	-1.43186	-0.35357	-516.18716	-516.21212	-517.96916
A3	-516.17222	0.03626	-1.43220	-0.35371	-516.20695	-516.23229	-517.98285
Abs TS	-516.14555	0.02785	-1.43190	-0.35361	-516.17997	-516.20508	-517.96344
Inv TS	-516.16655	0.03492	-1.43214	-0.35382	-516.20162	-516.22720	-517.97912
PCET TS	-516.13261	0.02683[d,e]	-1.43213	-0.35389	-516.16732	-516.19265	-517.95251

[a] Correction was calculated with CISD/cc-pwVTZ theory (see text).
[b] Correction was calculated with CCSD/cc-pwVTZ theory (see text).
[c] Energy calculated by adding scaled ZPE, scalar relativistic and core-valence corrections, and a correction of -0.00134 for Cl-atom spin-orbit coupling to aug-CBS electronic energy (see text).
[d] Vibrational frequencies not fully converged (see text).
[e] Contains two imaginary vibrational frequencies (see text).

Table 5.4. Comparison of computed thermochemistry for NH_3Cl stationary points relative to Cl + NH_3.

Δ_rH_0(A1) (kJ mol^{-1})	Δ_rH_0(A2) (kJ mol^{-1})	Δ_rH_0(A3) (kJ mol^{-1})	Δ_rH_0(Abs TS) (kJ mol^{-1})	Δ_rH_0(NH_2 + HCl) (kJ mol^{-1})	Investigators
-37.5	-1.4	-47.7	8.8	17.0	[a]Gao et al.
-15.0	2.5	-29.7	17.6	19.2	[b]Xu and Lin
-23.2	-1.1	-37.1	13.9	16.6	[c]Current Work
				16.4 ± 0.2	[d]Experimental

[a] Computed with MPWB1K/6-31++G(2df,2p) theory, ref. [77] (see text).

[b] Computed with G2M(CC2)//B3LYP/6-311+G(3df,2p) theory, ref. [139] (see text).

[c] Computed with UCCSD(T)/CBS//UCCSD(T)/aug-cc-pVTZ theory (see text).

[d] From (D_0(H-Cl) = 427.648 ± 0.0066 kJ mol^{-1}), ref. [124], and (D_0(H-NH_2) = 444. 0 ± 0.2 kJ mol^{-1}), ref.[132].

Table 5.5. Energy transfer parameters, loose hindered Gorin-type transition state properties, and rate constants for the NH_3Cl reaction system.

T (K)	290	350	400	500	600
r_{max} (Å)	6.54	6.39	6.28	6.09	5.94
K-Rotor (amu Å^2)	1.33	1.33	1.33	1.33	1.33
2D Moment of Inertia-NH_2 (amu Å^2)	1.62	1.62	1.62	1.62	1.62
2D Moment of Inertia-HCl (amu Å^2)	1.60	1.60	1.60	1.60	1.60
J-Rotor (amu Å^2)	474.03	451.84	436.33	410.84	390.40
$<\Delta E>_{down}$ (cm^{-1})	421.7	463.4	498.1	567.6	637.1
c_2 (cm^{-1})	0.26	0.29	0.31	0.36	0.40
[a]$k_{a(HS)}$ (cm^3 $molec^{-1}$ s^{-1})	4.30E-10	4.73E-10	5.05E-10	5.65E-10	6.19E-10
[b]K_c (cm^3 $molec^{-1}$)	1.53E-21	4.34E-22	2.10E-22	8.10E-23	4.61E-23
[c]K_{eq}	4.39E-03	1.83E-02	4.38E-02	1.51E-01	3.45E-01
[d]$k_{\infty,uni}$ (s^{-1})	2.96E11	1.12E12	2.49E12	7.04E12	1.37E13
[e]$k_{\infty,d}$ (cm^3 $molec^{-1}$ s^{-1})	4.53E-10	4.86E-10	5.22E-10	5.71E-10	6.32E-10
[e,f]k_d (cm^3 $molec^{-1}$ s^{-1})	1.79E-11	1.46E-11	1.32E-11	1.17E-11	1.10E-11
[f,g]k_1 (cm^3 $molec^{-1}$ s^{-1})	7.87E-14	2.68E-13	5.80E-13	1.77E-12	3.79E-12
Wigner Tunneling correction	1.98	1.67	1.52	1.33	1.23

[a] Hard Sphere Rate Constants for NH_2 + HCl = A2 via Gorin-type TS.
[b] Equilibrium constant for NH_2 + HCl = A2.
[c] Equilibrium constant for NH_3 + Cl = NH_2 + HCl.
[d] Rate constants for A2 = NH_2 + HCl.
[e] Rate constants for NH_2 + HCl = A2.
[f] Do not include Wigner correction.
[g] Rate constants for NH_3 + Cl = NH_2 + HCl obtained via sum of states of Gorin-type TS.

CHAPTER 6

THE REACTION BETWEEN BENZENE AND ATOMIC CHLORINE*

6.1. Introduction

The reaction between benzene and the Cl atom as well as its reverse process involving the phenyl radical and HCl have been investigated using laser flash photolysis coupled with resonance fluorescence (reactions 6.1 and 6.2).

$$C_6H_6 + Cl \xrightarrow{k_1} C_6H_5 + HCl \quad (6.1)$$

$$C_6H_5 + HCl \xrightarrow{k_2} C_6H_6 + Cl \quad (6.2)$$

Reaction 6.1 leads to the formation of the phenyl radical, a species that is important in combustion chemistry due to its involvement in soot formation.[151] Several investigators have probed reaction 6.1 at room temperature using relative rate techniques in order to try to gain some insight into the role of aromatic species in atmospheric chemistry.

The first measurement of reaction 6.1 in the literature indicated that the reaction proceeds at a considerable rate at room temperature, with a rate constant $k_1 = (1.5 \pm 0.9) \times 10^{-11}$ cm^3 molecule^{-1} s^{-1}.[152] Two subsequent studies concluded that the reaction is at least one order of magnitude slower than originally thought, with the work of Wallington et al.[153] and Nozière et

* This chapter was partially adapted from the publication of *J. Phys. Chem. A*, Vol. 111, Alecu, I. M., Gao, Y., Hsieh, P.-C., Sand, J. P., Ors, A., McLeod, A., and Marshall, P., "Studies of the Kinetics and Thermochemistry of the Forward and Reverse Reaction Cl + C_6H_6 = HCl + C_6H_5," Pages 3970-3976, Copyright (2007), with permission from the American Chemical Society.

al.[154] yielding upper limits to k_1 of $\leq 4 \times 10^{-12}$ and $\leq 5 \times 10^{-16}$ cm^3 $molecule^{-1}$ s^{-1}, respectively. In a later study, Shi and Bernhard monitored the loss of benzene in relation to the loss of difluorochloromethane as they reacted with Cl atoms, which for benzene yielded a k_1 value of $(1.3 \pm 0.3) \times 10^{-15}$ cm^3 $molecule^{-1}$ s^{-1}.[155] This result is in disagreement with the most recent value of $(1.3 \pm 1.0) \times 10^{-16}$ cm^3 $molecule^{-1}$ s^{-1} obtained in a study by Sokolov et al, where the investigators employed steady-state photolysis of benzene/Cl_2 mixtures and a reference compound.[156]

The differences among the range of the k_1 values obtained have not been resolved, although it has been noted that possible complications arising from secondary chemistry as well as trace impurities are likely to influence relative rate experiments.[155,156] It has also long been proposed that benzene and Cl can first form an adduct, which can in turn be responsible for the abstraction of an H atom from another benzene molecule and slowly yield HCl.[155] However, Sokolov et al.[156] have concluded that only a very small portion of the reactants will proceed via this channel as the equilibrium constant for this process is only about $(1\text{-}2) \times 10^{-18}$ cm^3 $molecule^{-1}$.

Absolute rate constants obtained with laser flash photolysis coupled with resonance fluorescence for the forward and reverse processes given in equations 6.1 and 6.2 are presented in this work, the behaviors of which have also been investigated as a function of temperature.[157] The ratio of these rate constants (k_1/k_2) yields the equilibrium constant K_{eq}, which can be used to access thermodynamic information about the system. These results serve as a check to the recent revisions to the C_6H_5-H bond dissociation enthalpy D_{298}, which have been obtained through ion chemistry thermocycles by Davico et al.[158] and by the interpretation of a number of kinetic

experiments by Heckmann et al.[159] The primary kinetic isotope effects in the two reactions, for which there are no prior data, were also investigated via the reactions

$$C_6D_6 + Cl \xrightarrow{k_{1b}} C_6D_5 + DCl \qquad (6.1b)$$

and

$$C_6H_5 + DCl \xrightarrow{k_{2b}} C_6H_5D + Cl \qquad (6.2b)$$

The current work has also been able to generate some kinetic information about the reactions of phenyl iodide with Cl and C_6H_5. The former process has been studied only once, at room temperature,[160] while there appears to be no kinetic information in the literature concerning the latter.

Finally, the MPWB1K and CCSD(T)/CBS methods, previously discussed in chapter 3, were employed to explore the potential energy surface of the C_6H_6Cl system. In particular, stationary points corresponding to a simple H-abstraction reaction were characterized and are discussed here for the first time. The potential energy diagram obtained with CCSD(T)/CBS theory was subsequently used in modified transition state theory (MTST) calculations in order to rationalize the PES. Due to the ongoing controversy regarding the structure of the chlorocyclohexadienyl adduct, of which Tanko and Suleman[161] and Tsao et al.[162] provide detailed chronological accounts, the addition of Cl to C_6H_6 was also investigated with both computational methods.

6.2. Methodology

6.2.1. Measurements of $Cl + C_6H_6 \rightarrow HCl + C_6H_5$

Argon bath gas containing benzene and either of the two Cl atom precursors, CCl_4 for experiments in the 578-724 K temperature range, or NaCl at 922 K, was flowed into the reactor. NaCl was employed at the highest temperature by introducing a porcelain boat containing NaCl (s) into the gas entry side arm and allowing some to evaporate into the reactor; this was done because, as noted by Adusei and Fontijn, CCl_4 is not suitable for such high temperatures.[163] The radical species in both cases were then generated via pulsed photodissociation of the precursors by ultraviolet radiation of 193 nm from the excimer laser, and the resultant Cl atoms were monitored by time-resolved fluorescence at 130-140 nm using photon counting and signal averaging. The pseudo-first order approximation has been employed, whereby the system has been flooded with a much higher $[C_6H_6]$ relative to the Cl atom concentration, yielding first order kinetics as shown in equation 6.3. A plot of the ensuing pseudo-first order rate coefficient k_{ps1} against $[C_6H_6]$ should be linear, as shown in figure 6.1, with slope k_1 and intercept k', and the error bars accompanying the concentration points as well as the uncertainty in the slope were calculated as described in section B1 of Appendix B..

$$d[Cl]/dt = -k_1[Cl][C_6H_6] - k'[Cl] = (-k_1[C_6H_6] - k')[Cl] = -k_{ps1}[Cl] \qquad (6.3)$$

The experiment was repeated at two of the temperatures used in reaction 6.1 using C_6D_6 instead of benzene in order to explore kinetic isotope effects (reaction 6.1b). Experimental parameters such as photolysis energy F, pressure, and the average gas residence time inside the reactor τ_{res}, were varied in order to assess any possible dependence of the second-order rate constants upon such parameters, as well as to ensure that secondary chemistry was negligible as were thermal decomposition and mixing effects.

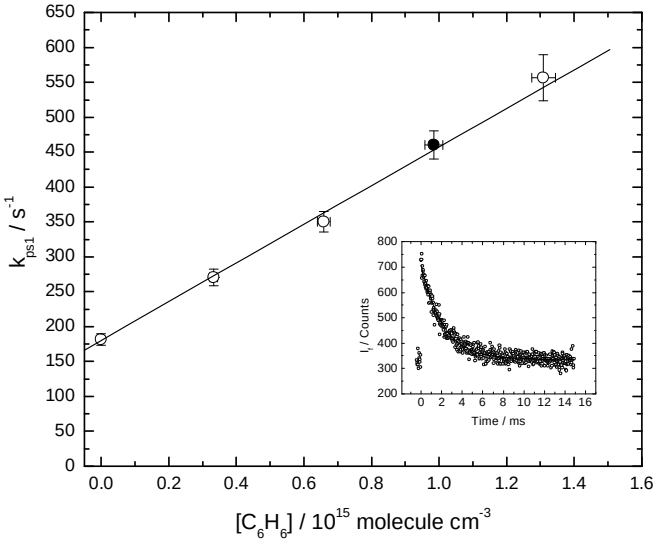

Figure 6.1. Pseudo-first-order decay coefficient for Cl in the presence of excess C_6H_6 at 676 K and 69 mbar total pressure with Ar. Error bars represent ± 1σ. The inset shows the signal corresponding to the filled point.

6.2.2. Measurements of $C_6H_5 + HCl \rightarrow Cl + C_6H_6$

The reverse reaction of 6.1, in which the phenyl radical abstracts the hydrogen from HCl (6.2), was also investigated over a wide range of temperature (292-748K). In this reaction, the C_6H_5 radical was generated from pulsed laser photolysis of a C_6H_5I precursor, which was then allowed to react with an excess of HCl, and in a different set of trials, an excess of DCl was used instead in order to assess the isotope effects (6.2b). The formation and disappearance of Cl atoms were monitored via time-resolved fluorescence at 130-140 nm, and as before, experimental parameters were varied in order to check for dependence of the rate constant on any such parameters. The HCl mixtures were flowed through the reactor for at least an hour before experiments were carried out in order to passivate the surfaces in the apparatus. The

observed constancy of the kinetics over the course of roughly 5 hours per each given run confirms that HCl was not lost significantly on the reactor walls during the measurements.

Because our apparatus is set up to monitor the time-resolved fluorescence of Cl atoms, in the case of (6.2) an increase in this signal is expected as the reaction proceeds because Cl atoms are now being formed, followed by a slow decay to the background as the result of diffusion. Thus, in order to fit this kind of data (which can no longer be fit using one single exponential decay function), a potential mechanism including the reverse reaction was hypothesized as follows:

$$C_6H_5 + HCl \xrightarrow{k_2} C_6H_6 + Cl \qquad (6.2)$$

$$C_6H_5I + Cl \xrightarrow{k_4} \text{products} \qquad (6.4)$$

$$Cl \xrightarrow{k_5} \text{diffusion} \qquad (6.5)$$

$$C_6H_5 + C_6H_5I \xrightarrow{k_6} \text{products} \qquad (6.6)$$

Cl is formed in reaction 6.2 and lost in reaction 6.4 and via diffusion in reaction 6.5. There is a competition between reactions 6.6 and 6.2 in regard to phenyl radical consumption. This mechanism leads to the following rate laws for the phenyl radical and Cl, respectively:

$$\frac{d[C_6H_5]}{dt} = -k_2[HCl][C_6H_5] - k_6[C_6H_5][C_6H_5I] = k_2'[C_6H_5] - k_6'[C_6H_5]$$
$$= (-k_2' + k_6')[C_6H_5]$$
$$\therefore [C_6H_5] = [C_6H_5]_0 e^{-(k_2' + k_6')t}$$

$$\frac{d[Cl]}{dt} = k_2[C_6H_5][HCl] - k_4[C_6H_5I][Cl] - k_5[Cl] = k_2'[C_6H_5] - k_4'[Cl] - k_5[Cl]$$
$$= k_2'[C_6H_5] - (k_4'+k_5)[Cl] = k_2'[C_6H_5]_0 e^{-(k_2'+k_6')t} - (k_4'+k_5)[Cl]$$
$$\therefore \frac{d[Cl]}{dt} + (k_4'+k_5)[Cl] = k_2'[C_6H_5]_0 e^{-(k_2'+k_6')t}$$

where the primed quantities represent pseudo-first order rate constants. This result concerning d[Cl]/dt can be solved analytically by noting that the quantity $e^{(k_4'+k_5)t}$ is the integration factor[21] needed to obtain an exact differential on the left hand side, so multiplying both sides by this quantity yields

$$e^{(k_4'+k_5)t} \times \frac{d[Cl]}{dt} + (k_4'+k_5)[Cl]e^{(k_4'+k_5)t} = k_2'[C_6H_5]_0 e^{-(k_2'+k_6')t} \times e^{(k_4'+k_5)t}$$
$$\therefore e^{(k_4'+k_5)t} \times \frac{d[Cl]}{dt} + (k_4'+k_5)[Cl]e^{(k_4'+k_5)t} = k_2'[C_6H_5]_0 e^{(k_4'+k_5-k_2'-k_6')t}$$

where the entire left side is now simply equivalent to: $\frac{d}{dt}\left([Cl]e^{(k_4'+k_5)t}\right)$, so integrating both sides from t = 0 to t = t results in

$$\int_0^t \frac{d}{dt}\left([Cl]e^{(k_4'+k_5)t}\right) = \int_0^t k_2'[C_6H_5]_0 e^{(k_4'+k_5-k_2'-k_6')t}$$
$$\therefore [Cl]_t e^{(k_4'+k_5)t} - [Cl]_0 e^{(k_4'+k_5)0} = k_2'[C_6H_5]_0 \left\{ \left(\frac{e^{(k_4'+k_5-k_2'-k_6')t}}{k_4'+k_5-k_2'-k_6'} \right) - \left(\frac{1}{k_4'+k_5-k_2'-k_6'} \right) \right\}$$

Finally, accounting for the fact that $[Cl]_0$ is zero and dividing both sides by $e^{(k_4'+k_5)t}$ leads to the solution for $[Cl]_t$:

$$[Cl]_t = \frac{k_2'[C_6H_5]_0}{k_4'+k_5-k_2'-k_6'} \times \left\{ \left(\frac{e^{(k_4'+k_5-k_2'-k_6')t}}{e^{(k_4'+k_5)t}} \right) - \left(\frac{1}{e^{(k_4'+k_5)t}} \right) \right\}$$
$$\therefore [Cl]_t = \frac{k_2'[C_6H_5]_0}{k_4'+k_5-k_2'-k_6'} \times \left\{ \left(e^{-(k_2'+k_6')t} \right) - \left(e^{-(k_4'+k_5)t} \right) \right\} \quad (6.7)$$

This solution can be expressed more generally as

$$\frac{AB}{(B+D)-C} \left(e^{-Ct} - e^{-(B+D)t} \right) \quad (6.8)$$

where in the present case

$$A = [C_6H_5]_0 \qquad B = k_2[HCl] \qquad C = k_4[C_6H_5I] + k_5 \qquad D = k_6[C_6H_5I]$$

A similar set of solutions apply to the reaction with DCl, and the ensuing rate constants are denoted by the subscript b.

An example fluorescence signal is shown as the inset in figure 6.2. After the subtraction of the constant background arising from the small amount of scattered resonance radiation in the reactor, the value of which was approximated from the pre-trigger signal, the remaining signal was fit by varying the A, B, C and D parameters until the sum of the squared deviations was minimized. The Solver feature in Microsoft Excel was used to carry out the fitting procedure described. Profiles of Cl as a function of [HCl] were obtained based usually on five values of [HCl], and figure 6.2 shows a plot of the B parameter vs. [HCl]. The slope of this plot represents the reverse rate constant k_2, and the intercept is close to zero as expected. The uncertainty in B was estimated based on the amount of variation in this parameter that could be reasonably tolerated in the fits to the Cl signal. In general, it was found that the B parameter could be changed by as much as ± 30% before it no longer sensibly represented the data, and this value was taken as an estimate of 2σ for B, an example of which is shown in figure 6.3.

As may also be seen in figure 6.2, the C and D parameters are basically constant and small compared to B, so that any errors in these terms have little impact on k_2. The $[C_6H_5I]$ was not varied systematically, however, an approximate ballpark figure for k_6 was obtained by dividing the D parameter by $[C_6H_5I]$. In a similar fashion, an estimate of k_4 was obtained by dividing the C parameter by $[C_6H_5I]$. Because of the neglect of the unknown diffusional contribution, k_5, this estimate of k_4 is in fact only an upper limit. While k_5 may be somewhat similar to the k' term from the CCl_4 photolysis experiments, k' also includes contributions from secondary chemistry which are likely to be different in the C_6H_5I/HCl system.

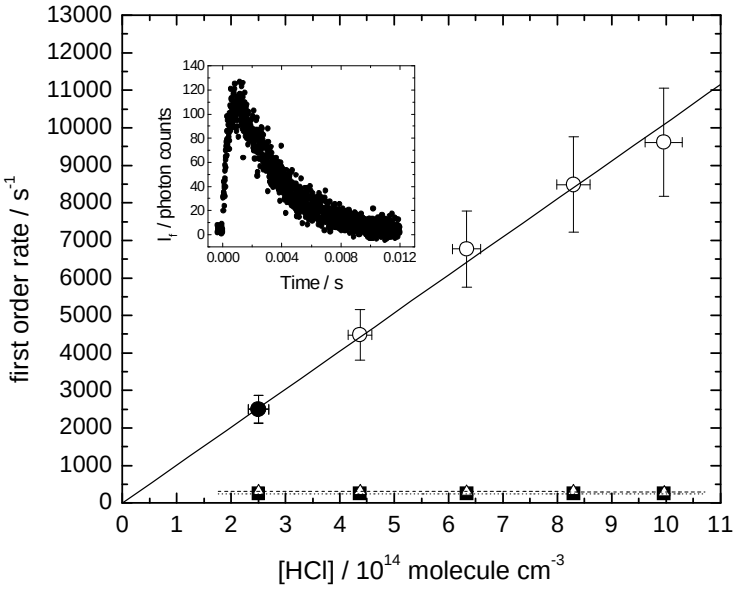

Figure 6.2. First order rates in fit to Cl growth and decay in the C_6H_5 + HCl reaction at 294 K and 65 total pressure with Ar. Circles: k_2[HCl]; open triangles: $k_4[C_6H_5I] + k_5$; solid squares: $k_6[C_6H_5I]$; solid line: fit to k_2[HCl] data; dashed line: fit to : $k_4[C_6H_5I] + k_5$ data; dotted line: fit to $k_6[C_6H_5I]$ data. Error bars represent ± 1σ. The inset shows a signal corresponding to the filled circle.

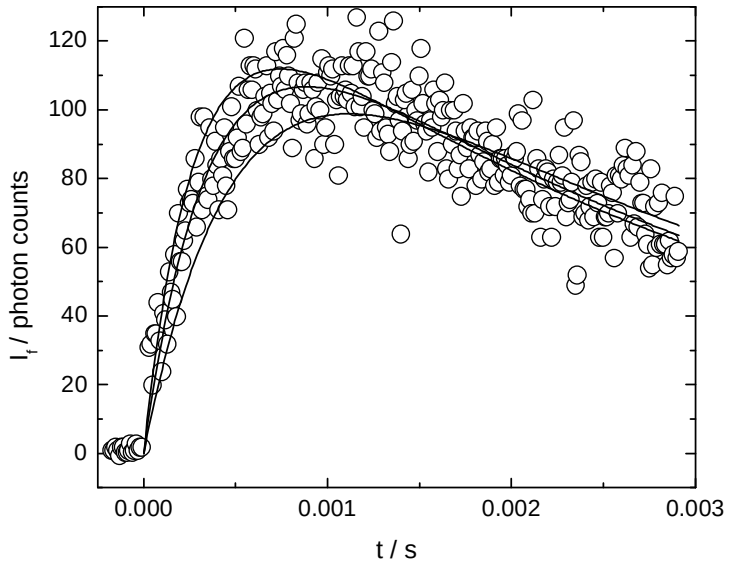

Figure 6.3. Example of fit to Cl growth and decay signal (background subtracted) at 294 K. The central line is the best fit, and the upper and lower lines represent the effect of increasing or reducing the B parameter by 30%, taken to approximate ± 2σ.

6.2.3. Computational Methodology

The geometries, vibrational frequencies, and energies of stationary points along the potential energy surface (PES) for the reaction between HCl and C_6H_5, were investigated with two levels of theory. The first was the MPWB1K hybrid meta density functional theory (DFT) method developed by Zhao and Truhlar,[36] which incorporates the modified Perdew and Wang 1991 exchange functional (MPW)[37] along with Becke's 1995 meta correlation functional (B95).[38] The modified G3Large basis set (MG3)[36] was used in conjunction with this method, which is essentially 6-311++G(3d2f,2df,2p) for H-Si, but has been improved for P-Ar. This was the largest basis set tested by Zhao and Truhlar, and their recommended value of 0.9567 was used to scale the frequencies obtained with MPWB1K/MG3.[36]

The second approach was the UQCISD/UHF[44] *ab initio* method with the 6-311G(d,p) basis set. A scaling factor of 0.954[59] was employed to scale the vibrational frequencies in this case. The QCISD geometries and zero point energies were employed in UCCSD(T)/ROHF[50] single-point calculations with correlation consistent basis sets,[56,57] extrapolated to the complete basis set limit. The reactants and products were also optimized with the B3LYP DFT method, and several versions of the CBS-QB3[129] and G3[41] composite methods were applied, to assess the reaction enthalpy $\Delta_r H_0$ with a variety of electronic structure methods. The Gaussian 03 and Molpro 2002.6 program suites[61,62] were used to carry out the computations.

6.3. Results and Discussion

6.3.1. Kinetics

Table 6.1 summarizes 32 determinations of the second-order rate constant k_1. This rate constant seemed to have a systematic dependence on the photolysis pulse energy at the low end of the temperature range, as is shown in figure 6.4. In order to obtain k_1 in the absence of secondary chemistry, this dependence was extrapolated to zero F using a weighted linear least-squares fit, and the ensuing values for k_1 at zero F are also listed in Table 6.1 along with their statistical uncertainty. No such systematic variation with F was observed at the highest temperature, and instead the measurements were averaged. Furthermore, no systematic dependences were observed in k_1 upon variation of other parameters such as pressure and residence time, which indicates that mixing or thermal decomposition did not have large effects.

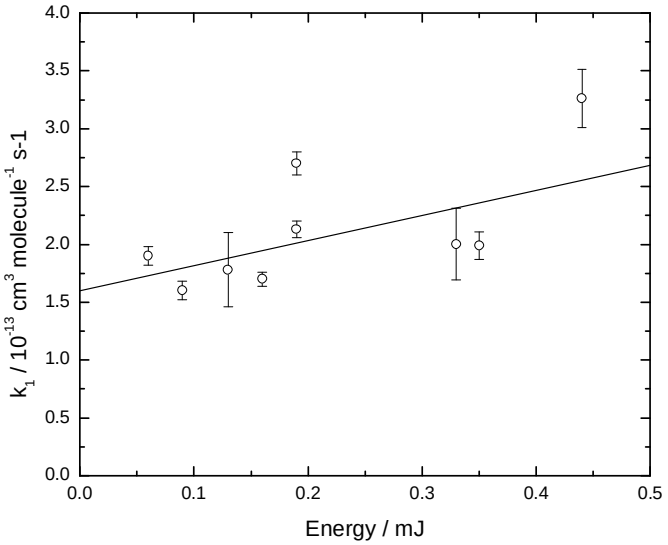

Figure 6.4. Dependence of observed k_1 on laser photolysis energy F at 622 K. Error bars represent ± 1σ.

The temperature dependence of k_1 was analyzed through the means of the Arrhenius expression, and the resulting plot of the k_1 data is depicted in figure 6.5. From this graph, the way in which the k_1 depends on temperature may be represented as

$$k_1 = (6.4 \pm 2.8) \times 10^{-12} \exp(-18.1 \pm 2.3 \text{ kJ mol}^{-1}/RT) \text{ cm}^3 \text{ molecule}^{-1} \text{ s}^{-1} \quad (6.9)$$

over 578-922 K. This fit includes the statistical uncertainty in k_1 as well as that in the temperature ($\sigma_T/T = 2\%$). Along with the Arrhenius parameters given above are their 1 σ uncertainties, which taken together with the covariance as well as with the allowance for potential systematic errors of around 10%, yield the overall 95% confidence limits for k_1 of ± 26%. More details on the treatment of uncertainty can be found in Appendix B.

The range of k_1 data can be extended down to around room temperature by incorporating the 296 K measurement of Sokolov et al.[156] The resulting unweighted fit to the combined data set yields the recommendation

$$k_1 = (6.1 \pm 3.2) \times 10^{-11} \exp(-31.6 \pm 2.1 \text{ kJ mol}^{-1}/RT) \text{ cm}^3 \text{ molecule}^{-1} \text{ s}^{-1} \quad (6.10)$$

for the range 296-922 K. This new fit also represents the present data reasonably well, except for the smallest k_1 value which is 1.8 times larger than the fit. This factor is outside the confidence limits, but it must be noted that the k_1 point at 578 K is the most vulnerable to systematic error because the primary reaction is the slowest at this point, and as such it is harder to separate from any potentially interfering secondary processes. This second k_1 expression is used in the thermochemical analysis to follow as it covers a wider range of temperature.

Experiments using C_6D_6 instead of benzene at two temperatures are summarized in Table 6.2 and Fig. 6.5. The results over the range 635-922 K can be expressed as

$$k_{1b} = 6.2 \times 10^{-12} \exp(-22.8 \text{ kJ mol}^{-1}/RT) \text{ cm}^3 \text{ molecule}^{-1} \text{ s}^{-1} \quad (6.11)$$

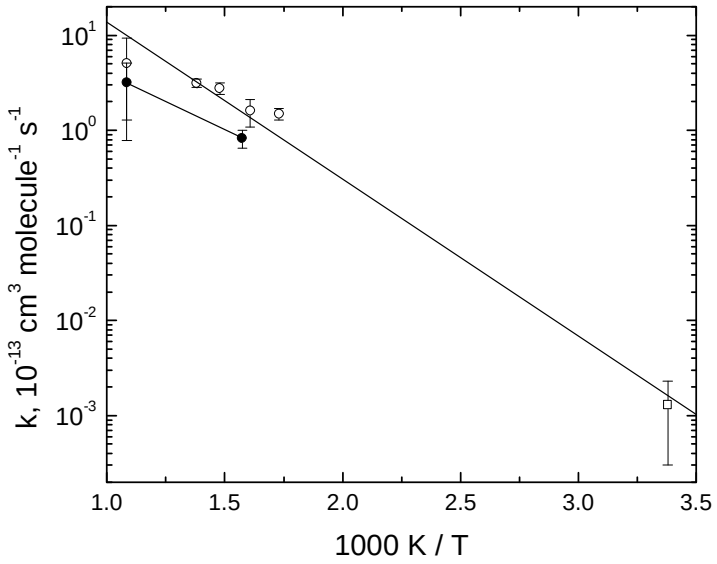

Figure 6.5. Arrhenius plot of k_1 and k_{1b}. Open circles and square: Cl + C_6H_6, this work and Sokolov et al.; filled circles: Cl + C_6D_6, this work. Error bars represent ± 2σ.

Table 6.3 summarizes the 28 measurements of k_2 for the reverse reaction. Variation of parameters such as the photolysis energy, initial phenyl concentration, and the residence time, has shown that the rate constant does not depend significantly on such parameters, which indicates k_2 has been isolated from secondary processes. The average k_2 values at each temperature are plotted in Arrhenius form in figure 6.6, and yield

$$k_2 = (1.14 \pm 0.13) \times 10^{-12} \exp(+5.2 \pm 0.3 \text{ kJ mol}^{-1}/RT) \text{ cm}^3 \text{ molecule}^{-1} \text{ s}^{-1} \quad (6.12)$$

over 294-748 K. As before, taking the uncertainties in the Arrhenius parameters with the covariance resulted in the 2σ statistical uncertainties in the fitted k_2. The range of these uncertainties was between 6 and 12%, and upon also allowing for a possible 10% systematic error, the overall confidence limits of ± 13% are proposed.

Eight measurements with DCl instead of HCl at two temperatures, corresponding to reaction 6.2b, are listed in Table 6.4 and may be summarized as

$$k_{2b} = 7.7 \times 10^{-13} \exp(+4.9 \text{ kJ mol}^{-1}/RT) \text{ cm}^3 \text{ molecule}^{-1} \text{ s}^{-1} \quad (6.13)$$

over 292-546 K.

Information regarding reactions 6.4 and 6.6 (and the deuterated analogs) can also be extracted from these studies, and the resultant rate constants are presented in Tables 6.3 and 6.4 as well. As previously mentioned, an upper limit to k_4 was estimated by dividing the B term by $[C_6H_5I]$. The lowest k_4 and k_{4b} values obtained at each temperature in experiments with HCl and DCl respectively, are combined in the Arrhenius plot shown in figure 6.7, and can be expressed approximately as

$$k_4 \leq 5.3 \times 10^{-12} \exp(+2.8 \text{ kJ mol}^{-1}/RT) \text{ cm}^3 \text{ molecule}^{-1} \text{ s}^{-1} \quad (6.14)$$

over 300–750 K. Due to the large amount of scatter, an uncertainty of at least a factor of 1.5 in k_4 is suggested. Figure 6.7 also shows the k_6 values from both sets of experiments, which exhibit considerable scatter as well. These data may be summarized roughly as

$$k_6 = (2 \pm 1) \times 10^{-11} \text{ cm}^3 \text{ molecule}^{-1} \text{ s}^{-1} \quad (6.15)$$

over 300 – 750 K.

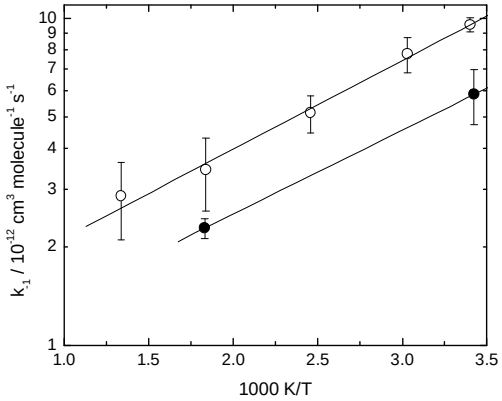

Figure 6.6. Arrhenius plot of k_2 and k_{2b}. Open circles: HCl + C_6H_5; filled circles: DCl + C_6H_5. Error bars represent ± 1σ.

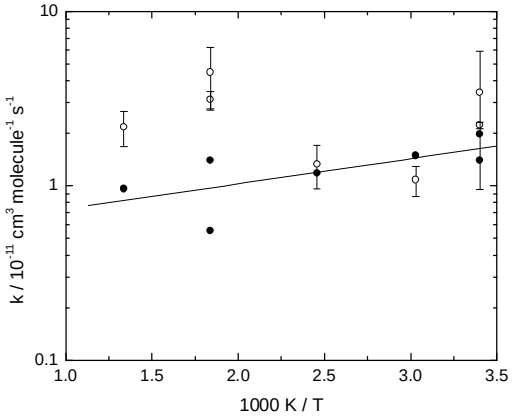

Figure 6.7. Arrhenius plot of k_4 for the Cl + C_6H_5I reaction, solid circles (upper limit) and line, and k_6 for the C_6H_5 + C_6H_5I reaction, open circles with 1σ error bars.

The rate constant corresponding to reaction 6.2, k_2, has not been measured previously. Yu and Lin[164] have investigated the analogous C_6H_5 + HBr reaction and found a rate constant of a similar order of magnitude to k_2. However, a positive activation energy $E_a = 4.6 \pm 1.7$ kJ mol^{-1} was obtained by these workers which is not the case for the E_a observed for reaction 6.2. As can be seen from the Arrhenius expression for k_2, a negative activation energy E_a was found for reaction 6.2. Negative activation energies have been encountered earlier in the cases involving alkyl and silyl radical reactions with HBr and HI,[165-170] although these experiments have been criticized.[171] The current findings extend the scope of this phenomenon to radical plus HCl chemistry, which are rationalized further in section 6.3.3 based on PES calculations for this system.

The potential for adduct formation between Cl and C_6H_6 has been briefly noted earlier, but the binding energy in the chlorocyclohexadienyl adduct of 30 ± 10 kJ mol^{-1} is too small for such an adduct to be present in significant quantities at elevated temperatures.[156] Furthermore, the primary kinetic isotope effects for both k_1 and k_2, of $k_H/k_D = 2.2 \pm 0.3$ and 1.6 ± 0.1, respectively, are consistent with an abstraction mechanism ($k_H/k_D > 1$).

The expression for k_4 yields an upper limit of 1.7×10^{-11} cm^3 molecule^{-1} s^{-1} at 296 K, with an uncertainty of a factor of 1.5. Because diffusion of atomic Cl is in all likelihood modest when compared to this reaction, k_4 may indeed be close to this limit. There is reasonable accord between this value and that of $(3.3 \pm 0.7) \times 10^{-11}$ cm^3 molecule^{-1} s^{-1} from a smog chamber measurement.[160] Addition of Cl to C_6H_5I followed by elimination of I was proposed by Andersen et al.[160] as a viable mechanism for reaction 6.4, and the small negative E_a presently observed is consistent with such an addition step. No prior data for the reaction between phenyl and phenyl iodide were found in the literature. The proposed magnitude for k_6 would imply a

small energy barrier if any at all, and by analogy with reaction 6.4, possible products for this process might be biphenyl and I atoms.

6.3.2. Thermochemistry

The ratio k_1/k_2 is equivalent to the equilibrium constant $K_{eq,}$ which was found to fit to the expression

$$K_{eq} = 53.5 \times e^{(-4430K/T)} \tag{6.16}$$

within the overlapping temperature range of 296-748 K between the two reactions. K_{eq} was evaluated at 10 temperatures from this expression and used to construct a van't Hoff plot as shown in figure 6.8. As demonstrated in equation 6.17 below, the van't Hoff method relies on plotting $\ln(K_{eq})$ against 1/T in order to yield a slope from which $\Delta_r H$ can be extracted.

$$\ln\left(K_{eq}\right) = -\frac{\Delta_r H}{R} \times \frac{1}{T} + \frac{\Delta_r S}{R} \tag{6.17}$$

To directly obtain $\Delta_r H_{298}$ for reaction 6.1 from such a plot, a small temperature correction[165] of $-(\Delta S_T - \Delta S_{298})/R + (\Delta H_T - \Delta H_{298})/RT$ must be added to $\ln(K_{eq})$. The correction is small, $\leq$ 0.14, and it is expressed in terms of $\Delta_r C_p$ as

$$-\frac{1}{R}\int_{298}^{T}\frac{\Delta_r Cp}{T}dT + \frac{1}{RT}\int_{298}^{T}(\Delta_r Cp)dT \tag{6.18}$$

following standard thermodynamic relations.[172] The temperature dependences of ΔS and ΔH were also evaluated via $\Delta_r C_p$ for reaction 6.1, and thus it is appropriate at this time to elaborate on how this quantity was calculated.

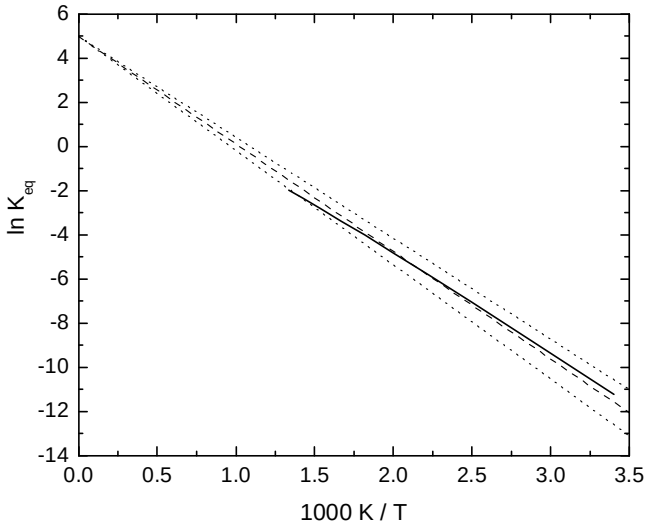

Figure 6.8. van't Hoff plot for the equilibrium constant of Cl + C_6H_6 = HCl + C_6H_5 (solid line, experiment; dashed line, third law fit with Δ_rH_{298} = 40.5 kJ mol^{-1} constrained to pass through computed $\Delta S_{298}/R$). Dotted lines indicate Δ_rH_{298} = 38.0 kJ mol^{-1} and 43.0 kJ mol^{-1}.

While thermochemical data for Cl and HCl as a function of temperature were available and taken from the JANAF Tables,[173] no such data were found for C_6H_6 or C_6H_5, and were instead calculated via standard relations[173] from moments of inertia and vibrational frequencies, and are listed in Table 6.5. Measured vibrational frequencies for C_6H_6 were obtained from Shimanouchi's tabulation[174] and frequencies for C_6H_5 were taken from the work of Łapiński et al.[175] The product of the moments of inertia for C_6H_6 was taken from Herzberg's book[176], and has a value of 6.43 x 10^{-135} kg^3 m^6. The product of the moments of inertia for C_6H_5 has not been experimentally determined, thus it had to be computationally approximated and was found to be 5.61 x 10^{-135} kg^3 m^6. QCISD/6-31G(d) theory was used to obtain this value, which was chosen because it reproduced the known value for C_6H_6 to within 0.2%. The accumulation of the aforementioned values enabled the heat capacity of each of the four species involved in reaction 6.1 to be calculated at several temperatures over the range 50-3000 K. The difference between

the summed heat capacities of the products and those of the reactants is $\Delta_r C_p$, a quantity which was evaluated at each of the temperatures in Table 6.5, plotted, and then fit to a polynomial function. Thus, the temperature dependence of $\Delta_r C_p$ was established and the temperature correction to $\ln(K_{eq})$ as well as ΔH and ΔS could be calculated.

The linear fit to the van't Hoff plot was constrained to have an intercept equal to the derived $\Delta S_{298} = 41.50$ J K^{-1} mol^{-1} divided by the gas constant R. The slope of this line is $-\Delta H_{298}/R$, from which $\Delta H_{298} = 40.5$ kJ mol^{-1} was obtained. The maximum deviation from the fit in figure 6.8 is 0.5. The uncertainty in ΔH_{298} was approximated via an assumed factor of 2 uncertainty in the K_{eq} value in the center of the range, primarily arising from uncertainty in k_1. This analysis results in confidence limits for ΔH_{298} of ± 2.5 kJ mol^{-1}, which are also included and depicted graphically in figure 6.8.

The use of statistical mechanics to calculate the reaction entropy from experimental or computed structural parameters and frequencies, followed by the inclusion of this quantity in a van't Hoff plot, is referred to as the Third-Law method for obtaining reaction enthalpies. This method is termed thusly because it essentially relies on the absolute entropies of the reactants and products, which can be calculated very accurately from experimental or computational information, consequently leading to Third-Law enthalpies that are somewhat more accurate than those which would be obtained from the Second-Law method.[177] In the Second-Law approach, the enthalpy of reaction is obtained from the difference of the activation energies for the forward and reverse reactions.[134] The use of other experimental or computed data is not necessary for attaining reaction enthalpies via the Second-Law method, which essentially permits the determination of this quantity directly from kinetic measurements. This method is particularly useful if the forward and reverse rate constants have been accurately measured over a wide

overlapping range of temperature, in which case the activation energies for the forward and reverse reactions can be obtained at the central temperature and used in the analysis. If only limited kinetic information is available for the forward and reverse reactions at overlapping temperatures, or if one or both the reactions are difficult to isolate for direct study, such as reaction 6.1 in the present case, it is more reasonable to use the Third-Law approach, in which the limited data can be "anchored" by the accurate intercept determined from Third-Law entropies.[177]

As explained earlier, the present implementation of the Third-Law approach yielded ΔH_{298} of 40.5 ± 2.5 kJ mol^{-1} for reaction 6.1. Inclusion of the bond dissociation enthalpy D_{298}(H-Cl)[173] yields $D_{298}(C_6H_5\text{-}H)$ = 472.1 ± 2.5 kJ mol^{-1}. Combination of this quantity with the enthalpies of formation $\Delta_f H_{298}(C_6H_6)$[178] = 82.9 ± 0.5 and $\Delta_f H_{298}(H)$[173] = 218.0 kJ mol^{-1} yields $\Delta_f H_{298}(C_6H_5)$ = 337.0 ± 2.5 kJ mol^{-1}.

The room temperature values of k_1 determined by Shi and Bernhard[155] and Sokolov et al.[156] divided by the k_2 value obtained in the present analysis give K_{eq} and hence ΔG through the following relation:

$$\Delta G = -RT \times \ln(K_{eq}) \qquad (6.19)$$

Taking these ΔG values and adding TΔS to them yields respective ΔH values, where the ΔS used is the one derived earlier in the thermochemistry. The results give $D_{298}(C_6H_5\text{-}H)$ = 466 ± 1 and 472 ± 3 kJ mol^{-1}, respectively, and for comparison, two recent experimental assessments of this quantity yielded 474.9 ± 2.5 kJ mol^{-1} and 472.2 ± 2.2 kJ mol^{-1}.[158,179] Therefore the Shi and Bernhard rate constant appears to be slightly too high, and consequently the Sokolov et al. value was employed in the recommendation for k_1 above. This recommended k_1 divided by k_2 yields $\Delta_f H_{298}(C_6H_5)$ kJ mol^{-1} = 337.0 ± 2.5 kJ mol^{-1}, a result which is in agreement with the recent

determinations of 339.4 ± 2.5 kJ mol^{-1}, 338 ± 3 kJ mol^{-1}, and 337.1 ± 3 kJ mol^{-1},[158,159,179] and also with the older value of 334.7 ± 4.2 kJ mol^{-1} obtained by Rodgers et al.[180] Thus, this work supports the revision upward from the prior recommendations of 328.9 ± 8.4 kJ mol^{-1} and 330.1 ± 3.3 kJ mol^{-1} for this quantity.[177,181] These values are further compared in Table 6.6.

6.3.3. Computations

6.3.3.1. Geometries

Stationary points along the PES for reaction 6.1 located with both MPWB1K/MG3 theory and QCISD/6-311G(d,p) theory (excluding Cl) are shown in figure 6.9. The Cartesian coordinates, rotational constants, and vibrational frequencies of all of the species are provided in Appendix C.

The geometrical parameters of benzene obtained with both levels of theory compare well with the values proposed by Gauss and Stanton.[182] They used CCSD(T)/cc-pVQZ theory combined with a reanalysis of experimental rotational constants to arrive at recommended values of r_e(C-C) = 1.3914 ± 0.0010 Å and r_e(C-H) = 1.0802 ± 0.0020 Å (1 Å = 10^{-10} m). In this work, values of 1.379 and 1.400 Å were obtained for r_e(C-C) and 1.076 and 1.087 Å for r_e(C-H) using the MPWB1K/MG3 and QCISD/6-311G(d,p) methods, respectively.

The calculated r_e values for HCl were 1.269 Å with MPWB1K/MG3 theory and 1.276 Å with QCISD/6-311G(d,p) theory, both of which agree well with the experimental value of 1.2746 Å.[183]

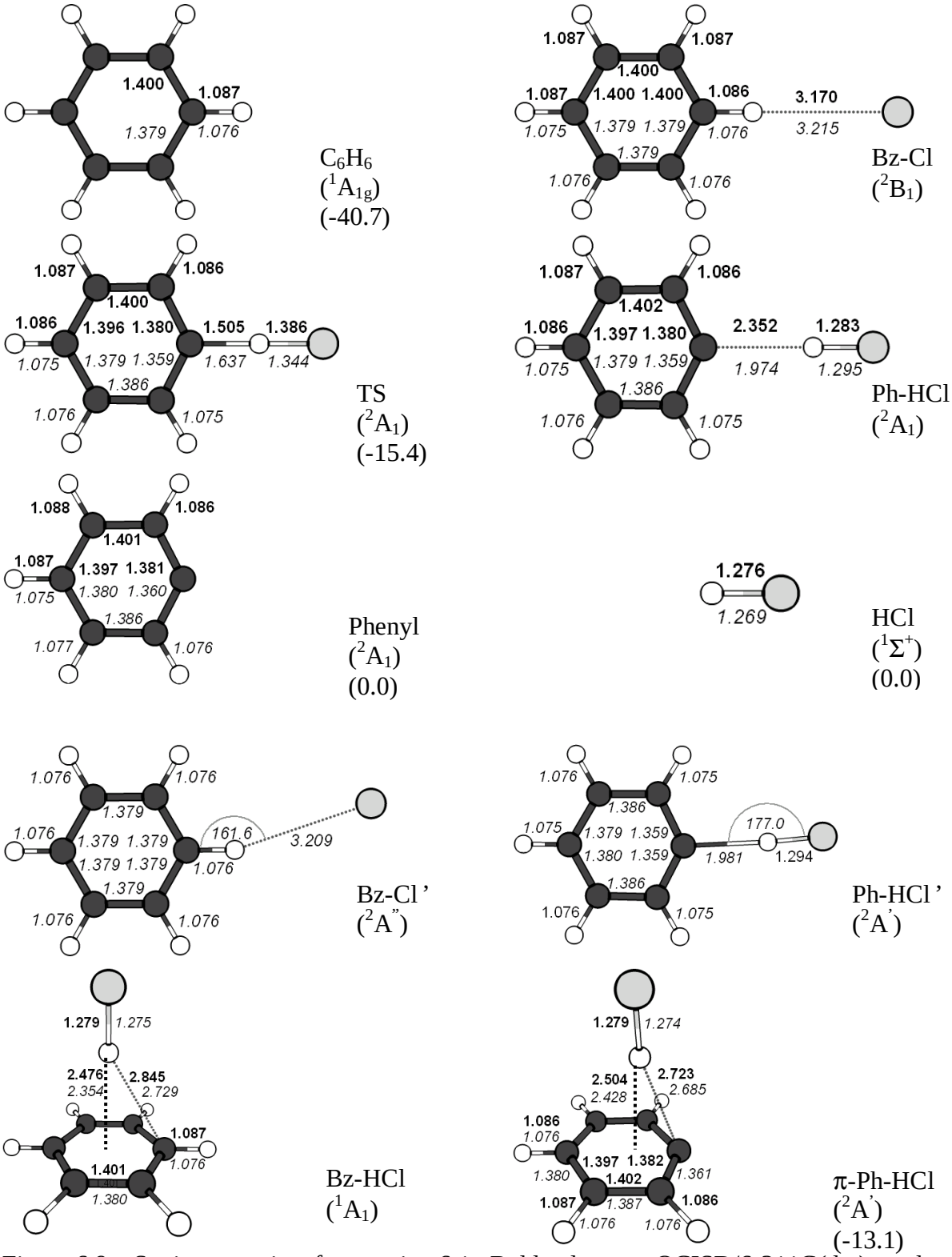

Figure 6.9. Stationary points for reaction 6.1. Bold values are QCISD/6-311G(d,p) results and italicized values indicate results obtained with MPWB1K/MG3 theory. Prime quantities are exclusive to MPWB1K/MG3 theory. Values in parentheses are CCSD(T)/CBS enthalpies of product set relative to the appropriate reactants in kJ mol^{-1} at 0 K.

For the phenyl radical, the calculated C-H r_e values are all within ± 0.001 Å of those of benzene at both levels of theory, however, the C-C bond distances have decreased by as much as 0.019 Å (see Fig. 6.9). The greatest geometrical difference between benzene and phenyl is the C-C(rad)-C angle, which has increased from 120.0º to 126.1º and 125.4º in the case of MPWB1K/MG3 and QCISD/6-311G(d,p) theories, respectively. No geometrical parameters have been measured, and the best level of theory previously used to optimize this molecule seems to be CCSD(T)/6-31G(d).[184] A comparison of r_e(C-C) = 1.4017 Å and r_e(C-H) = 1.0910 Å in benzene obtained with CCSD(T)/6-31G(d) theory with the corresponding values obtained by Gauss and Stanton[182] suggests that this level of theory does not outperform the QCISD/6-311G(d,p) theory used in this work.

The transition state that connects phenyl + HCl to benzene + Cl was found to be of C_{2v} symmetry (see Fig. 6.9), and visualization of the imaginary mode indicated that the reaction coordinate is a simple hydrogen abstraction from HCl by the phenyl radical, with a C-H-Cl angle of 180º. Following the intrinsic reaction coordinate from this transition state yielded two structures denoted Bz-Cl and Ph-HCl in figure 6.9. Both these structures had an imaginary frequency at the DFT level of theory. Visualization of the imaginary normal mode of Bz-Cl indicated that the energy of the MPWB1K/MG3 structure is lowered by distortion of the C-H-Cl angle to less than 180º in the plane of the molecule, leading to the Bz-Cl' structure shown in figure 6.9. C_{2v} Bz-Cl was a true adduct (all frequencies real) at the QCISD/6-311G(d,p) level of theory. Similarly, C_{2v} Ph-HCl has an imaginary frequency with DFT and the true MPWB1K minimum is the C_s Ph-HCl' geometry shown in figure 6.9, where the C-H-Cl angle has distorted away from linearity but remains in the plane of the ring.

These DFT symmetry lowerings leave the bond lengths essentially unchanged, with a maximum difference of less than 0.01 Å. The C-H-Cl angles have changed from 180º to 177.0º and 161.6º in Ph-HCl' and Bz-Cl', respectively. As can be seen from Table 6.7, the electronic energies of these species decreased upon relaxation by 0.1 and 0.2 mE_H, respectively (1 E_H = 2625.5 kJ mol^{-1}), i.e., by up to 0.5 kJ mol^{-1}. The zero-point vibrational energies (ZPEs) have increased along with the increase in the number of real frequencies and, as can be seen from Table 6.6, scaling and adding these ZPEs to the electronic energies actually results in C_s species marginally less stable than the C_{2v} counterparts. Because these differences in total energy are small (less than 0.2 mE_H) at the MPWB1K/MG3 level of theory, it is hard to assign a definitive symmetry to the Ph-HCl and Bz-Cl adducts on the vibrationally adiabatic DFT PES.

At long ranges the multiple electronic states arising from the interaction of Cl ($^2P_{3/2,1/2}$) with C_6H_6 ($^1A_{1g}$) become degenerate, so the loose atomic complexes are expected to show multireference character. This means that the assignment of $^2B_1$ and ^2A" to Bz-Cl and Bz-Cl' may not imply true non-adiabatic behavior but rather deficiencies in the single-reference treatment used here. These weakly bound long-range complexes are not important kinetically and are not considered further.

Interestingly, in the case of QCISD/6-311G(d,p) theory, the relaxed C_s structure for Ph-HCl is significantly different from the original C_{2v} species. The new structure, denoted as π-Ph-HCl in figure 6.9, has no imaginary frequencies. A similar minimum is characterized with DFT. A similar adduct, with HCl normal to the aromatic ring, has been observed spectroscopically between benzene and HCl.[185-187] For comparison, this benzene-HCl complex has been characterized with DFT and *ab initio* theory, and is presented as Bz-HCl in figure 6.9. The distance between the center of the benzene ring and the Cl atom (r_e) and the well depth (D_e) were

found to be 3.63 Å and 13.6 kJ mol^{-1} respectively with MPWB1K/MG3 theory and 3.76 Å and 14.1 kJ mol^{-1} with QCISD/6-311G(d,p) theory. These results are in reasonable accord with the values of Read et al. of r_e = 3.63 Å and D_e = 8.6 and 23.3 kJ mol^{-1}, which were obtained by modeling the Bz-HCl complex as a pseudodiatomic molecule, and fitting parameters from Fourier transform microwave spectroscopy to a Lennard-Jones 6 – 12 potential.[185] Furthermore, adding in the corresponding computed ZPEs to the Bz-HCl complex yields D_0 values of 10.1 and 11.9 kJ mol^{-1} with the MPWB1K/MG3 and QCISD/6-311G(d,p) theories, respectively, which agree with the range of $7.5 \leq D_0 \leq 15.9$ kJ mol^{-1} quoted in a later study by Gotch and Zwier,[187] and with the value of $D_0 = 12.1 \pm 2.1$ kJ mol^{-1} derived in a recent review by Mons et al.[188] from the experiments of Walters et al.[186]

In the similar π-Ph-HCl structure, the HCl fragment is involved in a hydrogen-bonding interaction with the π-electron system like in Bz-HCl, however, it also interacts with the radical carbon center in phenyl. The most noticeable effect of this second interaction is that the Cl-H-ring angle is not 180º as in Bz-HCl, but rather the H atom in HCl is displaced toward the carbon radical in the phenyl ring. The calculated distance between the center of the phenyl ring and the Cl atom (r_e) and the well depth (D_e) are 3.68 Å and 12.2 kJ mol^{-1} respectively with MPWB1K/MG3 theory, and 3.77 Å and 13.2 kJ mol^{-1} with QCISD/6-311G(d,p) theory. We also note that the H-Cl bond length is nearly identical between the two complexes, with a 0.001 Å difference at the MPWB1K/MG3 level of theory and no change with QCISD/6-311G(d,p) theory. These results suggest that the interaction between the HCl fragment and phenyl is similar to that in HCl and benzene.

6.3.3.2. Vibrational frequencies

The unscaled frequencies for all of the stationary points located with MPWB1K/MG3 theory and QCISD/6-311G(d,p) theory can be found in the Appendix C. The scaled frequencies for the phenyl radical obtained with both methods can be compared to the frequencies summarized by Łapiński et al.[175] The lowest frequency of A_2 symmetry has not been detected experimentally and has been excluded from the comparative analysis. In the case of the frequencies obtained with the DFT method, the agreement with the experimental values was reasonable, with the mean absolute deviation of 1.4%, no frequency in disagreement by more than 5%, and an overestimation of the ZPE by 2.1 kJ mol^{-1} (0.9%). The frequencies obtained with QCISD/6-311G(d,p) theory had a mean absolute deviation of 2.7%, with four of the frequencies being in disagreement with experimental values by more than 5%. These modes of motion correspond to the out-of-plane bending of the phenyl ring (($\omega_3(B_1)$, in error by 5.1%), the in-plane compression of the ring ($\omega_5(A_1)$, in error by 9.9%), the out-of-plane alternant bending of the five H atoms (($\omega_9(B_1)$, in error by 6.6%), and the in-plane bending of the five H atoms, which appears to be symmetric with respect to each pair of consecutive H atoms (($\omega_{17}(B_2)$, in error by 6.9%). The ZPE was underestimated by 3.4 kJ mol^{-1} (1.5%) with QCISD/6-311G(d,p) theory. A linear fit to a plot of the experimental frequencies against the unscaled QCISD/6-311G(d,p) frequencies, constrained to pass through the origin, yielded a slope of 0.961 (see Fig. 6.10). Repetition of the above frequency analysis with this 0.961 scaling factor, which is still in the optimal range of 0.954 ± 0.020 calculated by Irikura et al.[59], yielded a mean absolute deviation of 2.3%, with the errors in ω3, ω5, ω9, and ω17 reduced to 4.4, 9.2, 5.9, and 6.2% respectively, and the ZPE underestimated by 1.8 kJ mol^{-1} (0.8%). This is only a marginal improvement.

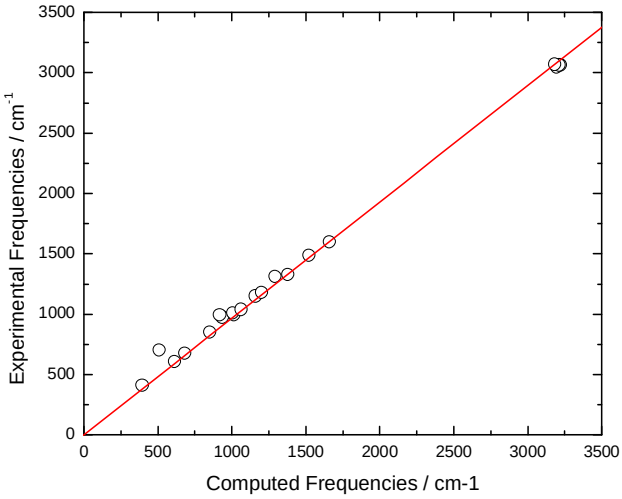

Figure 6.10. Linear plot of the experimental versus the unscaled QCISD/6-311G(d,p) vibrational frequencies of benzene constrained to go through the origin.

A similar frequency analysis was performed for benzene, and it was found that the agreement was reasonable once again with DFT, with a mean absolute deviation of 1.3% and no scaled frequencies differing by more than 5% from the experimental values taken from Herzberg.[176] The frequencies obtained with QCISD/6-311G(d,p) theory had a mean absolute deviation of 4.2%, with seven of the frequencies being in disagreement with experimental values by more than 5%. These frequencies included two sets of degenerate E_{2u} modes: (ω1 and ω2), in error by 8.0% and (ω9 and ω10), in error by 7.4%, two B_{2g} modes, ω6 and ω12, in error by 30.7% and 11.9%, respectively, and a B_{2u} mode, ω19, in error by 5.8%. The ZPEs were in reasonable agreement with literature, with an overestimation of 2.4 kJ mol^{-1} (0.9%) in the case of MPWB1K/MG3 theory, and an underestimation of 6.4 kJ mol^{-1} (2.5%) with QCISD/6-31G(d,p) theory. As before, a linear plot of the experimental versus the unscaled QCISD/6-311G(d,p) frequencies was constrained to go through the origin, which yielded an optimal scaling factor of

0.965 for benzene (See Fig. 6.11). Repeating the frequency analysis with this scaling factor decreased the mean absolute deviation to 3.6%, with the errors in ω1 and ω2, ω9 and ω10, ω6, ω12, and ω19 reduced to 6.9, 7.3, 29.9, 10.9, and 4.6%, respectively, and the ZPE underestimated by 3.6 kJ mol^{-1} (1.4%), which once more marks only a marginal improvement.

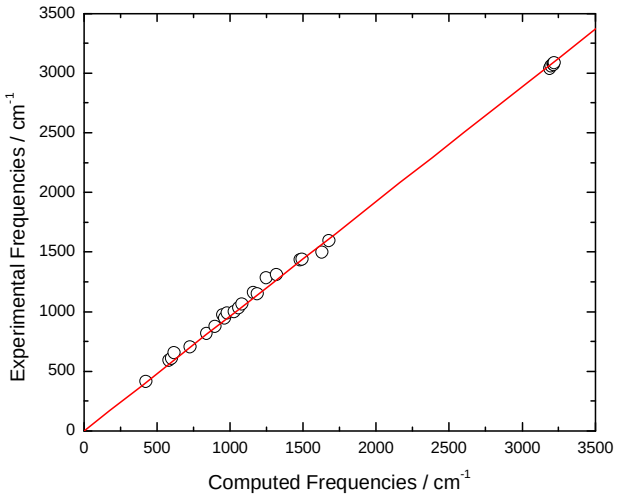

Figure 6.11. Linear plot of the experimental versus the unscaled QCISD/6-311G(d,p) vibrational frequencies of phenyl constrained to go through the origin.

The stretching frequency for HCl, ν_0, was found to be 2934 and 2908 cm^{-1} after the standard scaling with MPWB1K/MG3 and QCISD/6-311G(d,p) theories, respectively. These values correspond to overestimations of ν_0 of 0.6 kJ mol^{-1} and 0.3 kJ mol^{-1} when comparing to the literature value of 2885 cm^{-1},[183] and consequently the ZPEs are also overestimated by 0.3 kJ mol^{-1} (1.7%) with MPWB1K/MG3 theory and 0.1 kJ mol^{-1} (0.8%) with QCISD/6-311G(d,p) theory. We note that the optimal scaling factors for HCl are 0.941in the case of MPWB1K/MG3 theory, and 0.946 in the case of QCISD/6-311G(d,p) theory.

6.3.3.3. Reaction thermochemistry

Table 6.8 gives the total energy difference between the products and the reactants in kJ mol^{-1} at 0 K, $\Delta_r H_0$. This reaction enthalpy is the difference between the benzene C-H bond dissociation enthalpy ($BDE_0(C_6H_5\text{-}H)$) and the H-Cl bond dissociation enthalpy ($BDE_0(H\text{-}Cl)$), also tabulated. These enthalpy changes include a spin-orbit correction of -3.5 kJ mol^{-1} to the Cl atom.[60,141] Experimental values for these quantities are provided in the last row of Table 6.8 and conversions from 298 K to 0 K were made wherever necessary using the relation below.

$$\Delta_r H_0 = \Delta_r H_{298} - \sum_{prod}(H_{298} - H_0) + \sum_{reac}(H_{298} - H_0) \qquad (6.20)$$

MPWB1K and QCISD data and the results of several composite methods such as G3, G3B3, and CBS-QB3, applied to the reactants and products of reaction 6.2 as well as the H atom (in order to obtain the two respective BDEs), are shown. Literature values for some or all of the quantities of interest using two versions of the CcCA[189,190] method as well as two variants of G2 theory denoted G2M[140,191] are also compiled in Table 6.8. Further, the CCSD(T)/CBS and CCSD(T)/CBS-aug composite methods (along with the experimental spin-orbit correction for the Cl atom) described in section 3.2.4 were also used to assess the thermochemistry of reaction 6.2, and the results are given in Table 6.8. The various electronic energies used for the CBS extrapolations in CCSD(T)/CBS and CCSD(T)/CBS-aug are given in Table 6.9.

The possible impact of core-valence electron correlation and scalar relativistic effects on the bond strengths was also considered. CCSD(T)/cc-pwVTZ calculations made with the usual frozen-core approximation and with all electrons correlated indicate that inclusion of core-valence correlation changes the BDEs of C_6H_5-H and H-Cl by +0.6 and +0.9 kJ mol^{-1}, respectively. Mass-velocity and Darwin computations at the CISD/cc-pwVTZ level yield scalar relativistic corrections of -0.1 and -1.0 kJ mol^{-1}, respectively, to these bond strengths. Clearly

these are minor contributions, and they tend to cancel. The combined effect would be to change the enthalpy of formation of phenyl derived from the experimental value for benzene and the computed BDE by +0.5 kJ mol^{-1}.

The Δ_rH_0 value of -67.4 kJ mol^{-1} obtained with QCISD/6-311G(d,p) theory is in poor agreement with the value of -38.2 ± 2.5 kJ mol^{-1} obtained experimentally.[157] The BDE for the C-H bond in benzene is close to the experimental value, however, the BDE for HCl is in error by more than 30 kJ mol^{-1}. This is the major source of the discrepancy between the experimental and QCISD Δ_rH_0 values. As can be seen from figure 6.12, larger basis sets for HCl are more able to accommodate the polarity of this bond and the size difference between the two atoms. QCISD/cc-pVTZ and QCISD/cc-pVQZ theory yield 408.3 and 416.3 kJ mol^{-1}, respectively, for BDE_0(H-Cl). The inclusion of an additional tight d-function to Cl via the cc-pV(n+d)Z basis sets[122] seemed to have little effect, yielding 410.5 and 417.7 kJ mol^{-1} with n = T and Q, respectively. Extrapolation to the CBS limit yields 422.1 and 423.0 kJ mol^{-1} with the cc-pVnZ and cc-pV(n+d)Z basis sets, respectively, c.f. the experimental value of 427.648 ± 0.007 kJ mol^{-1} obtained from the Active Thermochemical Tables.[124]

Similar remarks can be seen to apply to the B3LYP functional, where enlarging the basis set improves the H-Cl BDE and the overall Δ_rH_0. With the more sophisticated MPWB1K functional, results with the MG3 basis set are improved over those from the small 6-31+G(d,p) basis set. The bond dissociation enthalpies for the two bonds in question obtained with the MPWB1K/MG3 method are both in good agreement with the experimental values for these quantities.[36] Because both of these values are slightly erroneous in the negative direction there is an ensuing fortuitous cancellation in Δ_rH_0, and the result of -38.2 kJ mol^{-1} is in excellent accord with experiment.

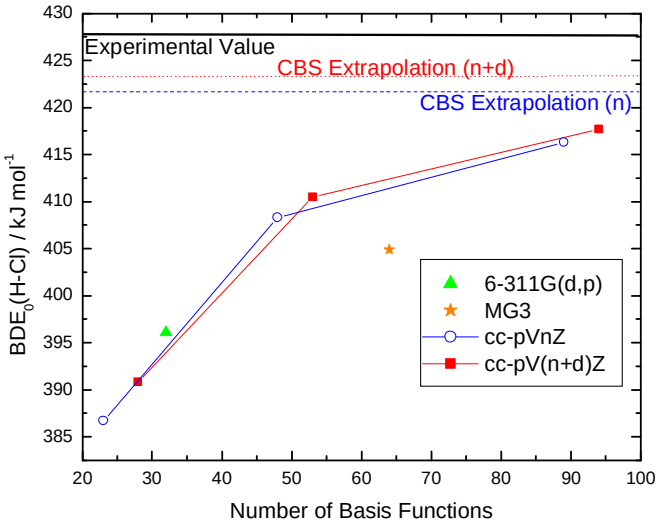

Figure 6.12. Effects of increasing the basis set size in a QCISD calculation for determining the bond strength of HCl.

The standard CBS-QB3 method[129] overestimates the H-Cl bond strength by ~ 5 kJ mol^{-1} and the C_6H_5-H bond strength by ~ 11 kJ mol^{-1}. Use of MPWB1K or QCISD geometries and ZPE corrections does not improve these results. Similarly, standard G3,[41] G3B3,[128] G3MP2,[39] G3MP2B3,[128] G3(MP2,CCSD)//B3LYP,[192] G3(CCSD)//B3LYP,[128] CBS-RAD,[193] and CcCA[189,190] approaches also overestimate $BDE_0(C_6H_5\text{-}H)$ significantly. Thus, it appears that composite methods relying on UHF reference wavefunctions, with the exception of G4,[194] cannot accurately compute the $BDE_0(C_6H_5\text{-}H)$. These normally accurate composite schemes may be impacted by the severe spin contamination in the phenyl radical, where the spin-unrestricted Hartree-Fock (UHF) wavefunction has an expectation value $\langle S^2 \rangle = 1.39$ rather than the ideal value of 0.75. Spin polarization effects arise in open-shell systems when the spatial component of the wavefunction is allowed to be different for α and β electrons. These effects lead to contamination of the doublet wavefunction, a phenomenon which has been reviewed by Bally

and Borden.[17] In general, large spin contamination has been found for systems where the singly occupied MO possesses nodes at some nuclei, and the subjacent doubly occupied bonding MO is high in energy and is easily polarized (typical of π-Mos), which certainly includes the phenyl radical.[17]

Unphysical UHF wavefunctions compromise composite methods where they are the basis for MP2, MP4, QCISD(T), and CCSD(T) correlation treatments. One solution is the use of spin-restricted open-shell Hartree-Fock (ROHF) wavefunctions, which eliminate spin contamination in the wavefunction. As can be seen from Table 6.8, using ROHF within the scheme of some of the composite methods yields much more accurate results. The modified ROCBS-QB3 method[195] agrees with the experimental value, as do G3(MP2)-RAD[196,197] and CcCA methods when based on ROHF wavefunctions. Moreover, because the three G3MP2-based methods tabulated form a chronological sequence of step-wise modifications to the original G3MP2 scheme, it can be systematically shown that the main factor necessary to accurately calculate $BDE_0(C_6H_5\text{-}H)$ is the implementation of ROHF reference wavefunctions. Replacement of the MP2(fu)/6-31G(d) geometries and HF/6-31G(d) ZPEs in G3MP2 by B3LYP/6-31G(d) analogs in G3MP2B3 improves $BDE_0(C_6H_5\text{-}H)$ by 2 kJ mol^{-1}, while replacing the UQCISD(T)/6-31G(d) single-point calculation with UCCSD(T)/6-31G(d) in G3(MP2,CCSD)//B3LYP marks an additional 1.2 kJ mol^{-1} improvement. However, the largest source of improvement, an additional 6.9 kJ mol^{-1}, comes from using ROMP2/6-31G(d) and URCCSD(T)/6-31G(d) single-point calculations in G3(MP2)-RAD, as opposed to the UHF-based analogs in G3(MP2,CCSD)//B3LYP. The CCSD(T)/CBS and CCSD(T)/CBS-aug data are close (0.3 kJ mol^{-1}) and compare well with the experimental values. Use of zero-point corrections from DFT improves the agreement further (see Table 6.8).

Lau and Ng have also used a CCSD(T)/CBS-type approach based on ROHF reference wavefunctions to calculate $\Delta_f H_0$ for the phenyl radical.[198] In their method, Lau and Ng used CCSD(T)/6-311G(2df,p) to calculate the geometry of the phenyl radical, followed by a two-point extrapolation to the CBS limit using CCSD(T) single point calculations with the cc-pVQZ and cc-pV5Z basis sets. Coupling the CBS energy with a core-valence correction obtained at the CCSD(T)/cc-pwCQZ level of theory, scalar relativistic effects calculated with CISD/cc-pVQZ, and anharmonic frequencies effectively obtained at the CCSD(T)/6-311G(2df,p) level of theory, Lau and Ng obtained $\Delta_f H_0$ = 351.4 kJ mol^{-1}.[198] More specifically, in the work of Lau and Ng, the effective CCSD(T)/6-311G(2df,p) frequencies were approximated by correcting the harmonic frequencies obtained at this level of theory with the average between the anharmonic effects obtained with MP2 and B3LYP theories, and the final zero-point virbrational energy (ZPVE) was estimated by averaging the harmonic and anharmonic ZPVEs. Combining their value for $\Delta_f H_0$ with the experimental $\Delta_f H_0$ values for the hydrogen atom (216.034 kJ mol^{-1})[124] and benzene (100.4 kJ mol^{-1})[199] yields $BDE_0(C_6H_5\text{-}H)$ of 467.0 kJ mol^{-1}, which is in reasonable agreement with the experimental value, and lies in between the values obtained with CCSD(T)/CBS with QCISD ZPEs and CCSD(T)/CBS with MPWB1K ZPEs in this work.

An alternative strategy for addressing spin-contamination is to use projection operators to remove higher spin contaminants from the wavefunction. This approach is employed in the G2M methodology, unfortunately with less success. The G2M values for the C-H bond strength in benzene are significantly higher than the experimental value, with G2M(rcc,MP2) overestimating this quantity by 13.7 kJ mol^{-1} and G2M(RCC,MP2) overestimating by 13.3 kJ mol^{-1} (see Table 6.8).

6.3.3.4. Chlorocyclohexadienyl Species

Five benzene/Cl atom complexes, not involved in the abstraction pathway, were found with MPWB1K/MG3 theory and are shown in figure 6.13, and their energies obtained with various theories are given in Table 6.10. These stationary points correspond to the five structures located by Tsao et al.[162] using BH&HLYP/6-311++G(d,p) theory and CASPT2(7,7)/6-31G(d) theory, and include σ and π η_1-chlorocyclohexadienyl radicals separated by a transition state, a C_{6v} η_6-chlorocyclohexadienyl complex, and an η_2-chorocyclohexadienyl transition state for Cl atom migration between two adjacent carbons.[162] The σ η_1-chlorocyclohexadienyl and η_2-chorocyclohexadienyl complexes have been examined with MP4SDQ/3-21G*//MP2/3-21G*by Jarzeba et al.,[200] and they found that the stabilization energy of the former is 31 ± 2 kJ mol^{-1} and that the latter is actually also a minimum with the level of theory they used, with a stabilization energy of 17 ± 2 kJ mol^{-1}. Sokolov et al.[156] used the BAC-MP4 *ab initio* method and found that the σ η_1-chlorocyclohexadienyl is exothermic in relation to benzene + Cl by 30 ± 10 kJ mol^{-1} at 298 K, a result that is in accord with the measurements of 33 and 30 ± 8 kJ mol^{-1} reported by Ritter et al.[201] and Benson et al.,[202] respectively. Berho et al.[203] have also calculated the stabilization energy at 298 K of the σ η_1-chlorocyclohexadienyl radical, and they obtained 30.1, 43.4, and 71.0 kJ mol^{-1} with the BAC-MP4, B3LYP/6-31G(d), and AM1 methods, respectively.

Like Tsao et al., we find that a complex of the η_1 type is lower in energy than the η_6 complex, which is not a minimum because it was found to possess two imaginary frequencies in their work and one here. Unlike Tsao et al., however, we found using MPWB1K/MG3 theory that the η_1-chlorocyclohexadienyl σ adduct is more stable than its π analog, though this difference was only 3.3 kJ mol^{-1}. It was also found that formation of the η_1-

chlorocyclohexadienyl π adduct from benzene + Cl is barrierless. Croft et al. have explored the reliability of a variety of functionals in a recent study that focused on the two η_1-chlorocyclohexadienyl complexes, and based on comparison with results they obtained from G3X(MP2)-RAD[204] calculations, they concluded that while BH&HLYP and a number of other functionals "should be regarded critically" for benzene/Cl atom complexes, MPWB1K calculations perform accurately but "require a large basis set to be reliable."[205] Furthermore, they found that the σ η_1-chlorocyclohexadienyl radical is 8.0 and 7.1 kJ mol^{-1} more stable than the π radical, based on results obtained with the G3X(MP2,MPWB1K)-RAD and G3X(MP2,MPW1K)-RAD composite methods, respectively.[205] These two variants of the G3X(MP2)-RAD method devised by Croft et al., implemented MPWB1K/6-31+G(d) or MPW1K/6-31+G(d) theories for the geometry optimizations and ZPEs (appropriately scaled), while retaining all of the other features of the G3(MP2)-RAD method, including unmodified HLCs. The stabilization energies (D_0) relative to C_6H_6 + Cl obtained by the G3X(MP2,MPWB1K)-RAD and G3X(MP2,MPW1K)-RAD composite methods were 29.0 kJ mol^{-1} with both for the π adduct, and 37.0 and 36.1 kJ mol^{-1} respectively, for the σ adduct, however, they note that "neither species can be ruled out as the experimentally active complex from these calculations alone," as the stabilization energies of both species "fall within the range predicted from experiment of 30-35 kJ mol^{-1} when uncertainty of the results are included."[205]

Application of QCISD/6-311G(d,p) theory did not yield the η_6 or the η_2 complexes, although, it did find the two η_1-chlorocyclohexadienyl adducts and the transition state between them (see Fig. 6.13), and at this level of theory, the η_1-chlrocyclohexadienyl σ adduct is more stable than the π analog by 17.4 kJ mol^{-1} at 0 K. At the highest level of theory used in this work,

denoted as CCSD(T)/CBS, it was found that the σ η_1-chlorocyclohexadienyl radical is more stable than the π radical by 9.0 kJ mol^{-1} at 0 K and 10.7 kJ mol^{-1} at 298 K (see Table 6.10).

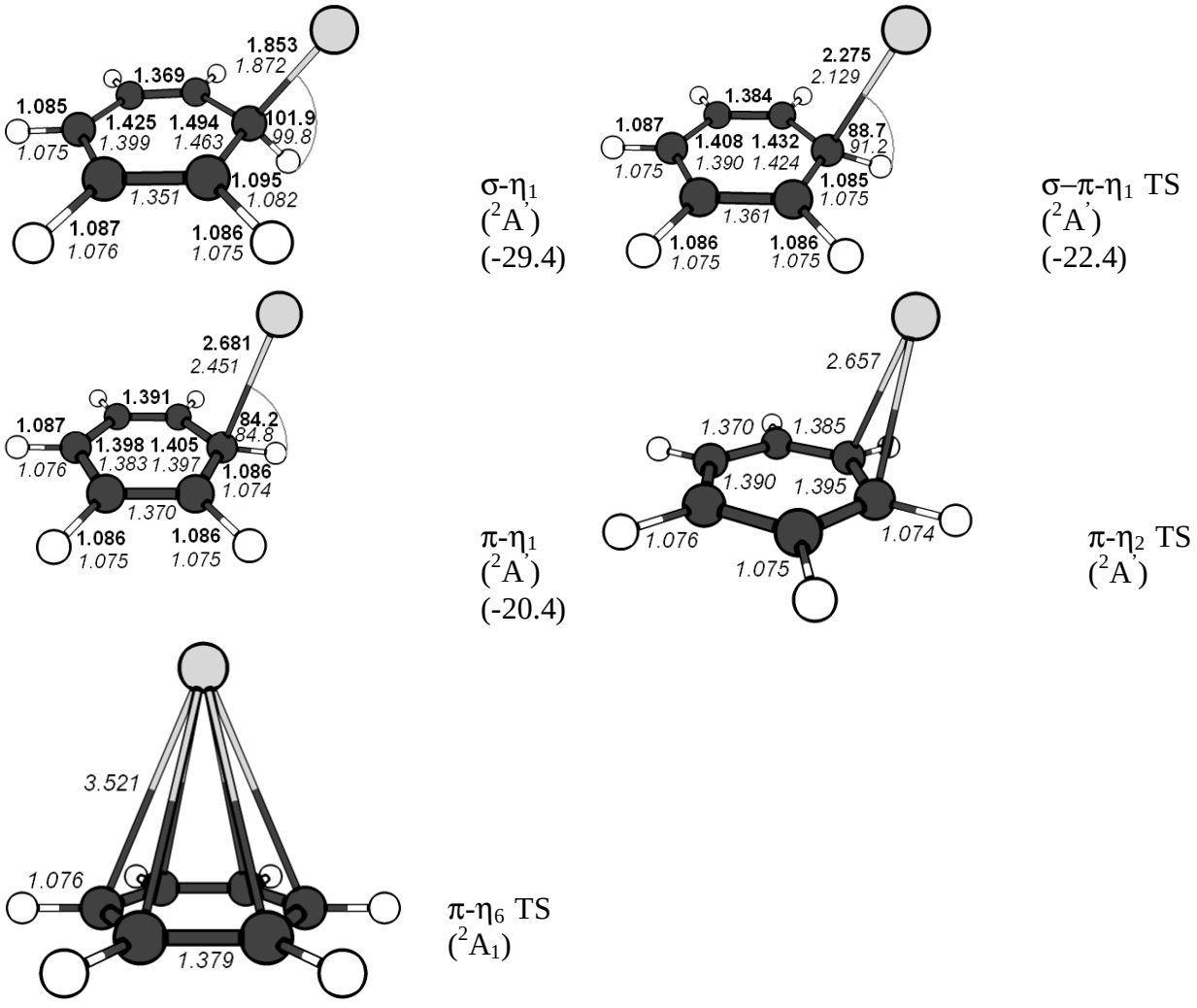

Figure 6.13. Chlorocyclohexadienyl structures. Bold values indicate QCISD/6-311G(d,p) theory and italicized values correspond to MPWB1K/MG3 theory. Values in parentheses represent CCSD(T)/CBS enthalpies in kJ mol^{-1} at 0 K relative to Cl + C_6H_6.

Furthermore, it was found that the transition state between two η_1-chlorocyclohexadienyl adducts is 2.0 kJ mol^{-1} and 5.2 kJ mol^{-1} lower in energy than the π η_1-chlorocyclohexadienyl radical at 0 K and 298 K, respectively, indicating that the π η_1-chlorocyclohexadienyl may not be an isolable species. These results confirm that the σ chlorocyclohexadienyl radical is the

most stable species, and is bound by 29.4 kJ mol^{-1} relative to Cl + C_6H_6 at 0 K and 31.3 kJ mol^{-1} at 298 K. This result quantitatively supports recent assignments of ca. 30 kJ mol^{-1} to the 298 K Cl-C_6H_6 bond dissociation enthalpy.[201,202] The weak bonding means that the adduct could be stable with respect to dissociation to Cl + C_6H_6 only at around room temperature or below. The σ adduct could therefore play a role in low temperature Cl + C_6H_6 kinetics, but it appears not to lie directly along the Ph + HCl reaction path.

6.3.3.5. Potential Energy Surface for C_6H_5 + HCl → C_6H_6 + Cl

Figures 6.14 and 6.15 depict potential energy diagrams obtained with the two respective levels of theory relative to the energy of the reactants, and, in addition to the classical energy profile, a second profile has been superimposed on the same axes in which the total energies include the scaled ZPEs. Figure 6.15 also contains a third plot, of CCSD(T)/CBS data.

A relaxed scan calculation shows that the conversion of the original Ph-HCl C_{2v} species to the π-Ph-HCl adduct is barrierless, and the C_{2v} species is interpreted as a transition state for motion of the HCl fragment from one face of the phenyl ring to the other. Similarly, it was found that the C_{2v} TS can rearrange to yield the Ph-HCl C_{2v} species without encountering a barrier, indicating that there is at least one path along the PES that connects the C_{2v} TS to the π-Ph-HCl adduct with a monotonic decrease in energy.

The B3LYP functional was unable to locate several of these stationary points (including the abstraction transition state). The inability of B3LYP to locate weak non-covalent complexes has been highlighted in recent literature and has been attributed to deficiencies of this functional in the description of long-range interactions such as dispersion.[43,162,205]

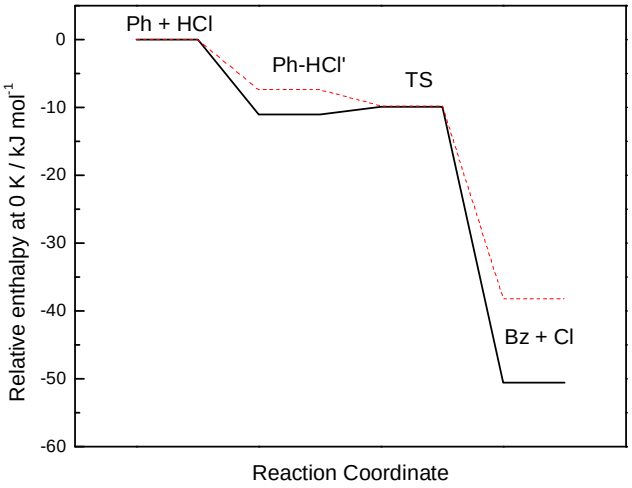

Figure 6.14. P.E. diagram for reaction 6.1 obtained with MPWB1K/MG3 theory. The solid line corresponds to the classical energies, and the dotted line represents the PES including scaled ZPEs and the spin-orbit correction for the Cl atom.

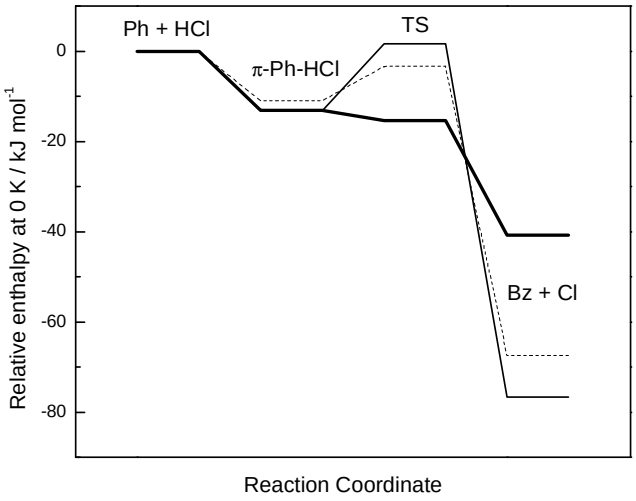

Figure 6.15. P.E. diagram for reaction 6.1 obtained with QCISD/6-311G(d,p) theory. The solid line corresponds to the classical energies, and the dotted line represents the PES including scaled ZPEs and the spin-orbit correction for the Cl atom. The bold line represents CCSD(T)/CBS results including QCISD/6-311G(d,p) ZPEs (see text).

6.3.3.6. Kinetic Analysis of the C_6H_6Cl Reaction System

Modified transition state theory (MTST), briefly outlined in chapter 3 and fully described elsewhere,[76] has been applied to the CCSD(T)/CBS data for reaction 6.2 by Dr. Lev Krasnoperov.[206,207] The MTST calculations take account of tunneling via an inverted parabola analysis,[76] which yielded correction factors of 1.3 and 1.02 at 298 and 1000 K, respectively.[206,207] As discussed in chapters 3 and 5, cases in which the energy of the TS lies below that of the reactants are inadequately treated by conventional TST, which overestimates the rate constant because it includes contributions from states of the TS which lie below the energy of the reactants. Though these states would eventually become populated at extremely high pressures, they are inaccessible under normal conditions and should therefore not be counted. Consequently, reaction systems characterized by such PESs are better accommodated by MTST, in which the energy levels of TS below those of the reactants are not counted, resulting in a more reasonable upper limit for the thermal rate constant.

The MTST results for reaction 6.2 are depicted in Arrhenius form in Figure 6.16. From this figure, it can be seen that MTST overestimates k_2 by a factor of ~5 over the overlapping temperature range between experiments and computations. The fact that the slopes of the observed and calculated k_2 data are nearly parallel suggests that the computed barrier height is reliable, indicating that the source of the disagreement may be the calculated partition function of the TS. A tighter TS would have a lower rotational partition function, and more importantly, a lower vibrational partition function, both of which would have the effect of reducing the MTST rate constant. In addition, the assignment of higher vibrational frequencies, in particular to the lowest internal modes, would also reduce the number of accessible states in the TS, which would further decrease the rate constant. The kinetic isotope effect $k_2(HCl)/k_{2b}(DCl)$ calculated via

MTST at 298 and 500 K is 2.8 and 2.3, respectively, which are only in qualitative accord with the experimental values obtained from expressions 6.14 and 6.15 of 1.7 ± 0.1 and 1.6 ± 0.1 at the two respective temperatures. However, even if just qualitatively, the calculations reinforce the claim of a hydrogen-abstraction mechanism since the kinetic isotope effect is larger than 1. Moreover, any errors in the calculation of the kinetic isotope effect would tend to cancel, which further indicates that perhaps there may be problems with the lowest internal modes in the TS or their treatment as harmonic oscillators.

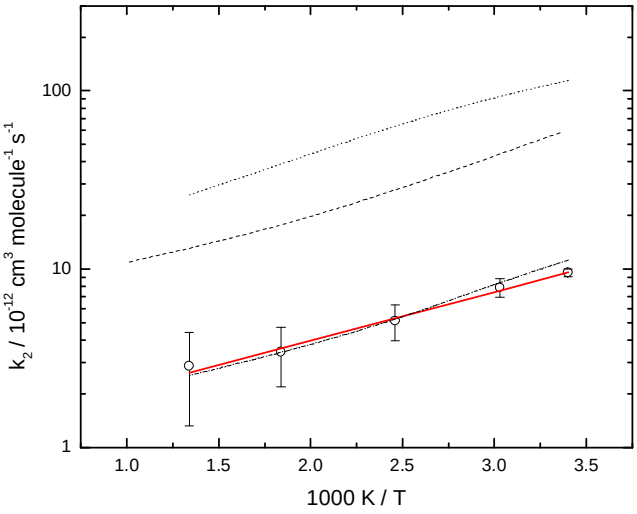

Figure 6.16. Arrhenius plot of C_6H_5 + HCl rate constants. Solid line: experiment, ref. [157]; dashed line: modified TST, ref. [206,207]; dotted line: RRKM based on hindered Gorin-type TS with hindrance fitted to match hard sphere rate constants (see text); dash-dott line: RRKM based on hindered Gorin-type TS with hindrance fitted to match experimental $k_2(T)$ (see text).

MultiWell-based RRKM calculations have also been carried out for reaction 6.2 based on the CCSD(T)/CBS data, at a constant pressure of 0.1 bar. The hindered Gorin model[66,100,101] described in chapter 3 was used to obtain and fit the properties of the loose TS at the entrance channel to the hard sphere collision rate constants calculated for this system (Table 6.11). The

hindrance parameters arising from the steric interactions between the two molecular fragments are given in Table 6.10. The corresponding Morse parameters used for π-Ph-HCl were r_e = 3.773 Å, υ_e = 66.0 cm^{-1}, and D_e = 15.3 kJ mol^{-1}. The results of this procedure are also given in Table 6.11 and shown in Figure 6.16. Wigner tunneling corrections, previously described in chapter 5, have been applied to the RRKM results in Figure 6.16, and the values of these tunneling corrections as well as of the RRKM rate constants are also found in Table 6.11. Lennard-Jones and energy transfer parameters were calculated following the methodology set forth in chapter 3. As usual, sample input files may be found in Appendix D.

As can be seen in Figure 6.16, the RRKM results overestimate the experimental results by about an order of magnitude over the entire overlapping temperature range. The fact that the high-pressure limiting k_a values from RRKM are in good agreement with the original k_a values from the hard-sphere model $k_{a(HS)}$ suggests that the equilibrium constants used to get the recombination rate constants from the unimolecular constants via equation 3.32 at each temperature are reasonable. Therefore, the failure of RRKM theory in the present case can likely be attributed to the probable overestimation of $k_a(T)$ by $k_{a(HS)}(T)$, which is crucial in the selection of reliable hindrance parameters from which the sum of states of the loose Gorin-type TS can be accurately calculated.

Generally, the rate constants used for fitting in the hindered Gorin TS analysis are those for the high-pressure limiting recombination at the desired temperatures. In the present case, however, since k_2 was found to be independent of pressure over the pressure range used in our experiments, the values of k_2 were used to approximate the high-pressure limiting recombination rate constants at each temperature in a second hindered Gorin-type TS analysis. This assumption was found to be valid, as the ratio of the experimental k_2 to the calculated $k_{a,\infty}$ was between 0.94

– 1.04 over the temperature range considered, indicating that the formation of the π-Ph-HCl essentially is at the high-pressure limit under the experimental conditions used. The results of this alternative analysis are also given in Table 6.11 and depicted in figure 6.16, and as can be seen, they agree quite well with the measured $k_2(T)$. These findings serve as evidence that the original $k_{a(HS)}$ values were too large.

6.4. Conclusions

Results for the reaction of phenyl with HCl have been presented for the first time in this work, and both experiments and computations indicate that this process is barrierless. The recommended rate constant for Cl + benzene was derived from high-temperature measurements in combination with the most recent and what is believed to be the most accurate literature data at room temperature. An abstraction mechanism is supported by the kinetic isotope effects observed in both the forward and reverse directions. A third law analysis of the equilibrium constant yielded thermochemical results that have been found to be consistent with other recent determinations.

Investigations of the PES using hybrid DFT and *ab initio* methods agree with negative barrier for the reaction of the phenyl radical with HCl. Although both computational methods have found the reaction of Cl and benzene to be endothermic, the hybrid DFT method gave remarkable agreement with experiment while the QCISD/6-311G(d,p) level of theory was in error by almost 30 kJ mol^{-1} due to severe underestimation of the bond strength of HCl. A C_s geometry seems to be favored over C_{2v} by both adducts located with both theories, however, this symmetry lowerings do not conclusively lead to increased stabilization. The CCSD(T)/CBS and CCSD(T)/CBS-aug composite methods yielded reaction enthalpies that were in good agreement

with experiment, demonstrating that these methods are capable of accurately treating severely spin-contaminated species. The σ chlorocyclohexadienyl radical was found to be the most stable among chlorocyclohexadienyl species, but because it is weakly bound, this adduct could be stable with respect to dissociation to Cl + C_6H_6 only at around room temperature or below.

MTST calculations overestimate $k_2(T)$ which could be the result of an exaggerated partition function for the TS caused by the treatment of small internal modes as harmonic oscillators. However, these MTST calculations support the small kinetic isotope effects observed for reaction 6.2, suggesting that a simple H-abstraction mechanism is plausible. RRKM calculations of $k_2(T)$ based on a hindered Gorin treatment of the loose TS at the entrance channel are in good agreement with experiment if the hindrance parameters are selected to match the experimental $k_2(T)$, and also seem to reveal that the rate constant for the formation of the π-Ph-HCl adduct has reached its high-pressure limit at the experimental conditions used in this study.

Table 6.1. Summary of measurements of the rate constant k_1 for Cl + C_6H_6.

T, K	τ_{res}, s	F, mJ	p, mbar	$[CCl_4]$, 10^{15} molecule cm^{-3}	$[C_6H_6]_{max}$, 10^{15} molecule cm^{-3}	$[Cl]_0$, 10^{12} molecule cm^{-3}	$k_1 \pm \sigma_{k1}$, 10^{-13} cm^3 $molecule^{-1}$ s^{-1}
579	1.0	0.26	70	2.40	5.31 ± 0.18	0.9	2.16 ± 0.06
578	1.0	0.24	71	1.48	1.36 ± 0.05	0.5	2.20 ± 0.18
578	1.0	0.16	71	1.48	1.36 ± 0.06	0.3	1.91 ± 0.11
577	1.1	0.21	145	1.63	1.12 ± 0.02	0.5	2.02 ± 0.10
578[a]							**1.49 ± 0.10[b]**
622	0.9	0.44	67	2.00	1.87 ± 0.06	1.4	3.26 ± 0.25
622	0.9	0.19	67	2.00	1.87 ± 0.06	0.6	2.70 ± 0.10
621	0.9	0.19	69	2.05	1.92 ± 0.07	0.6	2.13 ± 0.07
621	0.9	0.06	69	2.05	1.92 ± 0.07	0.2	1.90 ± 0.08
619	0.5	0.09	71	1.21	1.64 ± 0.05	0.2	1.60 ± 0.08
623	0.9	0.35	70	2.02	2.96 ± 0.10	1.0	1.99 ± 0.12
623	0.9	0.16	70	2.02	2.96 ± 0.06	0.5	1.70 ± 0.06
622	2.0	0.33	145	2.62	3.25 ± 0.11	1.2	2.00 ± 0.31
622	2.0	0.13	145	2.62	3.25 ± 0.07	0.5	1.78 ± 0.32
622[a]							**1.60 ± 0.26[b]**
676	0.4	0.33	29	0.88	1.66 ± 0.06	0.5	2.61 ± 0.18
676	0.4	0.14	29	0.88	1.66 ± 0.06	0.2	2.35 ± 0.15
677	0.9	0.21	70	1.23	2.69 ± 0.09	0.5	2.79 ± 0.36
677	0.9	0.14	70	1.23	2.69 ± 0.07	0.3	2.75 ± 0.23
674	0.5	0.17	69	1.21	1.31 ± 0.03	0.3	2.71 ± 0.07
674	0.5	0.11	69	1.21	1.31 ± 0.03	0.2	2.77 ± 0.09
676[a]							**2.76 ± 0.19[b]**
725	1.2	0.53	76	2.59	1.96 ± 0.09	2.0	5.66 ± 0.32
725	0.9	0.74	77	1.94	2.03 ± 0.07	2.1	6.07 ± 0.21
725	0.9	0.50	77	1.94	2.03 ± 0.07	1.4	5.10 ± 0.23
725	0.9	0.34	77	1.94	2.03 ± 0.07	0.9	4.60 ± 0.10
722	1.0	0.34	152	1.41	2.33 ± 0.06	0.8	4.09 ± 0.23
722	1.0	0.23	152	1.41	2.33 ± 0.06	0.5	3.83 ± 0.16
722	1.0	0.15	152	1.41	2.33 ± 0.06	0.3	3.80 ± 0.10
724[a]							**3.14 ± 0.16[b]**

(Table continues on next page)

(Table 6.1. Continued)

T, K	τ_{res}, s	F, mJ	p, mbar	$[CCl_4]$, 10^{15} molecule cm^{-3}	$[C_6H_6]_{max}$, 10^{15} molecule cm^{-3}	$[Cl]_0$, 10^{12} molecule cm^{-3}	$k_1 \pm \sigma_{k1}$, 10^{-13} cm^3 $molecule^{-1}$ s^{-1}
922	0.4	0.99	41	d	0.57 ± 0.02		7.84 ± 0.57
922	0.4	0.46	41	d	0.57 ± 0.02		5.75 ± 0.59
922	0.4	0.60	41	d	0.94 ± 0.05		2.70 ± 0.55
922	0.4	0.28	41	d	0.94 ± 0.05		2.58 ± 0.56
921	0.4	0.83	43	d	0.48 ± 0.02		6.77 ± 1.65
921	0.4	0.38	43	d	0.48 ± 0.02		4.73 ± 0.40
922[a]							**5.06 ± 2.14[c]**

[a] Average temperature. [b] Extrapolation to zero F. [c] Mean value. [d] NaCl used as source rather than CCl_4.

Table 6.2. Summary of measurements of the rate constant k_{1b} for Cl + C_6D_6.

T, K	τ_{res}, s	F, mJ	p, mbar	$[CCl_4]$, 10^{15} molecule cm^{-3}	$[C_6D_6]_{max}$, 10^{15} molecule cm^{-3}	$[Cl]_0$, 10^{12} molecule cm^{-3}	$k_{1b} \pm \sigma_{k1b}$, 10^{-13} cm^3 $molecule^{-1}$ s^{-1}
635	0.9	0.74	71	2.54	2.34 ± 0.08	2.7	2.11 ± 0.14
635	0.9	0.35	71	2.54	2.34 ± 0.08	1.4	1.48 ± 0.17
635	0.9	0.22	69	2.47	1.81 ± 0.06	0.8	1.31 ± 0.07
635	0.9	0.16	69	2.47	1.81 ± 0.06	0.6	1.06 ± 0.06
635[a]							**0.82 ± 0.08[b]**
922	0.4	0.55	42	c	0.62 ± 0.02		6.06 ± 0.52
922	0.4	0.26	42	c	0.62 ± 0.02		5.52 ± 0.19
923	0.4	0.37	42	c	0.68 ± 0.02		6.53 ± 0.92
923	0.4	0.17	42	c	0.68 ± 0.02		7.34 ± 0.75
922	0.4	0.75	44	c	0.36 ± 0.01		11.75 ± 0.46
922	0.4	0.40	44	c	0.36 ± 0.02		4.99 ± 0.53
921	0.3	0.72	41	c	0.25 ± 0.02		10.89 ± 1.08
923	0.3	1.03	40	c	0.21 ± 0.01		10.22 ± 1.28
923	0.3	0.76	40	c	0.21 ± 0.01		8.67 ± 1.09
922[a]							**3.18 ± 0.95[b]**

[a] Average temperature. [b] Extrapolation to zero F. [c] NaCl used as source rather than CCl_4.

Table 6.3. Summary of kinetic measurements in the C_6H_5 + HCl system.

T, K	τ_{res}, s	F, mJ	p, mbar	$[C_6H_5I]$, 10^{13} molecule cm^{-3}	$[HCl]_{max}$, 10^{15} molecule cm^{-3}	$[C_6H_5]_0$, 10^{12} molecule cm^{-3}	$k_{-1} \pm \sigma_{k-1}$, 10^{-12} cm^3 $molecule^{-1}$ s^{-1}	$(k_4' + k_5) \pm \sigma_{(k4'+k5)}$, s^{-1}	$k_6 \pm \sigma_{k6}$, 10^{-11} cm^3 $molecule^{-1}$ s^{-1}
294	1.2	0.27	50	1.18	1.00 ± 0.03	0.2	9.55 ± 1.15	306 ± 12	2.12 ± 0.07
294	1.2	0.40	51	1.62	0.67 ± 0.02	0.4	9.79 ± 0.77	319 ± 11	2.26 ± 0.07
294	0.6	0.49	25	1.37	0.22 ± 0.01	0.4	9.32 ± 0.69	309 ± 13	2.28 ± 0.14
294[a]							**9.55 ± 0.24**[b]		**2.22 ± 0.09**[b]
330	1.3	0.23	52	2.13	0.88 ± 0.04	0.3	7.53 ± 1.11	327 ± 83	1.19 ± 0.03
331	1.3	0.23	52	2.11	0.70 ± 0.03	0.3	7.87 ± 0.66	412 ± 73	1.19 ± 0.01
330	2.2	0.10	52	3.52	0.98 ± 0.06	0.2	8.67 ± 1.56	543 ± 50	0.71 ± 0.01
330	1.3	0.46	51	2.06	0.84 ± 0.04	0.6	7.82 ± 0.59	368 ± 83	1.22 ± 0.01
330	1.3	0.31	50	2.67	0.40 ± 0.02	0.5	7.51 ± 0.60	397 ± 61	1.11 ± 0.02
330[a]							**7.88 ± 0.47**[b]		**1.08 ± 0.21**[b]
407	1.8	0.36	52	3.00	1.21 ± 0.06	0.7	4.48 ± 0.10	353 ± 31	0.85 ± 0.01
407	1.8	0.17	52	2.98	1.21 ± 0.06	0.3	4.45 ± 0.12	367 ± 14	0.85 ± 0.01
406	1.0	0.29	50	1.64	1.06 ± 0.05	0.3	5.87 ± 0.61	247 ± 31	1.58 ± 0.03
407	1.1	0.34	52	1.70	1.10 ± 0.05	0.4	5.05 ± 1.15	245 ± 26	1.50 ± 0.02
407	1.0	0.22	51	1.65	1.02 ± 0.05	0.2	5.51 ± 0.35	222 ± 20	1.61 ± 0.05
407	1.0	0.18	51	1.67	0.75 ± 0.03	0.2	5.41 ± 0.39	242 ± 33	1.59 ± 0.03
407[a]							**5.13 ± 0.58**[b]		**1.33 ± 0.37**[b]

(Table continues on next page)

(Table 6.3. Continued)

T, K	τ_{res}, s	F, mJ	p, mbar	$[C_6H_5I]$, 10^{13} molecule cm^{-3}	$[HCl]_{max}$, 10^{15} molecule cm^{-3}	$[C_6H_5]_0$, 10^{12} molecule cm^{-3}	$k_{-1} \pm \sigma_{k-1}$, 10^{-12} cm^3 $molecule^{-1}$ s^{-1}	$(k_4' + k_5) \pm \sigma_{(k4'+k5)}$, s^{-1}	$k_6 \pm \sigma_{k6}$, 10^{-11} cm^3 $molecule^{-1}$ s^{-1}
545	1.0	0.85	51	0.63	0.55 ± 0.02	0.3	3.08 ± 0.35	106 ± 8	3.86 ± 1.49
545	1.0	0.62	51	0.63	0.55 ± 0.02	0.2	3.14 ± 0.41	104 ± 8	3.30 ± 3.21
542	0.6	0.72	51	0.34	0.47 ± 0.02	0.2	3.88 ± 0.28	97 ± 5	6.72 ± 3.38
545	1.0	0.65	51	1.13	0.41 ± 0.02	0.5	4.31 ± 0.76	62 ± 3	2.59 ± 1.92
544	1.0	0.37	49	0.61	0.53 ± 0.02	0.1	2.78 ± 0.25	172 ± 120	5.89 ± 0.73
544[a]							**3.44 ± 0.63[b]**		**4.47 ± 1.76[b]**
749	1.0	0.84	52	2.15	0.55 ± 0.03	1.1	3.43 ± 0.34	305 ± 56	1.25 ± 0.11
749	0.6	0.47	54	1.26	0.48 ± 0.02	0.4	3.32 ± 0.32	208 ± 55	2.00 ± 0.35
745	0.5	0.24	25	1.06	0.54 ± 0.03	0.2	1.87 ± 0.64	226 ± 64	2.79 ± 0.34
746	0.5	0.79	26	1.10	0.52 ± 0.02	0.6	4.12 ± 0.35	163 ± 31	2.95 ± 0.46
747	0.5	0.46	27	1.14	0.53 ± 0.03	0.3	3.10 ± 0.29	162 ± 41	2.26 ± 0.54
746	1.0	0.41	54	1.73	0.66 ± 0.03	0.4	1.80 ± 0.21	170 ± 42	1.81 ± 0.77
750	1.1	0.25	53	2.21	0.68 ± 0.02	0.3	2.73 ± 0.21	213 ± 56	2.13 ± 0.22
750	1.0	0.31	52	2.09	0.65 ± 0.02	0.4	2.23 ± 0.19	272 ± 47	2.03 ± 0.19
750	1.0	0.35	52	2.09	0.65 ± 0.02	0.5	3.14 ± 0.27	233 ± 38	2.27 ± 0.34
748[a]							**2.86 ± 0.77[b]**		**2.17 ± 0.50[b]**

[a] Average temperature. [b] Average rate constant.

Table 6.4. Summary of kinetic measurements in the C_6H_5 + DCl system.

T, K	τ_{res}, s	F, mJ	p, mbar	$[C_6H_5I]$, 10^{13} molecule cm^{-3}	$[DCl]_{max}$, 10^{15} molecule cm^{-3}	$[C_6H_5]_0$, 10^{12} molecule cm^{-3}	$k\text{-}_{1b} \pm \sigma_{k\text{-}1b}$, 10^{-12} cm^3 $molecule^{-1}$ s^{-1}	$(k_{4b}' + k_{5b}) \pm \sigma_{(k4b'+ k5b)}$, s^{-1}	$k_{6b} \pm \sigma_{k6b}$, 10^{-11} cm^3 $molecule^{-1}$ s^{-1}
292	0.7	0.64	25	2.44	0.35 ± 0.01	1.0	4.93 ± 1.73	345 ± 52	2.16 ± 0.02
292	0.7	0.36	25	2.44	0.35 ± 0.01	0.6	5.61 ± 1.58	329 ± 104	4.17 ± 0.03
292	0.9	0.45	25	2.50	0.26 ± 0.01	0.7	7.72 ± 0.76	432 ± 43	7.41 ± 0.04
292	0.9	0.32	25	2.51	0.26 ± 0.01	0.5	5.99 ± 1.12	441 ± 42	2.22 ± 0.01
292	0.7	0.59	25	2.38	0.40 ± 0.01	0.9	5.00 ± 0.75	513 ± 74	1.17 ± 0.01
292[a]							**5.85 ± 1.13**[b]		**3.43 ± 2.48**[b]
546	0.5	0.89	25	1.38	0.20 ± 0.01	0.8	2.19 ± 0.34	190 ± 18	2.82 ± 0.27
546	0.5	0.39	25	1.38	0.20 ± 0.01	0.3	2.46 ± 0.22	191 ± 15	3.01 ± 0.36
546	0.4	0.48	25	1.41	0.23 ± 0.01	0.4	2.19 ± 0.44	206 ± 9	3.50 ± 0.21
546[a]							**2.28 ± 0.16**[b]		**3.11 ± 0.35**[b]

[a] Average temperature. [b] Average rate constant

Table 6.5. Thermodynamic functions for C_6H_6 and C_6H_5.

	Benzene			Phenyl		
T, K	C_p, J K^{-1} mol^{-1}	S, J K^{-1} mol^{-1}	H_T-H_0, kJ mol^{-1}	C_p, J K^{-1} mol^{-1}	S, J K^{-1} mol^{-1}	H_T-H_0, kJ mol^{-1}
50	33.28	190.50	1.66	33.28	210.44	1.66
100	35.16	213.91	3.36	35.22	233.85	3.36
150	41.92	229.28	5.26	42.10	249.27	5.27
200	52.98	242.77	7.62	53.01	262.80	7.63
250	67.03	256.06	10.61	66.43	276.03	10.61
298.15	81.92	269.13	14.19	80.35	288.92	14.15
350	98.04	283.53	18.86	95.22	302.97	18.70
400	112.79	297.59	24.14	108.69	316.58	23.80
450	126.32	311.67	30.12	120.99	330.10	29.55
500	138.54	325.62	36.75	132.02	343.43	35.88
600	159.31	352.79	51.68	150.65	369.21	50.05
700	176.07	378.65	68.48	165.55	393.59	65.89
800	189.83	403.09	86.79	177.68	416.52	83.07
900	201.29	426.13	106.37	187.72	438.04	101.35
1000	210.95	447.85	126.99	196.14	458.27	120.56
1100	219.16	468.35	148.51	203.27	477.31	140.54
1200	226.18	487.73	170.78	209.34	495.26	161.18
1300	232.20	506.08	193.71	214.53	512.23	182.38
1400	237.39	523.48	217.20	219.00	528.30	204.06
1500	241.89	540.01	241.17	222.87	543.54	226.16
1600	245.79	555.75	265.55	226.22	558.03	248.61
1700	249.20	570.76	290.31	229.15	571.84	271.39
1800	252.19	585.09	315.38	231.70	585.01	294.43
1900	254.82	598.80	340.73	233.95	597.60	317.72
2000	257.13	611.93	366.33	235.94	609.65	341.21
2100	259.19	624.52	392.15	237.69	621.21	364.90
2200	261.01	636.62	418.16	239.26	632.30	388.75
2300	262.65	648.26	444.35	240.65	642.97	412.74
2400	264.10	659.47	470.69	241.90	653.24	436.87
2500	265.42	670.28	497.16	243.02	663.13	461.12
2600	266.60	680.71	523.77	244.03	672.68	485.47
2700	267.67	690.80	550.48	244.94	681.91	509.92
2800	268.63	700.55	577.30	245.76	690.83	534.46
2900	269.51	709.99	604.20	246.51	699.47	559.07
3000	270.32	719.14	631.20	247.20	707.84	583.76

Table 6.6. Experimental values for the enthalpy of formation of the phenyl radical at 298 K.

$\Delta_f H_{298}(C_6H_5)$ kJ mol^{-1}	Workers	Method
334.7 ± 4.2	Rodgers et al.[180] (1967)	Radical kinetics and thermochemistry
328.9 ± 8.4	McMillen et al.[181] (1982)	Critical Review
330.1 ± 3.3	Berkowitz et al.[177] (1994)	Review: Negative ion thermochemical cycles
339.4 ± 2.5	Davico et al.[158] (1995)	Negative ion photoelectron spectroscopy
338 ± 3	Heckmann et al.[159] (1996)	Third law analysis of Phenyl Equilibria data
337.1 ± 3	Ervin et al.[179] (2002)	Gas-phase acidity scale revision
337.0 ± 2.5	Alecu et al.[157] (2007)	LFP/RF and Third law analysis

Table 6.7. Energies and zero point energies in E_H for species on the PES of reaction 6.1.

	MPWB1K/MG3			QCISD/6-311G(d,p)		
Species	Electronic Energy	Unscaled ZPE	Total Energy[a]	Electronic Energy	Unscaled ZPE	Total Energy[a]
H	-0.49790	0	-0.49790	-0.49981	0	-0.49981
Cl	-460.21244	0	-460.21377	-459.60167	0	-459.60300
C_6H_6	-232.19111	0.10279	-232.09277	-231.61410	0.09957	-231.51911
HCl	-460.87977	0.00699	-460.87308	-460.26032	0.00695	-460.25369
C_6H_5	-231.50449	0.08948	-231.41888	-230.92624	0.08754	-230.84273
Bz-Cl	-692.40402	0.10305	-692.30676	-691.21657	0.09980	-691.12269
TS	-692.38805	0.09653	-692.29569	-691.18591	0.09247	-691.09769
Ph-HCl	-692.38837	0.09766	-692.29493	-691.19007	0.09546	-691.09900
Bz-Cl′	-692.40421	0.10328	-692.30673	N/A	N/A	N/A
Ph-HCl′	-692.38846	0.09792	-692.29478	N/A	N/A	N/A
π-Ph-HCl	-692.38892	0.09775	-692.29540	-691.19158	0.09539	-691.10058
Bz-HCl	-693.07608	0.11118	-692.96971	-691.87976	0.10737	-691.77733

[a] Energy was calculated by adding scaled ZPE to the electronic energy as well as a correction for Cl-atom spin-orbit coupling in the cases of Cl, Bz-Cl, and Bz-Cl′.

Table 6.8. Bond dissociation enthalpies and enthalpies of reaction for reaction 6.2 at 0 K (kJ mol^{-1}).

Method	$\Delta_r H_0$	$BDE_0(C_6H_5\text{-}H)$	$BDE_0(H\text{-}Cl)$
MPWB1K/MG3	-38.2	461.9	423.7
QCISD/6-311G(d,p)	-67.4	463.5	396.1
B3LYP/6-31G(d,p)	-60.1	457.1	397.0
B3LYP/6-311G(2d,d,p)	-40.2	456.7	416.5
MPWB1K/6-31+G(d,p)	-50.8	466.4	415.6
CBS-QB3	-44.1	476.7	432.6
[a]CBS-QB3//MPWB1K	-44.3	476.7	432.4
[b]CBS-QB3//QCISD	-48.0	480.6	432.6
[c]ROCBS-QB3	-36.0	467.0	431.0
G3	-45.5	472.7	427.2
G3B3	-46.1	472.1	426.0
G3MP2	-48.9	478.0	429.1
G3MP2B3	-47.1	476.0	428.9
[d]G2M(rcc,MP2)		482.0	
[d]G2M(RCC,MP2)		481.6	
CcCA_P	-49.0[e]	479.0[e]	430.0[e]
CcCA_P (ROHF)	-39.2[e]	468.9[e]	429.7[e]
CcCA_S4	-49.0[e]	479.0[e]	430.0[e]
CcCA_S4 (ROHF)	-39.2[e]	469.0[e]	429.8[e]
[f]CCSD(T)/CBS	-40.7	469.6	428.9
[f]CCSD(T)/CBS-aug	-41.0	469.6	428.6
[g]CCSD(T)/CBS	-37.6	466.3	428.7
[g]CCSD(T)/CBS-aug	-37.9	466.3	428.4
[h]G3(MP2,CCSD)//B3LYP	-45.2	474.8	429.5
[h]G3(CCSD)//B3LYP	-43.6	471.0	427.4
[i]G3(MP2)-RAD	-39.0	467.9	428.9
[j]G4	-39.0	465.0	426.0
[k]CBS-RAD	-44.9	476.6	431.7
Experimental Values	-38.2 ± 2.5[l]	465.9 ± 2.5[l]	427.648 ± 0.007[m]

[a] CBS-QB3 performed with MPWB1K/MG3 geometries and frequencies. [b] CBS-QB3 performed with QCISD/6-311G(d,p) geometries and frequencies. [c] Reference [195] [d] References[140,191]. [e] Provided by Dr. Nathan DeYonker. [f] See text. [g] ZPEs obtained with MPWB1K/MG3 theory were used. [h] Reference [192] [i] References [196,197] [j] Reference [194] [k] Reference [193] [l] Reference [157] [m] Reference[124]

Table 6.9. UCCSD(T)/ROHF energies in E_H for species on the PES of reaction 6.1.

Species	Electronic Energy (cc-pVTZ)	Electronic Energy (cc-pVQZ)	Electronic Energy (CBS)	Electronic Energy (aug-cc-pVTZ)	Electronic Energy (aug-cc-pVQZ)	Electronic Energy (aug-CBS)
Cl	-459.67178	-459.69327	-459.70895	-459.67619	-459.69471	-459.70822
C_6H_6	-231.80580	-231.87159	-231.91960	-231.82041	-231.87735	-231.91891
HCl	-460.33722	-460.36213	-460.38032	-460.34324	-460.36417	-460.37944
C_6H_5	-231.11753	-231.18210	-231.22921	-231.13196	-231.18780	-231.22855
Bz-Cl	N/A	N/A	N/A	N/A	N/A	N/A
TS	-691.45825	-691.54800	-691.61348	N/A	N/A	N/A
π-Ph-HCl	-691.46034	-691.54996	-691.61537	N/A	N/A	N/A
Bz-HCl	-692.14914	-692.23999	-692.30629	N/A	N/A	N/A

Table 6.10. Energies in E_H for chlorocyclohexadienyl species.

Species	MPWB1K/MG3 Electronic Energy	MPWB1K/MG3 Unscaled ZPE	MPWB1K/MG3 Total Energy[a]	QCISD/6-311G(d,p) Electronic Energy	QCISD/6-311G(d,p) Unscaled ZPE	QCISD/6-311G(d,p) Total Energy[a]	CCSD(T)/ cc-pVTZ Total Energy[b]	CCSD(T)/ cc-pVQZ Total Energy[b]	CCSD(T)/ CBS Total Energy[c]
σ-η_1	-692.41666	0.10254	-692.31856	-691.22337	0.10023	-691.12776	-691.48573	-691.57591	-691.64172
σ–π-η_1 TS	-692.41496	0.10234	-692.31705	-691.21674	0.10074	-691.12064	-691.48374	-691.57380	-691.63952
π-η_1	-692.41614	0.10331	-69231731	-691.21724	0.10074	-691.12113	-691.48460	-691.57374	-691.63879
π-η_2 TS	-692.41553	0.10347	-692.31654	N/A	N/A	N/A	N/A	N/A	N/A
π-η_6 TS	-692.40660	0.10294	-692.30812	N/A	N/A	N/A	N/A	N/A	N/A

[a] Energy was calculated by adding scaled ZPE to the electronic energy. [b] Single-point CCSD(T)/cc-pVnZ on QCISD/6-311G(d,p) geometries and ZPEs.
[c] Complete basis set extrapolation of CCSD(T)/cc-pVnZ (n = 3,4) single-point calculations on QCISD/6-311G(d,p) geometries and ZPEs (see text).

Table 6.11. Energy transfer parameters, loose Gorin-type transition state properties, and rate constants for the C_6H_6Cl reaction system.

T (K)	294	330	407	544	748
[a]r_{max} (Å)	7.28	7.16	6.94	6.62	6.27
[a]K-Rotor (amu Å^2)	171.1	171.1	171.1	171.1	171.1
Hindrance Parameter [b](γ)	0.066	0.059	0.047	0.037	0.034
Hindrance Parameter [b](η)	0.996	0.997	0.998	0.999	0.999
Hindrance Parameter [c](γ)	0.575	0.584	0.605	0.633	0.672
Hindrance Parameter [c](η)	0.669	0.659	0.634	0.600	0.549
[a]J-Rotor (amu Å^2)	1300.91	1257.84	1180.79	1076.43	964.23
[a]$\langle\Delta E\rangle_{down}$ (cm^{-1})	424.4	449.5	503.0	598.2	740.0
[a]c_2 (cm^{-1})	0.35	0.37	0.42	0.51	0.64
[d]K_c (cm^3 molec^{-1})	1.08E-21	7.37E-22	4.38E-22	2.92E-22	2.59E-22
$k_{a(HS)}$ (cm^3 molec^{-1} s^{-1})	5.68E-10	6.02E-10	6.68E-10	7.72E-10	9.06E-10
[b,e]$k_{\infty,uni}$ (s^{-1})	5.36E11	8.24E11	1.56E12	2.67E12	3.52E12
[b,f]$k_{\infty,a}$ (cm^3 molec^{-1} s^{-1})	5.80E-10	6.07E-10	6.83E-10	7.81E-10	9.11E-10
[b,g]k_2 (cm^3 molec^{-1} s^{-1})	9.06E-11	7.78E-11	5.66E-11	3.60E-11	2.51E-11
[c,e]$k_{\infty,uni}$ (s^{-1})	9.13E9	1.06E10	1.14E10	1.19E10	1.04E10
[c,f]$k_{\infty,a}$ (cm^3 molec^{-1} s^{-1})	9.89E-12	7.81E-12	4.99E-12	3.48E-12	2.69E-12
[c,g]k_2 (cm^3 molec^{-1} s^{-1})	8.84E-12	7.02E-12	4.53E-12	3.14E-12	2.43E-12
Wigner Tunneling correction	1.26	1.21	1.14	1.08	1.04

[a] Same for both sets of hindered Gorin-TS calculations.
[b] From fitting to hard-sphere rate constants.
[c] From fitting to experimental k_2 rate constants.
[d] Equilibrium constant for $C_6H_5 + HCl = \pi$-Ph-HCl.
[e] Rate constant for π-Ph-HCl = $C_6H_5 + HCl$.
[f] Rate constant for $C_6H_5 + HCl = \pi$-Ph-HCl.
[g] Do not include Wigner correction for tunneling.

CHAPTER 7

THE REACTION BETWEEN ETHYLENE AND ATOMIC CHLORINE

7.1. Introduction

The loss of chlorine atoms and non-methane hydrocarbons such as ethylene in the atmosphere can have significant effects, such as a reduced destruction of the stratospheric ozone layer.[13] The release of Cl atoms during combustion processes, such as the incineration of chlorinated hydrocarbons and fuel contaminants, provide an additional set of conditions under which these free radicals can interact with hydrocarbons.[14,15]

Due to its atmospheric and combustive importance, the reaction between atomic chlorine and ethylene has received appreciable attention. At low temperatures, Cl is primarily lost through reaction 7.1, the addition to ethylene to form the β-chloroethyl radical (CH_2CH_2Cl).[152,208-216]

$$Cl + C_2H_4 \xrightarrow{k_1} C_2H_4Cl \qquad (7.1)$$

Reaction 7.1 is the reverse recombination reaction for the unimolecular dissociation of the β-chloroethyl radical, and its observed pressure dependence has been interpreted in terms of the Lindemann-Hinshelwood mechanistic scheme:

$$Cl + C_2H_4 \longrightarrow C_2H_4Cl^* \qquad (7.2)$$

$$C_2H_4Cl^* \longrightarrow Cl + C_2H_4 \qquad (7.3)$$

$$C_2H_4Cl^* + M \longrightarrow C_2H_4Cl + M \quad (7.4)$$

Within this context, the initially excited chloroethyl adduct, denoted by *, can either dissociate back to the reactants or become stabilized via collisions with a third body M. As explained in chapter 3, recombination reactions such as these can be physically interpreted through the employment of Troe's empirical formalism.[72,73] According to this treatment, fitting the observed rate constant to equation 7.5

$$k_{rec} = \left(\frac{k_0[M]}{1 + k_0[M]/k_\infty} \right) F_{cent}^{\left\{1+[\log_{10}(k_0[M]/k_\infty)/(0.75-1.27\log_{10}F_{cent})]^2\right\}^{-1}} \quad (7.5)$$

yields the physically meaningful rate constants k_0 and k_∞, which are the low- and high-pressure limiting rate constants, respectively. F_{cent} is an empirical broadening parameter necessary for the proper description of the fall-off region. In our experiments, Ar was used as M, and k_0 and k_∞ have third and second-order units, respectively.

At higher temperatures, the dissociation of the β-chloroethyl radical back to Cl and ethylene becomes increasingly favored due to the exothermic equilibrium. In fact, this dissociation step becomes so dominant at temperatures exceeding 500 K that reaction 7.1 is no longer important in the consumption of Cl atoms. Instead, it is believed that at such elevated temperatures, the dominant process through which Cl is lost is H-atom abstraction.[217] The abstraction reaction pathway, which is clearly important at combustion temperatures, has also been the subject of several kinetic investigations.[209,217-221]

Combining the addition and abstraction rate constants with those measured for their respective reverse processes has enabled the determination of useful thermochemical information such as the heats of formation of the β-chloroethyl and vinyl radicals.[209,217-220,222,223] The thermochemistry of the C_2H_4Cl system has also been investigated computationally using *ab*

initio and DFT theories.[166,223-230] Furthermore, the kinetics of reaction 7.1 and its reverse have also been modeled using the potential energy surfaces obtained from computations.[223,231]

In this work, kinetic measurements of the absolute rate constants for the addition and abstraction reactions of C_2H_4 + Cl are presented over the wide temperature range of 292 – 1058 K. The study of the addition process at moderate temperatures also allowed for the direct measurement of the rate constant of its reverse dissociation process, enabling the determination of the equilibrium constant and thus the thermochemistry using a Third-Law procedure.[165] Low-pressure limiting rate constants have been obtained and expressed as a function of temperature over the range of 293 – 431 K. High level *ab initio* computations have been carried out in order to explore the potential energy surface and thermochemistry of the C_2H_4Cl system, and subsequent RRKM calculations have been carried out using the MultiWell program suite[85,86] to rationalize the PES.

7.2. Methodology

7.2.1. Experimental Method

The laser flash photolysis – resonance fluorescence (LFP – RF) technique was employed to generate chlorine atoms and monitor their fluorescence intensity I_f as a function of time. Atomic Cl was produced from the photolysis of CCl_4 at 193 nm over the temperature range of 292 – 346 K. In order to assess whether absorption of 193 nm radiation by C_2H_4 had an impact on the observed kinetics, Cl atoms were also generated by photolyzing SO_2Cl_2 at 248 nm over the temperature range of 296 – 378 K. At higher temperatures, it was found that both CCl_4 and SO_2Cl_2 were inefficient sources of Cl atoms, possibly due to thermal decomposition[157,163,232], and Cl atoms were instead generated via pulsed laser photolysis of C_6H_5Cl using 193 nm radiation.[233]

This precursor was also utilized at low temperatures to check against the data obtained with CCl_4 and SO_2Cl_2. Further details regarding the experimental technique and the apparatus for LFP – RF can be found in chapter 2.

The absorption cross-sections of CCl_4 ($8.6 \pm 0.5 \times 10^{-19}$ cm^2)[26], SO_2Cl_2 ($2.40 \pm 0.30 \times 10^{-19}$ cm^2)[234], and C_6H_5Cl ($9.62 \pm 0.14 \times 10^{-18}$ cm^2)[233] were used in combination with other experimental parameters such as the precursor concentrations, the photolysis energy F, and the beam cross section of approximately 7×8 mm^2 to estimate the initial atomic concentration $[Cl]_0$ following the procedure outlined in chapter 2. The quantum yield for Cl-atom formation from the photo-dissociation of SO_2Cl_2 was assumed to be ~ 2, resulting in an estimation of the upper bound to $[Cl]_0$. The Cl quantum yields of CCl_4 and C_6H_5Cl are known from experiments, and are 1.5 ± 0.1 and 1, respectively.[26,235,236] Finally, in order to account for the loss of photon intensity at the reactor entry window, the $[Cl]_0$ was corrected by a measured factor of $F^*/F = 0.63$, which was obtained as described in section 2.5.2. Unlike the 0.84 factor obtained in section 2.5.2 and in chapter 4, which was based on only a single measurement made by Dr. Yide Gao,[30] the 0.63 ± 0.13 correction factor reported here is the average of fifty five measurements, which are included in Tables 7.3 and 7.6. This correction factor was found to decrease between experiments conducted on successive days, which led to the hypothesis that perhaps trace amounts of UV-light-absorbing dirt was depositing on the windows, in spite of the efforts undertaken to prevent this through the circulation of Ar near the windows. Cleaning the windows more frequently did in fact reduce the fractional loss of laser radiation, and as a result, the normal experimental procedure was amended to include the cleaning of the windows before each experiment as opposed to just weekly.

Low photon intensities were employed to isolate the primary reaction from potential secondary processes involving photolysis fragments of C_2H_4 and/or any of the Cl-atom precursors. Any potential H-atom radiation at 121.6 nm was blocked through the use of calcium fluoride windows, and no signal was detected from the photolysis of C_2H_4 by itself. Lastly, the average gas residence time inside the reactor τ_{res} was varied in order to check for any thermal decomposition or mixing effects.

At room temperature, Cl is primarily consumed via reaction 7.1, diffusion, and any secondary chemistry. As usual, the method of flooding was used to satisfy the pseudo-first order condition of $[C_2H_4]>>[Cl]$. As shown in equation 7.6, the pseudo-first order approximation enables the combination of the second order rate constant and the rate constant for Cl-atom loss via diffusion and secondary chemistry into a single decay coefficient k_{ps1}, which can be obtained directly from fitting to the fluorescence intensity temporal profiles as described in chapter 2.

$$d[Cl]/dt = - k_1[C_2H_4][Cl] - k_8[Cl] = - k_{ps1}[Cl] \quad (7.6)$$

An example of an exponential decay of the fluorescence signal is shown as the inset in Figure 7.1. According to equation 7.6, plotting k_{ps1} vs. $[C_2H_4]$ should result in a line with slope k_1, as illustrated in Figure 7.1. The intercept in Figure 7.1 corresponds to the rate constant of Cl-atom loss in the absence of C_2H_4, k_8, which was observed to be effectively first order and is attributed to diffusion and potential secondary chemistry. Typically, each determination of k_1 relied on five concentrations of $[C_2H_4]$, ranging from zero to $[C_2H_4]_{max}$, with the lowest non-zero $[C_2H_4]$ being equal to approximately one fourth of $[C_2H_4]_{max}$. The average non-zero room temperature $[C_2H_4]_{avg}$ / $[Cl]_0$ ratios were 74, 107, and 70 in the cases of CCl_4, SO_2Cl_2, and C_6H_5Cl precursors, respectively.

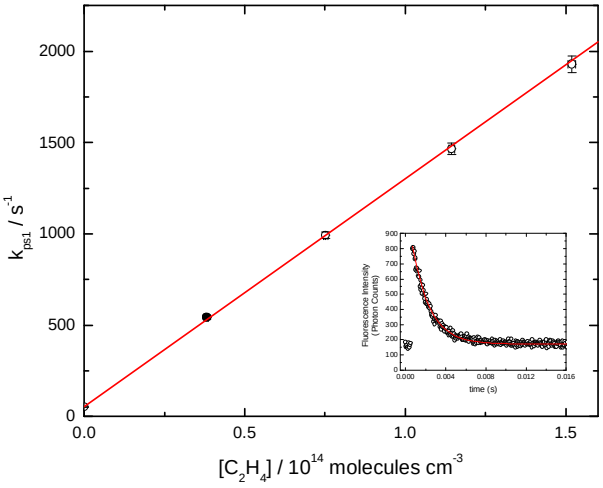

Figure 7.1. Plot of k_{ps1} vs. $[C_2H_4]$ with CCl_4 precursor at 292 K and 67 mbar Ar pressure. The inset shows the exponential decay of [Cl] at $[C_2H_4] = 3.8 \times 10^{13}$ molecules cm^{-3}.

The exothermic equilibrium between the reactants and the β-chloroethyl radical indicates that as the temperature is increased, the formation of the β-chloroethyl radical should become less favorable while its dissociation back to reactants should occur rapidly enough to become significant. In light of these facts, the kinetic scheme below has been proposed in order to properly describe the possible kinetic processes which may occur as the temperature is increased.

$$Cl + C_2H_4 \xrightarrow{k_1} C_2H_4Cl \qquad (7.1)$$

$$C_2H_4Cl \xrightarrow{k_7} Cl + C_2H_4 \qquad (7.7)$$

$$Cl \xrightarrow{k_8} \text{loss} \qquad (7.8)$$

$$C_2H_4Cl \xrightarrow{k_9} \text{loss} \qquad (7.9)$$

This scheme is composed of the usual processes through which Cl atoms can be lost (reaction with C_2H_4 and diffusion/secondary chemistry), while also accounting for the dissociation of chloroethyl back to reactants via equation 7.7 and the potential loss of this adduct through processes which do not lead to the regeneration of Cl atoms (equation 7.9). Application of the Laplace transform method[21,237] to the mechanism above led to the solution for the Cl-atom concentration as a function of time, and as can be seen from equation 7.10 below, this solution implies bi-exponential decays for the Cl-atom concentration.

$$\lambda_{1,2} = -\frac{(k_1[C_2H_4] + k_7 + k_9 + k_8) \pm \sqrt{(k_1[C_2H_4] + k_8 + k_7 + k_9)^2 - 4(k_1k_9[C_2H_4] + k_8k_7 + k_8k_9)}}{2}$$

$$[Cl]_t = [Cl]_0 \frac{(\lambda_1 + k_7 + k_9)e^{\lambda_1 t} - (\lambda_2 + k_7 + k_9)e^{\lambda_2 t}}{\lambda_1 - \lambda_2} \qquad (7.10)$$

Bi-exponential decays were in fact observed from ~ 400 to 430 K, above which adduct dissociation became too fast, resulting in weak Cl signal that was difficult to measure. An example of the bi-exponential decays observed using the C_6H_5Cl precursor at 400 K is shown as the inset in Figure 7.2a and re-plotted on a log scale in Figure 7.2b, in which the non-linearity of the data further accentuates the non-exponential nature of the decay. The fits to these data using equation 7.10 were carried out by fixing k_8 at the value obtained from photolysis of the C_6H_5Cl in the absence of C_2H_4, and directly adjusting $k_1[C_2H_4]$, k_7 and k_9. A plot of $k_1[C_2H_4]$ vs. $[C_2H_4]$ should be linear with a slope of k_1, as shown in Figure 7.2a. According to the kinetic scheme proposed above, the intercepts of such plots should in principle be zero, and overall were not found to be statistically different than zero, with average values of 45 ± 71 and 98 ± 123 s^{-1} at 401 and 430 K, respectively.

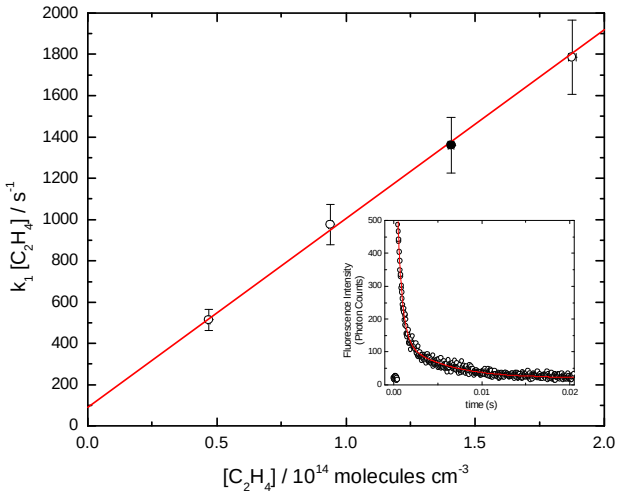

Figure 7.2a. Plot of $k_1[C_2H_4]$ vs. $[C_2H_4]$ with C_6H_5Cl precursor at 400 K and 133 mbar Ar pressure. The inset shows the bi-exponential decay of [Cl] at $[C_2H_4] = 1.4 \times 10^{14}$ molecules cm^{-3}.

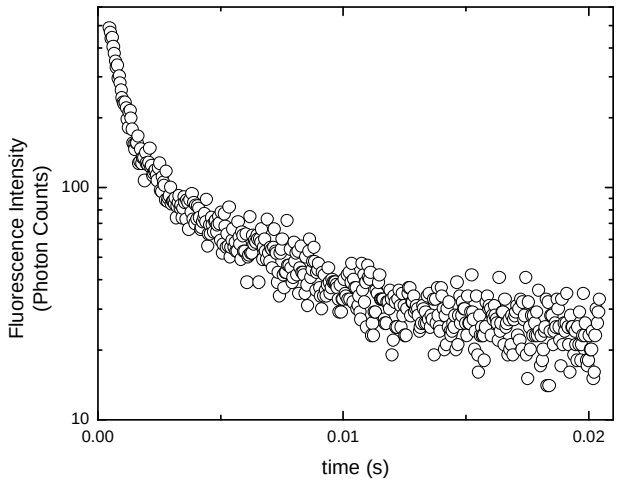

Figure 7.2b. The above decay plotted on a log scale to highlight the bi-exponential behavior.

As the temperature was raised beyond 550 K, the fluorescence intensity signal became strong enough to allow for sensible measurements again. It is believed that under these conditions the H-abstraction channel becomes the dominant reaction path for Cl atoms (reaction 7.11).[217] The second-order rate constant was found to be independent of pressure at temperatures in the range of 550 – 1057 K, which supports the notion of a mechanism change.

$$C_2H_4 + Cl \xrightarrow{k_{11}} C_2H_3 + HCl \qquad (7.11)$$

The Cl-atom fluorescence intensity signal was found to decay exponentially with time at these elevated temperatures, as shown in the inset on Figure 7.3. Pseudo-first-order rate coefficients were obtained from the usual non-linear least squares fitting procedure and plotted against $[C_2H_4]$ to yield a line with a slope corresponding to the abstraction rate constant k_{11}, and an intercept of k_8, which once again accounts for diffusion and potential secondary chemistry. Figure 7.3 depicts a plot of k_{ps1} vs. $[C_2H_4]$ with C_6H_5Cl precursor at 610 K.

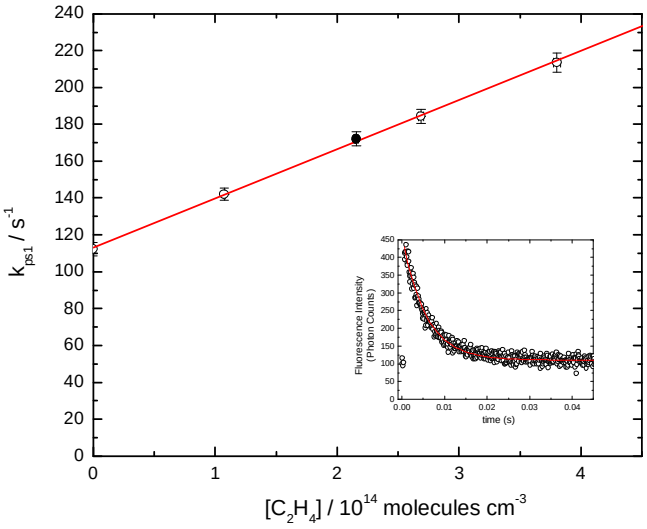

Figure 7.3. Plot of k_{ps1} vs. $[C_2H_4]$ with C_6H_5Cl precursor at 610 K and 200 mbar Ar pressure. The inset shows the exponential decay of [Cl] at $[C_2H_4] = 2.2 \times 10^{14}$ molecules cm^{-3}.

7.2.2. Computational Method

CCSD(T)/CBS-aug theory has been used to locate and characterize the stationary points on the potential energy surface of the C_2H_4Cl system. CCSD(T)/CBS-aug is a composite method which utilizes spin-unrestricted QCISD/6-311G(d,p) theory for the geometries and scaled frequencies and UCCSD(T)/ROHF theory for accurate single-point energy calculations. The UCCSD(T)/ROHF energies obtained with the aug-cc-pVTZ and aug-cc-PVQZ basis sets are then used to extrapolate to the CBS limit. The results obtained with CCSD(T)/CBS-aug theory have also been corrected for scalar relativistic effects, atomic spin-orbit coupling, and core-valence effects. Further details may be found in section 3.2.4.

7.3. Kinetics and Thermochemistry

7.3.1. The Addition Channel

The fifteen measurements of the second-order rate constant k_1 utilizing CCl_4 as a precursor are given in Table 7.1. Though k_1 exhibited fall-off behavior as the pressure was raised at 292 and 345 K, the observed rate constant was found to be independent of other parameters such as F, $[Cl]_0$, and τ_{res}, suggesting that potential secondary chemistry and mixing effects were negligible. However, because C_2H_4 has a fairly significant absorption cross-section at 193 nm (~1.0×10^{-20} cm^2), reaction 7.1 was also investigated using the milder photolysis of SO_2Cl_2 precursor at 248 nm in order to further test whether potential secondary reactions involving photolysis fragments of C_2H_4 had an impact on k_1.

Table 7.2 summarizes the twenty three measurements of reaction 7.1 obtained with SO_2Cl_2 precursor over the temperature range 296 – 378 K, and once again, it was found that the second-order rate constant was independent of F, $[Cl]_0$, and τ_{res}, and demonstrated a dependence

on pressure. Recent experiments have shown SO_2Cl_2 begins to significantly decompose into SO_2 and Cl_2 at temperatures in excess of ~373 K,[232] and indeed, we found that at temperatures exceeding 378 K, the intensity signal became quite weak, indicating that SO_2Cl_2 is no longer a suitable precursor.

Finally, because SO_2Cl_2 is thermally unstable above ~ 380 K and due to the fact that CCl_4 has been shown to be unsuitable at temperatures exceeding ~ 900 K,[157,163] a third precursor, C_6H_5Cl, was also used in the investigation of reaction 7.1. The nineteen determinations of k_1 using this precursor over the range of 292 – 431 K are summarized in Table 7.3. The large absorption cross-section of C_6H_5Cl enabled the detection and accumulation of intensity signal at very low photolysis energies, as can be seen from Table 7.3.

Figure 7.4 depicts the observed fall-off of k_1 with increasing bath gas density at room temperature for all three precursors. While the C_6H_5Cl and CCl_4 precursor data are in good agreement, the k_1 measurements obtained with SO_2Cl_2 precursor were found to be slower at each [Ar], systematically amounting to only ~ 70 – 75 % of the second-order rate constants obtained with the other two precursors. Therefore, distinguishing whether the SO_2Cl_2 data or the CCl_4/C_6H_5Cl data were affected by secondary chemistry became critical. This distinction was made by taking more room temperature data with C_6H_5Cl, but this time N_2 was used as the bath gas in order to allow for direct comparison to the most extensive study conducted to date for the pressure-dependence of reaction 7.1 (Table 7.4).[208,209] As can be seen from Figure 7.5, our data is in good accord with the previous studies of Kaiser and Wallington, which have also been adopted in the NASA-JPL critical review[98] of this reaction, indicating that the photolysis of C_6H_5Cl or CCl_4 at 193 nm does not systematically affect the observed second-order rate

constant. Furthermore, we postulate that the extreme sensitivity of SO_2Cl_2 to moisture and temperature may have impacted the observed kinetics using this precursor.[232]

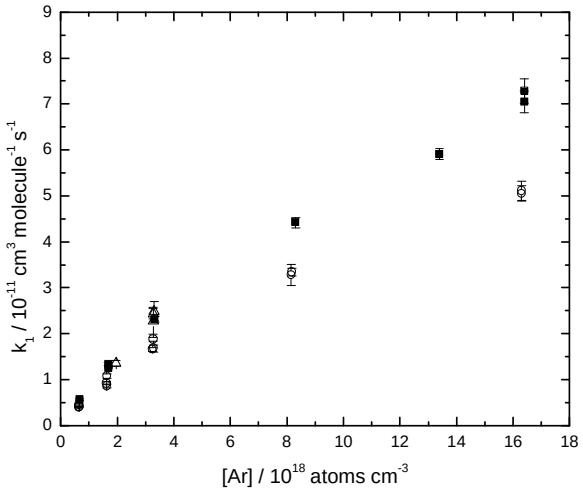

Figure 7.4. Fall-off of the observed second-order rate constant for Cl + C_2H_4 as a function of [Ar] at 294 K average temperature. Open circles represent the data obtained with SO_2Cl_2 precursor, filled squares correspond to data obtained with CCl_4 precursor, and open triangles indicate data obtained with using C_6H_5Cl as a precursor.

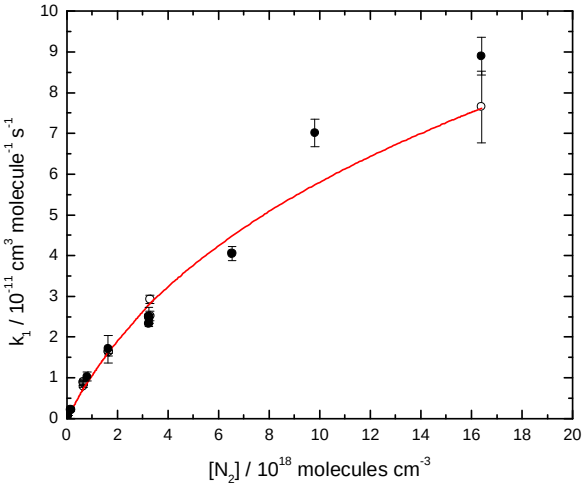

Figure 7.5. Fall-off of the observed second-order rate constant for Cl + C_2H_4 as a function of [N_2] at 292 K. Filled circles represent the data of Kaiser and Wallington,[208,209] open circles represent current work, and line is Troe fit to our data using F_{cent} = 0.6.

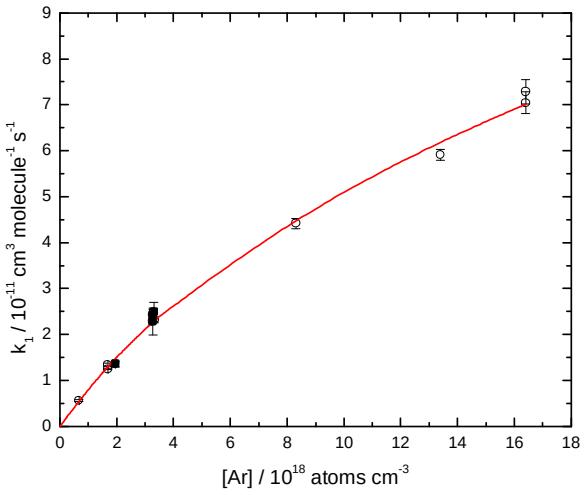

Figure 7.6. Fall-off of the observed second-order rate constant for Cl + C_2H_4 as a function of [Ar] at 293 K average temperature. Open circles represent CCl_4 precursor data, filled squares correspond C_6H_5Cl precursor data, and line is Troe fit to combined data using F_{cent} = 0.6.

Figure 7.6 shows the combined CCl_4/C_6H_5Cl k_1 data at an average temperature of 293 K. As can be seen from this figure, the data seem to lie in the fall-off region. Use of the formalism set forth by Troe[72,73] with the recommended F_{cent} value[98,238] for this reaction of 0.6 yielded a k_0 = 9.8×10^{-30} cm^6 molecule^{-2} s^{-1} and $k_\infty = 3.6 \times 10^{-10}$ cm^3 molecule^{-1} s^{-1} with Ar at 293 K. Similarly, it was found that $k_0 = 1.4 \times 10^{-29}$ cm^6 molecule^{-2} s^{-1} and $k_\infty = 2.9 \times 10^{-10}$ cm^3 molecule^{-1} s^{-1} with N_2 at 298 K when employing an F_{cent} of 0.6 for the fitting (Figure 7.5). Both these values compare well with the NASA-JPL recommendations of $(1.6 \pm 0.8) \times 10^{-29}$ cm^6 molecule^{-2} s^{-1} and $(3.1 \pm 1.6) \times 10^{-10}$ cm^3 molecule^{-1} s^{-1} for k_0 and k_∞, respectively, which are based largely on the extensive relative rate studies of Wallington and Kaiser.[98,208,209] Fall-off was also observed at 345 K. However, at higher temperatures the measurements were in the low-pressure limiting regime and consequently precluded the evaluation of k_∞. The high-pressure and low-pressure limiting rate constants obtained with Ar as a function of temperature

are summarized in Table 7.5. The temperature dependence of the low-pressure limiting rate constant is shown in Figure 7.7 and may be expressed as

$$k_0(T) = 9.1 \times 10^{-30} (T / 300\ K)^{-3.18}\ cm^6\ molecule^{-2}\ s^{-1} \qquad (7.12)$$

This temperature dependence is in good agreement with the -3.3 exponent given in the NASA-JPL critical review,[98] which is once again due to the work of Kaiser and Wallington.[210]

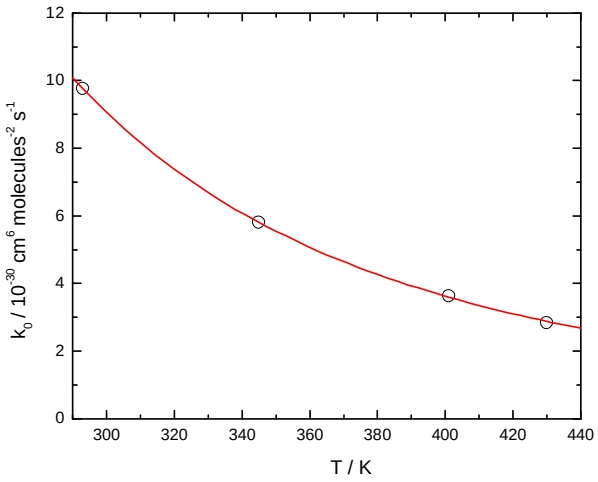

Figure 7.7. Temperature dependence of the low-pressure limiting rate constant for C_2H_4 + Cl.

The observed bi-exponential decays at 401 and 430 K allowed for the measurements of the rate constants k_7 and k_9, for β-chloroethyl radical dissociation back to the reactants and other loss processes for this radical, respectively. These rate constants are given in Table 7.3, and as can be seen, neither depend on F, $[Cl]_0$, $[C_2H_4]$, or τ_{res}, suggesting that secondary chemistry was minimized. In general, k_9 was found to be independent of pressure, while k_7 clearly increased with [Ar] at 401 K, as expected, but the limited data obtained at 430 K did not exhibit a smooth pressure trend. This could be because the bi-exponential decays at 430 K were less pronounced and more difficult to obtain and analyze than those at 401 K.

The average ratio k_1 / k_7, or K_c, can be converted to the unitless thermodynamic equilibrium constant K_{eq} via equation 7.13,

$$K_{eq} = K_c \times (RT/p^\circ)^{\Delta n} \tag{7.13}$$

where p° is the standard pressure (1 bar) and Δn is the net change in the number of moles for the reaction, which in this case is -1. The values of K_{eq} at 401 and 430 K are given in Table 7.5. Following the conversion of these equilibrium constants to the standard state of 1 bar, a van't Hoff plot was used to interpret the temperature dependence of K_{eq} in terms of the thermochemistry for addition. Due to the limited temperature data obtained for K_{eq}, the van't Hoff plot, shown in Figure 7.8, was constrained to go through an intercept of $\Delta S_{298} / R = -10.88$, the calculation of which is discussed in section 7.4.2, and in order to directly obtain $\Delta_r H_{298}$ from such a plot, a small temperature correction[165] of $-(\Delta S_T - \Delta S_{298})/R + (\Delta H_T - \Delta H_{298})/RT$ was added to $\ln(K_{eq})$. The correction was found to be small, having values of -0.004 and -0.006 at 401 and 430 K, respectively, and has the effect of converting the generic $\Delta_r S_T$ and $\Delta_r H_T$ quantities on the right hand side of the van't Hoff equation to their temperature-specific counterparts at 298 K (see eqn. 6.17). The $\Delta_r H_{298}$ for reaction 7.1 was found to be -76.6 ± 1.0 kJ mol^{-1} from the slope of the van't Hoff plot and considerations of its uncertainty, such as the uncertainties in k_1 and k_7 (determined in accordance with section B2 of Appendix B), and the uncertainty in temperature. Using this value in combination with $\Delta_f H_{298}(Cl)$[124] = 121.3026 ± 0.0017 kJ mol^{-1} and $\Delta_f H_{298}(C_2H_4)$[133] = 52.4 ± 0.5 kJ mol^{-1}, yields $\Delta_f H_{298}$(β-chloroethyl radical) = 97.1 ± 1.1 kJ mol^{-1}. This value is in good agreement with the value obtained by Holmes and Lossing from an electron impact study of 95.4 ± 8.4 kJ mol^{-1}, and with the 97.5 ± 3.0 kJ mol^{-1} value also obtained via a Third-Law study of the β-C_2H_4Cl + HBr = C_2H_5Cl + Br equilibrium by Seetula, in which the

entropy of the radical was calculated with MP2/6-31G(d,p) theory.[226,239] In the same study, Seetula also obtained a value for $\Delta_f H_{298}$(β-chloroethyl radical) of 93.0 ± 2.4 kJ mol^{-1} via a Second-Law procedure, which relied on the combination of kinetic measurements obtained via a tubular flow system for the β-chloroethyl + HBr reaction, with rate constants available for the reverse reaction from previous relative rate studies.[226] The Second-Law and Third-Law methods for obtaining the enthalpy of reaction are discussed in chapter 6. The $\Delta_f H_{298}$(β-chloroethyl radical) value obtained here is slightly outside the range of the older estimation of Miyokawa and Tschuikow-Roux of 91.2 ± 4.1 kJ mol^{-1}.[240] However, it has been noted by Seetula that this older result is based on the fortuitous cancellation of several Arrhenius parameters which have been estimated incorrectly.[226]

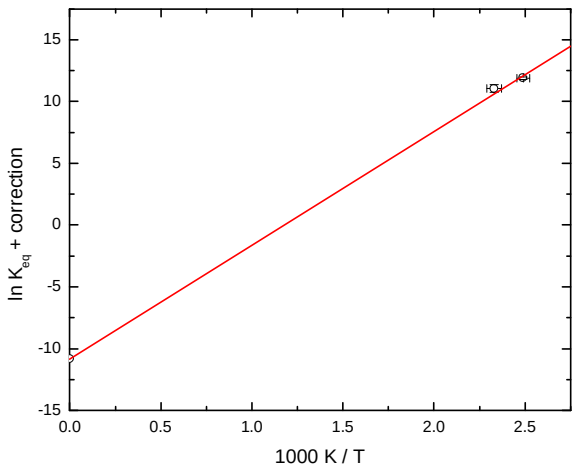

Figure 7.8. van't Hoff plot for Cl addition to C_2H_4.

7.3.2. The Abstraction Channel

Thirty six measurements of the second-order rate constant for hydrogen abstraction along with the experimental conditions used are summarized in Table 7.6. These measurements, spanning the temperature range of 548 – 1048 K, were found to be independent of F, $[Cl]_0$, τ_{res}, and P, indicating that reaction 7.11 is effectively bimolecular and unaffected appreciably by secondary chemistry, thermal decomposition, or mixing effects.

The weighted average of the second-order rate constants for abstraction at the corresponding average temperatures are given Table 7.7 and plotted in Arrhenius form in Figure 7.9. As usual, these weighted averages along with their 1σ uncertainties were then fit using a linear least squares algorithm,[120] yielding

$$k_{11} = (1.97 \pm 0.83) \times 10^{-10} \exp(-32.0 \pm 2.4 \text{ kJ mol}^{-1} / RT) \text{ cm}^3 \text{ molecule}^{-1} \text{ s}^{-1} \qquad (7.14)$$

In equation 7.14, the uncertainties in the Arrhenius parameters are $\pm 2\sigma$, and the combination of these with the covariance of -30.19 yielded the statistical 95 % confidence margins for k_{11}, in the manner described in Appendix B. These confidence limits ranged from 9 to 16 % over the temperature range of 551 – 1055 K, with a minimum at the central temperature. The allowance for potential systematic errors of up to 5 % along with the statistical 95 % uncertainties resulted in the final recommended average confidence limits for k_{11} of $2\sigma = \pm 14$ %. The evaluation of equation 7.13 at 298.15 K yields $(4.9 \pm 2.8) \times 10^{-16}$ cm^3 molecule^{-1} s^{-1}. Overall, our measurements for this reaction are in good agreement with the most recent results of Kaiser and Wallington,[209] Pilgrim and Taatjes,[217] and Takahashi et al.,[221] but disagree with the older very low-pressure reactor measurements of Benson et al.[218-220] This can be seen from Figure 7.10 which summarizes all the abstraction data available in the literature.

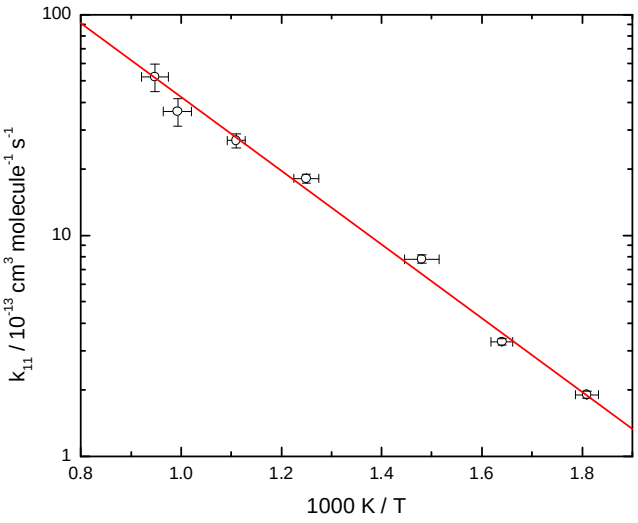

Figure 7.9. Arrhenius plot for Cl + C_2H_4 abstraction. Each point represents the weighted average of the measurements at that temperature. Error bars are ± 2σ.

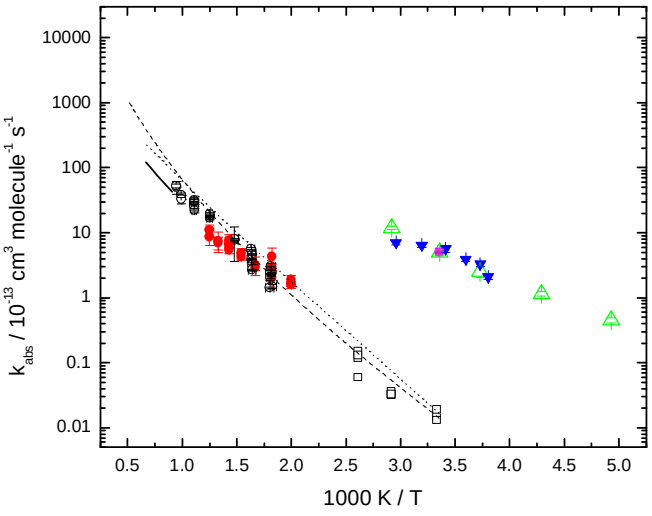

Figure 7.10. Arrhenius plot of kinetic data for Cl + C_2H_4 abstraction: solid line ref. [221]; filled circles ref. [217]; open triangles ref. [219]; filled triangles ref. [220]; open squares ref. [209]; filled square ref. [218]; open circles current work; dashed line TST with Wigner tunneling correction; dotted line RRKM based on hindered Gorin-type TS. Error bars are ± 1σ.

7.4. Computational Analysis

7.4.1. The Addition PES

The computations performed with CCSD(T)/CBS-aug are summarized in Table 7.8 and in Appendix C. Figure 7.11 – 7.13 depict the PES for addition, the PES for abstraction, and the species found along these surfaces, respectively. In the case of addition, an entrance complex A1 was found with QCISD/6-311G(d,p) theory, but is actually not bound according to CCSD(T)/CBS-aug theory, as it has a higher energy than the loose TS (Add TS) for the formation of β-chloroethyl. As can be seen from Figure 7.11, β-chloroethyl is bound by 73.6 kJ mol^{-1} relative to the reactants at 0 K, and the TSs for isomerization to α-chloroethyl (Iso TS) and hydrogen displacement (Dis TS1) are quite high.

The PES for addition obtained with CCSD(T)/CBS-aug theory is in qualitative agreement with the PES obtained by Brana et al. using QCISD/6-31G(d,p) theory and MP2 theory in combination with basis sets ranging from 6-31G(d,p) to 6-311++G(3df,3pd).[241] As here, they found that the addition channel involves the formation of the A1 complex, which was either not bound or only very weakly bound depending on the level of theory used, followed by the passage through the non-symmetrical Add TS. The intrinsic reaction coordinate was followed via IRC calculations in both studies, and it was verified that TS Add connects A1 with β-chloroethyl.

These findings are in disagreement with the older *ab initio* calculations of Engels et al. and Knyazev et al., both of whom concluded that the minimum energy pathway for addition involves the passage through the symmetrical TS for 1,2 Cl-atom migration followed by a shuttling of the Cl atom toward a carbon center to form the β-chloroethyl radical.[223,224] Engels et al. used large-scale multireference configuration interactions to obtain partially optimized geometries and their corresponding energies, while Knyazev et al. relied on PMP4/6-

31G**//UMP2/6-31G** theory. The main source of disagreement between these two studies came from the fact that the TS for the non-symmetric addition of Cl to ethylene found by Engels et al. could not be located with PMP4/6-31G**//UMP2/6-31G** theory, and it is argued by Knyazev et al. that this may in fact be due to the fact that Engels et al. only relied on partially optimized structures.

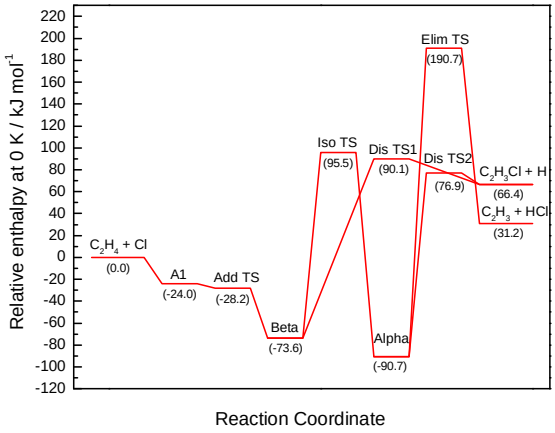

Figure 7.11. PE diagram for addition of Cl to C_2H_4 obtained with CCSD(T)/CBS-aug theory.

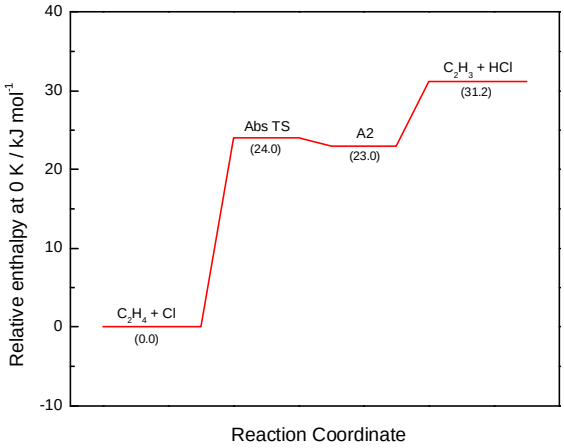

Figure 7.12. PE diagram for C_2H_4 + Cl abstraction obtained with CCSD(T)/CBS-aug theory.

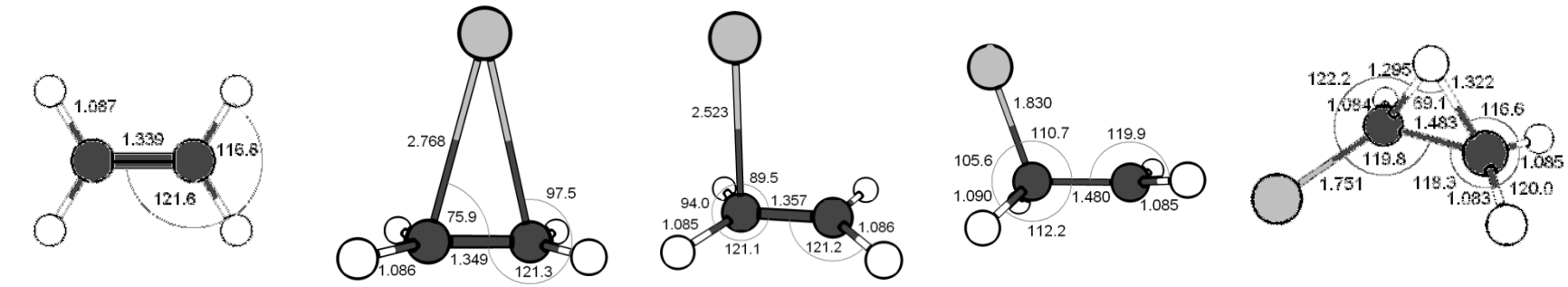

C_2H_4 (^1A_g) (0.0) A1 ($^2A_1$) (-24.0) Add TS ($^2A'$) (-28.2) Beta ($^2A'$) (-73.6) Iso TS (^2A) (95.5)

Dis TS1 (^2A) (90.1) Alpha (^2A) (-90.7) Dis TS2 (^2A) (76.9) Elim TS (^2A) (190.7) C_2H_3Cl ($^1A'$) (66.4)

Abs TS (^2A) (24.0) A2 ($^2A'$) (23.0) C_2H_3 ($^2A'$) (31.2) HCl ($^1\Sigma^+$) (31.2) H_2 ($^1\Sigma_g$)

Figure 7.13. Species in the C_2H_4Cl reaction system. Geometries were obtained with QCISD/6-311G(d,p) theory. Values in parentheses are relative CCSD(T)/CBS-aug enthalpies of each product set in kJ mol^{-1} at 0 K, with relativistic and core-valence effects.

The partially optimized non-symmetrical TS of Engels et al. was found to be 8 kJ mol^{-1} higher in energy than the reactants, which is in qualitative agreement with findings of an older study performed by Schlegel and Sosa using MP2/6-31G*//HF/6-31G* calculations.[230] However, in contrast to the results of Engels et al. and of Knyazev et al., which indicate that the symmetric pathway is barrierless, Schlegel and Sosa and Hoz et al.,[228,229] who used UHF and multiconfiguration SCF procedures, both found that an intermediate in the symmetric addition of Cl to ethylene lies above the energy of the reactants, but noted that a lower energy symmetric addition pathway involving Cl migration may be possible.

Using CCSD(T)/CBS-aug, it has also been found that the vinyl radical and hydrogen chloride can also be produced through the 1,2 HCl elimination from α-chloroethyl. This happens through the high energy TS denoted as Elim TS in Figure 7.11, and marks the first characterization of an elimination of any kind from a chloroethyl radical. A similar TS structure was optimized in the case of the β-chloroethyl radical, however, this structure was found to possess two imaginary frequencies and thus corresponds to a second-order saddle point rather than a TS. The possibility of H_2 elimination from the two radicals was also considered, and though no TS structures were characterized for these processes, it is noted that ensuing product sets of H_2 + trans β-chlorovinyl, cis β-chlorovinyl, and α-chlorovinyl were found to possess CCSD(T)/CBS-aug energies that were respectively 99.7, 104.0, and 85.2 kJ mol^{-1} above those of Cl + C_2H_4. These possible products are therefore too endothermic to be important under the experimental conditions used in this work. The QCISD/6-311G(d,p) geometries and scaled frequencies of the chlorovinyl species are given elsewhere,[242] and their CCSD(T)/CBS-aug energies are listed in Table 7.8. Finally, as briefly mentioned earlier, the TS structure corresponding to the H-atom displacement from β-chloroethyl has also been found, as has its α-

counterpart, and are denoted as Dis TS1 and Dis TS2, respectively. The large barrier heights for displacement and the considerable endothermicity associated with the H_2 elimination channels from the chloroethyl radicals suggest that these reactions would not occur appreciably under the experimental conditions of this study.

7.4.2. Thermochemistry of the chloroethyl radicals

The thermal corrections to the enthalpies at 298.15 K were obtained from the JANAF tables for C_2H_4 and Cl (10.518 and 6.272 kJ mol^{-1} respectively),[173] and calculated for β-chloroethyl using standard relations with Gaussian 03 (13.797 kJ mol^{-1}), yielding Δ_rH_{298} = -76.6 kJ mol^{-1}, which exactly matches the experimental value determined in this work. Consequently, combining this value with the experimental values for Δ_fH_{298} of the reactants also exactly agrees with our experimental value of Δ_fH_{298}(β-chloroethyl) = 97.1 ± 1.1 kJ mol^{-1}.

To further refine the thermochemistry, the lowest vibrational mode in the β-chloroethyl radical, corresponding to torsion of the CH_2 and CH_2Cl around the partial double bond, was re-analyzed as a hindered internal rotation. Initial relaxed scans of the H4-C2-C1-Cl dihedral angle defined in Figure 7.14, hereafter referred to as D_1, indicated that (β)C-(α)CH_2 moiety is planar at the initial value of D_1 = 0°, but as the dihedral angle is increased, the optimal structure involves a slight distortion from planarity, with the H4-C2-C1-H3 dihedral angle (D_2) reaching values of as low as 165° (Figure 7.14). This suggests that there is a coupling between the torsion mode and the inversion motion corresponding to the second lowest vibrational mode. To test the extent of this coupling, a double relaxed scan was performed at the QCISD/6-311G(d,p) level of theory, which sought the optimal value for D_2 at each value of D_1. The potential energy surface generated by this dual relaxed scan of the two dihedral angles is shown as a contour map in

Figure 7.15 and as a three-dimensional surface in Figure 7.16. As can be seen from these figures, as the coordinate for internal rotation is increased, D_2 gradually drops from the C_s TS structure at 180° to 165° at around D_1 = 80°, which is the minimum corresponding to the β-chloroethyl radical (optimized D_1 = 82.13°). The computed classical barrier for rotation is 8.7 kJ mol^{-1} at the QCISD/6-311G(d,p) level of theory, which is reduced to 5.4 kJ mol^{-1} with the addition of scaled ZPEs (and 6.7 kJ mol^{-1} if the torsional frequency is excluded from the ZPE of the β-chloroethyl radical), both in accord with the results from previous computational studies,[224,225,230] but considerably lower than the barrier of ~ 20 kJ mol^{-1} estimated from older ESR studies.[243,244] As D_1 keeps increasing, D_2 gradually returns to 180°, however, it then slowly falls off back down to 165° by the time D_1 = 180°. At this value of D_1, the energy along the D_2 coordinate changes by less than 0.1 kJ mol^{-1} in going from 165° to 180°, and since the structure at D_1 = 0° should be equivalent to the structure at D_1 =180°, the apparent minimum at D_2 = 165° is likely an artifact of QCISD/6-311G(d,p) theory caused by the flatness of the potential in this region. The energies of points along the MEP for torsion in the β-chloroethyl radical are given in Table 7.9.

The minimum energy pathway (MEP) along the PES in figures 7.15 and 7.16, given in Table 7.9, was then used to calculate the energy levels for this one-dimensional potential by using the Fourier Grid Hamiltonian method to solve the one-dimensional Schrodinger equation variationally,[245] using the FGH1D program.[246] For internal rotations, this method requires the evaluation of the reduced moment of inertia for the rotation of the two moieties around the axis of rotation. The reduced moment of inertia was calculated with the Mominert program contained in the MultiWell 2008.3 Program Suite,[86] which calculates the moments of inertia for each of the rotating fragments about the axis of rotation via equation 7.15, where m_i and r_i are the mass and

distance from the axis of rotation of the i^{th} atom in the rotating fragment, and then combines them to yield the reduced moment of inertia via equation 7.16. This procedure was repeated for each of the structures corresponding to the points along the MEP, and the average reduced moment of inertia of 1.751 amu $Å^2$ was used to generate one-dimensional solutions to the Schrodinger equation. The reduced moments of inertia for each of the points along the MEP were close to this average value, such that the standard deviation for the set of structures was only ± 0.013 amu $Å^2$, with a maximum deviation of 0.029 amu $Å^2$ at D_1 =170°. The MEP and resulting energy levels are depicted in Figure 7.17.

$$I_{Frag} = \sum_i (m_i \times r_i^{\,2}) \tag{7.15}$$

$$I_{Red} = \frac{I_{Frag1} \times I_{Frag2}}{I_{Frag1} + I_{Frag2}} \tag{7.16}$$

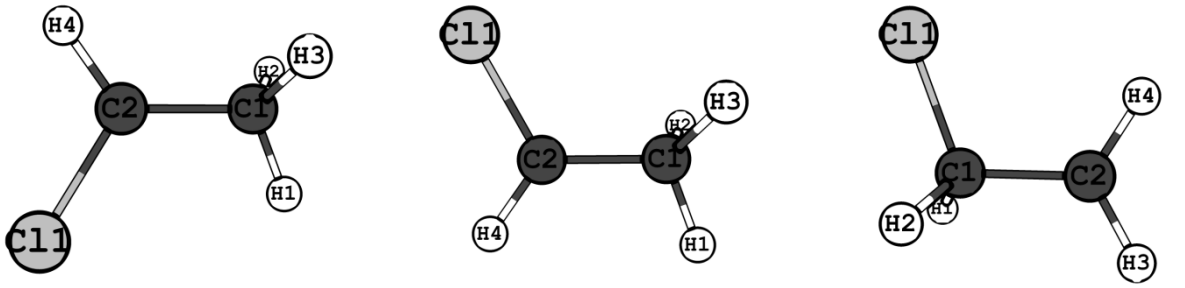

α-Chloroethyl Torsion TS (^{2}A") | α-Chloroethyl Inversion TS (^{2}A") | β-Chloroethyl Torsion TS (^{2}A")

Figure 7.14. Transition states for torsion and inversion in the α- and β-chloroethyl radicals obtained with QCISD/6-311G(d,p) theory.

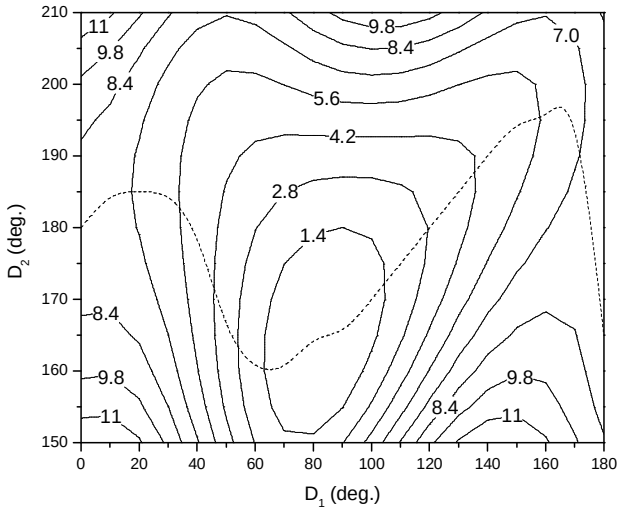

Figure 7.15. Contour map of the PES (in kJ mol^{-1}) for the torsion and inversion modes of the β-chloroethyl radical obtained with QCISD/6-311G(d,p) theory. Dashed line represents the MEP.

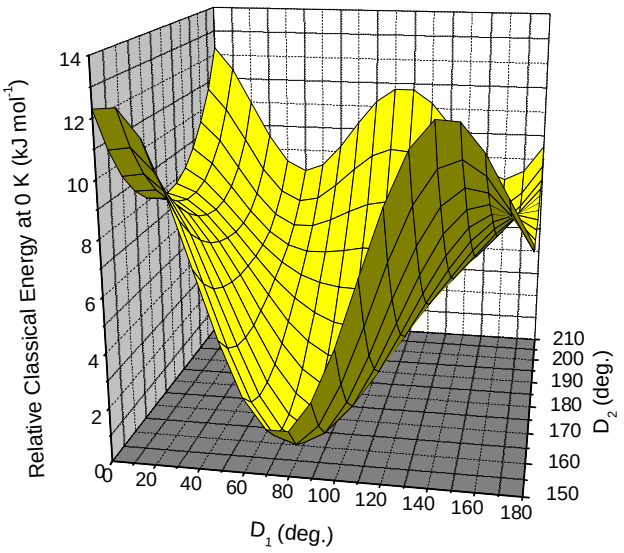

Figure 7.16. Three-dimensional representation of the PES for the torsion and inversion modes of the β-chloroethyl radical obtained with QCISD/6-311G(d,p) theory.

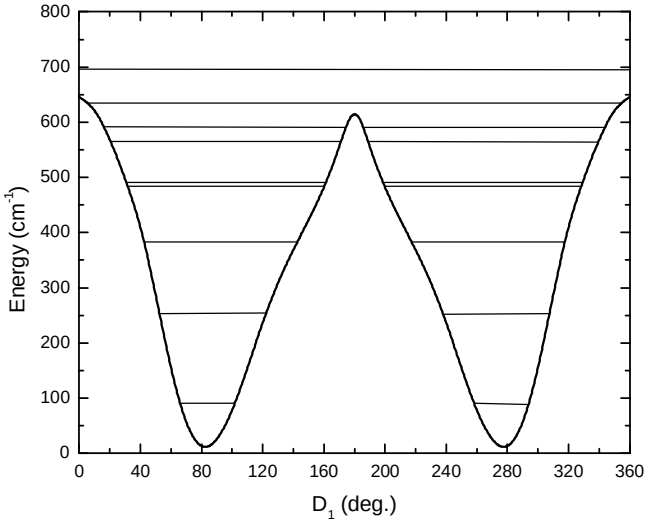

Figure 7.17. Potential energy diagram for the torsion in β-chloroethyl radical computed with QCISD/6-311G(d,p) theory, and anharmonic energy levels.

Knowledge of the energy levels for this internal rotation enable the calculation of its partition function, which can in turn be used to access the various thermochemistry contributions via standard relations from statistical mechanics. The entropy of this mode, its heat capacity, and its integrated heat capacity at temperature intervals spanning the range over which the experiments were conducted, are listed in Table 7.10. The values in Table 7.10 were used to replace the corresponding quantities calculated by Gaussian 03 for this mode, and the ensuing thermochemistry for the β-chloroethyl radical was combined with the known thermochemistry of C_2H_4 and Cl to obtain the value of the intercept and the corrections to K_{eq} in the van't Hoff plot discussed in section 7.3.1 (Figure 7.8).[173] Over the range of 350 – 500 K, the integrated heat capacity for reaction 7.1 can be expressed as a function of temperature by the third-order polynomial given in equation 7.17. Furthermore, replacement of the thermochemical contributions of the low frequency with those of the hindered internal rotation yielded $\Delta_f H_{298}$(β-

chloroethyl) = 97.7 kJ mol^{-1} and $\Delta_r H_{298}$ of -76.0 kJ mol^{-1} for the formation of β-chloroethyl, both of which agree nicely with experimental values.

$$\Delta_r C_p^\circ = -6.28 + 5.05\times10^{-2}T - 1.15\times10^{-4}T^2 + 8.19\times10^{-8}T^3 \qquad (7.17)$$

A similar analysis was conducted for the hindered internal rotation in the α-chloroethyl radical. Once again, due to the apparent coupling between the two lowest vibrational modes, torsion followed by inversion, characterized by D_1 = Cl-C2-C1-H1 and D_2 = Cl-C2-C1-H4, respectively (Figure 7.14), a double relaxed scan was performed in order to map out the MEP manually along the PES. The resulting PES is shown as a contour diagram in Figure 7.18, and as a three-dimensional surface in Figure 7.19. As can be seen from these figures, the MEP starts with a C_s structure with D_2 = 180° at D_1 = 0°, which has been characterized as the TS for torsion, and then proceeds to the minimum corresponding to the α-chloroethyl radical. After the passage through one of the minima, the MEP along the D_1 coordinate involves a gradual return to D_2 = 180°, eventually leading back to the TS for torsion at D_1 = 120°, after which the potential repeats. In fact, two degenerate minima can be seen on the PES, separated by the TS for inversion along the D_2 coordinate. The TS for torsion is 4.9 kJ mol^{-1} higher in energy than the α-chloroethyl radical, while the barrier for inversion is only 1.1 kJ mol^{-1} at the QCISD/6-311G(d,p) level of theory. The two TS structures and the definitions for D_1 and D_2 in α-chloroethyl are shown in Figure 7.14. Inclusion of scaled ZPEs reduces the barrier for torsion to 2.7 kJ mol^{-1} and actually makes the TS for inversion 1.2 kJ mol^{-1} lower in energy than the α-chloroethyl radical. The barrier for torsion is increased by 1.0 kJ mol^{-1} if the torsional frequency is excluded from the ZPE of the α-chloroethyl radical. These results are in good agreement with the similar analysis performed at the UMP2/6-311G(d,p)//UMP2/6-31G(d) and UHF/6-31G(d) levels of theory by Chen and Tschuikow-Roux.[225]

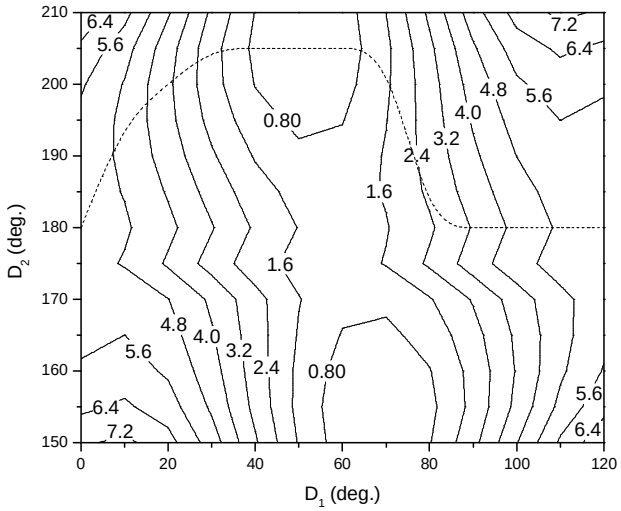

Figure 7.18. Contour map of the PES (in kJ mol^{-1}) for the torsion and inversion modes of the α-chloroethyl radical obtained with QCISD/6-311G(d,p) theory. Dashed line represents the MEP.

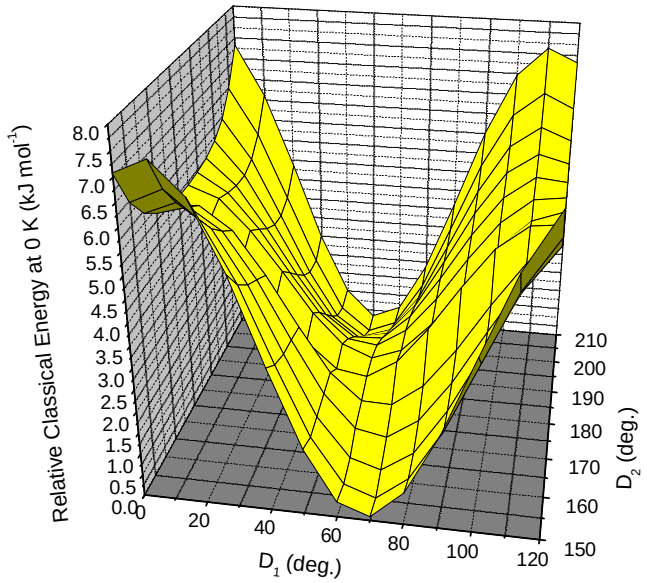

Figure 7.19. Three-dimensional representation of the PES for the torsion and inversion modes of the α-chloroethyl radical obtained with QCISD/6-311G(d,p) theory.

The Fourier Grid Hamiltonian method[245] was then used to solve the one-dimensional Schrodinger equation for the potential corresponding to the MEP, using the FGH1D program,[246] and the averaged reduced moment of inertia for the points along the MEP of 3.057 ± 0.006 amu $Å^2$ was used in this analysis. As can be seen from the standard deviation, the individual reduced moments of inertia for the points along the MEP were all close to their average, with the maximum deviation being only 0.008 amu $Å^2$ at D_1 = 0°, 50°, 120°, 170°, 240°, and 290°. The MEP is given as a function of D_1 in Table 7.11, and shown along with the resulting energy levels in Figure 7.20. The calculated entropy, heat capacity, and integrated heat capacity over 298.15 – 500 K for the torsion mode in α-chloroethyl are listed in Table 7.12.

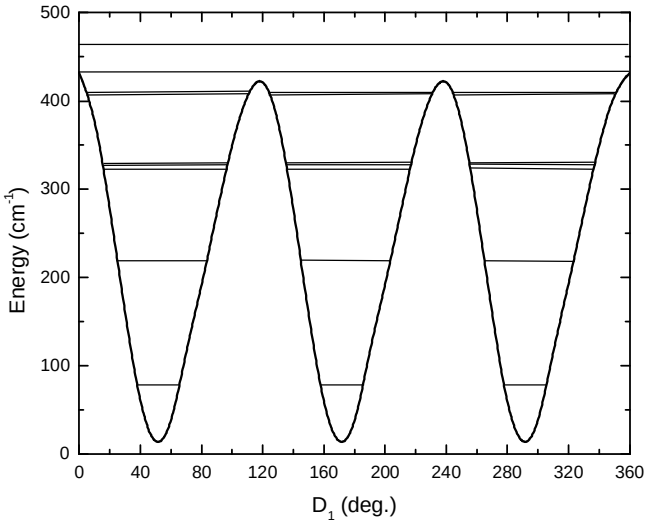

Figure 7.20. Potential energy diagram for the torsion in α-chloroethyl radical computed with QCISD/6-311G(d,p) theory, and anharmonic energy levels.

7.4.3. The Abstraction Channel

Figure 7.12 shows the abstraction potential energy diagram obtained with CCSD(T)/CBS-aug theory. Along this pathway, the reactants go directly through a TS (Abs TS) that is 24.0 kJ mol^{-1} higher in energy and pass through the weakly bound adduct A2 before forming vinyl and hydrogen chloride. As was the case for addition, this PE diagram is also in qualitative accord with the results of Brana et al.[241] A value for $\Delta_r H_{298}$ = 33.7 kJ mol^{-1} was calculated for the abstraction process, and combining this value with $\Delta_f H_{298}(HCl)$[124] = -92.1763 ± 0.0066 kJ mol^{-1} and those for Cl and C_2H_4 mentioned earlier, yields $\Delta_f H_{298}(C_2H_3)$ = 299.6 kJ mol^{-1}. This value is in very good agreement with the 299.6 ± 3.3 kJ mol^{-1} photoelectron spectroscopic measurement of Ervin et al.[247] Furthermore, our *ab initio* value is also in good accord with the values of 299.6 ± 1.3 and 295.4 ± 1.7 kJ mol^{-1} obtained via Third-Law analyses by Pilgrim and Taatjes,[217] and Kaiser and Wallington,[209] respectively, and with the values both of these studies also obtained via the Second-Law method, of 298.3 ± 5.4 and 291.2 ± 6.7 kJ mol^{-1}, respectively. The Second- and Third-Law analyses performed by Pilgrim and Taatjes and Kaiser and Wallington relied on the temperature-dependent rate constants and activation energy for the C_2H_3 + HCl reaction, measured by Russell et al.[222]

While spin contamination is small in the α- and β-chloroethyl radicals, having values of $\langle S^2 \rangle$ = 0.765 and 0.766, respectively, the $\langle S^2 \rangle$ value of 0.982 found for the vinyl radical suggested that perhaps, as was the case with the severely spin-contaminated phenyl radical in chapter 6, composite methods which rely on UHF reference wavefunctions may not accurately treat this system. As was discussed in chapter 6, when the spatial component of the wavefunction is unrestricted, spin polarization effects arise in open-shell systems, which can lead to contamination of the doublet wavefunction.[17] The extent of spin contamination depends on

the system, though it has been found that in general, systems in which the singly occupied MO has nodes at nuclear positions, and the subjacent bonding MO is easily polarized and is high in energy (such as is the case for the vinyl radical), usually exhibit a large degree of spin contamination.[17]

For consistency, the C-H bond strength ($BDE_0(C_2H_3\text{-}H)$) was computed with several composite methods to assess if the effects of spin-contamination considerably impact normally accurate composite methods, as was found by analyzing the C-H bond strength in benzene in chapter 6. Based on observations from the previous chapter, it may be expected that composite methods which depend on UHF reference wavefunctions as the basis for MP2, MP4, QCISD(T), and CCSD(T) correlation treatments, will significantly overestimate the C-H bond strength, and that the use of spin-restricted open-shell Hartree-Fock (ROHF) wavefunctions, which eliminate spin contamination in the wavefunction, will improve the accuracy. Table 7.13 lists the values for $BDE_0(C_2H_3\text{-}H)$ computed by several composite methods, which, with the exception of the CCSD(T)/CBS-aug results, have been obtained from combining the computed enthalpies of formation of C_2H_3 from the work of Henry et al.,[197] with the experimental heats of formation of C_2H_4[133] and H[124] at 0 K, of 60.99 ± 0.50 and 216.034 ± 0.0001 kJ mol^{-1}, respectively. Similarly, the experimental value of 458.8 ± 3.3 kJ mol^{-1} for $BDE_0(C_2H_3\text{-}H)$ listed in Table 7.13 is the result of combining the aforementioned experimental heats of formation of C_2H_4 and H with the heat of formation reported by Berkowitz et al. for C_2H_3 at 0 K, 303.8 ± 3.3 kJ mol^{-1}.[177]

As can be seen, the tabulated UHF-based composite methods actually tend to underestimate the $BDE_0(C_2H_3\text{-}H)$, with the exception of CBS-QB3, which is actually in good agreement with the experimental value. As expected, using ROHF within the scheme of some of the composite methods does improve the accuracy, except in the case of the G3(MP2) and

G3(MP2)-RAD pair, where the ROHF-based result actually underestimates the bond strength by an additional 1.1 kJ mol^{-1}. The UHF-based CBS-QB3 method also obtains a result that is closer to 458.8 kJ mol^{-1} than its ROHF counterpart CBS-RAD, however, since the results of both of these methods are within the experimental uncertainty, in principle, the extent of their accuracy is indistinguishable. Overall, it can be concluded that while ROHF-based composite methods yield more accurate results for spin-contaminated systems than their UHF-based analogs, both sets of composite methods provide reasonable results in the case of the vinyl radical, which exhibits considerably less spin-contamination than the phenyl radical. Finally, for comparison, the $BDE_0(C_2H_3\text{-}H)$ has also been computed with CCSD(T)/CBS-aug theory, and as can be seen in Table 7.13, this result is in excellent agreement with the experimental value.

7.4.4. Kinetic Analysis

RRKM calculations using the MultiWell program were carried out for the addition reaction based on a simplified version of the PES in Figure 7.11. In this simplified PES, the unimportant and unbound complex A1 was neglected, as were any further reactions after the formation of the β-chloroethyl radical, as it was assumed that TS structures for isomerization and H-atom displacement are too high to overcome appreciably at the temperatures at which addition was experimentally explored. The density of states and sum of states for the β-chloroethyl radical and for the loose TS (Add TS) were obtained via the direct count method employed by MultiWell based on the scaled vibrational frequencies and moments of inertia obtained using QCISD/6-311G(d,p) theory for these structures. The Lennard-Jones parameters chosen were σ = 4.94 Å and ε/k_B = 400 K, where σ was approximated using the empirical rules of Reid and Sherwood[95] while ε/k_B was arbitrarily assigned as usual. The Lennard-Jones parameters used for

Ar are the ones given in chapter 3, and the parameters for N_2 were taken from the same source, the work of Hippler et al, and have values of σ = 3.74 Å and ε/k_B = 82.0 K.[94] The collisional stabilization parameters were selected based on the simple exponential-down model described in chapter 3.

The results of these RRKM calculations did not agree very well with experiments when using the sum of states of Add TS to evaluate microcanonical rate constants, a procedure which underestimated the thermal rate constant by about an order of magnitude. Conventional TST calculations have revealed that if Add TS is used as the bottle neck in the entrance channel, the high-pressure limiting thermal rate constant would have a value of 1.5×10^{-7} cm^3 molecule^{-1} s^{-1}, which is about 420 times larger than the 3.6×10^{-10} cm^3 molecule^{-1} s^{-1} value obtained from the empirical Troe fit of the experimental data. This shows that the QCISD saddle point at Add TS is not the bottleneck for reaction.

The hindered Gorin-type TS treatment described in chapter 3 can also be used to assess the nature of the generally loose TS associated with the entrance channel. This method is particularly appealing in this case since the experimental value for the high-pressure limiting recombination rate constant for Cl + C_2H_4 was measured in this work, and can be used to determine the hindrance parameters. The value for k_∞ is independent of the identity of the bath gas, and though the values for this quantity obtained experimentally were slightly different between Ar and N_2 (which is indicative of the amount of uncertainty associated with the Troe fits), the average value of 3.3×10^{-10} cm^3 molecule^{-1} s^{-1} was used to obtain the hindrance parameters at 293 K. The parameters used in the Morse potential analysis for the dissociation of the β-chloroethyl radical were r_e = 1.830 Å, υ_e = 602.0 cm^{-1}, and D_e = 64.4 kJ mol^{-1}. The resultant properties of the hindered Gorin-type TS are listed in Table 7.14. Table 7.14 also

contains the energy transfer parameters, high- and low- pressure limiting rate constants, and the equilibrium constant for the C_2H_4 + Cl = β-Chloroethyl radical reaction at 293 K. The RRKM results for both Ar and N_2 data are shown if Figure 7.21, and as can be seen, the calculated fall-off is in good agreement with the Troe analysis of the experimental measurements based on F_{cent} values of 0.6 for both bath gases. The calculated collision efficiencies for Ar and N_2 of β^{Ar} = 0.58 and β^{N2} = 0.72, which are not unreasonable, though they are somewhat larger than their typical value of ~0.4 in each case. Sample MultiWell input files are given in Appendix D.

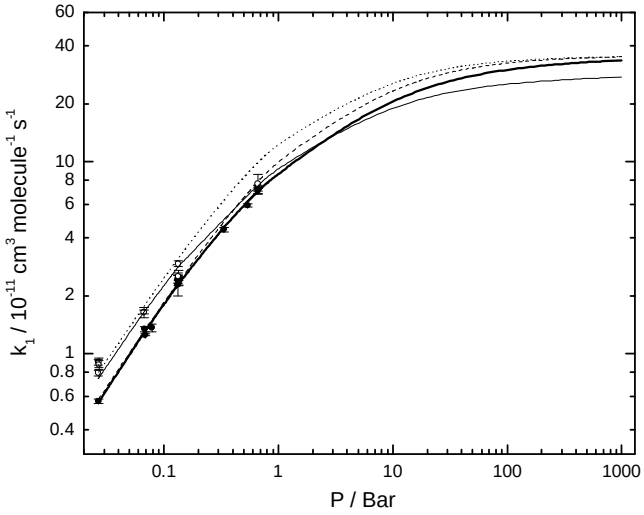

Figure 7.21. Comparison of experimental and RRKM second-order rate constants for addition in the fall-off region, at 293 K. Open circles: experimental data ± 1σ in Ar bath gas; filled circles: experimental data ± 1σ in N_2 bath gas; solid line: empirical Troe fit to Ar data; bold line: empirical Troe fit to N_2 data; dashed line: RRKM result for Ar; dotted line: RRKM result for N_2.

MultiWell-based RRKM calculations have also been carried out for the reverse of reaction 7.11 (C_2H_3 + HCl) based on the CCSD(T)/CBS-aug data and PES in Figure 7.12, at a constant pressure of 0.1 bar. Subsequently, the rate constants for reaction 7.11 have been obtained via the equilibrium constant evaluated at each temperature and given in Table 7.15.

The three lowest vibrations in A2 and the two lowest vibrations in Abs TS seemed to correspond to hindered rotations, and were treated as such in the evaluation of the equilibrium constants, densities, and sums of states. The reduced moments of inertia for the sterically hindered rotations of the HCl fragment around C_2H_3 were found to be 1.82 and 0.09 amu $Å^2$ in the case of A2 and Abs TS, respectively. The hindered Gorin model[66,100,101] described in chapter 3 was used to obtain and fit the properties of the loose TS at the entrance channel by fitting to rate constants calculated based on the hard sphere model for this system. These rate constants were evaluated at each temperature and are also listed in Table 7.15, along with the hindrance parameters arising from the steric interactions between C_2H_3 and HCl. The parameters used in the Morse potential analysis for A2 were r_e = 3.839 Å, υ_e = 83.3 cm^{-1}, and D_e = 8.9 kJ mol^{-1}. Wigner tunneling corrections, previously described in chapter 5, have been applied to the RRKM results and may be found in Table 7.15. Energy transfer parameters pertaining to A2 were calculated in the same way outlined in chapter 3, based on an assumed $<E>_{all}$ for Ar of -2.633 kJ mol^{-1}, and the Lennard-Jones parameters for this system were assumed to be the same as for the β-chloroethyl radical. These parameters are also included in Table 7.15. The RRKM results are shown in Figure 7.10. As usual, sample MultiWell input files are provided in Appendix D.

As can be seen in Figure 7.10, the RRKM results are in reasonable agreement with the measured k_{11} over the entire overlapping temperature range, though these rate constants are still somewhat overestimated. In the future, it is likely that the replacement of the crude hard sphere collision rate constants with more physically meaningful counterparts will yield improved hindrance parameters, which should further increase the agreement with experiment.

Finally, Canonical Transition State Theory was applied to the PES of Figure 7.12 in order to assess the upper bound to potential future MTST results. The conventional TST formalism

described in Chapter 3 was applied to the forward rate constant to directly calculate k_{11} from the results obtained with CCSD(T)/CBS-aug theory. In addition, the effect of tunneling on the TST rate constant was approximated by including the Wigner tunneling correction[82,143] described in chapter 5. The tunneling correction had the effect of increasing the TST rate constant by 76 % at 298 K, 27 % at 500 K, and decreased to only 2% by 2000 K. The TST results are depicted in Figure 7.10, and as can be seen, these results agree well with our measurements of $k_{11}(T)$ as well as with other recent measurements, though as expected, they overestimate the rate constant, particularly at high temperatures. Though the overestimation by TST is only slight in this case, the application of MTST should markedly reduce the calculated rate constant, and therefore, it is expected that the MTST results will agree quite nicely with experimental findings.

7.5. Conclusions

The kinetics of the reaction between atomic chlorine and ethylene have been measured over 293 – 1057 K. Addition was observed over the range of 293 – 430 K, and the dissociation of the β-chloroethyl radical back to the reactants became fast enough above 400 K to allow its measurement and provide access to the thermochemistry of this radical via the equilibrium constant. The enthalpy of formation of the β-chloroethyl radical determined from a Third-Law analysis marks the most precise determination of this quantity to date. The temperature dependence of the low-pressure limiting rate constant was found to be in line with that obtained via relative rate measurements in previous studies. Abstraction was observed at temperatures exceeding 550 K, and the temperature dependence of the ensuing rate constant was found to be in good agreement with other recent kinetic determinations, but in discord with older kinetic measurements.

Ab initio results provided good agreement with the measured thermochemistry of the β-chlroethyl radical. These computations also yielded accurate thermochemistry for the vinyl radical, which further supports the spectroscopic and recent kinetic measurements of this value while also invalidating the old values from prior kinetic measurements. MultiWell-based RRKM calculations reproduced the observed fall-off behavior in the case of addition, and in the case of abstraction, the calculated rate constants were found to be in reasonable agreement with the measured rate constants for abstraction over the entire temperature range considered. Conventional TST results only slightly exaggerated the rate constant for abstraction, suggesting that in principle, the application of MTST to this system would yield theoretical rate constants in good agreement with experiment.

Table 7.1. Summary of kinetic measurements for Cl + C_2H_4 using CCl_4 precursor.

T, K	τ_{res}, s	F, mJ	p, mbar	$[CCl_4]$, 10^{15} molecule cm^{-3}	$[C_2H_4]_{max}$, 10^{14} molecule cm^{-3}	$[Cl]_{0,max}$, 10^{11} molecule cm^{-3}	$k_1 \pm \sigma_{k1}$, 10^{-12} cm^3 molecule^{-1} s^{-1}
292	1.2	0.54	67	1.26	1.52	7.9	13.4 ± 0.37
292	1.2	0.26	67	1.26	1.52	3.8	12.5 ± 0.16
293	0.8	0.39	27	1.21	1.56	5.5	5.64 ± 0.15
293	3.0	0.68	133	1.90	1.54	14.9	23.2 ± 0.68
293	5.2	0.41	333	1.60	0.78	7.6	44.2 ± 1.13
293	7.8	1.22	667	1.06	0.31	15.0	72.8 ± 2.63
293	7.8	0.63	667	1.06	0.31	7.7	70.4 ± 2.35
293	9.8	0.6	533	1.53	0.39	10.6	59.1 ± 1.19
345	0.5	1.21	27	0.72	1.09	10.1	3.11 ± 0.16
345	0.5	0.36	27	0.72	1.09	3.0	2.81 ± 0.04
346	1.3	0.83	67	0.80	1.11	7.7	6.40 ± 0.08
346	1.3	0.21	67	0.80	1.11	1.9	5.88 ± 0.11
345	2.6	0.82	133	0.80	1.07	7.7	11.2 ± 0.23
345	6.6	0.98	333	0.80	1.09	9.2	19.7 ± 0.62
345	4.5	0.94	667	0.45	0.23	4.9	36.6 ± 1.14

Table 7.2. Summary of kinetic measurements for Cl + C_2H_4 using SO_2Cl_2 precursor.

T, K	τ_{res}, s	F, mJ	p, mbar	$[SO_2Cl_2]$, 10^{15} molecule cm^{-3}	$[C_2H_4]_{max}$, 10^{14} molecule cm^{-3}	$[Cl]_{0,max}$, 10^{11} molecule cm^{-3}	$k_1 \pm \sigma_{k1}$, 10^{-12} cm^3 $molecule^{-1}$ s^{-1}
297	1.7	1.15	67	1.03	1.22	6.5	8.63 ± 0.40
297	1.7	0.59	67	1.05	1.18	3.4	9.20 ± 0.34
297	1.7	2.44	67	1.05	1.18	14.2	10.8 ± 0.53
297	3.5	1.14	133	1.02	1.20	6.4	16.6 ± 0.43
297	1.8	1.14	133	1.08	1.21	6.8	18.8 ± 0.41
297	7.0	1.14	133	1.01	1.02	6.4	16.8 ± 0.78
296	1.3	1.61	27	1.10	1.12	9.8	4.51 ± 0.26
296	1.3	0.77	27	1.10	1.12	4.7	4.14 ± 0.27
296	1.3	0.36	27	1.10	1.12	2.2	4.03 ± 0.14
295	3.0	0.77	333	2.01	0.49	8.6	33.4 ± 0.78
296	3.0	0.77	333	0.20	0.50	0.9	32.8 ± 2.28
296	3.6	1.03	667	1.05	0.30	6.0	50.5 ± 1.66
296	3.6	0.48	667	1.05	0.30	2.8	51.1 ± 2.07
376	5.5	1.16	333	1.00	0.57	6.4	6.10 ± 0.29
376	5.4	0.57	333	1.00	0.57	3.2	5.78 ± 0.23
377	0.7	2.06	27	1.01	1.26	11.5	0.64 ± 0.03
377	0.7	0.92	27	1.01	1.26	5.1	0.66 ± 0.06
375	1.8	2.19	67	1.05	1.27	12.7	1.52 ± 0.07
375	1.8	0.76	67	1.05	1.27	4.4	1.57 ± 0.08
378	2.8	2.09	133	1.02	0.77	11.8	3.00 ± 0.11
377	2.7	1.97	132	0.50	0.74	5.4	2.74 ± 0.10
376	2.8	1.89	665	1.05	0.18	11.0	11.3 ± 0.36
374	5.7	1.89	667	1.08	0.18	11.3	12.5 ± 0.59

Table 7.3. Summary of kinetic measurements for Cl + C_2H_4 addition using C_6H_5Cl precursor in Ar bath gas.

T, K	τ_{res}, s	F, mJ	F*/F	p, mbar	$[C_6H_5Cl]$, 10^{14} molecule cm^{-3}	$[C_2H_4]_{max}$, 10^{14} molecule cm^{-3}	$[Cl]_{0,max}$, 10^{11} molecule cm^{-3}	$k_1 \pm \sigma_{k1}$, 10^{-12} cm^3 molecule^{-1} s^{-1}	$k_7 \pm \sigma_{k7}$, s^{-1}	$k_9 \pm \sigma_{k9}$, s^{-1}
292	1.1	0.35	0.74	133	3.19	0.38	9.6	24.9 ± 2.13		
294	0.8	0.12	0.82	39	2.31	0.87	2.4	13.6 ± 0.59		
294	1.2	0.13	0.74	133	3.01	0.38	3.4	22.8 ± 2.93		
294	1.2	0.35	0.74	133	3.01	0.38	9.1	24.3 ± 1.12		
345	1.2	0.14	0.60	132	5.09	0.85	6.1	14.2 ± 0.53		
345	1.2	0.04	0.60	132	5.09	0.85	1.8	12.8 ± 0.47		
400	0.9	0.13	0.41	27	2.95	1.05	3.3	1.63 ± 0.40	289 ± 59	66 ± 28
400	0.9	0.08	0.41	27	2.96	1.05	2.0	1.73 ± 0.18	190 ± 13	99 ± 23
401	1.0	0.11	0.35	67	2.95	2.80	2.8	4.21 ± 0.41	441 ± 78	172 ± 17
401	1.0	0.07	0.35	67	2.95	2.80	1.8	4.22 ± 0.28	453 ± 103	158 ± 28
401	1.0	0.11	0.34	27	2.85	2.98	2.7	1.16 ± 0.08	226 ± 12	119 ± 19
401	1.0	0.03	0.34	27	2.85	2.99	0.7	1.42 ± 0.32	266 ± 52	115 ± 34
402	1.0	0.09	0.61	100	3.33	1.46	2.6	6.51 ± 0.71	421 ± 120	176 ± 57
400	1.0	0.13	0.36	133	4.89	1.88	5.5	9.13 ± 0.33	374 ± 53	183 ± 32
429	0.9	0.12	0.54	27	2.91	3.78	3.0	0.72 ± 0.20	260 ± 72	123 ± 29
431	0.9	0.07	0.77	27	2.91	7.94	1.8	0.80 ± 0.36	1032 ± 249	216 ± 94
429	0.3	0.07	0.73	67	2.21	1.98	1.3	2.86 ± 1.20	470 ± 174	206 ± 85
431	0.3	0.04	0.73	67	2.26	1.94	0.8	3.49 ± 2.15	577 ± 218	243 ± 128
430	1.0	0.07	0.51	133	3.84	4.55	2.3	6.57 ± 0.34	1402 ± 262	192 ± 10

Table 7.4. Summary of kinetic measurements for Cl + C_2H_4 addition using C_6H_5Cl precursor in N_2 bath gas.

T, K	τ_{res}, s	F, mJ	p, mbar	$[C_6H_5Cl]$, 10^{14} molecule cm^{-3}	$[C_2H_4]_{max}$, 10^{13} molecule cm^{-3}	$[Cl]_{0,max}$, 10^{11} molecule cm^{-3}	$k_1 \pm \sigma_{k1}$, 10^{-12} cm^3 $molecule^{-1}$ s^{-1}
292	1.0	0.17	67	2.93	7.30	4.3	16.4 ± 1.04
292	1.0	0.3	67	2.93	7.28	7.6	16.4 ± 0.38
293	1.6	0.33	133	4.19	4.54	11.9	29.3 ± 0.99
293	1.6	0.33	133	1.42	4.63	4.0	25.2 ± 1.12
293	4.5	0.53	667	3.99	0.80	18.2	76.5 ± 8.82
293	0.9	0.31	27	3.15	13.1	8.4	7.92 ± 0.27
293	0.9	1.03	27	3.15	13.1	28.0	8.99 ± 0.31
289	0.9	0.19	27	3.08	11.2	5.1	8.96 ± 0.50
289	1.0	0.14	27	2.25	11.5	2.7	8.71 ± 0.47

Table 7.5. High- and low-pressure limiting rate constants obtained with Ar bath gas and equilibrium constant for C_2H_4 + Cl addition.

T, K	k_0, 10^{-30} cm^6 molecule^{-2} s^{-1}	k_∞, 10^{-10} cm^3 molecule^{-1} s^{-1}	K_{eq}, 10^{-15} cm^3 molecule^{-1}
293	9.8	3.6	–
345	5.8	1.8	–
401	3.6	–	8.20 ± 0.46
430	2.8	–	3.76 ± 0.58

Table 7.6. Summary of kinetic measurements for Cl + C_2H_4 abstraction using C_6H_5Cl precursor in Ar bath gas.

T, K	τ_{res}, s	F, mJ	F*/F	p, mbar	$[C_6H_5Cl]$, 10^{14} molecule cm^{-3}	$[C_2H_4]_{max}$, 10^{14} molecule cm^{-3}	$[Cl]_{0,max}$, 10^{11} molecule cm^{-3}	$k_{11} \pm \sigma_{k1}$, 10^{-13} cm^3 $molecule^{-1}$ s^{-1}
551	0.7	0.06	0.59	27	2.37	4.46	1.2	3.03 ± 0.32
551	0.7	0.03	0.59	27	2.37	4.44	0.6	2.81 ± 0.18
551	0.9	0.03	0.59	67	4.01	5.91	1.0	2.25 ± 0.10
551	0.9	0.03	0.59	67	1.40	6.15	0.4	2.41 ± 0.22
548	1.3	0.03	0.54	267	2.47	8.23	0.6	1.49 ± 0.10
555	1.2	0.03	0.77	267	1.20	8.03	0.3	1.42 ± 0.06
550	1.2	0.07	0.80	133	2.49	3.75	1.5	2.58 ± 0.16
550	1.2	0.03	0.80	133	2.49	3.75	0.6	2.39 ± 0.08
554	1.2	0.07	0.77	200	2.48	3.36	1.5	2.46 ± 0.52
554	1.2	0.03	0.77	200	2.48	3.36	0.6	2.07 ± 0.22
612	0.6	0.06	0.73	27	2.48	1.97	1.3	5.14 ± 0.38
608	1.2	0.07	0.58	267	2.59	2.14	1.6	2.94 ± 0.27
611	0.6	0.06	0.55	67	2.51	1.97	1.3	3.73 ± 0.24
611	1.2	0.06	0.55	67	2.53	2.14	1.3	3.84 ± 0.15
613	0.6	0.06	0.73	13	2.46	2.07	1.3	5.61 ± 0.39
612	1.2	0.05	0.70	133	2.47	2.18	1.1	4.23 ± 0.24
610	1.2	0.07	0.44	267	2.59	2.12	1.6	3.19 ± 0.64
610	1.2	0.07	0.44	133	2.43	2.19	1.5	4.64 ± 0.15
610	1.2	0.07	0.80	200	2.49	3.80	1.5	2.67 ± 0.07
676	0.7	0.06	0.62	67	3.27	3.47	1.7	7.92 ± 0.43
676	0.7	0.02	0.62	67	3.27	3.47	0.6	7.62 ± 0.29
676	0.8	0.06	0.62	67	1.14	3.61	0.6	7.90 ± 0.22
798	0.7	0.03	0.66	67	0.88	4.38	0.2	16.8 ± 0.83
798	0.7	0.03	0.66	67	2.84	4.23	0.7	18.0 ± 0.70
798	0.5	0.06	0.68	27	2.11	2.74	1.1	19.0 ± 1.23
798	0.5	0.03	0.68	27	2.11	2.74	0.5	19.4 ± 0.90
902	0.4	0.04	0.69	27	2.08	1.36	0.7	26.8 ± 3.74
902	0.4	0.02	0.69	27	2.09	1.36	0.4	25.2 ± 3.64
902	0.7	0.04	0.69	67	1.13	2.22	0.4	29.0 ± 1.68
902	0.6	0.04	0.69	67	3.21	2.08	1.1	31.4 ± 2.97

(Table continues on next page)

(Table 7.6. Continued)

T, K	τ_{res}, s	F, mJ	F*/F	p, mbar	$[C_6H_5Cl]$, 10^{14} molecule cm^{-3}	$[C_2H_4]_{max}$, 10^{14} molecule cm^{-3}	$[Cl]_{0,max}$, 10^{11} molecule cm^{-3}	$k_{11} \pm \sigma_{k1}$, 10^{-13} cm^3 $molecule^{-1}$ s^{-1}
900	0.8	0.04	0.63	267	2.40	2.65	0.8	22.0 ± 1.80
900	1.6	0.04	0.63	267	2.77	2.83	1.0	30.1 ± 2.75
1007	0.7	0.06	0.74	267	2.53	1.52	1.3	37.6 ± 3.02
1007	1.4	0.06	0.74	267	2.48	1.49	1.3	33.0 ± 5.18
1052	1.3	0.05	0.75	267	2.75	1.23	1.2	49.7 ± 11.0
1058	0.7	0.06	0.72	267	2.69	1.21	1.4	52.6 ± 3.94

Table 7.7. Weighted mean k_{11} values for Cl + C_2H_4 abstraction with statistical uncertainties.

T, K	$k_{11} \pm \sigma_{k11}$, 10^{-13} cm^3 molecule^{-1} s^{-1}
551	1.90 ± 0.04
611	3.29 ± 0.05
676	7.81 ± 0.16
798	18.1 ± 0.43
901	26.9 ± 0.97
1007	36.4 ± 2.61
1055	52.3 ± 3.71

Table 7.8. Energies and zero point energies in E_H for species in the C_2H_4Cl reaction system.

[a]Species	Electronic Energy QCISD/ 6-311G(d,p)	Unscaled ZPE QCISD/ 6-311G(d,p)	[b]Scalar Relativistic correction	[c]Core-Valence correction	Electronic Energy CCSD(T)/ aug-cc-pVTZ	Electronic Energy CCSD(T)/ aug-cc-pVQZ	Electronic Energy aug-CBS	[d]Total Energy
H	-0.49981	0	-0.00001	0	-0.49982	-0.49995	-0.50004	-0.50005
Cl	-459.60167	0	-1.40334	-0.30271	-459.67619	-459.69471	-460.70822	-461.41561
C_2H_4	-78.37291	0.05100	-0.02940	-0.09688	-78.44373	-78.46352	-78.47795	-78.55559
HCl	-460.26032	0.00695	-1.40294	-0.30305	-460.34324	-460.36417	-460.37944	-462.07881
C_2H_3	-77.69179	0.03685	-0.02943	-0.09663	-77.75764	-77.77613	-77.78962	-77.88052
C_2H_3Cl	-537.43393	0.04289	-1.43230	-0.39992	-537.58490	-537.62517	-537.65456	-539.44585
H_2	-1.16834	0.01007	-0.00001	0.00000	-1.17264	-1.17387	-1.17476	-1.16517
A1	-537.98044	0.05260	-1.43276	-0.39956	-538.13103	-538.16986	-538.19819	-539.98033
Add TS	-537.98011	0.05213	-1.43274	-0.39953	-538.13214	-538.17103	-538.19941	-539.98195
Beta	-537.99909	0.05284	-1.43230	-0.39968	-538.14916	-538.18876	-538.21766	-539.99922
Iso TS	-537.92412	0.04813	-1.43224	-0.39982	-538.07908	-538.11932	-538.14868	-539.93482
Alpha	-538.00469	0.05282	-1.43222	-0.39984	-538.15457	-538.19475	-538.22407	-540.00575
Dis TS1	-537.92384	0.04466	-1.43231	-0.39979	-538.07786	-538.11806	-538.14739	-539.93689
Dis TS2	-537.92855	0.04436	-1.43230	-0.39985	-538.08232	-538.12264	-538.15207	-539.94191
Elim TS	-537.88278	0.04603	-1.43241	-0.39939	-538.04242	-538.08187	-538.11066	-539.89855
Abs TS	-537.94972	0.04331	-1.43241	-0.39979	-538.10337	-538.14257	-538.17118	-539.96207
A2	-537.95548	0.04511	-1.43233	-0.39973	-538.10554	-538.14478	-538.17342	-539.96245
t-β-C_2H_2Cl	-536.75075	0.02940	-1.43236	-0.39960	-536.89674	-536.93569	-536.96412	-538.76804
c-β-C_2H_2Cl	-536.74889	0.02909	-1.43235	-0.39964	-536.89462	-536.93369	-536.96219	-538.76643
α-C_2H_2Cl	-536.75541	0.02968	-1.43235	-0.39964	-536.90208	-536.94129	-536.96990	-538.77358

[a] See text or Figures 7.11 and 7.12 for nomenclature.
[b] Correction was calculated with CISD/cc-pwVTZ theory (see text).
[c] Correction was calculated with CCSD/cc-pwVTZ theory (see text).
[d] Energy calculated by adding scaled ZPE, scalar relativistic and core-valence corrections, and a correction of -0.00134 for Cl-atom spin-orbit coupling to aug-CBS electronic energy (see text).

Table 7.9. Data for MEP of torsion in the β-chloroethyl radical.

D_1 (Degrees)	Relative E (kJ mol^{-1})	D_2 (Degrees)	I_{red} (amu $Å^2$)
0	7.72	180	1.741
10	7.49	185	1.744
20	6.83	185	1.745
30	5.96	185	1.745
40	4.98	180	1.739
50	3.46	165	1.752
60	1.78	160	1.767
70	0.56	160	1.767
80	0.03	165	1.753
90	0.23	165	1.753
100	0.89	170	1.742
110	1.85	175	1.732
120	2.84	180	1.736
130	3.72	185	1.739
140	4.42	190	1.749
150	5.04	195	1.762
160	5.73	195	1.764
170	6.60	200	1.780
[a]180	[a]7.64	[a]165	[a]1.762

[a] The values in this row were replaced with those from the row corresponding to $D_1 = 0°$ in the calculation of energy levels (see text).

Table 7.10. Calculated entropy, heat capacity, and integrated heat capacity of the torsion mode in the β-chloroethyl radical.

T / K	S° / J mol^{-1} K^{-1}	C_p° / J mol^{-1} K^{-1}	ΔrC_p° / kJ mol^{-1}
298.15	18.58	8.63	2.00
350	19.91	7.96	2.43
400	20.94	7.39	2.81
450	21.78	6.90	3.17
500	22.48	6.50	3.51

Table 7.11. Data for MEP of torsion in the α-chloroethyl radical.

D_1 (Degrees)	Relative E (kJ mol^{-1})	D_2 (Degrees)	I_{red} (amu $Å^2$)
0	5.17	180	3.049
10	4.61	195	3.052
20	3.35	200	3.056
30	1.89	205	3.06
40	0.60	205	3.063
50	0.03	205	3.065
60	0.33	205	3.064
70	1.42	205	3.062
80	2.28	180	3.057
90	3.27	180	3.053
100	4.23	180	3.052
110	4.92	180	3.05
120	5.17	180	3.049

Table 7.12. Calculated entropy, heat capacity, and integrated heat capacity of the torsion mode in the α-chloroethyl radical.

T / K	S° / J mol^{-1} K^{-1}	C_p° / J mol^{-1} K^{-1}	ΔrC_p° / kJ mol^{-1}
298.15	22.45	7.02	1.91
350	23.53	6.44	2.26
400	24.36	5.99	2.57
450	25.04	5.61	2.86
500	25.62	5.28	3.13

Table 7.13. Comparison of computed bond dissociation enthalpies for C-H bond in ethylene with various composite methods at 0 K (kJ mol^{-1}).

Method	$BDE_0(C_2H_3\text{-}H)$
[a]G3	454.3
[a]G3X	453.6
[a]G3(MP2)	453.4
[a]G3X(MP2)	452.4
[a]CBS-QB3	459.9
[a]G3-RAD	455.8
[a]G3X-RAD	456.4
[a]G3(MP2)-RAD	452.3
[a]G3X(MP2)-RAD	452.9
[a]CBS-RAD	461.1
[b]CCSD(T)/CBS-aug	459.0
Experimental Values	458.8 ± 3.3[c]

[a] Calculated based on computed enthalpies of formation given in reference [197]. [b] See Text. [c] Reference [177].

Table 7.14. Energy transfer parameters, hindered Gorin-type transition state properties, high- and low- pressure limiting rate constants, and equilibrium constant for the MultiWell RRKM analysis of the C_2H_4 + Cl = β-chloroethyl radical reaction at 293 K.

Pressure (bar)	0.027	0.067	0.133	0.333	0.533	0.667	1.0	10.0	100.0	1000.0
[a]k_0^{SC} (10^{-30} cm^6 molec^{-2} s^{-1})	16.7	16.7	16.7	16.7	16.7	16.7	16.7	16.7	16.7	16.7
[b]k_0^{SC} (10^{-30} cm^6 molec^{-2} s^{-1})	19.0	19.0	19.0	19.0	19.0	19.0	19.0	19.0	19.0	19.0
[a,b]$k_{\infty,uni}$ (s^{-1})	31.0	31.0	31.0	31.0	31.0	31.0	31.0	31.0	31.0	31.0
[a,b]$k_{\infty,rec}$ (10^{-10} cm^3 molec^{-1} s^{-1})	3.53	3.53	3.53	3.53	3.53	3.53	3.53	3.53	3.53	3.53
[a]k_{rec} (10^{-11} cm^3 molec^{-1} s^{-1})	0.58	1.31	2.37	4.88	6.81	7.93	10.22	26.11	33.85	35.12
[b]k_{rec} (10^{-11} cm^3 molec^{-1} s^{-1})	0.80	1.78	3.15	6.34	8.66	9.98	12.59	28.26	34.28	35.17
K_c (10^{-11} cm^3 molec^{-1})	1.14	1.14	1.14	1.14	1.14	1.14	1.14	1.14	1.14	1.14
[a]$\langle\Delta E\rangle_{down}$ (cm^{-1})	759.9	759.9	759.9	759.9	759.9	759.9	759.9	759.9	759.9	759.9
[a]c_2 (cm^{-1})	0.117	0.117	0.117	0.117	0.117	0.117	0.117	0.117	0.117	0.117
[b]$\langle\Delta E\rangle_{down}$ (cm^{-1})	1245.1	1245.1	1245.1	1245.1	1245.1	1245.1	1245.1	1245.1	1245.1	1245.1
[b]c_2 (cm^{-1})	0.196	0.196	0.196	0.196	0.196	0.196	0.196	0.196	0.196	0.196
[a,b]r_{max} (Å)	3.31	3.31	3.31	3.31	3.31	3.31	3.31	3.31	3.31	3.31
[a,b]Hindrance Parameter (γ)	0.355	0.355	0.355	0.355	0.355	0.355	0.355	0.355	0.355	0.355
[a,b]K-Rotor (amu Å^2)	15.5	15.5	15.5	15.5	15.5	15.5	15.5	15.5	15.5	15.5
[a,b] $\gamma \times I_{2D}$ (C_2H_4) (amu Å^2)	6.60	6.60	6.60	6.60	6.60	6.60	6.60	6.60	6.60	6.60
[a,b]J-Rotor (amu Å^2)	170.6	170.6	170.6	170.6	170.6	170.6	170.6	170.6	170.6	170.6

[a] Pertaining to Ar bath gas.
[b] Pertaining to N_2 bath gas.

Table 7.15. Energy transfer parameters, hindered Gorin-type transition state properties, and rate constants for reaction 7.11.

T (K)	298.15	350	400	500	700	1000	1500
r_{max} (Å)	6.20	6.07	5.96	5.78	5.49	5.16	4.70
Hindrance Parameter (γ)	0.487	0.498	0.509	0.524	0.554	0.591	0.650
Hindrance Parameter (η)	0.763	0.752	0.741	0.726	0.694	0.651	0.578
K-Rotor (amu Å^2)	14.7	14.7	14.7	14.7	14.7	14.7	14.7
$\gamma \times I_{2D}$ (C_2H_3) (amu Å^2)	8.14	8.32	8.51	8.74	9.25	9.87	10.85
$\gamma \times I_{2D}$ (HCl) (amu Å^2)	0.78	0.80	0.82	0.84	0.89	0.95	1.04
J-Rotor (amu Å^2)	593.21	568.83	548.69	515.31	465.22	411.07	340.21
$<\Delta E>_{down}$ (cm^{-1})	427.3	463.4	498.1	567.6	706.6	915.1	1262.6
c_2 (cm^{-1})	0.61	0.71	0.83	1.17	1.72	2.18	2.29
[a]$k_{a(HS)}$ (cm^3 $molec^{-1}$ s^{-1})	4.90E-10	5.31E-10	5.68E-10	6.35E-10	7.51E-10	8.98E-10	1.10E-9
[b]$k_{\infty,uni}$ (s^{-1})	1.62E12	2.46E12	3.32E12	4.76E12	6.85E12	8.40E12	9.00E12
[c]$k_{\infty,a}$ (cm^3 $molec^{-1}$ s^{-1})	5.05E-10	5.42E-10	5.85E-10	6.44E-10	7.62E-10	9.13E-10	1.11E-9
[c]k_a (cm^3 $molec^{-1}$ s^{-1})	9.72E-12	7.97E-12	6.94E-12	5.42E-12	4.09E-12	3.75E-12	3.97E-12
[d]K_c (cm^3 $molec^{-1}$)	3.12E-22	2.20E-22	1.76E-22	1.35E-22	1.11E-22	1.09E-22	1.23E-22
[e]K_{eq}	9.77E-5	7.373E-4	3.19E-3	2.53E-2	2.72E-1	1.57	5.71
[f]k_{11} (cm^3 $molec^{-1}$ s^{-1})	9.49E-16	5.88E-15	2.22E-14	1.37E-13	1.11E-12	5.91E-12	2.26E-11
Wigner Tunneling Correction	1.76	1.55	1.42	1.27	1.14	1.07	1.03

[a] Rate constants for C_2H_3 + HCl = A2 obtained from hard sphere model.
[b] Rate constants for A2 = C_2H_3 + HCl via Gorin-type TS.
[c] Rate constants for C_2H_3 + HCl = A2 via Gorin-type TS.
[d] Equilibrium constant for C_2H_3 + HCl = A2.
[e] Equilibrium constant for C_2H_4 + Cl = C_2H_3 + HCl.
[f] Does not include Wigner tunneling correction.

CHAPTER 8

OVERVIEW AND CONCLUSIONS

Absolute rate constants for the gas phase kinetics of the chlorine atom reactions with hydrogen sulfide, ammonia, benzene, and ethylene have been measured using the laser flash photolysis experimental technique coupled with resonance fluorescence. These measurements span a large range of conditions, and the results offer new accurate kinetic and thermodynamic information for use in the fields of atmospheric and combustion chemistry. More specifically, these comprehensive studies provide fundamental insight into important chemical details used to interpret a system's reactivity, such as the nature of the transition state and the associated activation energy, through the determination of Arrhenius parameters. In addition, investigations of the kinetics of the reverse processes of some of the elementary reactions studied, either by working at optimal conditions for the direct observation of equilibration or from a separate set of measurements of the rate constants for the reverse reactions, enabled access to the system's thermochemistry, which can be used to gauge its stability.

The Third-Law method has been used to obtain the enthalpy of the abstraction reaction involving C_6H_5 and HCl, and the addition of Cl to C_2H_4. These reaction enthalpies were then used in conjunction with other known thermochemical quantities to evaluate the C-H bond strengths in benzene and ethylene, and the enthalpies of formation for the phenyl and β-chloroethyl radicals, which resulted in the most precise determinations of these quantities to date. These analyses indicate that the C-H bond in benzene is stronger than its counterpart in ethylene

by 7.0 ± 4.1 kJ mol^{-1}. In addition, high-level *ab initio* computations indicate that the Cl-C_2H_4 bond in the β-chloroethyl radical is stronger than the Cl-C_6H_6 bond in the σ η_1-chlorocyclohexadienyl radical, with a difference between the two respective BDEs at 0 K of ~44 kJ mol^{-1}. This difference between the BDEs is attributed to the fact that the formation of σ η_1-chlorocyclohexadienyl radical is accompanied by the unfavorable loss of aromaticity, though the reduction in stability is less than typically expected for this process due to the large extent of delocalization still present in the π-system of the σ η_1-chlorocyclohexadienyl radical.

Perhaps one of the most intriguing findings, shared by all four of the reaction systems studied, has been that the overall abstraction reactions of H by Cl, or the corresponding reverse processes involving HCl, have negative activation energies. This negative activation energy was measured directly for the two exothermic abstraction reactions studied, Cl + H_2S and HCl + C_6H_5, and inferred for the reverse processes of the reactions between Cl + NH_3 and C_2H_4, where the measured positive activation energy was found to be smaller than the overall endothermicity. The latter observations challenge the assumption that in the case of endothermic reactions, the thermochemistry can be used to set a lower bound to the activation energy. This assumption is generally legitimate in the case of adduct dissociation, in which there is usually little or no barrier beyond the endothermicity, but is clearly invalid for cases involving classical abstraction reactions. The observed pressure independence of these reactions confirms that a stabilized adduct is not the product, however, this is not evidence against the idea that an energized adduct might participate in the mechanism. The activation energy is defined as the slope of a plot of the natural logarithm of the rate constant against the reciprocal temperature. Fundamentally, when this quantity has a positive value, it can be used as a measure of the energy penalty for the electronic rearrangement associated with going from the reactants to the products in a given

reaction. This energy penalty can also be interpreted as the energetic "barrier" that must be overcome in order to form the final products. Consequently, the negative activation energies observed for the reactions studied here indicate that these reactions occur without an apparent energy barrier. Theoretically, RRKM calculations have revealed that a large fraction of the energized adduct dissociates back to the reactants, and that as the temperature is raised, this fraction increases. This phenomenon leads to a negative temperature dependence for product formation via chemical activation, and rationalizes the observed negative activation energies.

The stability and reactivity of each reaction system was further rationalized based on computed potential energy surfaces, obtained with high-level *ab initio* quantum mechanical methods and refined through the consideration of the effects arising from the special theory of relativity. Despite the fact that high-level *ab initio* methods have been repeatedly shown to compute thermochemistry of chemical accuracy caliber (within 4 – 9 kJ mol^{-1} of the corresponding experimental quantity), composite methods based on the UHF-analogues of these *ab initio* theories were found to be inadequate for accurately calculating the thermochemistry of species in the C_6H_6Cl reaction system. This inadequacy has been linked with the extent of spin-contamination that arises in the UHF ground-state wavefunction of the phenyl radical, which is the only reference used by more refined single-reference *ab initio* theories to evaluate a series of excited configurations as a means of accounting for electron correlation. As discussed in a review of this phenomenon by Bally and Borden, in systems such as the phenyl radical, in which the singly occupied MO possesses nodes at some nuclei and the subjacent doubly occupied bonding MO is high in energy and is easily polarized (typical of π-MOs), the doublet wavefunction may become severely spin-contaminated due to spin polarization effects.[17]

Technically, neither UHF nor ROHF wavefunctions are eigenfunctions of the S^2 operator, however, spin-adapted ROHF wavefunctions that are eigenfunctions of the S^2 operator can be constructed from the appropriate linear combinations of the original ROHF wavefunctions, while UHF wavefunctions cannot be spin-adapted.[248] So, by comparing the expectation values that result from the operation of the S^2 operator on a UHF wavefunction to the eigenvalues that are normally obtained in the case of spin-adapted ROHF eigenfunctions, it is possible to assess the extent of spin-contamination in the UHF wavefunctions. In the case of the phenyl radical, the UHF wavefunction has an expectation value $\langle S^2 \rangle = 1.39$ rather than the ideal value of 0.75, which indicates that the UHF wavefunction is severely spin-contaminated.

In chapter 6, normally accurate composite methods were found to be significantly impacted by the severe spin-contamination associated with the phenyl radical, and it was shown through the systematic breakdown of the steps within these composite methods, that the largest source of error comes from the use of spin-contaminated UHF-based QCISD or CCSD(T) single-point energy calculations. This observation led to the formulation of a composite method in which the single-point calculations relied on a ROHF reference wavefunction. This method, commonly denoted as CCSD(T)/CBS throughout this dissertation, is discussed in detail in chapter 3. In short, it relies on UQCISD/6-311G(d,p) geometries and frequencies, and performs single-point energy calculations with RCCSD(T) theory in conjunction with the correlation-consistent basis sets, which are then extended to the complete basis set limit. RCCSD(T)/CBS theory was also used when computing the properties of species on the C_2H_4Cl PES, as the vinyl radical was also found to have a considerably spin-contaminated wavefunction ($\langle S^2 \rangle = 0.98$). For the H_2SCl and NH_3Cl projects, the extent of spin-contamination was negligible as all species on the respective PESs were found to have $\langle S^2 \rangle$ values of less than 0.80, so the UHF-analogue

of CCSD(T)/CBS theory was conveniently used. The use of RCCSD(T)/CBS and UCCSD(T)/CBS theories has provided more accurate and extensive thermodynamic information for the systems of interest than was previously available in the literature, which led to important findings for each system: the possibility of an addition-elimination mechanism in H_2S + Cl, the unlikelihood of a proton-coupled electron transfer mechanism for the NH_3 + Cl reaction, the identification of the σ chlorocyclohexadienyl radical as the most stable among chlorocyclohexadienyl species, and further evidence that the enthalpy of formation for the vinyl radical is more in line with the value from recent kinetic and spectroscopic determinations, with which the computed result agreed exactly, rather than the old value from previous kinetic determinations.

Furthermore, the accurate potential energy surfaces computed with CCSD(T)/CBS theory also found all of the aforementioned abstraction reactions to be barrierless, and further revealed that the principal reaction mechanism in each case, does in fact involve the excitation of an adduct via chemical activation followed by the passage through a low-lying TS to yield the products. Though rate constants can be conveniently obtained directly from the PES via simple conventional TST, in the case of a chemical activation scenario, TST has been shown to be unsuitable.[76,77] For reactions which proceed through chemical activation, and as a consequence of microscopic reversibility, also for the reverse processes of such reactions, TST inevitably leads to unrealistic rate constants due to the inclusion of the contributions from states in the TS which lie below the critical energy, which would not be populated until extremely large pressures. The erroneous counting of these low-lying states in the calculation of the partition function of the TS results in theoretical rate constants that can considerably overestimate rate constants measured at normal pressures.

The observed pressure independence for the abstraction channels confirms that a stabilized adduct is not the product, however, this is not evidence against the idea that an energized adduct might participate in the mechanism. Therefore MTST, an appropriate adaptation of TST which excludes the contributions of the inaccessible states in the TS to the rate constant, or an RRKM treatment which relied on the stochastic evaluation of a hybrid master equation, were used to examine the nature of the competition between the collisional stabilization and the dissociation to products of the energized adduct. MTST analyses were carried out only for the NH_3Cl and C_6H_6Cl systems, in both cases by Dr. Lev Krasnoperov, a collaborator on the two projects, and the results obtained were in reasonable accord with experiment. For the NH_3Cl system, the MTST analysis was performed on an initial PES obtained with DFT, and it was subsequently shown through the evaluation of the upper bound to the MTST result via conventional TST, that a future MTST analysis of the previously unavailable coupled-cluster PES is expected to generate rate constants which should be in very good agreement with experiment. This conclusion was also reached for the C_2H_4Cl system based on similar considerations, so it is likely that MTST will also be applied to this system in the future. In the case of the C_6H_6Cl system, where a CCSD(T)/CBS PES was used in the MTST treatment, the agreement between the MTST rate constant and experiment is likely to be improved by the future treatment of the loose internal modes identified in the TS as anharmonic oscillators.

MultiWell-based RRKM analyses had only modest success in producing thermal rate constants in quantitative accord with experiment. In the H_2SCl system, the RRKM analysis yielded rate constants that were actually within a factor of 2 at room temperature, but due to the computed non-Arrhenius temperature behavior for abstraction, which is in qualitative

disagreement with the observed temperature dependence, this overestimation became more significant at the high end of the temperature range. The qualitative discord between the temperature dependences of the observed and computed rate constants, as well as the resultant quantitative disagreement at high temperatures, are issues which are currently being investigated further in collaboration with Dr. David Golden of Stanford University.

Similar MultiWell-based RRKM calculations were conducted based on the chemical activation PESs for the NH_3Cl, C_6H_6Cl, and C_2H_4Cl systems. These analyses relied on a hindered Gorin treatment of the loose TS at the entrance channel, in which the hindrance parameters were set by matching the hard sphere collision rate coefficient. The resulting rate constants exhibited temperature dependences that were in qualitative accord with experiment, though they overestimated the experimental results in each case, indicating that the crude hard sphere rate constants used to set the hindrance parameters may be unreasonably large. This idea was tested in the case of of C_6H_5 + HCl, and it was found that empirically reducing the rate constants used to calculate hindrance parameters yields results which are in good agreement with experiment. The application of this formalism to NH_3Cl and C_2H_4Cl systems in the future is also expected to improve the agreement with experiment, and more efforts are needed for a more reasonable evaluation of the collision rate constant used to set hindrance parameters, such as the potential VTST treatment used in the case of the H_2SCl system in chapter 4.

Finally, MultiWell-based RRKM calculations reproduced the observed fall-off behavior in the case of the addition of Cl to C_2H_4, though the resultant collision efficiencies computed for the Ar and N_2 bath gases were about a factor of 2 larger than one would expect. Of course, given the uncertainty in the experimental high- and low- pressure limiting rate constants empirically determined from Troe fits using an approximate broadening factor, as well as the somewhat

arbitrary choice of Lennard-Jones parameters and assumed simple exponential-down model for the process of collisional energy transfer, the computed collision efficiencies can be said to be quite reasonable. Furthermore, aside from having better hindrance and energy transfer parameters from which to choose, it is expected that the use of a RRKM formalism in which the master equation takes into account not just vibrational states, but also the conservation of angular momentum, which requires solving a two-dimensional master equation, will yield more accurate results for all of the systems considered in this work.

APPENDIX A

CALIBRATION AND UNITS OF MASS FLOW CONTROLLERS

A1. Measurement of Flow Rate

Mass flow controllers are used to measure and control the rates of flow of gases into the reactor. Mass flow controllers are composed of an inlet port, a mass flow sensor, a proportional control valve, and an outlet port. As gas enters a mass flow controller through the inlet port, the mass flow sensor measures the amount of the gas in terms of the voltage signals generated by its mass. These voltage signals are then used by the mass flow sensor to adjust the proportional control valve such that the amount of gas exiting the outlet port matches the preset amount input by the operator. Though analog mass flow controllers are designed to be used exclusively with a specific gas, digital mass flow controllers can often be calibrated and used to control a range of gases.

The mass flow controllers measure the flow rate in units of standard cm^3 per minute (sccm). This unit is simply the volume flow of a certain gas per unit time under standard conditions. Specifically, the sccm is a unit describing the flow rate of 1 cm^3 of gas per minute at the standard pressure and temperature of 1 atm and 20 °C, respectively. The use of standard units of measurement is convenient because it facilitates the comparison of measurements taken under different conditions.

The conversion of sccm to more conventional units can be achieved through the manipulation of the Ideal Gas Law. As a practical example, the flow rate range of 100 to 1000 sccm, which is typically used in our experiments for the Ar bath gas, will be converted here to $\mu mol\ s^{-1}$. First, the Ideal Gas Law must be rearranged so that it can be solved in terms of the number of moles n, as below.

$$n = \frac{PV}{RT} \tag{A1}$$

In equation A1, P is the standard pressure of 101,325 Pa (1 atm), T is the standard temperature of 293.15 K (20 °C), R is the gas constant 8.314 J mol^{-1} K^{-1}, and V is the volume of gas desired, which in this case is 1.0×10^{-4} m^3 (100 cm^3). Solving equation A1 based on the quantities given above, n is found to be 4.16×10^{-3} mol, which is the amount of gas flowed per minute. This quantity is the same as 69.3 μmol s^{-1}, and similarly, it can be shown that 1000 sccm is 693 μmol s^{-1}, so the range of 100 to 1000 sccm corresponds to ~ 70 – 700 μmol s^{-1}.

A2. Calibration of Mass Flow Controllers

A Teledyne Hastings-Raydist bubble meter (HBM-1-A) was used to calibrate the mass flow controllers for Ar. The calibration relies on accurately measuring the amount of time it takes a flow controller to flow a specific volume of gas, converting this flow rate to that which would occur under standard conditions, and comparing this actual flow rate to the one for which the flow controller was manually preset. This is achieved by connecting the outlet port of the flow controller to the bubble meter and monitoring the amount the ensuing bubble is displaced up the graduated cylinder of the bubble meter.

Tables A1 – 4 contain the flow data for the four mass flow controllers calibrated. The actual flows given in the last column of Tables A1 – 4 was calculated via equation A2, in which V are the volumes in the second columns and t are the times in the third columns. Because the local pressure measured is not directly comparable to the barometric pressure usually reported at standard conditions, gravity, temperature, and water vapor corrections were made to the room pressure (746.0 torr) to yield the final laboratory pressure at standard conditions.[249-251] However, the pressure was not corrected for elevation in relation to sea level. Specifically, the standard gravity is the nominal acceleration due to gravity at the Earth's surface at a latitude of 45.5°,

9.80665 m s^{-2}, the standard temperature is 293.15 K, and the water vapor pressure at that temperature is subtracted from the atmospheric pressure in order to yield standard conditions in a "dry" environment (zero water vapor pressure), attaining an entirely standardized reference set of conditions denoted Standard Temperature Pressure Dry (STPD).[252,253] These corrections were -0.711, -3.024, and -23.876 torr for gravity, temperature, and water vapor effects, respectively, and were derived by interpolating between the appropriate values given in the relevant tables of the bubble meter manual.[252] The ratios of the corrected room pressure P (718.4 torr) to standard pressure P_s (760 torr) and of the standard temperature T_s (293.15 K) to the room temperature T (298.15 K) are used to convert the actual flow rate to flow rate under standard conditions.

$$\text{Actual Flow Rate} = \frac{V}{t} \times \frac{P}{P_s} \times \frac{T_s}{T} \qquad \text{(A2)}$$

The reproducibility of the gas flows was graphically evaluated by plotting the actual flows (F) against the flows displayed by the mass flow controllers (F'), with the inclusion of the origin (0,0). It was found that the slopes of linear plots of F versus F' were not statistically different than those of graphs where F was constrained to be proportional to F', and that the correlation coefficients, which are often interpreted as a measure of the "goodness" of the fit, were the same for both the linear and the proportional fits for each flow controller. Therefore, the proportional relation between F and F' was selected for convenience, as this simplifies the error analysis and allows the slopes of such graphs to be essentially used as scaling factors. Table A5 gives the slopes, the uncertainties in the slopes, and the correlation coefficients of each of the four graphs in which the actual flow rates were constrained to be proportional to the displayed flow rates. The four proportional graphs are shown in Figures A1 – 4. The uncertainty in the slopes was obtained using a linear least squares fitting algorithm.[120]

Table A1. Flow rate data from the calibration of mass flow controller 1.

Displayed Flow (sccm)	Volume (cm^3)	Time (min)	Actual Flow (sccm)
2	1	1.188	0.783
2	1	1.214	0.766
2	1	1.235	0.753
5	4	1.815	2.048
5	3	1.378	2.023
5	2	0.915	2.031
10	4	0.872	4.265
10	3	0.642	4.342
10	4	0.869	4.279
15	7	0.991	6.564
15	7	0.988	6.586
15	7	0.990	6.574
19	9	0.997	8.391
19	9	0.992	8.432
19	9	0.994	8.414

Table A2. Flow rate data from the calibration of mass flow controller 2.

Displayed Flow (sccm)	Volume (cm^3)	Time (min)	Actual Flow (sccm)
2	1	0.914	1.017
2	1	0.914	1.017
2	1	0.918	1.012
5	3	0.983	2.835
5	3	0.976	2.856
5	3	0.980	2.845
10	5	0.776	5.987
10	5	0.774	6.003
10	5	0.780	5.959
20	10	0.758	12.267
20	10	0.761	12.218
20	10	0.758	12.256
49	30	0.907	30.741
49	30	0.914	30.500
49	30	0.905	30.797

Table A3. Flow rate data from the calibration of mass flow controller 3.

Displayed Flow (sccm)	Volume (cm^3)	Time (min)	Actual Flow (sccm)
2	4	1.100	3.379
2	4	1.097	3.390
2	4	1.100	3.379
5	10	0.892	10.415
5	10	0.888	10.472
5	10	0.888	10.462
10	20	0.838	22.190
10	20	0.833	22.319
10	20	0.835	22.265
20	50	1.025	45.322
20	50	1.024	45.395
20	50	1.025	45.359
50	100	0.819	113.456
50	100	0.818	113.595
50	100	0.821	113.249
80	200	1.030	180.407
80	200	1.008	184.404
80	200	0.995	186.813

Table A4. Flow rate data from the calibration of mass flow controller 4.

Displayed Flow (sccm)	Volume (cm^3)	Time (min)	Actual Flow (sccm)
100	30	1.041	26.775
100	30	1.029	27.096
100	30	1.030	27.070
500	200	0.903	205.884
500	200	0.906	205.202
500	200	0.902	206.151
1000	400	0.860	432.110
1000	400	0.866	429.200
1000	400	0.866	429.365
1500	600	0.856	651.573
1500	600	0.859	649.171
1500	600	0.858	649.927
3000	1000	0.721	1289.038
3000	1000	0.718	1295.326
3000	1000	0.719	1292.923

Table A5. Slopes, uncertainties, and correlation coefficients for the actual flow vs. displayed flow proportional fits.

Flow Controller (#)	Slope	Uncertainty	Correlation Coefficient (R^2)
1	0.438	0.002	0.99982
2	0.623	0.002	0.99995
3	2.288	0.008	0.99984
4	0.431	0.001	0.99992

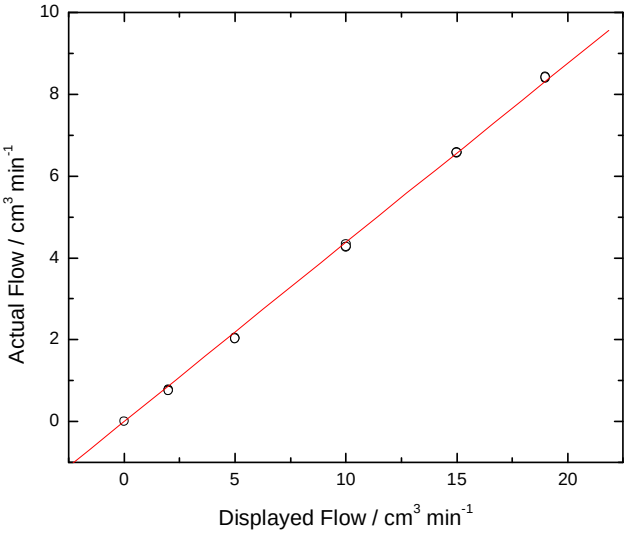

Figure A1. Actual flow vs. displayed flow data for flow controller 1. The line represents the constrained proportional fit.

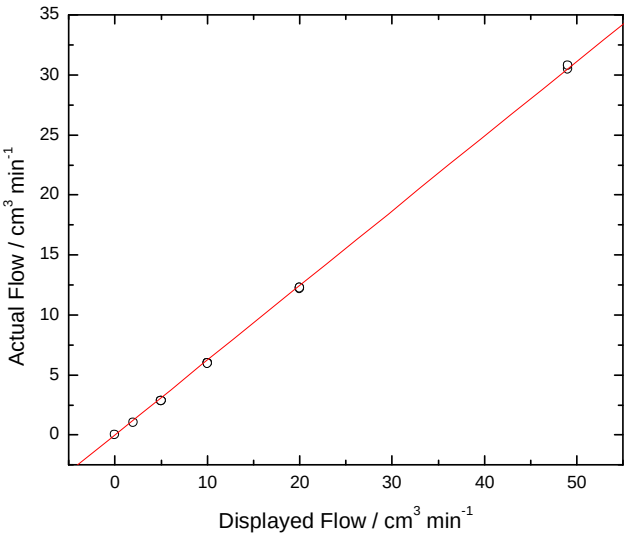

Figure A2. Actual flow vs. displayed flow data for flow controller 2. The line represents the constrained proportional fit.

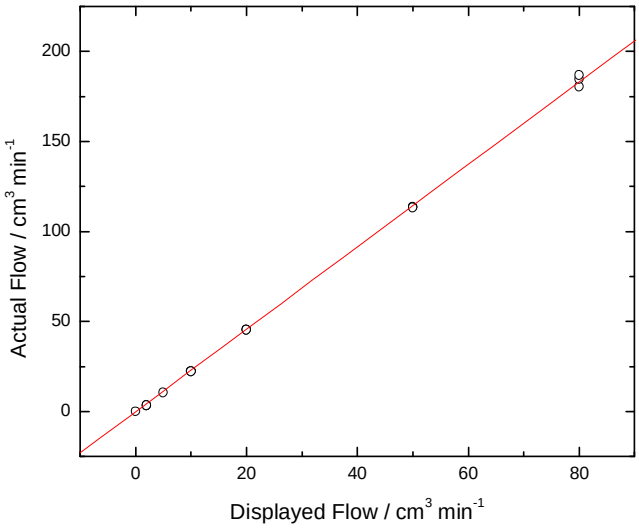

Figure A3. Actual flow vs. displayed flow data for flow controller 3. The line represents the constrained proportional fit.

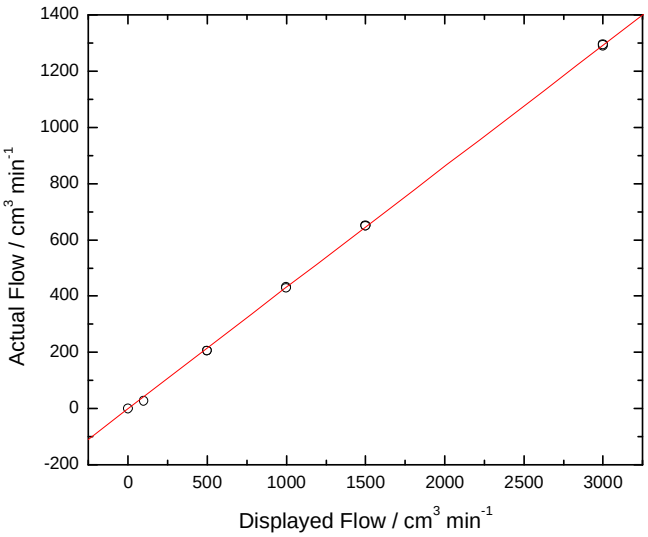

Figure A4. Actual flow vs. displayed flow data for flow controller 4. The line represents the constrained proportional fit.

APPENDIX B

TREATMENT OF UNCERTAINTY

B1. Uncertainty in Reactant Concentration and the Second Order Rate Constant

The reaction between Cl atoms and benzene will be used as an example throughout this discussion, and the general uncertainty treatment outlined in this section has been applied to the projects involving chlorine atoms with ammonia (chapter 5) and benzene (chapter 6). The concentration of benzene is calculated based on its partial pressure using the ideal gas law relation

$$[C_6H_6] = \frac{n}{V} = \frac{P_{C_6H_6}}{RT} \qquad \text{(B1)}$$

where R is the gas constant and has a value of 1.036×10^{-19} torr cm^3 $molecule^{-1}$ K^{-1}. The partial pressure of benzene is obtained from

$$P_{C_6H_6} = \frac{P_{C_6H_6(bulb)}}{P_{tot(bulb)}} \times \frac{F_{C_6H_6}}{F_{tot}} \times P_{tot} = a_{bulb} \times \frac{F_{C_6H_6}}{F_{tot}} \times P_{tot} \qquad \text{(B2)}$$

where a_{bulb} is the ratio between the pressure of benzene and the total pressure in the bulb upon dilution with Argon. Combining the above results yields

$$[C_6H_6] = \frac{a_{bulb} \times \frac{F_{C_6H_6}}{F_{tot}} \times P_{tot}}{R \times T} \qquad \text{(B3)}$$

and because the errors in each of the parameters are independent of one another, the overall uncertainty in the concentration of benzene is given by

$$\sigma_{[C_6H_6]} = [C_6H_6] \times \left\{ \left(\frac{\sigma_{P_{tot}}}{P_{tot}} \right)^2 + \left(\frac{\sigma_{F_{C_6H_6}}}{F_{C_6H_6}} \right)^2 + \left(\frac{\sigma_{F_{tot}}}{F_{tot}} \right)^2 + \left(\frac{\sigma_{a_{bulb}}}{a_{bulb}} \right)^2 + \left(\frac{\sigma_T}{T} \right)^2 \right\}^{1/2} \quad \text{(B4)}$$

where the $(\sigma_R/R)^2$ term has been excluded because it is equal to zero.

In the cases of partial pressure, total pressure, and temperature, the overall uncertainty is composed of the instrumental uncertainty, reported as a percentage by the manufacturer, and the precision limits for how well the instrument can be read. These two sources of uncertainty are independent and can thus be combined in quadrature to obtain the overall uncertainty in the quantity of interest. These considerations lead to equation B5 below,

$$\left(\frac{\sigma_X}{X} \right)^2 = \sigma_{prop}{}^2 + \left(\frac{\sigma_{det}}{X} \right)^2 \quad \text{(B5)}$$

where X is the quantity of interest, σ_{prop} is the reported proportional uncertainty in the quantity, and σ_{det} is the uncertainty that arises from the precision limits for the detection of the quantity, or how well the instrument can be read. Table B1 shows the values for σ_{prop} and σ_{det} that pertain to the measurements of the flow, pressure, and temperature. Because a_{bulb} is simply the ratio of the pressure of benzene to the total pressure in the bulb,

$$\left(\frac{\sigma_{a_{bulb}}}{a_{bulb}} \right)^2 = \left(\frac{\sigma_{P_{C_6H_6}}}{P_{C_6H_6}} \right)^2 + \left(\frac{\sigma_{P_{tot}}}{P_{tot}} \right)^2 \quad \text{(B6)}$$

As discussed in Appendix A, a bubble meter was used to calibrate the mass flow controllers, and the reproducibility of the gas flows was then assessed graphically by plotting the actual flows (F) against the flows displayed by the controllers (F'). F and F' were found to be nearly proportional in the case of each controller, and the graphs were thus constrained to be

proportional so that the slopes could be used as scaling factors. Therefore, since F is simply the product of F' and the scaling factor (m) for the mass-flow controller in question, this leads to

$$\left(\frac{\sigma_F}{F}\right)^2 = \left(\frac{\sigma_m}{m}\right)^2 + \left(\frac{\sigma_{F'}}{F'}\right)^2 \tag{B7}$$

where the last term concerning F' is actually the quadrature between σ_{prop} and σ_{det}, as in equation B5 above, and $\frac{\sigma_m}{m}$ for all four flow controllers were generally in the range of 0.4 to 1.4 %.

Finally, upon calculating the uncertainty in each individual flow, the squared uncertainty in the total flow F_{tot} is simply

$$\sigma_{F_{tot}}{}^2 = \sum_{i=1}^{N} \sigma_{F_i}{}^2 \tag{B8}$$

where N is the number of flow controllers (or flows) and is equal to 4 in the present case: one each for the precursor and benzene, and two for Argon. Taking this squared uncertainty and dividing it by $F_{tot}{}^2$ yields the desired F_{tot}-containing term in the initial overall expression for the uncertainty in the concentration of benzene given in equation B4.

As explained in Chapter 2, k_{ps1} is obtained at five different concentrations of the reactant in excess at each set of conditions, and according to equation 2.7, a plot of the k_{ps1} vs. concentration data should be linear with slope k_1 and intercept k' (Figure B1). The line through the data in Figure B1 represents a weighted linear least squares fit, which yields the statistical uncertainty in the slope, which is taken to be the overall standard deviation ($\pm 1\sigma$) in the second order rate constant k_1 for the corresponding set of conditions.

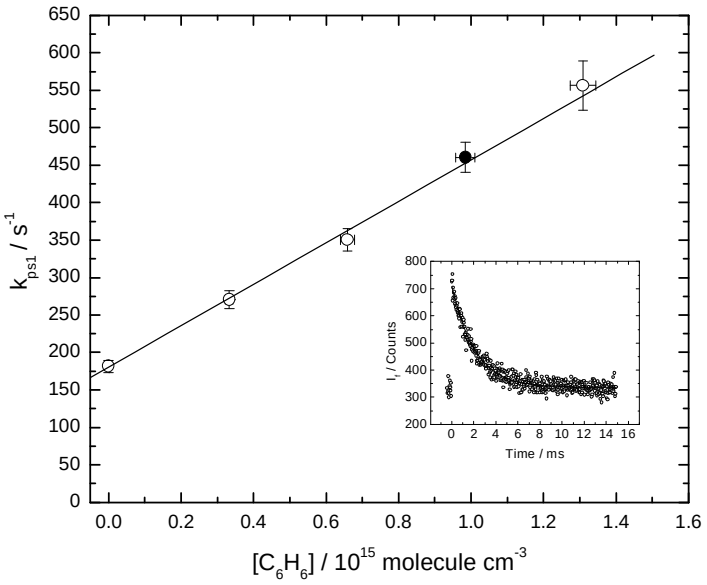

Figure B1. Pseudo-first-order decay coefficient for Cl in the presence of excess C_6H_6 at 676 K and 69 mbar total pressure with Ar. Error bars represent ± 1σ. The inset shows the signal corresponding to the filled point.

B2. Alternative Treatment of the Uncertainties in Concentration and k_1

Though the error propagation procedure proposed in section B1 is an acceptable way of treating uncertainties, a slight modification in the manner the uncertainties in the concentration and the second order rate constant are handled was later adopted after further considerations. These considerations led to the realization that the uncertainties in temperature and the dilution ratio a_{bulb} are systematic in the course of a single determination of k_1. Therefore it seemed more appropriate to exclude these quantities from the calculation of the uncertainty in concentration and the weighted linear least squares fit, which are meant to assess random errors and scatter. This was achieved by simply removing the last two terms in equation B4 and then performing the least squares fits. The ensuing uncertainty in the slope represents the statistical uncertainty in

k_1, which is then combined with the systematic uncertainties in the temperature and the dilution ratio to yield the overall 1σ uncertainty in k_1, as shown in equation B9.

$$\sigma_{k1} = \left\{ \left(\sigma_{slope}\right)^2 + \left(\frac{\sigma_{a_{bulb}}}{a_{bulb}} \right)^2 + \left(\frac{\sigma_T}{T} \right)^2 \right\}^{1/2} \qquad \text{(B9)}$$

The k_1 values for the Cl + H_2S and Cl + C_2H_4 projects were obtained in this manner, and it was found that in general, k_1 values obtained as described in this section are not statistically different than those obtained through the formalism proposed in section B1. Therefore, it appears that the uncertainty treatments set forth in sections B1 and B2 are both reasonable methods for data analysis.

B3. Uncertainties in Arrhenius Parameters

As discussed in chapter 2, the Arrhenius equation can be manipulated and rewritten in linear form, as in equation B10.

$$\ln(k_1) = -E_a/R \times (1/T) + \ln(A) \qquad \text{(B.10)}$$

According to equation B10, a plot of $\ln(k_1)$ against 1/T will result in a straight line with slope and intercept of $-E_a/R$ and ln(A), respectively. The ln(k) vs. 1/T data, along with the associated 1σ uncertainties in these quantities, are used in a weighted linear fit performed with the aid of a weighted linear least squares algorithm.[120] Because when fitting a straight line through a scattered set of data small changes in the slope will also affect the intercept, and vice versa, the uncertainties in the two quantities are also correlated. This correlation of uncertainties naturally affects the overall uncertainty in the y-coordinate, ln(k) in this case, and therefore the assessment of this correlation becomes necessary in order to correctly evaluate the error margins of the

second order rate constant k_1. The magnitude of this correlation is reflected in the covariance between the slope and the intercept, Cov(a,b), which can be obtained from the off-diagonal elements of the covariance matrix.[254] The weighted linear least squares algorithm used to obtain the uncertainties in the Arrhenius parameters also calculates the covariance, and the ensuing uncertainties in the Arrhenius parameters are then combined with the covariance to yield statistical 95% confidence limits for $\ln(k_1)$ (and consequently also for k_1) at each temperature explored. Equation B11 below is used to calculate the variance in the y-coordinate,

$$\mathrm{Var}(y_i) = \sigma_a^{\,2} + (2/T) \times \mathrm{Cov}(a,b) + (2/T^2) \times \sigma_b^{\,2} \qquad \text{(B.11)}$$

where $\sigma_a^{\,2}$ represents the variance in the intercept ($\ln(A)$), $\sigma_b^{\,2}$ denotes the variance in the slope ($-E_a/R$), and Cov(a,b) designates the covariance between the two quantities. As an example, the uncertainties in the Arrhenius parameters and the covariance between them in the H_2S + Cl reaction at 298 K will now be employed in the calculation of the 95% confidence limits for k_1. The weighted linear least squares algorithm evaluated the uncertainty in the intercept, the uncertainty in the slope, and the covariance, and found them to be 1.16×10^{-2}, 6.51 K, and -6.99×10^{-2} K^{-1}, respectively. Application of equation B.11 above yields a variance (σ^2) in $\ln(k_1)$ of 3.77×10^{-4} at 298 K, leading to a $\sigma_{\ln(k1)}$ of 1.94×10^{-2}, which can further be translated to a $2\sigma_{k1}$ of 3.88%. The combination of $2\sigma_{k1}$ in quadrature with a 5 % allowance for potential systematic errors yields the final 95 % confidence limits for k_1 of ± 6.3% at 298 K. In general, the covariance is negative, thus decreasing the uncertainty associated with the y-coordinate, and usually, it can be shown that k_1 possess the smallest uncertainty at the central temperature considered.

Table B1. Proportional errors and uncertainty arising from the detection limits of the flow, pressure, and temperature.

Property	σ_{prop}	Description of σ_{prop}	σ_{det}	Description of σ_{det}
Flow	0.01	Reported Instrument uncertainty	0.1-1.0 sccm	How well mass flow controllers can be read
Pressure	0.0025	Reported Instrument uncertainty	0.1-1.0 torr	How well pressure gauge can be read
Temperature	0.02	Calibration: shielded and unshielded thermocouples	1.0 K	How well temperature gauge can be read

APPENDIX C

STRUCTURAL PARAMETERS AND VIBRATIONAL FREQUENCIES

Cartesian coordinates (Å), unscaled vibrational frequencies (cm^{-1}), and rotational constants (GHz) of all stationary points identified in chapters 4-7.

C1. Parameters for the H_2SCl system obtained with QCISD/6-311G(d,p) theory

1. C_{2v} H_2S ($^1A_1$)

Cartesian Coordinates				**Frequencies**		**Rotational Constants**	
S	0.000000	0.000000	0.103091	1231	309.9	270.0	144.3
H	0.000000	0.963770	-0.824732	2767			
H	0.000000	-0.963770	-0.824732	2783			

2. C_s A1 ($^2A'$)

Cartesian Coordinates				**Frequencies**		**Rotational Constants**	
H	0.872837	-1.398064	0.966766	136	144.1	3.6	3.6
S	-0.052899	-1.374380	0.000000	284			
H	0.872837	-1.398064	-0.966766	296			
Cl	-0.052899	1.458012	0.000000	1228			
				2761			
				2778			

3. C_1 TS1 (^2A)

Cartesian Coordinates				**Frequencies**		**Rotational Constants**	
Cl	1.479654	0.003643	-0.011975	1400**i**	256.9	3.4	3.4
H	-0.076714	-0.153297	0.429258	201			
S	-1.476606	-0.073402	-0.016437	402			
H	-1.451713	1.265789	0.037321	993			
				1118			
				2757			

4. C_s A2 (^{2}A")

Cartesian Coordinates				Frequencies		Rotational Constants	
S	0.037351,	1.999655	0.000000	65	307.3	1.9	1.9
H	-1.263720	2.332897	0.000000	124			
H	0.031124	-0.698098	0.000000	212			
Cl	0.037351	-1.978193	0.000000	320			
				2735			
				2989			

5. C_1 TS2 (^{2}A)

Cartesian Coordinates				Frequencies		Rotational Constants	
S	1.015611	-0.016261	-0.044859	1051**i**	103.7	6.7	6.4
H	0.893582	1.669869	0.319693	454			
H	1.017778	-1.310546	0.416333	533			
Cl	-1.068303	-0.005832	-0.001076	689			
				977			
				2379			

6. $C_{\infty v}$ HCl ($^1\Sigma^+$)

Cartesian Coordinates				Frequency		Rotational Constants	
Cl	0.000000	0.000000	0.070876	3049	317.0	317.0	
H	0.000000	0.000000	-1.204894				

7. $C_{\infty v}$ SH ($^2\Pi$)

Cartesian Coordinates				Frequency		Rotational Constants	
S	0.000000	0.000000	0.079006	2735	286.9	286.9	
H	0.000000	0.000000,	-1.264094				

8. C_1 HSCl (^{1}A')

Cartesian Coordinates				Frequencies		Rotational Constants	
S	0.039169	1.032567	0.000000	511	293.2	6.9	6.7
Cl	0.039169	-1.040233	0.000000	935			
H	-1.292570	1.162885	0.000000	2764			

C2. Parameters for the NH_3Cl system obtained with CCSD(T)/aug-cc-pVTZ theory.

1. C_{3v} NH_3 ($^1A_1$)

Cartesian Coordinates				Frequencies	Rotational Constants		
N	0.000000	0.000000	0.116006	1063	296.8	296.8	189.8
H	0.000000	0.938347	-0.270680	1672			
H	0.812633	-0.469174	-0.270680	1673			
H	-0.812633	-0.469174	-0.270680	3463			
				3592			
				3593			

2. C_{2v} NH_2 ($^2B_1$)

Cartesian Coordinates				Frequencies	Rotational Constants		
N	0.000000	0.000000	0.142377	1540	698.7	388.5	249.7
H	0.000000	0.803312	-0.498321	3360			
H	0.000000	-0.803312	-0.498321	3454			

3. $C_{\infty v}$ HCl ($^1\Sigma^+$)

Cartesian Coordinates				Frequency	Rotational Constants	
Cl	0.000000	0.000000	0.071050	2991	315.4	315.4
H	0.000000	0.000000	-1.207843			

4. C_{3v} A1 ($^2A_1$)

Cartesian Coordinates				Frequencies		Rotational Constants		
Cl	0.000000	0.000000	0.914432	244	1606	173.2	6.9	6.9
N	0.000000	0.000000	-1.623169	375	3512			
H	0.000000	0.982389	-1.394389	378	3695			
H	0.850774	-0.491194	-1.394389	544	3696			
H	-0.850774	-0.491194	-1.394389	1606				

5. C_{2v} A2 ($^2B_1$)

Cartesian Coordinates				Frequencies		Rotational Constants		
N	0.000000	0.000000	-2.068032	152	1538	380.9	4.1	4.1
H	0.000000	0.000000	-0.122792	159	2723			
Cl	0.000000	0.000000	1.175813	211	3388			
H	0.000000	0.811374	-2.694898	555	3486			
H	0.000000	-0.811374	-2.694898	569				

6. C_{3v} A3 ($^2A_1$)

Cartesian Coordinates				Frequencies		Rotational Constants		
Cl	0.000000	0.000000	0.919601	286	1644	180.1	7.2	7.2
N	0.000000	0.000000	-1.470999	319	3492			
H	0.000000	0.963339	-1.778742	321	3652			
H	0.834276	-0.481670	-1.778742	904	3653			
H	-0.834276	-0.481670	-1.778742	1644				

7. C_s Abs TS ($^2A'$)

Cartesian Coordinates				Frequencies		Rotational Constants		
N	0.031279	1.734169	0.000000	977**i**	1153	243.8	6.1	6.1
H	0.356870	0.430096	0.000000	403	1562			
Cl	0.031279	-0.965704	0.000000	439	3410			
H	-0.553787	1.923843	0.818589	682	3512			
H	-0.553787	1.923843	-0.818589	1064				

8. C_{3v} Inv TS ($^2A_1$)

Cartesian Coordinates				Frequencies		Rotational Constants		
Cl	0.000000	0.000000	0.906059	385**i**	1583	168.2	7.1	7.1
N	0.000000	0.000000	-1.577307	327	3551			
H	0.000000	0.996751	-1.453950	384	3756			
H	0.863212	-0.498375	-1.453950	389	3757			
H	-0.863212	-0.498375	-1.453950	1581				

9. C_{2v} PCET TS ($^2B_1$)

Cartesian Coordinates				Frequencies		Rotational Constants		
N	0.000000	0.000000	-1.760877	1791**i**	1466	340.4	5.5	5.5
H	0.000000	0.000000	-0.639840	1319**i**	1573			
Cl	0.000000	0.000000	1.033438	269	3511			
H	0.000000	0.858280	-2.301230	507	3640			
H	0.000000	-0.858280	-2.301230	808				

C3. Parameters for the C_6H_6Cl system and the C_6H_6-HCl Complex obtained with MPWB1K/MG3 theory.

1. D_{6h} Benzene ($^1A_{1g}$)

Cartesian Coordinates				**Frequencies**				**Rotational Constants**		
C	0.000000	1.378955	0.000000	419	1026	1372	3267	5.8	5.8	2.9
C	1.194210	0.689477	0.000000	419	1036	1406	3267			
C	1.194210	-0.689477	0.000000	620	1038	1551	3277			
C	0.000000	-1.378955	0.000000	620	1052	1551				
C	-1.194210	-0.689477	0.000000	708	1089	1702				
C	-1.194210	0.689477	0.000000	728	1089	1702				
H	0.000000	2.454934	0.000000	894	1187	3240				
H	2.126035	1.227467	0.000000	894	1221	3251				
H	2.126035	-1.227467	0.000000	1026	1221	3251				
H	0.000000	-2.454934	0.000000							
H	-2.126035	-1.227467	0.000000							
H	-2.126035	1.227467	0.000000							

2. C_{2v} Bz-Cl Complex ($^2B_1$)

Cartesian Coordinates				**Frequencies**				**Rotational Constants**		
C	0.000000	0.000000	-3.012968	59**i**	895	1187	3241	5.8	0.59	0.53
H	0.000000	0.000000	-4.088938	20	896	1220	3250			
C	0.000000	1.193969	-2.323455	57	1026	1221	3254			
C	0.000000	-1.193969	-2.323455	419	1027	1374	3267			
C	0.000000	1.193838	-0.944416	420	1037	1406	3271			
C	0.000000	-1.193838	-0.944416	621	1039	1552	3280			
H	0.000000	2.125868	-2.861317	622	1052	1554				
H	0.000000	-2.125868	-2.861317	709	1089	1702				
H	0.000000	2.125713	-0.406477	729	1091	1704				
H	0.000000	-2.125713	-0.406477							
C	0.000000	0.000000	-0.254459							
H	0.000000	0.000000	0.821439							
Cl	0.000000	0.000000	4.036594							

3. C_{2v} Transition State ($^2A_1$)

Cartesian Coordinates				**Frequencies**				**Rotational Constants**		
C	0.000000	0.000000	-2.607343	125**i**	691	1105	1783	5.7	0.95	0.82
H	0.000000	0.000000	-3.682741	7	756	1195	3249			
C	0.000000	1.199871	-1.926882	60	839	1199	3256			
C	0.000000	-1.199871	-1.926882	411	937	1337	3270			
C	0.000000	1.216547	-0.541282	416	988	1358	3274			
C	0.000000	-1.216547	-0.541282	556	1013	1508	3279			
H	0.000000	2.130171	-2.467803	595	1033	1508				
H	0.000000	-2.130171	-2.467803	608	1054	1637				
H	0.000000	2.138065	0.012425	674	1077	1702				
H	0.000000	-2.138065	0.012425							
C	0.000000	0.000000	0.064365							
H	0.000000	0.000000	1.700892							
Cl	0.000000	0.000000	3.045202							

4. C_{2v} Ph-HCl Complex ($^2A_1$)

Cartesian Coordinates				**Frequencies**				**Rotational Constants**		
C	0.000000	0.000000	-2.696528	41**i**	687	1103	2630	5.7	0.85	0.74
H	0.000000	0.000000	-3.771929	36	748	1194	3247			
C	0.000000	1.199810	-2.015773	60	839	1199	3254			
C	0.000000	-1.199810	-2.015773	367	932	1334	3267			
C	0.000000	1.216211	-0.629630	410	1000	1357	3270			
C	0.000000	-1.216211	-0.629630	448	1011	1506	3278			
H	0.000000	2.130028	-2.557097	455	1032	1514				
H	0.000000	-2.130028	-2.557097	595	1055	1637				
H	0.000000	2.139796	-0.078822	625	1080	1701				
H	0.000000	-2.139796	-0.078822							
C	0.000000	0.000000	-0.024138							
H	0.000000	0.000000	1.950236							
Cl	0.000000	0.000000	3.244845							

5. C_{2v} Phenyl Radical ($^2A_1$)

Cartesian Coordinates			
C	0.000000	0.000000	-1.306446
H	0.000000	0.000000	-2.381939
C	0.000000	1.198987	-0.623746
C	0.000000	-1.198987	-0.623746
C	0.000000	1.212577	0.762169
C	0.000000	-1.212577	0.762169
H	0.000000	2.129339	-1.165569
H	0.000000	-2.129339	-1.165569
H	0.000000	2.138348	1.310098
H	0.000000	-2.138348	1.310098
C	0.000000	0.000000	1.378412

Frequencies			Rotational Constants		
408	1008	1503	6.4	5.7	3.0
436	1030	1513			
599	1055	1640			
619	1078	1700			
693	1103	3241			
744	1193	3247			
849	1198	3261			
928	1334	3264			
1001	1359	3274			

6. $C_{\infty v}$ Hydrogen Chloride ($^1\Sigma^+$)

Cartesian Coordinates			
Cl	0.000000	0.000000	0.070496
H	0.000000	0.000000	-1.198425

Frequency	Rotational Constants	
3067.0	320.4	320.4

7. C_s Bz-Cl' Adduct (^{2}A")

Cartesian Coordinates			
C	-2.258681	1.940891	0.000000
H	-3.139609	2.558701	0.000000
C	-2.379646	0.567525	0.000000
C	-1.008500	2.522921	0.000000
C	-1.250440	-0.223977	0.000000
C	0.120560	1.731239	0.000000
H	-3.355070	0.113395	0.000000
H	-0.914138	3.594740	0.000000
H	-1.344319	-1.295880	0.000000
H	1.095937	2.185501	0.000000
C	0.000000	0.357765	0.000000
H	0.880096	-0.261044	0.000000
Cl	2.790432	-2.839623	0.000000

Frequencies				Rotational Constants		
8	895	1188	3240	5.8	0.60	0.54
51	895	1222	3250			
76	1026	1223	3252			
419	1027	1379	3267			
420	1039	1408	3268			
626	1040	1556	3278			
627	1053	1559				
708	1095	1706				
730	1097	1708				

8. C_s Ph-HCl' (^{2}A')

Cartesian Coordinates			
C	-0.237448	1.416871	0.000000
C	-1.571616	1.792544	0.000000
C	-2.564101	0.834392	0.000000
C	-2.250274	-0.508874	0.000000
C	-0.925560	-0.916120	0.000000
C	0.000000	0.078892	0.000000
H	0.551827	2.147196	0.000000
H	-1.827499	2.837970	0.000000
H	-3.595395	1.139197	0.000000
H	-3.032705	-1.247836	0.000000
H	-0.658519	-1.957853	0.000000
H	1.864620	-0.589048	0.000000
Cl	3.058333	-1.089168	0.000000

Frequencies				Rotational Constants		
43	687	1106	2636	5.7	0.85	0.74
54	750	1195	3245			
62	841	1201	3253			
368	933	1336	3265			
411	1001	1360	3270			
454	1012	1507	3276			
455	1034	1517				
598	1056	1642				
628	1083	1702				

9. C_{6v} Bz-HCl Adduct ($^1A_1$)

Cartesian Coordinates			
Cl	0.000000	0.000000	2.561457
H	0.000000	0.000000	1.286330
C	0.000000	1.380013	-1.067765
C	1.195127	0.690007	-1.067765
C	1.195127	-0.690007	-1.067765
C	0.000000	-1.380013	-1.067765
C	-1.195127	-0.690007	-1.067765
C	-1.195127	0.690007	-1.067765
H	0.000000	2.455711	-1.065261
H	2.126708	1.227855	-1.065261
H	2.126708	-1.227855	-1.065261
H	0.000000	-2.455711	-1.065261
H	-2.126708	-1.227855	-1.065261
H	-2.126708	1.227855	-1.065261

Frequencies				Rotational Constants		
56	718	1088	1698	2.9	1.2	1.2
60	743	1090	1700			
97	904	1188	3025			
156	904	1221	3246			
161	1036	1222	3256			
420	1037	1371	3256			
421	1039	1406	3271			
620	1050	1550	3271			
621	1062	1552	3281			

10. C_s π-Ph-HCl ($^2A'$)

Cartesian Coordinates			
C	-1.101837	1.313954	0.000000
H	-1.095623	2.389183	0.000000
C	-1.101800	0.631362	1.199611
C	-1.101800	0.631362	-1.199611
C	-1.101800	-0.755587	1.213264
C	-1.101800	-0.755587	-1.213264
H	-1.096202	1.173118	2.129558
H	-1.096202	1.173118	-2.129558
H	-1.097857	-1.303551	2.138896
H	-1.097857	-1.303551	-2.138896
C	-1.103827	-1.372707	0.000000
H	1.324821	-0.228881	0.000000
Cl	2.578594	-0.003307	0.000000

Frequencies				Rotational Constants		
54	698	1103	3015	3.0	1.2	1.2
58	752	1195	3247			
82	857	1199	3253			
159	936	1334	3265			
192	1003	1358	3267			
408	1017	1503	3278			
439	1043	1512				
599	1054	1637				
619	1078	1697				

11. C_s σ-η_1 Adduct (^{2}A')

Cartesian Coordinates			
C	-0.478654	2.059839	0.000000
H	-0.470739	3.134366	0.000000
C	-0.496842	1.358955	1.210381
C	-0.496842	1.358955	-1.210381
C	-0.496842	0.008352	1.233299
C	-0.496842	0.008352	-1.233299
H	-0.521980	1.905050	2.137102
H	-0.521980	1.905050	-2.137102
H	-0.512945	-0.531329	2.162900
H	-0.512945	-0.531329	-2.162900
C	-0.414799	-0.774968	0.000000
H	-1.086225	-1.623753	0.000000
Cl	1.230103	-1.669115	0.000000

Frequencies				**Rotational Constants**		
94	796	1182	3156	4.4	1.7	1.4
216	875	1192	3251			
310	914	1224	3255			
421	1014	1359	3273			
457	1016	1390	3275			
589	1019	1467	3283			
591	1030	1490				
647	1065	1596				
759	1154	1651				

12. C_s π-η_1 Adduct (^{2}A')

Cartesian Coordinates			
C	-0.695195	1.917664	0.000000
H	-0.691417	2.993540	0.000000
C	-0.697108	1.233419	1.202296
C	-0.697108	1.233419	-1.202296
C	-0.697108	-0.136652	1.207937
C	-0.697108	-0.136652	-1.207937
H	-0.696630	1.777083	2.129820
H	-0.696630	1.777083	-2.129820
H	-0.694218	-0.681880	2.134061
H	-0.694218	-0.681880	-2.134061
C	-0.677365	-0.838962	0.000000
H	-0.804332	-1.905185	0.000000
Cl	1.720200	-1.347775	0.000000

Frequencies				**Rotational Constants**		
62	874	1191	3253	3.8	1.6	1.4
87	919	1211	3266			
161	1009	1220	3270			
403	1028	1378	3281			
404	1034	1405	3283			
608	1036	1531	3293			
612	1049	1547				
687	1071	1653				
744	1091	1680				

13. C_s σ-π-η_1 Transition State (^{2}A')

Cartesian Coordinates			
C	-0.595159	1.974189	0.000000
H	-0.589652	3.049581	0.000000
C	-0.610756	1.284489	1.206837
C	-0.610756	1.284489	-1.206837
C	-0.610756	-0.076580	1.219267
C	-0.610756	-0.076580	-1.219267
H	-0.632716	1.830221	2.133119
H	-0.632716	1.830221	-2.133119
H	-0.626392	-0.621942	2.145010
H	-0.626392	-0.621942	-2.145010
C	-0.527138	-0.807378	0.000000
H	-0.886740	-1.820143	0.000000
Cl	1.493326	-1.478927	0.000000

Frequencies				**Rotational Constants**		
234**i**	842	1183	3254	4.1	1.7	1.4
113	929	1195	3262			
154	949	1219	3264			
369	1020	1365	3276			
406	1022	1400	3283			
597	1034	1508	3287			
598	1052	1523				
659	1064	1614				
748	1081	1653				

14. C_s π-η_2 Transition State (^{2}A')

Cartesian Coordinates			
Cl	-1.774253	1.275557	0.000000
C	0.718503	-0.522637	1.388337
C	0.718503	-0.522637	-1.388337
C	0.713099	-1.704054	0.695133
C	0.718503	0.677911	0.697317
C	0.718503	0.677911	-0.697317
C	0.713099	-1.704054	-0.695133
H	0.709175	-2.639407	1.226317
H	0.754038	1.611188	1.227843
H	0.754038	1.611188	-1.227843
H	0.709175	-2.639407	-1.226317
H	0.717304	-0.521338	-2.463226
H	0.717304	-0.521338	2.463226

Frequencies				**Rotational Constants**		
54**i**	881	1195	3253	3.7	1.6	1.4
82	914	1218	3265			
190	1016	1220	3271			
405	1031	1396	3280			
413	1035	1407	3284			
610	1038	1539	3295			
614	1057	1545				
716	1077	1672				
724	1091	1683				

15. C_{6v} π-η_6 Transition State ($^2A_1$)

Cartesian Coordinates			
Cl	0.000000	0.000000	2.305779
C	0.000000	1.379440	-0.933291
C	0.000000	-1.379440	-0.933291
C	1.194630	0.689720	-0.933291
C	-1.194630	-0.689720	-0.933291
C	-1.194630	0.689720	-0.933291
C	1.194630	-0.689720	-0.933291
H	0.000000	2.455220	-0.933291
H	0.000000	-2.455220	-0.933291
H	2.126283	1.227610	-0.933291
H	-2.126283	-1.227610	-0.933291
H	-2.126283	1.227610	-0.933291
H	2.126283	-1.227610	-0.933291

Frequencies				**Rotational Constants**		
1321**i**	749	1187	3244	2.9	1.5	1.5
153	906	1221	3254			
179	1032	1221	3254			
421	1034	1369	3269			
435	1035	1406	3270			
622	1039	1406	3279			
622	1050	1555				
713	1062	1701				
733	1091	1703				

C5. Parameters for the C_6H_6Cl system and the C_6H_6-HCl Complex obtained with QCISD/6-311G(d,p) theory.

1. D_{6h} Benzene ($^1A_{1g}$)

Cartesian Coordinates				**Frequencies**				**Rotational Constants**		
C	0.000000	1.399868	0.000000	396	937	1294	3212	5.7	5.7	2.8
C	1.212321	0.699934	0.000000	396	937	1380	3212			
C	1.212321	-0.699934	0.000000	511	1009	1524	3223			
C	0.000000	-1.399868	0.000000	615	1017	1524				
C	-1.212321	-0.699934	0.000000	615	1065	1663				
C	-1.212321	0.699934	0.000000	685	1065	1663				
H	0.000000	2.486896	0.000000	854	1161	3185				
H	2.153715	1.243448	0.000000	854	1202	3195				
H	2.153715	-1.243448	0.000000	919	1202	3195				
H	0.000000	-2.486896	0.000000							
H	-2.153715	-1.243448	0.000000							
H	-2.153715	1.243448	0.000000							

2. C_{2v} Bz-Cl Complex ($^2B_1$)

Cartesian Coordinates				**Frequencies**				**Rotational Constants**		
C	0.000000	0.000000	-3.029956	10	855	1162	3185	5.7	0.59	0.53
H	0.000000	0.000000	-4.117042	27	859	1202	3195			
C	0.000000	1.212275	-2.329931	35	921	1204	3198			
C	0.000000	-1.212275	-2.329931	396	937	1295	3211			
C	0.000000	1.211994	-0.930078	397	943	1381	3216			
C	0.000000	-1.211994	-0.930078	505	1009	1524	3226			
H	0.000000	2.153748	-2.873436	615	1017	1525				
H	0.000000	-2.153748	-2.873436	616	1065	1663				
H	0.000000	2.153299	-0.386268	689	1066	1663				
H	0.000000	-2.153299	-0.386268							
C	0000000	0.000000	-0.229492							
H	0.000000	0.000000	0.856988							
Cl	0.000000	0.000000	4.026839							

3. C_{2v} Transition State ($^2A_1$)

Cartesian Coordinates			
C	0.000000	0.000000	-2.604435
H	0.000000	0.000000	-3.690901
C	0.000000	1.213711	-1.914205
C	0.000000	-1.213711	-1.914205
C	0.000000	1.230426	-0.514054
C	0.000000	-1.230426	-0.514054
H	0.000000	2.153484	-2.460731
H	0.000000	-2.153484	-2.460731
H	0.000000	2.161054	0.045098
H	0.000000	-2.161054	0.045098
C	0.000000	0.000000	0.110038
H	0.000000	0.000000	1.615079
Cl	0.000000	0.000000	3.000740

Frequencies				**Rotational Constants**		
512**i**	731	1089	1684	5.6	0.97	0.83
61	738	1144	3196			
71	829	1162	3205			
401	838	1197	3220			
404	898	1249	3227			
457	955	1324	3230			
484	965	1488				
515	1023	1513				
601	1052	1639				

4. C_{2v} Ph-HCl Complex ($^2A_1$)

Cartesian Coordinates			
C	0.000000	0.000000	-2.834905
H	0.000000	0.000000	-3.921378
C	0.000000	1.213715	-2.143929
C	0.000000	-1.213715	-2.143929
C	0.000000	1.229893	-0.742438
C	0.000000	-1.229893	-0.742438
H	0.000000	2.153416	-2.691054
H	0.000000	-2.153416	-2.691054
H	0.000000	2.164519	-0.189289
H	0.000000	-2.164519	-0.189289
C	0.000000	0.000000	-0.117484
H	0.000000	0.000000	2.234926
Cl	0.000000	0.000000	3.517522

Frequencies				**Rotational Constants**		
13**i**	624	1085	2948	5.6	0.74	0.65
8	727	1160	3193			
54	831	1191	3201			
227	897	1248	3216			
280	951	1322	3220			
398	964	1482	3226			
426	981	1497				
546	1031	1628				
600	1063	1679				

5. C_{2v} Phenyl Radical ($^2A_1$)

Cartesian Coordinates			
C	0.000000	0.000000	-1.323800
H	0.000000	0.000000	-2.410452
C	0.000000	1.213297	-0.631704
C	0.000000	-1.213297	-0.631704
C	0.000000	1.227247	0.769537
C	0.000000	-1.227247	0.769537
H	0.000000	2.152865	-1.179520
H	0.000000	-2.152865	-1.179520
H	0.000000	2.162505	1.321982
H	0.000000	-2.162505	1.321982
C	0.000000	0.000000	1.402389

Frequencies			Rotational Constants		
399	966	1481	6.3	5.6	3.0
427	981	1497			
585	1030	1631			
603	1062	1678			
618	1084	3189			
729	1160	3197			
840	1190	3213			
900	1250	3217			
952	1321	3223			

6. $C_{\infty v}$ Hydrogen Chloride ($^1\Sigma_+$)

Cartesian Coordinates			
Cl	0.000000	0.000000	0.070876
H	0.000000	0.000000	-1.204894

Frequency	Rotational Constants
3048.7	317.0

7. C_{6v} Bz-HCl Adduct ($^1A_1$)

Cartesian Coordinates			
Cl	0.000000	0.000000	2.650128
H	0.000000	0.000000	1.371232
C	0.000000	1.400585	-1.105598
C	1.212942	0.700292	-1.105598
C	1.212942	-0.700292	-1.105598
C	0.000000	-1.400585	-1.105598
C	-1.212942	-0.700292	-1.105598
C	-1.212942	0.700292	-1.105598
H	0.000000	2.487382	-1.103645
H	2.154136	1.243691	-1.103645
H	2.154136	-1.243691	-1.103645
H	0.000000	-2.487382	-1.103645
H	-2.154136	-1.243691	-1.103645
H	-2.154136	1.243691	-1.103645

Frequencies				Rotational Constants		
18	616	1065	1660	2.9	1.2	1.2
18	691	1065	1660			
70	859	1164	3026			
120	859	1204	3190			
120	921	1204	3200			
393	940	1295	3200			
393	940	1381	3217			
504	1013	1523	3217			
616	1016	1523	3227			

8. C_s π-Ph-HCl (^{2}A')

Cartesian Coordinates			
C	-1.129544	1.381602	0.000000
H	-1.126361	2.467940	0.000000
C	-1.129317	0.689506	1.213874
C	-1.129317	0.689506	-1.213874
C	-1.129317	-0.712702	1.227975
C	-1.129317	-0.712702	-1.227975
H	-1.126297	1.237011	2.153262
H	-1.126297	1.237011	-2.153262
H	-1.127816	-1.265138	2.163134
H	-1.127816	-1.265138	-2.163134
C	-1.130935	-1.346276	0.000000
H	1.373189	-0.275765	0.000000
Cl	2.642817	-0.121736	0.000000

Frequencies				Rotational Constants		
26	619	1085	3023	3.0	1.2	1.2
32	733	1162	3195			
66	845	1192	3202			
123	904	1252	3217			
145	954	1321	3220			
397	967	1480	3227			
426	985	1496				
579	1030	1628				
603	1062	1676				

9. C_s σ-η_1 Adduct (^{2}A')

Cartesian Coordinates			
C	-0.418550	2.150873	0.000000
H	-0.418550	3.236285	0.000000
C	-0.418550	1.433672	1.231156
C	-0.418550	1.433672	-1.231156
C	-0.418550	0.065375	1.254772
C	-0.418550	0.065375	-1.254772
H	-0.418550	1.984701	2.168256
H	-0.418550	1.984701	-2.168256
H	-0.418550	-0.480317	2.194052
H	-0.418550	-0.480317	-2.194052
C	-0.418550	-0.746018	0.000000
H	-1.230205	-1.480786	0.000000
Cl	1.081809	-1.834233	0.000000

Frequencies				**Rotational Constants**		
71	767	1178	3091	4.5	1.7	1.3
232	818	1202	3196			
320	898	1255	3199			
405	925	1317	3217			
441	945	1364	3219			
583	994	1424	3230			
586	995	1464				
629	1037	1562				
701	1115	1618				

10. C_s π-η_1 Adduct (^{2}A')

Cartesian Coordinates			
C	0.000000	-0.758242	1.935530
H	0.000000	-0.758242	3.022525
C	1.213095	-0.758242	1.240695
C	-1.213095	-0.758242	1.240695
C	1.215498	-0.758242	-0.150690
C	-1.215498	-0.758242	-0.150690
H	2.152382	-0.758242	1.786772
H	-2.152382	-0.758242	1.786772
H	2.153531	-0.758242	-0.698621
H	-2.153531	-0.758242	-0.698621
C	0.000000	-0.758242	-0.854938
H	0.000000	-0.846194	-1.937073
Cl	0.000000	1.878478	-1.342669

Frequencies				**Rotational Constants**		
50	868	1156	3196	3.6	1.5	1.3
71	898	1205	3207			
101	951	1210	3209			
392	969	1279	3223			
398	970	1383	3224			
520	1010	1522	3233			
615	1019	1531				
617	1068	1664				
712	1076	1674				

11. C_s σ-π-η_1 Transition State (^{2}A')

Cartesian Coordinates			
C	-0.607837	2.034593	0.000000
H	-0.607837	3.121185	0.000000
C	-0.607837	1.335081	1.221942
C	-0.607837	1.335081	-1.221942
C	-0.607837	-0.048517	1.230415
C	-0.607837	-0.048517	-1.230415
H	-0.607837	1.884205	2.159233
H	-0.607837	1.884205	-2.159233
H	-0.607837	-0.600429	2.165223
H	-0.607837	-0.600429	-2.165223
C	-0.607837	-0.780547	0.000000
H	-0.965531	-1.804542	0.000000
Cl	1.522756	-1.579249	0.000000

Frequencies				**Rotational Constants**		
229**i**	839	1159	3201	4.0	1.6	1.4
107	901	1179	3211			
141	924	1206	3218			
364	943	1298	3228			
391	966	1380	3230			
553	1006	1494	3239			
600	1038	1508				
606	1061	1599				
719	1075	1625				

C4. Parameters for the C_2H_4Cl system obtained with QCISD/6-311G(d,p).

1. $C_{\infty v}$ HCl ($^1\Sigma^+$)

Cartesian Coordinates				**Frequency**		**Rotational Constants**	
Cl	0.000000	0.000000	0.070876	3049	317.0	317.0	
H	0.000000	0.000000	-1.204894				

2. D_{2h} C_2H_4 (^1A_g)

Cartesian Coordinates				**Frequencies**		**Rotational Constants**		
C	0.000000	0.000000	0.669265	830	1486	146.2	29.8	24.8
C	0.000000	0.000000	-0.669265	922	1691			
H	0.000000	0.926030	1.238603	968	3153			
H	0.000000	-0.926030	1.238603	1054	3172			
H	0.000000	-0.926030	-1.238603	1241	3234			
H	0.000000	0.926030	-1.238603	1381	3260			

3. C_s C_2H_3(^{2}A')

Cartesian Coordinates				**Frequencies**		**Rotational Constants**		
C	0.050534	-0.591516	0.000000	740	1639	230.9	32.3	28.3
C	0.050534	0.728180	0.000000	826	3097			
H	0.974473	-1.166790	0.000000	925	3200			
H	-0.881748	-1.163207	0.000000	1081	3262			
H	-0.699131	1.510017	0.000000	1408				

4. C_s C_2H_3Cl (^{1}A')

Cartesian Coordinates				**Frequencies**		**Rotational Constants**		
C	1.305757	1.031828	0.000000	402	1326	57.0	6.0	5.4
C	0.000000	0.761421	0.000000	624	1425			
H	2.056352	0.248343	0.000000	742	1677			
H	1.636754	2.065740	0.000000	901	3179			
H	-0.773457	1.520350	0.000000	978	3241			
Cl	-0.632600	-0.858466	0.000000	1056	3277			

5. $D_{\infty h}$ H_2 ($^1\Sigma_g$)

Cartesian Coordinates				Frequency		Rotational Constants	
H	0.000000	0.000000	0.371745	4420	1814.3	1814.3	
H	0.000000	0.000000	-0.371745				

6. C_s β-C_2H_4Cl (^{2}A')

Cartesian Coordinates				Frequencies			Rotational Constants		
Cl	-0.712457	-0.824097	0.000000	218	1102	3174	41.7	5.5	5.0
C	0.000000	0.861796	0.000000	308	1290	3187			
C	1.478809	0.805591	0.000000	602	1325	3285			
H	-0.394423	1.346390	0.893426	685	1485				
H	-0.394423	1.346390	-0.893426	791	1516				
H	2.013881	0.656276	-0.931894	1101	3125				
H	2.013881	0.656276	0.931894						

7. C_1 α-C_2H_4Cl (^{2}A)

Cartesian Coordinates				Frequencies			Rotational Constants		
H	-1.587784	-1.094468	-0.706178	177	1135	3097	32.7	5.7	5.2
C	-1.649970	-0.268304	0.010883	330	1339	3139			
C	-0.444212	0.607940	-0.081390	438	1437	3239			
H	-1.756295	-0.707740	1.014571	755	1488				
H	-2.550351	0.316884	-0.203543	1025	1504				
H	-0.456770	1.652557	0.204984	1061	3020				
Cl	1.112723	-0.129709	0.006659						

8. C_1 β-Disp TS (^{2}A)

Cartesian Coordinates				Frequencies			Rotational Constants		
C	-1.616602	-0.368387	0.011489	1069**i**	872	3180	36.9	5.7	5.3
C	-0.555520	0.451466	-0.172902	388	997	3240			
H	-2.616293	0.003115	-0.190721	461	1060	3283			
H	-1.504196	-1.357979	0.440827	468	1305				
H	-0.622686	1.388956	-0.711942	617	1407				
Cl	1.082410	-0.123021	0.005167	738	1588				
H	-0.625072	1.558786	1.342481						

9. C_1 α-Disp TS (^{2}A)

Cartesian Coordinates				Frequencies			Rotational Constants		
C	0.475636	0.556653	0.040413	792**i**	931	3180	38.9	5.5	5.1
C	1.580658	-0.169034	-0.215168	245	970	3244			
H	0.497054	1.595041	0.348398	371	1063	3281			
Cl	-1.118279	-0.121199	-0.000454	407	1319				
H	2.545956	0.327045	-0.233303	683	1412				
H	1.517396	-1.186300	-0.586762	750	1613				
H	2.112579	-1.001117	1.527914						

10. C_1 Elim TS (^{2}A)

Cartesian Coordinates				Frequencies			Rotational Constants		
C	1.727901	-0.393084	0.016607	1397**i**	1050	3125	34.4	4.4	4.0
C	0.947439	0.716214	-0.222730	247	1149	3217			
H	1.723178	-1.231290	-0.677617	385	1155	3232			
H	2.468218	-0.399356	0.817562	389	1386				
H	0.917343	1.582790	0.434005	832	1507				
H	0.430945	-0.436406	0.404085	892	1636				
Cl	-1.270101	-0.085560	0.015218						

11. C_1 Iso TS (^{2}A)

Cartesian Coordinates				Frequencies			Rotational Constants		
H	1.297882	0.323507	1.042356	2154**i**	1052	3173	43.2	5.5	5.0
C	1.676220	-0.321697	-0.047648	312	1178	3225			
C	0.492499	0.565718	0.057981	373	1275	3300			
H	1.535191	-1.385487	0.098684	719	1346				
H	2.569548	0.043952	-0.542544	735	1449				
H	0.568171	1.578653	-0.320469	771	2219				
Cl	-1.116653	-0.119103	-0.020002						

12. C_1 Abs TS (^{2}A)

Cartesian Coordinates				Frequencies			Rotational Constants		
C	-2.061235	-0.436022	0.000000	884**i**	826	3127	41.8	3.1	2.8
H	-1.684075	-1.455914	-0.000007	122	932	3227			
H	-3.144242	-0.300071	0.000011	284	942	3255			
C	-1.255316	0.608939	-0.000003	627	1183				
H	0.165635	0.287112	-0.000001	645	1406				
H	-1.385572	1.685266	0.000003	772	1661				
Cl	1.526327	-0.073759	0.000000						

13. C_s Add TS ($^2A'$)

Cartesian Coordinates				Frequencies			Rotational Constants		
C	0.657715	-1.511599	0.000000	131**i**	1012	3185	25.8	4.6	4.1
C	-0.655487	-1.169911	0.000000	148	1244	3262			
H	1.208948	-1.625673	0.928734	331	1351	3287			
H	1.208948	-1.625673	-0.928734	834	1485				
H	-1.215630	-1.098404	0.926926	933	1630				
H	-1.215630	-1.098404	-0.926926	1005	3171				
Cl	0.000000	1.266895	0.000000						

14. C_{2v} A1 ($^2A_1$)

Cartesian Coordinates				Frequencies			Rotational Constants		
Cl	0.000000	0.000000	1.302141	134	1019	3181	24.5	4.4	3.9
C	0.000000	0.674728	-1.382403	234	1241	3255			
C	0.000000	-0.674728	-1.382403	255	1372	3280			
H	0.927734	1.239452	-1.386890	834	1486				
H	-0.927734	1.239452	-1.386890	976	1658				
H	-0.927734	-1.239452	-1.386890	995	3167				
H	0.927734	-1.239452	-1.386890						

15. C_s A2 ($^2A'$)

Cartesian Coordinates				Frequencies			Rotational Constants		
C	0.705615	-2.229440	0.000000	34	807	3098	34.4	2.2	2.0
H	-0.379840	-2.145766	0.000000	35	929	3200			
H	1.119141	-3.241963	0.000000	83	1078	3268			
C	1.492939	-1.171951	0.000000	229	1409				
H	0.000000	0.695792	0.000000	285	1640				
H	2.556470	-0.967904	0.000000	740	2966				
Cl	-0.969829	1.533423	0.000000						

16. C_s α-Chloroethyl Torsion TS (^{2}A")

Cartesian Coordinates			**Frequencies**			**Rotational Constants**		
H -1.928186	-0.203862	0.000000	201**i**	1132	3079	43.6	5.4	4.9
C -1.493397	0.799274	0.000000	183	1351	3147			
C 0.000000	0.730916	0.000000	369	1437	3257			
H -1.863933	1.333899	0.885774	752	1488				
H -1.863933	1.333899	-0.885774	997	1508				
H 0.642010	1.601305	0.000000	1057	3029				
Cl 0.822025	-0.779199	0.000000						

17. C_s α-Chloroethyl Inversion TS (^{2}A")

Cartesian Coordinates			**Frequencies**			**Rotational Constants**		
H 1.848362	1.800392	0.000000	282**i**	1138	3080	42.1	5.5	5.0
C 1.491298	0.765688	0.000000	175	1333	3137			
C 0.000000	0.746421	0.000000	345	1439	3266			
H 1.898579	0.257029	0.884723	758	1484				
H 1.898579	0.257029	-0.884723	1015	1507				
H -0.635909	1.620305	0.000000	1068	3029				
Cl -0.821023	-0.765142	0.000000						

18. C_s β-Chloroethyl Torsion TS (^{2}A")

Cartesian Coordinates			**Frequencies**			**Rotational Constants**		
Cl -0.720804	-0.816277	0.000000	220**i**	1118	3104	35.9	5.8	5.1
C 0.000000	0.824575	0.000000	364	1182	3179			
C 1.492358	0.780895	0.000000	367	1358	3298			
H -0.386484	1.342711	0.884700	706	1477				
H -0.386484	1.342711	-0.884700	899	1489				
H 2.041957	1.716965	0.000000	1007	3065				
H 2.030525	-0.158502	0.000000						

APPENDIX D

GUIDE TO THE OPERATION OF THE MULTIWELL 2008.3 PROGRAM SUITE

D1. Overview

The use of the MultiWell Program Suite (version 2008.3)[86] to obtain thermal rate constants for recombination reactions from the kinetic analysis of an adduct assumed to be formed with the initial energy distribution corresponding to chemical activation is outlined in this appendix. It should be noted that this appendix is not intended to substitute the user manual for MultiWell, which can be obtained from the website contained in the above MultiWell reference, but rather to provide specific examples of the implementation of this software to the specific reactions studied in this dissertation. The suite of programs can be obtained from the same website, which is composed of the Multiwell, Densum, Mominert, and Thermo programs.

The function of the Mominert program is to calculate moments of inertia for a species from its Cartesian Coordinates and, if so desired, reduced moments of inertia for torsion around specified bonds of interest. The Densum program, which requires the one-dimensional moment of inertia and a listing of the vibrational frequencies of the species in question (the K-rotor), is used to calculate the sums and densities of states in the particular species in question, and it uses the Stein-Rabinovitch[96] adaptation of the Beyer-Swinehart[97] exact count algorithm. Following the suggestion of Barker et al.,[85] an energy grain of 10 cm^{-1} and a maximum energy of 85,000 cm^{-1} were used, and as a precaution, the number of array elements and its size (Imax1 and Isize) were usually optimized until fluctuations of less than 5% in the density of states of each species were achieved. The two dimensional moments of inertia are not included in the Densum calculation, instead, they are plugged directly in the Multiwell input files. Each species is assumed to be a symmetric top, such that the two-dimensional external inactive moment of inertia composing the J-Rotor is obtained from the geometric average of the two degenerate or near-degenerate moments of inertia in each species, I_B and I_C. The Thermo program can be used

for a variety of purposes, including the calculation of equilibrium constants, Gorin-type TS analyses, and TST calculations.

Finally, the Multiwell program is used to obtain the energy-specific microcanonical rate constants at the specified temperature and pressure, along with the fractional distribution of each of the product channels, which can then be used to obtain the thermal recombination rate constants via equation 3.28. The MultiWell program solves a hybrid master equation via the implementation Gillespie's stochastic method,[83] which has been shown to lead to the exact solution of a set of ordinary differential equations as the number of stochastic trials approaches infinity. In principle, convergence tests should be carried out to ensure that the number of stochastic trials used produces good statistics, and in this work, it was found that the use of 1,000,000 trials accomplishes this feat. It was also found that in general, no less than 10,000 trials should be used. The extent of collisional energy transfer also depends on reasonable convergence with respect to either time or number of collisions, and it was consistently found that the use of 100 collisions leads to fractional populations that appear to have stabilized.

Selected Mominert, Densum, Thermo, and Multiwell input files pertaining to the H_2SCl reaction system are given in section D2. Sections D3 – D5 contain sample input files for the NH_3Cl, C_6H_6Cl, and C_2H_4Cl systems, respectively. It should be noted that in general, Mominert files are unnecessary since the same information can be obtained directly from *Gaussian 03* output files, and as such, the Mominert program was only used for the C_2H_4Cl system, in order to obtain the reduced moments of inertia for torsion around the partial double bond in the α- and β-chloroethyl radicals. The corresponding chapters should be consulted for nomenclature conventions, elaboration on the selection of the Lennard-Jones and energy transfer parameters,

and the ensuing results of these MultiWell-based RRKM kinetic analyses. All of the sample input files pertain to room temperature calculations.

D2. Sample input files for the MultiWell-based kinetic analysis of the H_2SCl reaction system

D2.1. Sample Mominert input files

Disp_TS

```
4
S     1          1.015611   -0.016261   -0.044859
H     2          0.893582    1.669869    0.319693
H     3          1.017778   -1.310546    0.416333
Cl    4         -1.068303   -0.005832   -0.001076
0 0
```

D2.2. Sample Densum input files

Addition Elimination Adduct 1

```
'A1'
7 0  'HAR'
10.   3000   6000   85000.
1    vib  129.9      0. 1
2    vib  271.1      0. 1
3    vib  282.5      0. 1
4    vib  1171.6     0. 1
5    vib  2634.2     0. 1
6    vib  2650.2     0. 1
7    qro  3.5071     1. 1
```

Addition Elimination TS

```
'AddElim_TS'
6 0  'HAR'
10.   3000   6000   85000.
1    vib  191.7      0. 1
2    vib  383.6      0. 1
3    vib  947.3      0. 1
4    vib  1066.4     0. 1
5    vib  2630.3     0. 1
6    qro  1.9677     1. 1
```

Loose TS

```
'Loose_TS'
6 0  'HAR'
10.   3000   6000   85000.
1    vib  72.6       0. 1
2    vib  76.0       0. 1
3    vib  1168.0     0. 1
4    vib  2630.6     0. 1
5    vib  2651.2     0. 1
6    qro  3.4155     1. 1
```

Gorin TS

```
'Gorin_TS'
5 0  'HAR'
10.   3000   6000   85000.
1  vib   1174.0  0.0   1
2  vib   2639.2  0.0   1
3  vib   2654.5  0.0   1
4  qro   1.365   1.    2
5  qro   3.4360  1.    1
```

D2.3. Sample Thermo input files

Equilibrium Constant Calculation

```
KJOU  MCC
7
298, 350, 400, 500, 700, 1000, 1500
3
reac  H2S  29.0  34.0  2   1   1  5  'HAR'
H2S
0.0     1
1   vib    1174.0  0.    1
2   vib    2639.2  0.    1
3   vib    2654.5  0.    1
4   qro    3.5076  1.    1
5   qro    1.7496  1.    2
reac  Chlorine  0.0   35.0  1    1    2    0  'HAR'
Chlorine
0.0     4
882.36  2
prod  A1  0.0  69.0  1    1    1   8  'HAR'
A1
0.0   2
1     vib   129.9        0. 1
2     vib   271.1        0. 1
3     vib   282.5        0. 1
4     vib   1171.6       0. 1
5     vib   2634.2       0. 1
6     vib   2650.2       0. 1
7     qro   3.5113       1. 1
8     qro   140.4063     1. 2
```

Transition State Calculation

```
KJOU  MCC
17
100, 200, 298, 350, 400, 500, 600, 700, 800, 900, 1000, 1200, 1500, 1800, 2000, 2400, 3000
3
reac  H2S  29.0  34.0  2   1   1  5  'HAR'
H2S
0.0     1
1   vib    1174.0  0.    1
2   vib    2639.2  0.    1
3   vib    2654.5  0.    1
4   qro    3.5076  1.    1
5   qro    1.7496  1.    2
reac  Chlorine  0.0   35.0  1    1    2    0  'HAR'
Chlorine
0.0     4
882.36  2

ctst 'AddElim_TS' -3.6 69.0 1  1  1  7  'HAR'
Addition Elimination TS
0.0   2
1     vib   191.7          0. 1
2     vib   383.6          0. 1
3     vib   947.3          0. 1
4     vib   1066.4         0. 1
5     vib   2630.3         0. 1
6     qro   1.9677         1. 1
7     qro   149.48         1. 2
```

Gorin-type TS Calculation

```
KJOU  MCC
7
298, 350, 400, 500, 700, 1000, 1500
3
reac  H2S  0.0  34.0  2   1   1  5  'HAR'
H2S
0.0     1
1   vib    1174.0  0.    1
2   vib    2639.2  0.    1
3   vib    2654.5  0.    1
4   qro    3.5076  1.    1
5   qro    1.7496  1.    2
reac  Chlorine  0.0   35.0  1    1    2    0  'HAR'
Chlorine
0.0     4
882.36  2
ctst  Gorin_TS  0.0  69.0  1    1    1   6  'HAR'
Gorin_TS
0.0   2
1   vib    1174.0   0.0    1
2   vib    2639.2   0.0    1
3   vib    2654.5   0.0    1
4   fit    1.7496   1.     2
5   qro    3.4360   1.     1
6   gor    317.95   1.     2

6.12E-10 5.99E-10 5.95E-10 5.98E-10 6.21E-10 6.49E-10 6.29E-10
MORSE
136.1835
33.0
2.8323916
```

D2.4. Sample MultiWell input files

Sum of States Calculation

```
H2S + Cl Addition Elimination
10. 3000 6000 85000. 2113989025
'BAR' 'KJOU'
298.0 298.0
1
0.03
1 2
1 'A1' 0.0 140.4063 1 2 1
2 'H2S+Cl' 29.0
3 'SH+HCl' -20.5
3.47    114.    40.    69.       !Ar
1 4.64 400.0 10 40.0 0.16 1.0 0.0 0.0 0.0 0.0 0.0
'LJ'
2
1 2 'Coll_TS' 317.95 1 2 1 4.72e+13 29.0 'REV' 'FAST' 'NOTUN' 'NOCENT' 'SUM'
1 3 'AddElim_TS' 150.47 1 2 1 5.26e+12 25.4 'NOREV' 'FAST' 'NOTUN' 'NOCENT' 'SUM'
```

Inverse Laplace Transform Calculation (ILT)

```
H2S + Cl Addition Elimination
10. 3000 6000 85000. 2113989025
'BAR' 'KJOU'
298.0 298.0
1
0.03
1 2
1 'A1' 0.0 140.4063 1 2 1
2 'H2S+Cl' 29.0
3 'SH+HCl' -20.5
3.47    114.    40.    69.       !Ar
1 4.64 400.0 10 40.0 0.16 1.0 0.0 0.0 0.0 0.0 0.0
'LJ'
2
1 2 'Coll_TS' 317.95 1 2 1 4.72e+13 29.0 'REV' 'FAST' 'NOTUN' 'NOCENT' 'ILT'
1 3 'AddElim_TS' 150.47 1 2 1 5.26e+12 25.4 'NOREV' 'FAST' 'NOTUN' 'NOCENT' 'SUM'
1000000 'COLL' 100 'CHEMACT' 1 2 0.0
```

Gorin-type TS Calculation

```
H2S + Cl Addition Elimination
10. 3000 6000 85000. 2113989025
'BAR' 'KJOU'
298.0 298.0
1
0.03
1 2
1 'A1' 0.0 140.4063 1 2 1
2 'H2S+Cl' 29.0
3 'SH+HCl' -20.5
3.47    114.    40.    69.        !Ar
1 4.64 400.0 10 40.0 0.16 1.0 0.0 0.0 0.0 0.0 0.0
'LJ'
2
1 2 'Gorin_TS' 711.99 1 2 1 4.72e+13 29.0 'REV' 'FAST' 'NOTUN' 'NOCENT' 'SUM'
1 3 'AddElim_TS' 150.47 1 2 1 5.26e+12 25.4 'NOREV' 'FAST' 'NOTUN' 'NOCENT' 'SUM'
1000000 'COLL' 100 'CHEMACT' 1 2 0.0
```

D3. Sample input files for the MultiWell-based kinetic analysis of the NH_3Cl reaction system

D3.1. Sample Densum input files

```
A2
'A2'
10 0  'HAR'
10.    1000    2000    85000.
1  vib 148.0   0.0 1
2  vib 155.0   0.0 1
3  vib 206.0   0.0 1
4  vib 541.0   0.0 1
5  vib 554.0   0.0 1
6  vib 1499.0  0.0 1
7  vib 2655.0  0.0 1
8  vib 3303.0  0.0 1
9  vib 3399.0  0.0 1
10 qro 1.33    1.0 1
```

```
Abstraction TS
'Abs_TS'
9 0  'HAR'
10.    1000    2000    85000.
1  vib 393.0   0.0 1
2  vib 428.0   0.0 1
3  vib 665.0   0.0 1
4  vib 1038.0  0.0 1
5  vib 1124.0  0.0 1
6  vib 1523.0  0.0 1
7  vib 3325.0  0.0 1
8  vib 3424.0  0.0 1
9  qro 2.08    1.0 1
```

```
Gorin TS
'Gorin_TS'
7 0  'HAR'
10.    1000    2000    85000.
1 vib 1502.0 0.0 1
2 vib 3276.0 0.0 1
3 vib 3368.0 0.0 1
4 vib 2916.0 0.0 1
5 qro 0.89  1.0 2
6 qro 0.88  1.0 2
7 qro 1.33  1.0 1
```

D3.2. Sample Thermo input files

Equilibrium Constant Calculation

```
KJOU  MCC
5
290, 350, 400, 500, 600
3
reac  NH2  0.0  16.0  2   1   1  5  'HAR'
NH2
0.0     2
1 vib 1502.0 0.0 1
2 vib 3276.0 0.0 1
3 vib 3368.0 0.0 1
4 qro 0.72  1.0 1
5 qro 1.62  1.0 2
reac  HCl  17.7   36.0 1    1    1    2  'HAR'
HCl
0.0    1
1   vib    2916.0   0.    1
2   qro    1.60     1.    2
prod  A2  0.0  52.0  2    1    1   11  'HAR'
A2
0.0   2
1 vib 148.0 0.0 1
2 vib 155.0 0.0 1
3 vib 206.0 0.0 1
4 vib 541.0 0.0 1
5 vib 554.0 0.0 1
6 vib 1499.0 0.0 1
7 vib 2655.0 0.0 1
8 vib 3303.0 0.0 1
9 vib 3399.0 0.0 1
10 qro 1.33  1.0 1
11 qro 123.43  1.0 2
```

Gorin-type TS Calculation

```
KJOU  MCC
5
290, 350, 400, 500, 600
3
reac  NH2  0.0  16.0  2   1   1  5  'HAR'
NH2
0.0     2
1 vib 1502.0 0.0 1
2 vib 3276.0 0.0 1
3 vib 3368.0 0.0 1
4 qro 0.72  1.0 1
5 qro 1.62  1.0 2
reac  HCl  0.0   36.0 1    1    1    2  'HAR'
HCl
0.0    1
1   vib    2916.0   0.    1
2   qro    1.60     1.    2
ctst  Gorin_TS  0.0  52.0  2    1    1   8  'HAR'
Gorin_TS
0.0   2
1 vib 1502.0 0.0 1
2 vib 3276.0 0.0 1
3 vib 3368.0 0.0 1
4 vib 2916.0 0.0 1
5 fit 1.62  1.0 2
6 fit 1.60  1.0 2
7 qro 1.33  1.0 1
8 gor 123.4 1.0 2

4.3E-10 4.7E-10 5.1E-10 5.6E-10 6.2E-10

MORSE
159.0
25.9
3.24385
```

D3.3. Sample MultiWell input files

Sum of States Calculation Based on Gorin-type TS

```
NH2 + HCl Abstraction
10. 1000 2000 85000. 2113989025
'BAR' 'KJOU'
290.0 290.0
1
0.1
1 2
1 'A2' 0.0 123.43 2 2 1
2 'NH2+HCl' 17.7
3 'NH3+Cl' 1.1
3.47    114.    40.    52.        !Ar
1 4.29 400.0 10 40.0 0.26 1.0 0.0 0.0 0.0 0.0 0.0
'LJ'
2
1 2 'Gorin_TS' 474.03 2 2 1 1.18e+15 17.7 'REV' 'FAST' 'NOTUN' 'NOCENT' 'SUM'
1 3 'Abs_TS' 82.96 1 2 1 1.08e+12 15.0 'NOREV' 'FAST' 'NOTUN' 'CENT' 'SUM'
1000000 'COLL' 100 'CHEMACT' 1 2 0.0
```

D4. Sample input files for the MultiWell-based kinetic analysis of the C_6H_6Cl reaction system

D4.1. Sample Densum input files

Pi Adduct
'Pi_Ph_HCl'
34 0 'HAR'
10. 250 500 85000.
1 vib 24.5 0.0 1
2 vib 30.3 0.0 1
3 vib 63.0 0.0 1
4 vib 117.0 0.0 1
5 vib 138.3 0.0 1
6 vib 378.3 0.0 1
7 vib 406.3 0.0 1
8 vib 552.0 0.0 1
9 vib 574.9 0.0 1
10 vib 590.1 0.0 1
11 vib 699.6 0.0 1
12 vib 806.4 0.0 1
13 vib 862.5 0.0 1
14 vib 910.3 0.0 1
15 vib 922.8 0.0 1
16 vib 939.4 0.0 1
17 vib 982.5 0.0 1
18 vib 1012.9 0.0 1
19 vib 1034.6 0.0 1
20 vib 1108.6 0.0 1
21 vib 1136.7 0.0 1
22 vib 1193.9 0.0 1
23 vib 1260.5 0.0 1
24 vib 1412.2 0.0 1
25 vib 1427.3 0.0 1
26 vib 1553.5 0.0 1
27 vib 1598.7 0.0 1
28 vib 2883.9 0.0 1
29 vib 3048.0 0.0 1
30 vib 3055.1 0.0 1
31 vib 3068.6 0.0 1
32 vib 3072.3 0.0 1
33 vib 3078.5 0.0 1
34 qro 171.1 1.0 1

Abstraction TS
'Abs_TS'
33 0 'HAR'
10. 250 500 85000.
1 vib 58.2 0.0 1
2 vib 67.7 0.0 1
3 vib 382.6 0.0 1
4 vib 385.4 0.0 1
5 vib 436.0 0.0 1
6 vib 461.7 0.0 1
7 vib 491.3 0.0 1
8 vib 573.4 0.0 1
9 vib 697.4 0.0 1
10 vib 704.1 0.0 1
11 vib 790.9 0.0 1
12 vib 799.5 0.0 1
13 vib 856.7 0.0 1
14 vib 911.1 0.0 1
15 vib 920.6 0.0 1
16 vib 975.9 0.0 1
17 vib 1003.6 0.0 1
18 vib 1038.9 0.0 1
19 vib 1091.4 0.0 1
20 vib 1108.5 0.0 1
21 vib 1141.9 0.0 1
22 vib 1191.5 0.0 1
23 vib 1263.1 0.0 1
24 vib 1419.6 0.0 1
25 vib 1443.4 0.0 1
26 vib 1563.6 0.0 1
27 vib 1606.5 0.0 1
28 vib 3049.0 0.0 1
29 vib 3057.6 0.0 1
30 vib 3071.9 0.0 1
31 vib 3078.6 0.0 1
32 vib 3081.4 0.0 1
33 qro 90.6 1.0 1

Gorin TS
'Gorin_TS'
31 0 'HAR'
10. 250 500 85000.
1 vib 380.6 0.0 1
2 vib 407.4 0.0 1
3 vib 558.1 0.0 1
4 vib 575.3 0.0 1
5 vib 589.6 0.0 1
6 vib 695.5 0.0 1
7 vib 801.4 0.0 1
8 vib 858.6 0.0 1
9 vib 908.2 0.0 1
10 vib 921.6 0.0 1
11 vib 935.9 0.0 1
12 vib 982.6 0.0 1
13 vib 1013.1 0.0 1
14 vib 1034.1 0.0 1
15 vib 1106.6 0.0 1
16 vib 1135.3 0.0 1
17 vib 1192.5 0.0 1
18 vib 1260.2 0.0 1
19 vib 1412.9 0.0 1
20 vib 1428.1 0.0 1
21 vib 1556.0 0.0 1
22 vib 1600.8 0.0 1
23 vib 3042.3 0.0 1
24 vib 3049.9 0.0 1
25 vib 3065.2 0.0 1
26 vib 3069.0 0.0 1
27 vib 3074.7 0.0 1
28 vib 2908.5 0.0 1
29 qro 49.13 1.0 2
30 qro 0.92 1.0 2
31 qro 171.10 1.0 1

D4.2. Sample Thermo input files

Equilibrium Constant Calculation

```
KJOU  MCC
11
100, 200, 294, 298.15, 330, 407, 544, 748, 1000,
1500, 2000
3
reac  Phenyl  13.1  77.0  2   1   1  29  'HAR'
Phenyl
0.0    2
1 vib 380.6 0.0 1
2 vib 407.4 0.0 1
3 vib 558.1 0.0 1
4 vib 575.3 0.0 1
5 vib 589.6 0.0 1
6 vib 695.5 0.0 1
7 vib 801.4 0.0 1
8 vib 858.6 0.0 1
9 vib 908.2 0.0 1
10 vib 921.6 0.0 1
11 vib 935.9 0.0 1
12 vib 982.6 0.0 1
13 vib 1013.1 0.0 1
14 vib 1034.1 0.0 1
15 vib 1106.6 0.0 1
16 vib 1135.3 0.0 1
17 vib 1192.5 0.0 1
18 vib 1260.2 0.0 1
19 vib 1412.9 0.0 1
20 vib 1428.1 0.0 1
21 vib 1556.0 0.0 1
22 vib 1600.8 0.0 1
23 vib 3042.3 0.0 1
24 vib 3049.9 0.0 1
25 vib 3065.2 0.0 1
26 vib 3069.0 0.0 1
27 vib 3074.7 0.0 1
28 qro 171.0  1.0 1
29 qro 85.4   1.0 2
reac  HCl  0.0   36.0 1    1    1    2  'HAR'
HCl
0.0    1
1   vib    2908.5   0.    1
2   qro    1.6      1.    2
prod  Pi_Ph_HCl  0.0  113.0  1    1    1   35  'HAR'
Pi_Ph_HCl
0.0   2
1  vib 24.5   0.0 1
```

Gorin-type TS Calculation

```
KJOU  MCC
5
294, 330, 407, 544, 748
3
reac  Phenyl  0.0  77.0  2   1   1  29  'HAR'
Phenyl
0.0    2
1 vib 380.6 0.0 1
2 vib 407.4 0.0 1
3 vib 558.1 0.0 1
4 vib 575.3 0.0 1
5 vib 589.6 0.0 1
6 vib 695.5 0.0 1
7 vib 801.4 0.0 1
8 vib 858.6 0.0 1
9 vib 908.2 0.0 1
10 vib 921.6 0.0 1
11 vib 935.9 0.0 1
12 vib 982.6 0.0 1
13 vib 1013.1 0.0 1
14 vib 1034.1 0.0 1
15 vib 1106.6 0.0 1
16 vib 1135.3 0.0 1
17 vib 1192.5 0.0 1
18 vib 1260.2 0.0 1
19 vib 1412.9 0.0 1
20 vib 1428.1 0.0 1
21 vib 1556.0 0.0 1
22 vib 1600.8 0.0 1
23 vib 3042.3 0.0 1
24 vib 3049.9 0.0 1
25 vib 3065.2 0.0 1
26 vib 3069.0 0.0 1
27 vib 3074.7 0.0 1
28 qro 171.0  1.0 1
29 qro 85.4   1.0 2
reac  HCl  0.0   36.0 1    1    1    2  'HAR'
HCl
0.0    1
1   vib    2908.5   0.    1
2   qro    1.6      1.    2
ctst  Gorin_TS  0.0  113.0  1    1    1   32  'HAR'
Gorin_TS
0.0   2
1 vib 380.6 0.0 1
2 vib 407.4 0.0 1
```

2 vib 30.3 0.0 1
3 vib 63.0 0.0 1
4 vib 117.0 0.0 1
5 vib 138.3 0.0 1
6 vib 378.3 0.0 1
7 vib 406.3 0.0 1
8 vib 552.0 0.0 1
9 vib 574.9 0.0 1
10 vib 590.1 0.0 1
11 vib 699.6 0.0 1
12 vib 806.4 0.0 1
13 vib 862.5 0.0 1
14 vib 910.3 0.0 1
15 vib 922.8 0.0 1
16 vib 939.4 0.0 1
17 vib 982.5 0.0 1
18 vib 1012.9 0.0 1
19 vib 1034.6 0.0 1
20 vib 1108.6 0.0 1
21 vib 1136.7 0.0 1
22 vib 1193.9 0.0 1
23 vib 1260.5 0.0 1
24 vib 1412.2 0.0 1
25 vib 1427.3 0.0 1
26 vib 1553.5 0.0 1
27 vib 1598.7 0.0 1
28 vib 2883.9 0.0 1
29 vib 3048.0 0.0 1
30 vib 3055.1 0.0 1
31 vib 3068.6 0.0 1
32 vib 3072.3 0.0 1
33 vib 3078.5 0.0 1
34 qro 171.1 1.0 1
35 qro 430.7 1.0 2
3 vib 558.1 0.0 1
4 vib 575.3 0.0 1
5 vib 589.6 0.0 1
6 vib 695.5 0.0 1
7 vib 801.4 0.0 1
8 vib 858.6 0.0 1
9 vib 908.2 0.0 1
10 vib 921.6 0.0 1
11 vib 935.9 0.0 1
12 vib 982.6 0.0 1
13 vib 1013.1 0.0 1
14 vib 1034.1 0.0 1
15 vib 1106.6 0.0 1
16 vib 1135.3 0.0 1
17 vib 1192.5 0.0 1
18 vib 1260.2 0.0 1
19 vib 1412.9 0.0 1
20 vib 1428.1 0.0 1
21 vib 1556.0 0.0 1
22 vib 1600.8 0.0 1
23 vib 3042.3 0.0 1
24 vib 3049.9 0.0 1
25 vib 3065.2 0.0 1
26 vib 3069.0 0.0 1
27 vib 3074.7 0.0 1
28 vib 2908.5 0.0 1
29 fit 85.4 1.0 2
30 fit 1.6 1.0 2
31 qro 171.1 1.0 1
32 gor 430.7 1.0 2
9.55E-12 7.88E-12 5.13E-12 3.44E-12 2.86E-12
MORSE
66.0
15.3
3.773

D4.3. Sample MultiWell input files

Sum of States Calculation Based on Gorin-type TS

```
Phenyl + HCl Abstraction
10. 250 500 85000. 2113989025
'BAR' 'KJOU'
294.0 294.0
1
0.1
1 2
1 'Pi_Ph_HCl' 0.0 430.7 1 2 1
2 'Ph+HCl' 13.1
3 'Bz+Cl' -27.6
3.47    114.    40.    113.        !Ar
1 5.99 400.0 10 40.0 0.35 1.0 0.0 0.0 0.0 0.0 0.0
'LJ'
2
1 2 'Gorin_TS' 1300.91 1 2 1 3.11e+11 13.1 'REV' 'FAST' 'NOTUN' 'NOCENT' 'SUM'
1 3 'Abs_TS' 562.6 2 2 1 5.766e+3 -2.4 'NOREV' 'FAST' 'NOTUN' 'CENT' 'SUM'
1000000 'COLL' 100 'CHEMACT' 1 2 0.0
```

D5. Sample input files for the MultiWell-based kinetic analysis of the C_2H_4Cl reaction system

D5.1. Sample Mominert input files

```
Beta
7
Cl  1    -0.712457   -0.824097    0.000000
C   2     0.000000    0.861796    0.000000
C   3     1.478809    0.805591    0.000000
H   4    -0.394423    1.346390    0.893426
H   5    -0.394423    1.346390   -0.893426
H   6     2.013881    0.656276   -0.931894
H   7     2.013881    0.656276    0.931894
2 3
4
2 1 4 5
0 0
```

```
Alpha
7
H    1    -1.587784    -1.094468    -0.706178
C    2    -1.64997     -0.268304    0.010883
C    3    -0.444212    0.60794      -0.08139
H    4    -1.756295    -0.70774     1.014571
H    5    -2.550351    0.316884     -0.203543
H    6    -0.45677     1.652557     0.204984
Cl   7    1.112723     -0.129709    0.006659
2 3
4
2 1 4 5
0 0
```

```
A2
7
C   1   0.705615    -2.229440    0.000000
H   2  -0.379840    -2.145766    0.000000
H   3   1.119141    -3.241963    0.000000
C   4   1.492939    -1.171951    0.000000
H   5   0.000000     0.695792    0.000000
H   6   2.556470    -0.967904    0.000000
Cl  7  -0.969829     1.533423    0.000000
4 5
2
5 7
0 0
```

```
Abs TS
7
C  1   -2.061235    -0.436022    0.000000
H  2   -1.684075    -1.455914    -0.000007
H  3   -3.144242    -0.300071    0.000011
C  4   -1.255316     0.608939    -0.000003
H  5    0.165635     0.287112    -0.000001
H  6   -1.385572     1.685266    0.000003
Cl 7    1.526327    -0.073759    0.000000
4 5
2
5 7
0 0
```

D5.2. Sample Densum input files

Beta Chloroethyl Radical
'Beta_Rad'
16 0 'HAR'
10. 500 1000 85000.
1 hra 208.0 1.755 2
2 vib 293.0 0. 1
3 vib 575.0 0. 1
4 vib 653.0 0. 1
5 vib 754.0 0. 1
6 vib 1050.0 0. 1
7 vib 1051.0 0. 1
8 vib 1230.0 0. 1
9 vib 1264.0 0. 1
10 vib 1416.0 0. 1
11 vib 1446.0 0. 1
12 vib 2981.0 0. 1
13 vib 3028.0 0. 1
14 vib 3041.0 0. 1
15 vib 3134.0 0. 1
16 qro 15.50 1. 1

Abstraction TS
'Abs_TS'
15 0 'HAR'
10. 1000 2000 85000.
1 hra 117.0 0.09 1
2 hra 271.0 0.09 1
3 vib 598.0 0. 1
4 vib 615.0 0. 1
5 vib 737.0 0. 1
6 vib 788.0 0. 1
7 vib 889.0 0. 1
8 vib 899.0 0. 1
9 vib 1129.0 0. 1
10 vib 1342.0 0. 1
11 vib 1585.0 0. 1
12 vib 2983.0 0. 1
13 vib 3079.0 0. 1
14 vib 3105.0 0. 1
15 qro 12.1 1. 1

Gorin TS (C_2H_4 + Cl = β, 293K)
'Gorin_TS'
14 0 'HAR'
10. 500 1000 85000.
1 vib 792.0 0. 1
2 vib 879.0 0. 1
3 vib 923.0 0. 1
4 vib 1005.0 0. 1
5 vib 1183.0 0. 1
6 vib 1318.0 0. 1
7 vib 1418.0 0. 1
8 vib 1613.0 0. 1
9 vib 3008.0 0. 1
10 vib 3026.0 0. 1
11 vib 3085.0 0. 1
12 vib 3110.0 0. 1
13 qro 6.60 1. 2
14 qro 15.5 1. 1

A2
'A2'
16 0 'HAR'
10. 1000 2000 85000.
1 hra 32.0 1.8 1
2 hra 34.0 1.8 1
3 hra 79.0 1.8 1
4 vib 218.0 0. 1
5 vib 272.0 0. 1
6 vib 706.0 0. 1
7 vib 770.0 0. 1
8 vib 886.0 0. 1
9 vib 1028.0 0. 1
10 vib 1344.0 0. 1
11 vib 1564.0 0. 1
12 vib 2829.0 0. 1
13 vib 2956.0 0. 1
14 vib 3053.0 0. 1
15 vib 3117.0 0. 1
16 qro 14.7 1. 1

Gorin TS (C_2H_3 + HCl = A2, 298K)
'Gorin_TS'
13 0 'HAR'
10. 1000 2000 85000.
1 vib 706.0 0. 1
2 vib 788.0 0. 1
3 vib 883.0 0. 1
4 vib 1031.0 0. 1
5 vib 1344.0 0. 1
6 vib 1564.0 0. 1
7 vib 2955.0 0. 1
8 vib 3052.0 0. 1
9 vib 3112.0 0. 1
10 vib 2908.0 0. 1
11 qro 8.14 1. 2
12 qro 0.78 1. 2
13 qro 14.7 1. 1

D5.3. Sample Thermo input files

Equilibrium Constant Calculation (C_2H_3 + HCl = A2)

```
KJOU  MCC
7
298.15, 350, 400, 500, 700, 1000, 1500
3
reac  Vinyl  8.2  27.0  1   1   1  11  'HAR'
Vinyl Radical
0.0     2
1   vib    706.0    0.    1
2   vib    788.0    0.    1
3   vib    883.0    0.    1
4   vib    1031.0   0.    1
5   vib    1344.0   0.    1
6   vib    1564.0   0.    1
7   vib    2955.0   0.    1
8   vib    3052.0   0.    1
9   vib    3112.0   0.    1
10  qro    2.2    1.    1
11  qro    16.7   1.    2
reac  HCl  0.0   36.0 1    1    1    2  'HAR'
HCl
0.0    1
1   vib    2908.0   0.    1
2   qro    1.6   1.    2
prod  I_Abs  0.0  63.0  1    1    1   17  'HAR'
Abstraction Adduct
0.0   2
1   hra    32.0          1.8      1
2   hra    34.0          1.8      1
3   hra    79.0          1.8      1
4   vib    218.0         0.       1
5   vib    272.0         0.       1
6   vib    706.0         0.       1
7   vib    770.0         0.       1
8   vib    886.0         0.       1
9   vib    1028.0        0.       1
10  vib    1344.0        0.       1
11  vib    1564.0        0.       1
12  vib    2829.0        0.       1
13  vib    2956.0        0.       1
14  vib    3053.0        0.       1
15  vib    3117.0        0.       1
16  qro    14.7          1.       1
17  qro    240.4         1.       2
```

Gorin-type TS Calculation

```
KJOU  MCC
7
298.15, 350, 400, 500, 700, 1000, 1500
3
reac  Vinyl  0.0  27.0  1   1   1  11  'HAR'
Vinyl Radical
0.0     2
1   vib    706.0    0.    1
2   vib    788.0    0.    1
3   vib    883.0    0.    1
4   vib    1031.0   0.    1
5   vib    1344.0   0.    1
6   vib    1564.0   0.    1
7   vib    2955.0   0.    1
8   vib    3052.0   0.    1
9   vib    3112.0   0.    1
10  qro    2.2    1.    1
11  qro    16.7   1.    2
reac  HCl  0.0   36.0 1    1    1    2  'HAR'
HCl
0.0    1
1   vib    2908.0   0.    1
2   qro    1.6   1.    2
ctst  Gorin_TS  0.0  63.0  1    1    1   14  'HAR'
Gorin_TS
0.0   2
1   vib    706.0    0.    1
2   vib    788.0    0.    1
3   vib    883.0    0.    1
4   vib    1031.0   0.    1
5   vib    1344.0   0.    1
6   vib    1564.0   0.    1
7   vib    2955.0   0.    1
8   vib    3052.0   0.    1
9   vib    3112.0   0.    1
10  vib    2908.0   0.    1
11  fit    16.7   1.    2
12  fit    1.6    1.    2
13  qro    14.7    1.    1
14  gor    117.0   1.    2

4.9E-10 5.3E-10 5.7E-10 6.3E-10 7.5E-10 9.0E-10 1.1E-10
MORSE
83.3
8.9
3.83937
```

Equilibrium Constant Calculation (C_2H_4 + Cl = β-Chloroethyl)

```
KJOU  MCC
13
293, 298.15, 345, 378, 400, 430, 551, 611, 676, 798, 901, 1007, 1055
3
reac C2H4  73.6  28.0  4   1   1  14  'HAR'
C2H4
0.0    1
1   vib    792.0   0.    1
2   vib    879.0   0.    1
3   vib    923.0   0.    1
4   vib    1005.0  0.    1
5   vib    1183.0  0.    1
6   vib    1318.0  0.    1
7   vib    1418.0  0.    1
8   vib    1613.0  0.    1
9   vib    3008.0  0.    1
10  vib    3026.0  0.    1
11  vib    3085.0  0.    1
12  vib    3110.0  0.    1
13  qro    3.46    1.    1
14  qro    18.6    1.    2
reac  Chlorine  0.0   35.0  1    1    2    0  'HAR'
Chlorine
0.0    4
882.36  2
prod  Beta_Rad  0.0  63.0  1    1    1   17  'HAR'
Beta_Rad
0.0   2
1     hra   208.0       1.755 2
2     vib   293.0         0. 1
3     vib   575.0         0. 1
4     vib   653.0         0. 1
5     vib   754.0         0. 1
6     vib   1050.0        0. 1
7     vib   1051.0        0. 1
8     vib   1230.0        0. 1
9     vib   1264.0        0. 1
10    vib   1416.0        0. 1
11    vib   1446.0        0. 1
12    vib   2981.0        0. 1
13    vib   3028.0        0. 1
14    vib   3041.0        0. 1
15    vib   3134.0        0. 1
16    qro   15.5          1. 1
17    qro   92.5          1. 2
```

D5.4. Sample MultiWell input files

Sum of States Calulation Based on Gorin-type TS with N_2 Bath Gas

```
C2H4 + Cl Addition
10. 500 1000 85000. 2113989025
'BAR' 'KJOU'
293.0 293.0
1
0.027
1 1
1 'Beta_Rad' 0.0 92.5 1 2 1
2 'C2H4+Cl' 73.6
3.74    82.    28.    63.        !N2
1 4.94 400.0 10 40.0 0.196 1.0 0.0 0.0 0.0 0.0 0.0
'LJ'
1
1 2 'Gorin_TS' 170.64 1 2 1 2.52e+13 73.6 'REV' 'FAST' 'NOTUN' 'NOCENT' 'SUM'
1000000 'COLL' 100 'CHEMACT' 1 2 0.0
```

Sum of States Calculation Based on Gorin-type TS

```
C2H3 + HCl Abstraction
10. 1000 2000 85000. 2113989025
'BAR' 'KJOU'
298.15 298.15
1
0.1
1 2
1 'A2' 0.0 240.4 1 2 1
2 'C2H3+HCl' 8.2
3 'C2H4+Cl' -23.0
3.47    114.    40.    63.        !Ar
1 4.94 400.0 10 40.0 0.57 1.0 0.0 0.0 0.0 0.0 0.0
'LJ'
2
1 2 'Gorin_TS' 593.21 1 2 1 1.18e+14 8.2 'REV' 'FAST' 'NOTUN' 'NOCENT' 'SUM'
1 3 'Abs_TS' 171.4 1 2 1 1.08e+13 1.0 'NOREV' 'FAST' 'NOTUN' 'CENT' 'SUM'
1000000 'COLL' 100 'CHEMACT' 1 2 0.0
```

REFERENCES

(1) Solomons, G.; Fryhle, C. *Organic Chemistry*; John Wiley & Sons, Inc.: New York, 2002.

(2) Carroll, F. A. *Perspectives on Structure and Mechanism in Organic Chemistry*; Brooks/Cole Publishing Company: Pacific Grove, 1998.

(3) Molina, M. J.; Rowland, F. S. *Nature* **1974**, *249*, 810.

(4) World Meteorological Organization Global Ozone Research and Monitoring Project, Report No. 20; Scientific Assessment of Stratospheric Ozone, 1989.

(5) O'Dwyer, M.; Padgett, M. J.; McGonigle, A. J. S.; Oppenheimer, C.; Inguaggiato, S. *Geophys. Res. Lett.* **2003**, *30*, 1652.

(6) Lewis, J. S. *Earth Planet. Sci. Lett.* **1970**, *10*, 73.

(7) Hoffman, J. H.; Hodges, R. R.; Donahue, T. M.; McElroy, M. B. *J. Geophys. Res.* **1980**, *85*, 7882.

(8) Yung, Y. L.; DeMore, W. B. *Icarus* **1982**, *51*, 199.

(9) Tsunogai, S.; Ikeuchi, K. *Geochem. J.* **1968**, *2*, 157.

(10) Mader, C. L. *Numerical Modeling of Explosives and Propellants*, 2nd ed.; CRC Press: New York, 1998.

(11) Woodman, J. H.; Trafton, L.; Owen, T. *Icarus* **1977**, *32*, 314.

(12) Gulkis, S.; Janssen, M. A.; Olsen, E. T. *Icarus* **1978**, *34*, 10.

(13) Rowland, F. S.; Molina, M. J. *Rev. Geophys. Space. Phys.* **1975**, *13*, 1.

(14) Senkan, S. M. *Environ. Sci. Technol.* **1988**, *22*, 368.

(15) Tsang, W. *Combust. Sci. Technol.* **1990**, *74*, 99.

(16) Pilling, M. J.; Seakins, P. W. *Reaction Kinetics*; Oxford Science Publications: Oxford, 1995.

(17) Bally, T.; Borden, W. T. *Rev. Comput. Chem.* **1999**, *13*, 1.

(18) Braun, W.; Lenzi, M. *Faraday Society* **1967**, *44*, 252.

(19) Fontijn, A.; Felder, W. *Reactive Intermediates in the Gas Phase*; Academic: New York, 1979, ch. 2.

(20) Ding, L.; Marshall, P. *J. Chem. Soc. Trans.* **1993**, *89*, 419.

(21) Steinfeld, J. I.; Francisco, J. S.; Hase, W. L. *Chemical Kinetics and Dynamics*, 2nd ed.; Prentice Hall: Upper Saddle River, 1999.

(22) Marshall, P. *Comput. Chem.* **1987**, *11*, 219.

(23) Marshall, P. *Comput. Chem.* **1989**, *13*, 103.

(24) Okabe, H. *Photochemistry of Small Molecules*; Wiley: New York, 1978.

(25) Bemand, P. P.; Clyne, M. A. A. *J. Chem. Soc. Faraday Trans. 2* **1975**, *71*, 1132.

(26) Hanf, A.; Lauter, A.; Volpp, H.-R. *Chem. Phys. Lett.* **2003**, *368*, 445.

(27) Davies, P. B.; Russell, D. K. *Chem. Phys. Lett.* **1979**, *67*, 440.

(28) Tyndall, G. S.; Orlando, J. J. *J. Chem. Soc. Faraday Trans.* **1995**, *91*, 3055.

(29) Clark, R. H.; Husain, D. *J. Photochem.* **1983**, *21*, 93.

(30) Gao, Y., University of North Texas, personal communication, 2007.

(31) Lindemann, F. A. *Trans. Faraday Soc.* **1922**, *17*, 598.

(32) Arrhenius, S. *Z. Physic. Chem.* **1889**, *4*, 226.

(33) Holbrook, K. A.; Pilling, M. J.; Robertson, S. H. *Unimolecular Reactions*, 2nd ed.; John Wiley & Sons: Chichester, 1996.

(34) Bunker, D. L. *J. Chem. Phys.* **1964**, *40*, 1946.

(35) Perdew, J. P. *Phys. Rev. Lett* **1985**, *55*, 1665.

(36) Zhao, Y.; Truhlar, D. G. *J. Phys. Chem. A* **2004**, *108*, 6908.

(37) Perdew, J. P. *Electronic Structure of Solids '91*; Ziesche, P.; Eschig, H., Eds.; Akademie Verlag: Berlin, 1991.

(38) Becke, A. D. *J. Chem. Phys.* **1996**, *104*, 1040.

(39) Curtiss, L. A.; Redfern, P. C.; Raghavachari, K.; Rassolov, V.; Pople, J. A. *J. Chem. Phys.* **1999**, *110*, 4703.

(40) Frisch, M. J.; Pople, J. A.; Binkley, J. S. *J. Chem. Phys.* **1984**, *80*, 3265.

(41) Curtiss, L. A.; Raghavachari, K.; Redfern, P. C.; Rassolov, V.; Pople, J. A. *J. Chem. Phys.* **1998**, *109*, 7764.

(42) Fast, P. L.; Sanchez, M. L.; Truhlar, D. G. *Chem. Phys. Lett.* **1999**, *306*, 407.

(43) Zhao, Y.; Tishchenko, O.; Truhlar, D. G. *J. Phys. Chem. B* **2005**, *109*, 19046.

(44) Pople, J. A.; Head-Gordon, M.; Raghavachari, K. *J. Chem. Phys.* **1987**, *87*, 5968.

(45) Cizek, J. *J. Chem. Phys.* **1966**, *45*, 4256.

(46) Cizek, J. *Adv. Chem. Phys.* **1966**, *14*, 35.

(47) Gauss, J.; Lauderdale, W. J.; Stanton, J. F.; Watts, J. D.; Bartlett, R. J. *Chem. Phys. Lett.* **1991**, *182*, 207.

(48) Gauss, J.; Stanton, J. F.; Bartlett, R. J. *J. Chem. Phys.* **1991**, *95*, 2623.

(49) Watts, J. D.; Gauss, J.; Bartlett, R. J. *J. Chem. Phys.* **1993**, *98*, 8718.

(50) Raghavachari, K.; Trucks, G. W.; Head-Gordon, M.; Pople, J. A. *Chem. Phys. Lett.* **1989**, *157*, 479.

(51) Langhoff, S. R.; Davidson, E. R. *Int. J. Quantum Chem.* **1974**, *8*, 61.

(52) Cramer, C. J. *Essentials of Computational Chemistry: Theories and Models*, second ed.; Wiley: Chichester, 2006.

(53) Dunning Jr., T. H. *J. Chem. Phys.* **1989**, *90*, 1007.

(54) Wilson, A. K.; Woon, D. E.; Peterson, K. A.; Dunning Jr., T. H. *J. Chem. Phys.* **1999**, *110*, 7667.

(55) Wilson, A. K.; Woon, D. E.; Peterson, K. A.; Dunning Jr., T. H. *J. Am. Chem. Soc.* **1997**, *213*, 60.

(56) Kendall, R. A.; Dunning Jr., T. H.; Harrison, R. J. *J. Chem. Phys.* **1992**, *96*, 6796.

(57) Woon, D. E.; Dunning Jr., T. H. *J. Chem. Phys.* **1994**, *100*, 2975.

(58) Halkier, A.; Helgaker, T.; Jorgensen, P.; Klopper, W.; Koch, H.; Olsen, J.; Wilson, A. K. *Chem. Phys. Lett.* **1998**, *286*, 243.

(59) Irikura, K. K.; Johnson III, R. D.; Kacker, R. N. *J. Phys. Chem. A* **2005**, *109*, 8430.

(60) Moore, C. *Natl. Bur. Stand.* **1952**, Circ 467.

(61) Amos, R. D.; Bernhardsson, A.; Berning, A.; Celani, P.; Cooper, D. L.; Deegan, M. J. O.; Dobbyn, A. J.; Eckert, F.; Hampel, C.; Hetzer, G.; Knowles, P. J.; Korona, T.; Lindh, R.; Lloyd, A. W.; McNicholas, S. J.; Manby, F. R.; Meyer, W.; Mura, M. E.; Nicklass, A.; Palmieri, P.; Pitzer, R.; Rauhut, G.; Schutz, M.; Schumann, U.; Stoll, H.; Stone, A. J.; Tarroni, R.; Thorsteinsson, T.; Werner, H.-J. MOLPRO, version 2002.6.

(62) Frisch, M. J.; Trucks, G. W.; Schlegel, H. B.; Scuseria, G. E.; Robb, M. A.; Cheeseman, J. R.; Montgomery, J. A. J.; Vreven, T.; Kudin, K. N.; Burant, J. C.; Millam, J. M.; Iyengar, S. S.; Tomasi, J.; Barone, V.; Mennucci, B.; Cossi, M.; Scalmani, G.; Rega, N.; Petersson, G. A.; Nakatsuji, H.; Hada, M.; Ehara, M.; Toyota, K.; Fukuda, R.; Hasegawa, J.;

Ishida, M.; Nakajima, T.; Honda, Y.; Kitao, O.; Nakai, H.; Klene, M.; Li, X.; Knox, J. E.; Hratchian, H. P.; Cross, J. B.; Bakken, V.; Adamo, C.; Jaramillo, J.; Gomperts, R.; Stratmann, R. E.; Yazyev, O.; Austin, A. J.; Cammi, R.; Pomelli, C.; Ochterski, J. W.; Ayala, P. Y.; Morokuma, K.; Voth, G. A.; Salvador, P.; Dannenberg, J. J.; Zakrzewski, V. G.; Dapprich, S.; Daniels, A. D.; Strain, M. C.; Farkas, O.; Malick, D. K.; Rabuck, A. D.; Raghavachari, K.; Foresman, J. B.; Ortiz, J. V.; Cui, Q.; Baboul, A. G.; Clifford, S.; Cioslowski, J.; Stefanov, B. B.; Liu, G.; Liashenko, A.; Piskorz, P.; Komaromi, I.; Martin, R. L.; Fox, D. J.; Keith, T.; A, A.-L. M.; Peng, C. Y.; Nanayakkara, A.; Challacombe, M.; Gill, P. M. W.; Johnson, B.; Chen, W.; Wong, M. W.; Gonzalez, C.; Pople, J. A. Gaussian 03, revision C.02; Gaussian, Inc. Wallingford, CT, 2004.

(63) Eyring, H. *J. Chem. Phys.* **1935**, *3*, 107.

(64) Evans, M. G.; Polanyi, M. *Trans. Faraday Soc.* **1935**, *31*, 875.

(65) Laidler, K. J. *Theories of Chemical Reaction Rates*; McGraw-Hill: London, 1969.

(66) Gilbert, R. G.; Smith, S. C. *Theory of Unimolecular and Recombination Reactions*; Blackwell Scientific Publications: Oxford, 1990.

(67) Ochterski, J. W. Thermochemistry in Gaussian. Available from: http://www.gaussian.com/g_whitepap/thermo.htm; Gaussian Inc., 2006.

(68) Wigner, E. *J. Chem. Phys.* **1937**, *5*, 720.

(69) Horiuti, J. *Bull. Chem. Soc. Jpn.* **1938**, *13*, 210.

(70) Keck, J. C. *J. Chem. Phys.* **1970**, *53*, 2041.

(71) Truhlar, D. G.; Garrett, B. C. *Acc. Chem. Res.* **1980**, *13*, 440.

(72) Troe, J. *J. Chem. Phys.* **1977**, *66*, 4758.

(73) Troe, J. *J. Phys. Chem.* **1979**, *83*, 114.

(74) Troe, J. *Bur. Bunsenges. Phys. Chem.* **1983**, *87*, 161.

(75) Cobos, C. J.; Troe, J. *Z. Phys. Chem.* **2003**, *217*, 1031.

(76) Krasnoperov, L. N.; Peng, J.; Marshall, P. *J. Phys. Chem. A* **2006**, *110*, 3110.

(77) Gao, Y.; Alecu, I. M.; Hsieh, P.-C.; Morgan, B. P.; Marshall, P.; Krasnoperov, L. N. *J. Phys. Chem.* **2006**, *110*, 6844.

(78) Marcus, R. A. *J. Chem. Phys.* **1952**, *20*, 359.

(79) Marcus, R. A. *J. Chem. Phys.* **1965**, *43*, 2658.

(80) Marcus, R. A.; Rice, O. K. *J. Phys. and Colloid Chem.* **1951**, *55*, 894.

(81) Wieder, G. M.; Marcus, R. A. *J. Chem. Phys.* **1962**, *37*, 1835.

(82) Forst, W. *Unimolecular Reactions: A Concise Introduction*; Cambridge University Press: Cambridge, UK, 2003.

(83) Gillespie, D. T. *J. Phys. Chem.* **1977**, *81*, 2340.

(84) Pilling, M. J. *Chem. Soc. Rev.* **2008**, *37*, 676.

(85) Barker, J. R. *Int. J. Chem. Kinet.* **2001**, *33*, 232.

(86) Barker, J. R. MultiWell-2008.3 Software; Ortiz, N. F., Preses, J. M., Lohr, L. L., Maranzana, A., Stimac, P. J., contributors; University of Michigan: Ann Arbor, MI, 2008; http://aoss.engin.umich.edu/multiwell/.

(87) Barker, J. R.; Ortiz, N. F. *Int. J. Chem. Kinet.* **2001**, *33*, 246.

(88) Barker, J. R.; Yoder, L. M.; King, K. D. *J. Phys. Chem. A* **2001**, *105*, 796.

(89) Baggott, J. E.; Law, D. W. *J. Chem. Phys.* **1986**, *85*, 6475.

(90) Tardy, D. C.; Rabinovitch, B. S. *Chem. Rev.* **1977**, *77*, 369.

(91) Hirschfelder, J. O.; Curtiss, C. F.; Bird, R. B. *Molecular Theory of Gases and Liquids*; Wiley: New York, 1964.

(92) Dean, A. M. *J. Phys. Chem.* **1985**, *89*, 4600.

(93) Troe, J.; Gardiner Jr., W. C. *Combustion Chemistry*; Springer-Verlag: New York, 1984.

(94) Hippler, H.; Troe, J.; Wendelken, H. J. *J. Chem. Phys.* **1983**, *78*, 6709.

(95) Reid, R. C.; Sherwood, T. K. *The Properties of Gases and Liquids: their Estimation and Correlation*; McGraw-Hill: New York, 1958.

(96) Stein, S. E.; Rabinovitch, B. S. *J. Chem. Phys.* **1973**, *58*, 2438.

(97) Beyer, T.; Swinehart, D. F. *Comm. Assoc. Comput. Machines* **1973**, *16*, 379.

(98) Sander, S. P.; Friedl, R. R.; Golden, D. M.; Kurylo, M. J.; Moortgat, G. K.; Keller-Rudek, H.; Wine, P. H.; Ravishankara, A. R.; Kolb, C. E.; Molina, M. J.; Finlayson-Pitts, B. J.; Huie, R. E.; Orkin, V. L. *Chemical Kinetics and Photochemical data for Use in Stratospheric Modeling, JPL Publication 06-2, Evaluation Number 15.* **2006**.

(99) Troe, J. *J. Phys. Chem.* **1979**, *83*, 114.

(100) Benson, S. W. *Thermochemical Kinetics*, 2nd ed.; Wiley: New York, 1976.

(101) Smith, G. P.; Golden, D. M. *Int. J. Chem. Kinet.* **1978**, *10*, 489.

(102) Gorin, E. *Acta Physicochim., URSS* **1938**, *9*, 691.

(103) Polanyi, J. C. *Acc. Chem. Res.* **1972**, *5*, 161.

(104) Coombe, A. T.; Pritt Jr, A. T.; Philipovich, D. *Chem. Phys. Lett.* **1975**, *35*, 345.

(105) Dill, B.; Heydtmann, H. *Chem. Phys.* **1978**, *35*, 161.

(106) Braithwaite, M.; Leone, S. R. *J. Chem. Phys.* **1978**, *69*, 839.

(107) Nesbitt, D. J.; Leone, S. R. *J. Chem. Phys.* **1980**, *72*, 1722.

(108) Agrawalla, B. S.; Setser, D. W. *J. Phys. Chem.* **1986**, *90*, 2450.

(109) Hossenlopp, J. M.; Hershberger, J. F.; Flynn, G. W. *J. Phys. Chem.* **1990**, *94*, 1346.

(110) Chen, K.-S.; Cheng, S.-S.; Lee, Y.-P. *J. Chem. Phys.* **2003**, *119*, 4229.

(111) Nava, D. F.; Brobst, W. D.; Stief, L. J. *J. Phys. Chem.* **1985**, *89*, 4703.

(112) Nicovich, J. M.; Wang, S.; Wine, P. H. *Int. J. Chem. Kinet.* **1995**, *27*, 359.

(113) Wilson, C.; Hirst, D. M. *J. Chem. Soc. Faraday Trans.* **1997**, *93*, 2831.

(114) Resende, S. M.; Pliego Jr., J. R.; Vandresen, S. *Molec. Phys.* **2008**, *106*, 841.

(115) Clyne, M. A. A.; Ono, Y. *Chem. Phys. Lett.* **1983**, *94*, 597.

(116) Clyne, M. A. A.; MacRobert, A. J.; Murrells, T. P.; Stief, L. J. *J. Chem. Soc. Trans. 2* **1984**, *80*, 877.

(117) Lu, E. C. C.; Iyer, R. S.; Rowland, F. S. *J. Phys. Chem.* **1986**, *89*, 1988.

(118) Sander, S. P.; Friedl, R. R.; Golden, D. M.; Kurylo, M. J.; Moortgat, G. K.; Keller-Rudek, H.; Wine, P. H.; Ravishankara, A. R.; Kolb, C. E.; Molina, M. J.; Finlayson-Pitts, B. J.; Huie, R. E.; Orkin, V. L. *Chemical Kinetics and Photochemical data for Use in Stratospheric Modeling, JPL Publication 06-2,* **2006**.

(119) Baboul, A. G.; Schlegel, H. B. *J. Chem. Phys.* **1997**, *107*, 9413.

(120) Irvin, J. A.; Quickenden, T. I. *J. Chem. Educ.* **1983**, *60*, 711.

(121) Marshall, P.; Goumri, A., University of North Texas, personal communication, 2007.

(122) Dunning Jr., T. H.; Peterson, K. A.; Wilson, A. K. *J. Chem. Phys.* **2001**, *114*, 9244.

(123) Nobes, R. H.; Bouma, W. J.; Radom, L. *Chem. Phys. Lett.* **1982**, *89*, 497.

(124) Ruscic, B.; Pinzon, R. E.; Morton, M. L.; von Laszevski, G.; Bittner, S. J.; Nijsure, S. G.; Amin, K. A.; Minkoff, M.; Wagner, A. F. *J. Phys. Chem.* **2004**, *108*, 9979.

(125) Shiell, R. C.; Hu, X. K.; Hu, Q. J.; Hepburn, J. W. *J. Phys. Chem. A* **2000**, *104*, 4339.

(126) Ellingson, B. A.; Truhlar, D. G. *J. Am. Chem. Soc.* **2007**, *129*, 12765.

(127) Westenberg, A. A.; de Haas, N. *J. Chem. Phys.* **1977**, *67*, 2388.

(128) Baboul, A. G.; Curtiss, L. A.; Redfern, P. C.; Raghavachari, K. *J. Chem. Phys.* **1999**, *110*, 7650.

(129) Montgomery, J. A. J.; Frisch, M. J.; Ochterski, J. W.; Petersson, G. A. *J. Chem. Phys.* **1999**, *110*, 2822.

(130) Amos, R. D.; Bernhardsson, A.; Berning, A. *et al*., MOLPRO, version 2006.1, a package of *ab initio* programs; University of Birmingham: Birmingham, UK, 2006.

(131) Westenberg, A. A.; deHaas, N. *J. Chem. Phys.* **1977**, *67*, 2388.

(132) Mordaunt, D. H.; Dixon, R. N.; Ashfold, M. N. R. *J. Chem. Phys.* **1996**, *104*, 6472.

(133) Gurvich, L. V.; Veyts, I. V.; Alcock, C. B. *Thermodynamic Properties of Individual Substances*, 4th ed.; Hemisphere Pub. Co.: New York, 1989.

(134) Benson, S. W. *The Foundations of Chemical Kinetics*; McGraw-Hill: New York, 1960.

(135) Zhao, Z.; Huskey, D. T.; Olsen, K. J.; Nicovich, J. M.; McKee, M. L.; Wine, P. H. *Phys. Chem. Chem. Phys.* **2007**, *9*, 4383.

(136) McKee, M. L.; Nicolaides, A.; Radom, L. *J. Am. Chem. Soc.* **1996**, *118*, 10571.

(137) Krasnoperov, L. N., New Jersey Institute of Technology, personal communication, 2006.

(138) Marshall, P., University of North Texas, personal communication, 2006.

(139) Xu, Z. F.; Lin, M. C. *J. Phys. Chem.* **2007**, *111*, 584.

(140) Mebel, A. M.; Morokuma, K.; Lin, M. C. *J. Chem. Phys.* **1995**, *103*, 7414.

(141) Berry, R. J.; Schwartz, M.; Marshall, P. *Computational Thermochemistry;* Irikura, K. K.; Frurip, D. J., Eds.; ACS Symp Ser 677; Washington, DC, 1998; Chap 18.

(142) Foresman, J. B.; Frisch, A. *Exploring Chemistry with Electronic Structure Methods*, 2nd ed.; Gaussian, Inc.: Pittsburgh, PA, 1996.

(143) Wigner, E. *Z. Physik. Chem.* **1932**, *B19*, 203.

(144) Cuiker, R. I.; Nocera, D. G. *Annu. Rev. Phys. Chem.* **1998**, *49*, 337.

(145) Stubbe, J.; van der Donk, W. A. *Chem. Rev.* **1998**, *98*, 705.

(146) Hammes-Schiffer, S. *Acc. Chem. Res.* **2001**, *34*, 273.

(147) Mayer, J. M.; Hrovat, D. A.; Thomas, J. L.; Borden, W. T. *J. Am. Chem. Soc.* **2002**, *124*, 11142.

(148) Stubbe, J.; Nocera, D. G.; Yee, C. S.; Chang, M. C. Y. *Chem. Rev.* **2003**, *103*, 2167.

(149) Mayer, J. M. *Ann. Rev. Phys. Chem.* **2005**, *55*, 363.

(150) Lingwood, M.; Hammond, J. R.; Hrovat, D. A.; Mayer, J. M.; Borden, W. T. *J. Chem. Theory Comput.* **2006**, *2*, 740.

(151) Miller, J. A.; Pilling, M. J.; Troe, J. *Proc. Combust. Inst.* **2005**, *30*, 43.

(152) Atkinson, R.; Aschmann, S. M. *Int. J. Chem. Kinet.* **1985**, *17*, 33.

(153) Wallington, T. J.; Skewes, L. M.; Siegl, W. O. *J. Photochem. Photobiol. A: Chem.* **1988**, *45*, 167.

(154) Nozière, B.; Lesclaux, R.; Veyret, B. *J. Phys. Chem.* **1990**, *98*, 2864.

(155) Shi, J.; Bernhard, M. *Int. J. Chem. Kinet.* **1997**, *29*, 349.

(156) Sokolov, O.; Hurley, M. D.; Wallington, T. J.; Kaiser, E. W.; Platz, J.; Nielsen, O. J.; Berho, F.; Rayez, M.-T.; Lesclaux, R. *J. Phys. Chem. A* **1998**, *102*, 10671.

(157) Alecu, I. M.; Gao, Y.; Hsieh, P.-C.; Sand, J. P.; Ors, A.; McLeod, A.; Marshall, P. *J. Phys. Chem. A* **2007**, *111*, 3970.

(158) Davico, G. E.; Bierbaum, V. M.; DePuy, C. H.; Ellison, G. B.; Squires, R. R. *J. Am. Chem. Soc.* **1995**, *117*, 2590.

(159) Heckmann, E.; Hippler, H.; Troe, J. *J. Proc. Combust. Inst.* **1996**, *26*, 543.

(160) Andersen, M. P. S.; Ponomarev, D. A.; Nielsen, O. J.; Hurley, M. D.; Wallington, T. J. *Chem. Phys. Lett.* **2001**, *350*, 423.

(161) Tanko, J. M.; Suleman, N. K. *Energetics of Organic Free Radicals*; Simoes, J. A. M.; Greenberg, A.; Liebman, J. F., Eds.;Blackie Academic & Professional: London, 1996; Vol. 4.

(162) Tsao, M.-L.; Hadad, C. M.; Platz, M. S. *J. Am. Chem. Soc.* **2003**, *125*, 8390.

(163) Adusei, G. Y.; Fontijn, A. *Proc. Combust. Inst.* **1994**, *25*, 801.

(164) Yu, T.; Lin, M. C. *Int. J. Chem. Kinet.* **1994**, *26*, 771.

(165) Kalinovski, I. J.; Gutman, D.; Krasnoperov, L. N.; Goumri, A.; Yuan, W.-J.; Marshall, P. *J. Phys. Chem.* **1994**, *98*, 9551.

(166) Russell, J. J.; Seetula, J. A.; Gutman, D. *J. Am. Chem. Soc.* **1988**, *110*, 3092.

(167) Seakins, P. W.; Pilling, M. J.; Niiranen, J. T.; Gutman, D.; Krasnoperov, L. N. *J. Phys. Chem.* **1992**, *96*, 9847.

(168) Nicovich, J. M.; Van Dijk, C. A.; Kreutter, K. D.; Wine, P. H. *J. Phys. Chem.* **1991**, *95*, 9890.

(169) Niiranen, J. T.; Gutman, D.; Krasnoperov, L. N. *J. Phys. Chem.* **1992**, *96*, 5881.

(170) Seetula, J. A. *Phys. Chem. Chem. Phys.* **2002**, *4*, 455.

(171) Benson, S. W.; Dobis, O. *J. Phys. Chem. A* **1998**, *102*, 5175.

(172) Atkins, P.; de Paula, J. *Physical Chemistry*, 7th ed.; Oxford University Press: New York, 2002.

(173) *NIST-JANAF Thermochemical Tables*, 4th ed.; American Chemical Society and American Institute of Physics: Woodbury, N. Y., 1998.

(174) Shimanouchi, T. *Tables of Molecular Vibrational Frequencies*; National Bureau of Standards, 1972; Vol. Consolidated Volume I.

(175) Łapiński, A.; Spanget-Larsen, J.; Langgård, M.; Waluk, J.; Radziszewski, J. G. *J. Phys. Chem. A* **2001**, *105*, 10520.

(176) Herzberg, G. *Electronic spectra and electronic structure of polyatomic molecules*; Van Nostrand: New York, 1966; Vol. 3.

(177) Berkowitz, J.; Ellison, G. B.; Gutman, D. *J. Phys. Chem. A* **1994**, *98*, 2744.

(178) Prosen, E. J.; Johnson, W. H.; Rossini, F. D. *J. Res. Nat. Bur. Stand.* **1946**, *36*, 455.

(179) Ervin, K. M.; DeTuri, V. F. *J. Phys. Chem. A* **2002**, *106*, 9947.

(180) Rodgers, A. S.; Golden, D. M.; Benson, S. W. *J. Am. Chem. Soc.* **1967**, *89*, 4578.

(181) McMillen, D. F.; Golden, D. M. *Ann. Rev. Phys. Chem.* **1982**, *33*, 493.

(182) Gauss, J.; Stanton, J. F. *J. Phys. Chem. A* **2000**, *104*, 2865.

(183) Herzberg, G. *Constants of Diatomic Molecules*; Van Nostrand Reinhold Company: New York, 1979; Vol. 4.

(184) Johnson III, R. D. 2004 Computational Chemistry Comparison and Benchmark Database http://srdata.nist.gov/cccdbd/.

(185) Read, W. G.; Campbell, E. J.; Henderson, G. *J. Chem. Phys.* **1982**, *78*, 3501.

(186) Walters, E. A.; Grover, J. R.; White, M. G. *J. Phys. Chem.* **1985**, *89*, 3814.

(187) Gotch, A. J.; Zwier, T. S. *J. Chem. Phys.* **1990**, *93*, 6977.

(188) Mons, M.; Dimicoli, I.; Piuzzi, F. *Int. Rev. Phys. Chem.* **2002**, *21*, 101.

(189) DeYonker, N. J.; Grimes, T.; Yockel, S.; Dinescu, A.; Mintz, B.; Cundari, T. R.; Wilson, A. K. *J. Chem. Phys.* **2006**, *125*, 104111.

(190) DeYonker, N. J.; Cundari, T. R.; Wilson, A. K. *J. Chem. Phys.* **2006**, *124*, 114104.

(191) Mebel, A. M.; Lin, M. C.; Yu, T.; Morokuma, K. *J. Phys. Chem.* **1997**, *101*, 3189.

(192) Curtiss, L. A.; Raghavachari, K.; Redfern, P. C.; Baboul, A. G.; Pople, J. A. *Chem. Phys. Lett.* **1999**, *314*, 101.

(193) Mayer, P. M.; Parkinson, C. J.; Smith, D. M.; Radom, L. *J. Chem. Phys.* **1998**, *108*, 604.

(194) Curtiss, L. A.; Redfern, P. C.; Raghavachari, K. *J. Chem. Phys.* **2007**, *126*, 084108.

(195) Wood, G. P.; Radom, L.; Petersson, G. A.; Barnes, E. C.; Frisch, M. J.; Montgomery, J. A. J. *J. Chem. Phys.* **2006**, *125*, 094106.

(196) Henry, D. J.; Parkinson, C. J.; Mayer, P. M.; Radom, L. *J. Phys. Chem. A* **2001**, *105*, 6750.

(197) Henry, D. J.; Parkinson, C. J.; Radom, L. *J. Phys. Chem. A* **2002**, *106*, 7927.

(198) Lau, K.-C.; Ng, C. Y. *J. Chem. Phys.* **2006**, *124*, 044323.

(199) Frenkel, M.; Marsh, K. N.; Wilhoit, R. C.; Kabo, G. J.; Roganov, G. N. *Thermodynamics of Organic Compounds in the Gas State*; Thermodynamics Research Center: College Station, TX, 1994.

(200) Jarzeba, W.; Thakur, K.; Hormann, A.; Barbara, P. F. *J. Phys. Chem.* **1995**, *99*, 2016.

(201) Ritter, E. R.; Bozzelli, J. W.; Dean, A. M. *J. Phys. Chem.* **1990**, *94*, 2493.

(202) Benson, S. W. *J. Am. Chem. Soc.* **1993**, *115*, 6969.

(203) Berho, F.; Rayez, M.-T.; Lesclaux, R. *J. Phys. Chem. A* **1999**, *103*, 5501.

(204) Henry, D. J.; Sullivan, M. B.; Radom, L. *J. Chem. Phys.* **2003**, *118*, 4849.

(205) Croft, A. K.; Howard-Jones, H. M. *Phys. Chem. Chem. Phys.* **2007**, *9*, 5649.

(206) Krasnoperov, L. N., New Jersey Institute of Technology, personal communication, 2009.

(207) Marshall, P., University of North Texas, personal communication, 2009.

(208) Wallington, T. J.; Andino, J. M.; Lorkovic, I.; Kaiser, E. W.; Marston, G. *J. Phys. Chem.* **1990**, *94*, 3644.

(209) Kaiser, E. W.; Wallington, T. J. *J. Phys. Chem. A* **1996**, *103*, 3216.

(210) Kaiser, E. W.; Wallington, T. J. *J. Phys. Chem. A* **1998**, *102*, 6054.

(211) Wallington, T. J.; Skewes, L. M.; Siegl, W. O.; Wu, C. H.; Japar, S. M. *Int. J. Chem. Kinet.* **1988**, *20*, 867.

(212) Maricq, M. M.; Szente, J. J.; Kaiser, E. W. *J. Phys. Chem.* **1993**, *97*, 7970.

(213) Lee, F. S. C.; Rowland, F. S. *J. Phys. Chem.* **1977**, *81*, 86.

(214) Iyer, R. S.; Rogers, P. J.; Rowland, F. S. *J. Phys. Chem.* **1983**, *87*, 3799.

(215) Atkinson, R.; Aschmann, S. M. *Int. J. Chem. Kinet.* **1985**, *19*, 1097.

(216) Stutz, J.; Ezell, M. J.; Finlayson-Pitts, B. J. *J. Phys. Chem. A* **1997**, *101*, 9187.

(217) Pilgrim, J. S.; Taatjes, C. A. *J. Phys. Chem. A* **1997**, *101*, 4172.

(218) Dobis, O.; Benson, S. W. *J. Am. Chem. Soc.* **1990**, *112*, 1023.

(219) Dobis, O.; Benson, S. W. *J. Am. Chem. Soc.* **1991**, *113*, 6377.

(220) Parmar, S. S.; Benson, S. W. *J. Phys. Chem.* **1988**, *92*, 2652.

(221) Takahashi, K.; Yamamoto, O.; Inomata, T. *Proc. Combust. Inst.* **2002**, *29*, 2447.

(222) Russell, J. J.; Senkan, S. M.; Seetula, J. A.; Gutman, D. *J. Phys. Chem.* **1989**, *93*, 5184.

(223) Knyazev, V. D.; Kalinovski, I. J.; Slagle, I. R. *J. Phys. Chem. A* **1999**, *103*, 3216.

(224) Engels, B.; Peyerimhoff, S. D.; Skell, P. S. *J. Phys. Chem.* **1990**, *94*, 1267.

(225) Chen, Y.; Tschuikow-Roux, E. *J. Phys. Chem.* **1992**, *96*, 7266.

(226) Seetula, J. A. *J. Chem. Soc. Faraday Trans.* **1998**, *94*, 891.

(227) Seetula, J. A. *J. Chem. Soc. Faraday Trans.* **1998**, *94*, 1933.

(228) Hoz, T.; Sprecher, M.; Basch, H. *Isr. J. Chem.* **1983**, *23*, 109.

(229) Hoz, T.; Sprecher, M.; Basch, H. *J. Phys. Chem.* **1985**, *89*, 1664.

(230) Schlegel, H. B.; Sosa, C. *J. Phys. Chem.* **1984**, *88*, 1141.

(231) Barat, R. B.; Bozzelli, J. W. *J. Phys. Chem.* **1992**, *96*, 2494.

(232) Organisation for Economic Co-operation and Development Screening Information Data Set (OECD SIDS): Sulfuryl Chloride. Available from: http://www.chem.unep.ch/irptc/sids/OECDSIDS/7791255.pdf; UNEP Chemicals, 2002.

(233) Gao, Y.; Marshall, P. *Proc. Combust. Inst.* **2009**, *32*, 351.

(234) Uthman, A. P.; Demlein, P. J.; Allston, T. D.; Withiam, M. C.; McClements, M. J.; Takacs, G. A. *J. Phys. Chem.* **1978**, *82*, 2252.

(235) Ichimura, T.; Mori, Y. *J. Chem. Phys.* **1973**, *58*, 288.

(236) Ichimura, T.; Mori, Y.; Shinohara, H.; Nishi, N. *Chem. Phys. Lett.* **1994**, *189*, 117.

(237) Ahyens, Y. V.; Nicovich, J. M.; McKee, M. L.; Wine, P. H. *J. Phys. Chem. A* **1997**, *101*, 9382.

(238) Atkinson, R.; Baulch, D. L.; Cox, R. A.; Crowley, J. N.; Hampson, R. F.; Hynes, R. G.; Jenkin, M. E.; Rossi, M. J.; Troe, J. *Atmos. Chem. Phys.* **2006**, *6*, 3625.

(239) Holmes, J. L.; Lossing, F. P. *J. Am. Chem. Soc.* **1988**, *110*, 7343.

(240) Miyokawa, K.; Tschuikow-Roux, E. *J. Phys. Chem.* **1990**, *94*, 715.

(241) Brana, P.; Menendez, B.; Fernandez, T.; Sordo, J. A. *J. Phys. Chem. A* **2000**, *104*, 10842.

(242) Gao, Y.; Alecu, I. M.; Hsieh, P.-C.; McLeod, A.; McLeod, C.; Jones, M.; Marshall, P. *Proc. Combust. Inst.* **2007**, *31*, 193.

(243) Chen, K. S.; Elson, I. H.; Kochi, J. K. *J. Am. Chem. Soc.* **1973**, *95*, 5341.

(244) Kawamura, T.; Edge, D. J.; Kochi, J. K. *J. Am. Chem. Soc.* **1972**, *94*, 1752.

(245) Balint-Kurti, G. G.; Martson, C. C. *J. Chem. Phys.* **1989**, *91*, 3571.

(246) Johnson III, R. D. FGH1D Program, 1999. http://www.nist.gov/compchem/johnson/fgh/fgh1d.html.

(247) Ervin, K. M.; Gronert, S.; Barlow, S. E.; Gilles, M. K.; Harrison, A. G.; Bierbaum, V. M.; DePuy, C. H.; Lineberger, W. C.; Ellison, G. B. *J. Am. Chem. Soc.* **1990**, *112*, 5750.

(248) Szabo, A.; Ostlund, N. S. *Modern Quantum Chemistry: Introduction to Advanced Electronic Structure Theory*; Dover Publications, Inc.: Mineaola, NY, 1996.

(249) Letestu, S. Inernational Meteorological Tables; World Meteorological Organization, WMO-No. 118.TP.94: Geneva, Switzerland, 1966, with amendments thru July 1973.

(250) List, R. J. Smithsonian Meteorological Tables, Smithsonian Miscellaneous Collections, vol. 114, Publication 4014; Smithsonian Institute Press, 6th revised edition, 1949, 5th reprint 1971.

(251) *Manual of Barometry (WBAN)*, First ed.; U.S. Department of Commerce, Weather Bureau: Washington, D. C., 1963; Vol. 1.

(252) Teledyne Hastings-Raydist. In *Hastings Model HBM-1A Mini-Flo Calibrator* Hampton, VA, 1988.

(253) Powers, S. K.; Howley, E. T. *Exercise Physiology: Theory and Application of Fitness and Performance*; McGraw-Hill: New York, NY, 2004.

(254) Heberger, K.; Kemeny, S.; Vidozy, T. *Int. J. Chem. Kinet.* **1987**, *19*, 171.